Theses and Dissertations

2012

# Magnetoelectrocatalysis: enhanced heterogeneous electron transfer reactions at modified electrodes, Grätzel cells, and manganese dioxide electrodes

Garett Gordon Walter Lee

*University of Iowa*

MAGNETOELECTROCATALYSIS: ENHANCED HETEROGENEOUS

ELECTRON TRANSFER REACTIONS AT MODIFIED ELECTRODES,

GRÄTZEL CELLS, AND MnO$_2$ ELECTRODES

by

Garett Gordon Walter Lee

An Abstract

Of a thesis submitted in partial fulfillment
of the requirements for the Doctor of
Philosophy degree in Chemistry
in the Graduate College of
The University of Iowa

May 2012

Thesis Supervisor: Associate Professor Johna Leddy

ABSTRACT

Magnetoelectrocatalysis is a physical, catalytic process. When magnetic microparticles are incorporated at an electrode surface, increases in current and system efficiency are observed. These enhancements have been observed in both homogeneous and heterogeneous systems. Here, the effects of magnetic fields on three separate, yet related, systems are analyzed: fundamental heterogeneous electron transfer rates at modified electrodes, dye sensitized solar cells (DSSC), and $MnO_2$ electrodes for supercapacitor applications.

Previous studies of magnetic field effects on homogeneous systems utilized the cation exchange polymer Nafion and transition metal redox probes, such as tris(bipyridine)ruthenium(II), $Ru(bpy)_3^{2+}$. At electrodes modified with Nafion films, redox probes experience current enhancements in the presence of a magnetic field. This effect is attributed to increased self exchange, known as Dahms Ruff conduction or hopping between redox species. Here, the impacts of magnetic fields on heterogeneous electron transfer, the electron transfer between the redox probe and electrode, are demonstrated. A derivative of Nafion, TMODA Nafion, is used for electrode modification. For transition metal complex redox probes, peak splitting in cyclic voltammagrams are lower for magnetically modified electrodes as compared to analogous nonmagnetic films.

The effects of magnetic modification on DSSCs are analyzed. DSSCs are photoelectrochemical cells (PECs) that convert incident light (photons) to electrical power (electrons). DSSCs, or Grätzel cells, are heterogeneous, excitonic devices that undergo multiple electron transfer reactions. For studies here, magnetic modification

of the electrodes occurs within the semiconductor layer. Enhancements in current density ($J_{SC}$), fill factor (FF), and power output ($W_{max}$) are observed in a variety of systems for n-type and p-type, as well as, on glass and PET substrates, utilizing different magnetic microparticles.

Lastly, the effects of magnetic fields on the electrochemistry of electrolytic $MnO_2$ (EMD) electrodes are examined. $MnO_2$ is an abundant, naturally occurring oxide of manganese that is used ubiquitously in alkaline batteries. $MnO_2$ is a complex material, existing, as many transition metal oxides do, in several polymorphs, each with unique properties. For the studies here, the use of $MnO_2$ as a capacitor material in mild aqueous systems is examined. In comparison to traditional electrochemical capacitors, $MnO_2$ undergoes both nonfaradaic and faradaic charge storage. Magnetic field effects look to exploit this faradaic, pseudocapacitance behavior as a mechanism for increasing the energy and power density.

Abstract Approved:       _____

                   Thesis Supervisor

                   _____

                   Title and Department

                   _____

                   Date

MAGNETOELECTROCATALYSIS: ENHANCED HETEROGENEOUS

ELECTRON TRANSFER REACTIONS AT MODIFIED ELECTRODES,

GRÄTZEL CELLS, AND MnO$_2$ ELECTRODES

by

Garett Gordon Walter Lee

A thesis submitted in partial fulfillment
of the requirements for the Doctor of
Philosophy degree in Chemistry
in the Graduate College of
The University of Iowa

May 2012

Thesis Supervisor: Associate Professor Johna Leddy

Graduate College
The University of Iowa
Iowa City, Iowa

CERTIFICATE OF APPROVAL

_____

PH.D. THESIS

_____

This is to certify that the Ph.D. thesis of

Garett Gordon Walter Lee

has been approved by the Examining Committee for the thesis
requirement for the Doctor of Philosophy degree in Chemistry
at the May 2012 graduation.

Thesis Committee:  _____
                   Johna Leddy, Thesis Supervisor

                   _____
                   Mark A. Arnold

                   _____
                   Edward G. Gillan

                   _____
                   Lei Geng

                   _____
                   Julie Jessop

To my family.

ACKNOWLEDGEMENTS

Wow, what a journey! One that could not have happened without the support of family and friends. To my parents Gary and Lana, to my sister Bridget and my brother Spencer, to my nephew Cooper and the rest of my wonderful family. To my research advisor, Dr. Leddy, an accomplished and respected scientist who not only teaches all her students to think critically and independently, but also reminds us that there is more to life than just science. To my research group, members new and old, Chet Duda, Luke Haverhals, Krysti Knoche, Hueng Chan Lee, Perry Motsegood, Tim Paschkewitz, Jessica JJ Reed, Sarah Cyrus, and Emily Mrugacz. To my triathlon friends who helped me accomplish that other goal and who helped teach me that there is almost no better metaphor for the Ph.D. than the Ironman. Also, to The University of Iowa Department of Chemistry, Dr. Ed Gillan and his graduate student Nate Coleman, as well as glassblower Peter Hatch. And to the people before Iowa, my friends and mentors in Morris who sent me down this path.

TABLE OF CONTENTS

# LIST OF TABLES

LIST OF FIGURES

Figure

ix

CHAPTER 1

INTRODUCTION

Energy is a basic need, as energy use is ubiquitous in transportation, work, and leisure. However, anthropogenic production and consumption of energy is markedly inefficient. We derive much of our energy through the combustion of fossil fuels, yet, oxidation in engines with multiple parts is limited thermodynamically as described by Carnot [3]. This inefficiency is present in automobile internal combustion engines and fossil fuel power plants, and no matter what advancements occur, such as increased fuel efficiency vehicles, the fact remains that combustion is thermodynamically limited.

In addition to our poor use of energy, our thirst for energy nationally and globally is increasing [4]. Global development, especially in the far east, has led countries such as China to be the global leader in coal consumption [5]. This thirst for energy has ramifications on our planet's viability, including global climate change.

Electrochemistry offers energy solutions. Electrochemical systems often do not suffer the thermodynamic limitation of combustion derived energy. However, kinetic limitations exist [1].

One possible energy solution is photoelectrochemical cells. These devices convert incident radiation into electrical energy. This energy can be used directly in a manner akin to conventional p-n photovoltaics or the energy can be stored for later consumption. Fundamentally, the electrochemical process or paradigm for

photoelectrochemical systems is as in equation 1.

$$Capture \longrightarrow Convert \rightarrow Store \rightarrow Use \tag{1}$$

When the sun is shining, it makes sense to use this energy directly. However, having stored energy either chemically or electrochemically is necessary to provide uninterrupted energy once the sun sets. In nature, this process is realized in photosynthesis, where plants store photonic energy in chemical bonds. But photosynthesis is remarkably inefficient; only $\sim$0.1 % of incident radiation is converted to energy stored as biomass [6]. Photosynthesis, however, does offer researchers a template by which to capture, convert, and store energy through artificial photosynthetic means [4, 6, 7].

Photoelectrochemical cells offer a means of mimicking photosynthesis [8]. Devices that store the energy chemically are called photosynthetic cells. Often these man made devices are used to drive hydrolysis and energy is stored chemically as molecular hydrogen. Unused energy can also be stored electrochemically, in devices such as batteries and capacitors. The potential energy of sunlight makes these devices attractive. In fact, the energy from the sun is so large that we receive the equivalence of total energy demand for a year in one hour from the sun [4].

If electrochemistry has the potential to provide these solutions to our energy problem, why are electrochemical devices such as photoelectrochemical cells and chemical and electrochemical storage not yet common place? These devices may not suffer the thermodynamic limitations of combustion, however, many processes are kinetically limited.

Optimizing kinetic efficiency in each step of this energy hierarchy is a principal goal of electrochemical energy research. Two decades of research on Grätzel cells, a type of third generation photovoltaic, have resulted in efficiencies of only 12.3 %; these devices should in *principle* be far more efficient [9]. It is yet unknown, but it is speculated that these DSSC devices will not be limited by the Shockley-Queisser limit of 32 % [10].

Magnetic field effects offer a possible solution to increasing the kinetic efficiencies of electrochemical systems. Previous research at The University of Iowa has examined the physical catalytic effects of magnetic fields in electrochemical systems. This research is both fundamental and applied. Shelley Minteer, Wayne Gellett, and Heung Chan Lee examined the improved efficiency of homogeneous electron transfer reactions in the presence of magnetic fields [11–13]. Wayne Gellet, Drew Dunwoody, and Luke Haverhals demonstrated improved fuel cell efficiency for magnetically modified systems [12, 14]. Tesene and Ünlü improved battery efficiency with magnetically modified half cell electrodes [15, 16]. Most recently, H. C. Lee, demonstrated a reduction in the overpotential required to reduce hydrogen at magnetically modified p-Si electrodes. These effects are attributed to increases in electron transfer kinetic efficiency.

In this dissertation, I, too, have set out to analyze how local magnetic fields can increase the efficiency of electrochemical systems. In magnetoelectrocatalysis, a physical catalytic process, micromagnets supply magnetic fields that facilitate electron transfer events by physical catalysis. This dissertation details the capability magnets have to affect the electrochemical energy paradigm. Grätzel cells, a type of

photoelectrochemical cell, have been modified to demonstrate the catalytic potential of magnetic field effects in the capture and conversion steps in 1. Magnetically modified supercapacitors, an electrochemical power storage device, demonstrate how magnets affect the storage and use aspect of the paradigm.

## 1.1   Grätzel Cells

Grätzel cells are a type of dye sensitized solar cell (DSSC) that are more broadly classified as photoelectrochemical cells (PEC) [17]. Grätzel cells convert incident light into electrical energy. DSSC research began in the mid twentieth century with the sensitization of single crystalline semiconductors. However, it was not until 1991 when Grätzel and his coworkers showed that a creative combination of inexpensive materials can be used to produce a photovoltaic with conversion efficiencies at or near that of traditional p-n-junction solar cells [10]. These devices produce energy at low cost, $0.60/W, about a fifth the cost of traditional photovoltaics [4,18]. However, despite well established materials, improvements in photoconversion efficiency are made slowly because the complex DSSC system suffers from limitations in both materials and the fundamental dynamics of electron transfer kinetics and solid state diffusion. These devices suffer economically as well; energy from these devices is still many times more expensive than fossil fuel derived energy.

Grätzel cells are heterogeneous devices in that they separate the function of charge generation from charge transport into two distinct chemical phases. These devices incorporate multiple electron transfer reactions, both homogeneous and heterogeneous. These properties make them an ideal system to demonstrate

magnetic field effects.

Electronically, DSSCs are constrained by the standard reduction potential of the redox mediator in solution and the Fermi level of the semiconductor. The Fermi level is the average energy of the charge carriers in the semiconductor. To date, nanocrystalline $TiO_2$ is the best semiconductor for DSSCs, with an $E_f$ = -0.5 V vs. saturated calomel electrode (SCE). It is commonly coupled with the iodine triiodide couple in an organic solvent such as acetonitrile or propylene carbonate, which has an $E^0$ = 0.4 V vs. SCE [18]. This creates the maximum open circuit potential ($V_{OC}$) of 0.9 V. The $V_{OC}$, a thermodynamic or equilibrium process, is most likely unaffected by field effects. Given previous observations of magnetic field effects, increased current response manifests in increased photocurrent, which translates into increased power output and increased conversion efficiencies [12,13].

Here, the effects of magnetic fields on the efficiency of the Grätzel cells are examined. Magnetic modification of the system occurs within the semiconductor layer. In Chapter 3, considerations for fabricating electrodes that contain magnetic particles include particle field strength, morphology, coatings, and specifically the physical constraints that magnetic particles place on DSSC fabrication. Magnetic particles have been incorporated in both n- and p-type semiconductors and on both glass and plastic substrates. In Chapter 4, analysis and results of these studies are presented. It is shown that average photocurrent enhancements of 40 % are observed for magnetically modified electrodes versus control nonmagnetic electrodes; these observations are statistically vetted.

To demonstrate the potential of magnetic field effects throughout the electrochemical energy spectrum, magnetic field effects in electrochemical capacitors was also analyzed. This work follows that of Tesene and Ünlü, both of whom observed increases in electrochemical performance of magnetically modified alkaline batteries [15, 16]. Tesene concluded that the enhancement in performance can be attributed to an increase in electron transfer rates, or equivalent electron conduction, through the $MnO_2$ network. In the application here, $MnO_2$ is used in a mild aqueous solution as an electrochemical capacitor.

## 1.2    Supercapacitors

Supercapacitors are electrochemical power devices [19]. These devices fall between traditional electrostatic capacitors and batteries in the energy power hierarchy as displayed, for example on a Ragone plot. They have a higher power density and lower energy density than batteries. In supercapacitors, two mechanisms for charge storage exist: both nonfaradaic, electrostatic capacitance as in traditional electrochemical capacitors, and faradaic charge storage by a mechanism called pseudocapacitance. This faradaic mechanism involves a heterogeneous electron transfer from the metal oxide electrode to a solution based species that results in adsorbed surface charge.

Transition metal oxides, such as $MnO_2$ or $RuO_2$, allow this faradaic charge storage and are capable of capacitances of 100 to 200 F/gram for powder based electrodes, and 600 F/gram for thin films [20, 21]. In Chapter 5, it is demonstrated that magnetic fields increase pseudocapacitance at powder based $MnO_2$ electrodes. The increased capacitance is attributed to magnetic field effects on the faradaic

component of the $MnO_2$ system because of an increase in the efficiency of the heterogeneous electron transfer. The system has been prepared as thin pellet, powder based composite electrodes tested in half cells. Capacitance enhancement of up to 50 % are demonstrated over a variety of magnetic particle loading percentages and current densities. These results are statistically verified.

## 1.3    Heterogeneous Electron Transfer Rates

In addition to Grätzel cells and electrochemical capacitors, magnetic field effects on the heterogeneous electron transfer rate at modified electrodes with academically interesting transition metal redox probes were analyzed. These analyses show on a fundamental level the effects of magnetoelectrocatalysis. Measurements were performed using a chemically modified form of the ion exchange polymer Nafion®, TMODA (trimethyloctadecylamine) Nafion [22, 23].

TMODA Nafion has increased micellar pore size that results in increased diffusional flux. Increased pore size also minimizes the electron hopping mechanism seen in Nafion films as the pores are larger than a single redox moiety [11, 13]. In addition to the increased pore size, TMODA does not act as an cation selective polymer. This allowed for the first measurement of magnetic enhancements on an anionic redox species, $Fe(CN)_6^{3-}$. These measurements were then used to calculate the effect on the heterogeneous rate constant, $k^0$. Increases of an order of magnitude for the heterogeneous rate constant in the presence of a magnetic field were observed. These measurements clearly demonstrate a magnetic effect on heterogeneous electron transfer.

CHAPTER 2

MAGNETIC FIELD EFFECTS ON HETEROGENEOUS ELECTRON TRANSFER

REACTIONS

## 2.1   Introduction

Electron transfer reactions are a class of simple, chemical reactions. These reactions occur in both homogeneous and heterogeneous systems, and in both living systems and power sources. Chemical kinetics are used to describe these processes. No two processes are identical, they are affected by both chemical and physical system properties. When the electron transfer reaction is facile, the system is said to have fast kinetics and is associated with large rate constant, k. Systems with hindered reaction kinetics, also referred to as kinetically limited systems, have smaller values of k.

Magnetic fields have been shown to affect electron transfer reactions in both homogeneous and heterogeneous systems [11–13, 15]. Magnetic field effects on homogeneous systems have been studied experimentally and modeled [11, 13]. Fundamental analyses have focused extensively on magnetic enhancements of homogeneous, self exchange, reactions. These measurements are performed at polymer modified electrodes containing ferromagnetic microparticles. Academically interesting redox probes, such as transition metal complexes, are used to make these measurements. In the cation exchange polymer Nafion (DuPont), the equilibrated concentration of electroactive species reaches a point at which electron conduction

through the redox moiety occurs. It has been shown that in the presence of a magnetic field, this rate of conduction, also called hopping, increases. This increased hopping rate increases current response, i.e., the magnetic enhancement.

Magnetic field effects have also been implemented in electrochemical energy and power systems. In these systems, such as fuel cells and batteries, the phenomenon of magnetoelectrocatalysis increases a system's efficiency. In batteries, for example, increased conduction or hopping though the electroactive material increases the kinetic facility of the system. This produces a system in which power is high and efficiency approaches the thermodynamic limit.

To date, studies on the effects of magnetic fields on heterogeneous electron transfer reactions have been limited. Minteer mathematically modeled this effect on intersystem cross over reactions, however, the associated experimental data was limited. Conversely, Lee examined the effects of magnetic fields on the hydrogen evolution reaction at semiconductor electrodes. Lee observed a decrease on the overpotential required to drive the reaction by nearly *1200 mV*. This brought the applied potential (E) much nearer the thermodynamic value ($E^{0'}$). However, measurements *of heterogeneous electron transfer rates* at solid state electrodes have been limited.

Here, measurements of magnetic field effects on the heterogeneous electron transfer rate have been made. These are, to date, the first measurements of their kind. These measurements are performed using similar methodology to the aforementioned homogeneous measurements at polymer modified electrodes. For voltammetric measurements, increased current responses are observed as well

as decreases in the peak splittings. Commercially available, coated magnetite microparticles (Bangs Labs) are used to supply (or generate) the magnetic field. A Nafion derivative, TMODA (trimethyloctadecylamine) Nafion, creates a stable matrix for magnetic microparticles. Changes in physical and chemical properties with TMODA incorporation include increased micellar pore size, decreased ion selectivity, increased pH (less acidic); these properties radically change the extraction characteristics of Nafion. These differences are essential for making heterogeneous measurements. Data analysis consists of a method developed by Nicholson and Shain, as well as additional considerations found in Paul and Leddy [24–26].

### 2.1.1 Magnetic Effects on Homogeneous and Heterogeneous Electron Transfer Kinetics

Electrons have properties of mass, spin, and charge. Electric fields largely couple electrostatically with electron charge. Magnetic fields largely couple with electron spin. Magnetic field effects are apparent in electrochemical reactions because somewhere on the path from reactant to product, at least one reactant, product, or intermediate has an unpaired electron. Chemical species with unpaired electrons are radicals where 0, 1, 2, and 3 unpaired electrons are singlets (S), doublets (D), triplets (T), and quartets (Q).

Electrochemical reactions can occur in a single phase as a homogeneous electron transfer or at the interface between two phase as a heterogeneous electron transfer. Most typically, heterogeneous electron transfer refers to electron transfer between and electrode and a chemical species either in the bulk phase or as an adsorbate.

Homogeneous reactions include cross exchange reactions in which two distinct chemical species in a single phase come together and transfer an electron between them. The energy of the products and reactants are usually different. The simplest homogeneous electron transfer reaction is a self exchange reaction in which two different oxidation states of a single chemical species come together and transfer an electron such that the products and reactants are the same but the species undergo an effective transposition in space. If the reactant reduced species $M^{n+}$ is at position $x$ and the oxidized species $M^{n+1}$ is at position $y$, in the self exchange reaction positions are exchanged.

$$M_x^{n+} + M_y^{n+1} \rightleftharpoons M_x^{n+1} + M_y^{n+} \tag{2}$$
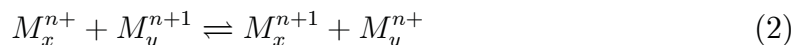
The energy of the reactants and products are the same. Transition metal complexes such as $Ru\,(bpy)_3^{2+}$ and $Ru\,(bpy)_3^{3+}$ are common in self exchange reactions. $Ru\,(bpy)_3^{2+}$ and $Ru\,(bpy)_3^{3+}$ are a singlet and doublet, respectively.

The energy along the reaction path is illustrated in the reaction coordinate diagram of Figure 1. The reactants and products are the same and therefore isoenergetic. In this diagram, the reaction of a singlet and doublet are shown. In the classical kinetic description of activated complex theory (ACT), the $S$ and $D$ come together to form an activated complex, represented as $[SD]$. There is an energetic tax of $\Delta H_0^{\ddagger}$ for this process. The entropy of the process, $\Delta S_0^{\ddagger}$ is represented by the width of the curve. The rate is established according to an Arrhenius expression based on the energy tax up to the instant of isoenergetic electron transfer. That is, all the atomic entities are appropriately configured that the isoenergetic electron
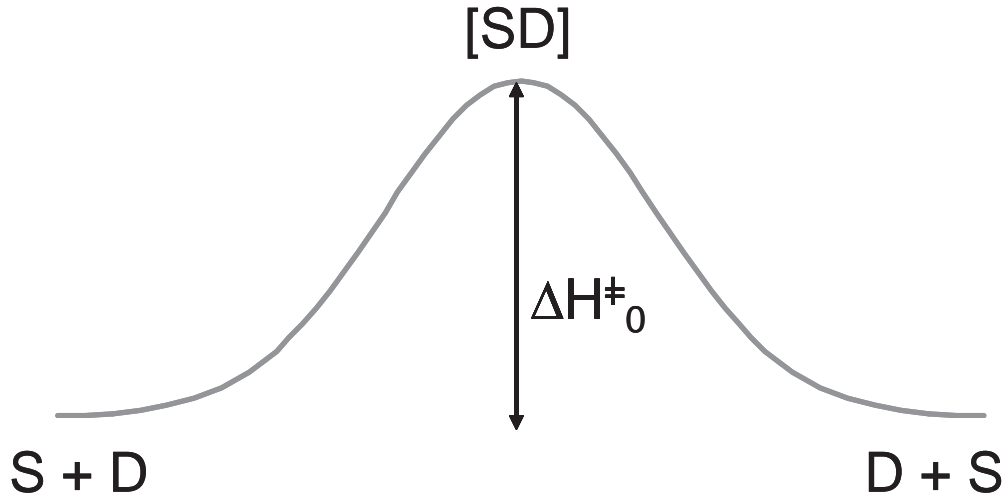
Figure 1. Isoenergtic reaction coordinate diagram for a singlet (S) doublet (D) self exchange reaction.

transfer is rapid (Franck Condon principle). Here, the correct configuration is represented as $[SD]$ The free energy of activation exclusive of magnetic effects, $\Delta G_0^{\ddagger}$, is then

$$\Delta G_0^{\ddagger} = \Delta H_0^{\ddagger} - T\Delta S_0^{\ddagger} \tag{3}$$

The subscript zero describes parameters exclusive of magnetic effects. In the Arrhenius development, the rate of a reaction is

$$k = A\exp\left[-\frac{\Delta G_0^{\ddagger}}{k_b T}\right] \tag{4}$$

$$= A\exp\left[-\frac{\Delta H_0^{\ddagger}}{k_b T}\right]\exp\left[\frac{\Delta S_0^{\ddagger}}{k_b}\right] \tag{5}$$

where the parameter $A$ is called the pre-exponential factor, collision frequency, or frequency factor. In classical rate theory as by Eyring, $A = k_b T/h$ where $k_b = 1.3806568 \times 10^{-23}\,\mathrm{J\,K^{-1}}$ is the Boltzmann constant and $h = 6.6260755 \times 10^{-34}\,\mathrm{J\,s}$

is Planck's constant.

The ACT model for self exchange is modified to account for the magnetic effects by accounting for two magnetically susceptible events: electron nuclear spin polarization and prepolarization of the electron spin of the reactants. This material is first proposed in the dissertation of Minteer [11] and then more fully developed in the dissertation of H.C. Lee [13].

**ensp:** In electron nuclear spin polarization (ensp) reaction between a singlet and a radical is best characterized. For illustration, allow the radical is a doublet. Represent the unpaired electron spin as $\upharpoonright$ such that the doublet is $D^{\upharpoonright}$. The singlet and doublet form an activated complex. Once in the activated complex, the electron spin on the nucleus couples to the nuclear spin of the singlet. Let the nuclear spin be represented as $\uparrow$ such that the nuclear spin of the singlet is shown as $S^{\uparrow}$. The nuclear spin is not a significant factor outside of the activated complex. The process is then

$$S + D^{\upharpoonright} \overset{K}{\rightleftharpoons} \left[ S^{\uparrow} D^{\upharpoonright} \right] \tag{6}$$

$$\left[ S^{\uparrow} D^{\upharpoonright} \right] \overset{k_1}{\underset{k_{-1}}{\rightleftharpoons}} \left[ SD \right]^{\uparrow\upharpoonright} \tag{7}$$
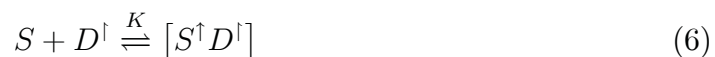
where $\left[ S^{\uparrow} D^{\upharpoonright} \right]$ is the state of the complex just prior to ensp and $\left[ SD \right]^{\uparrow\upharpoonright}$ denotes the complex immediately after ensp where $\uparrow\upharpoonright$ indicates that the radical unpaired electron is now polarized or coupled to the nuclear spin of the singlet.

The pre-equilibrium constant $K$ characterizes the electrostatic components of bringing the components together. $K$ is based in activity theory and largely arises out DeBye Huckel considerations. $K$ is unchanged from $K$ from ACT absent spin

effects. It is likely that that the bulk of the enthalpy of activation, $\Delta H_0^{\ddagger}$, for outer sphere electron transfer events is the electrostatic component of forming the complex.

The rate constants $k_1$ and $k_{-1}$ are the rates of formation and disassociation of the electron nuclear spin polarized complex. $k_1$ and $k_{-1}$ are introduced to ACT to characterize the magnetic effects on spin. Both are included as rates because the time constant for forming electron nuclear spin polarized complex is not rapid as compared to mass transport events in solution. The energy of the complex prior to ensp, $\left[S^{\uparrow}D^{\uparrow}\right]$, is $gHS\beta$ above $\Delta H_0^{\ddagger}$. The energy of the complex after ensp is $gHS\beta$ below $\Delta H_0^{\ddagger}$. The magnetic properties of the radical are embedded in the measured $g$ value and spin $S$. For an isolated unpaired electron, $g = 2$ and $S = 1/2$. The magnetic intensity is $H$ in Tesla or Gauss, where $1\ T = 10^4\ G$. When the matrix is not magnetizable as in an electrolyte solution, the magnetic intensity and magnetic field are the same. The Bohr magneton, $\beta = 9.2740154 \times 10^{-24}\ \mathrm{J\,T^{-1}}$. The complex is at the instant of electron transfer once $[SD]^{\uparrow\uparrow}$ is formed.

The ensp events are part of the information summarized in Figure 2. The grey line is the classical ACT model shown in Figure 1 where magnetic effects are not considered. The enthalpy absent magnetic effects is the height of this curve, $\Delta H_0^{\ddagger}$. Magnetic effects are shown in the black line. The energetics of ensp are shown about the middle of the figure at the tops of the barrier. The complex prior ensp, $\left[S^{\uparrow}D^{\uparrow}\right]$, is shown above $\Delta H_0^{\ddagger}$ by $gHS\beta$. The complex after ensp, $\left[S^{\uparrow}D^{\uparrow}\right]$, is shown below $\Delta H_0^{\ddagger}$ by $gHS\beta$. In this model, it is assumed that the spin of the complex is inherited from the reactants. If spin is inherited, there is no change in the spin entropy once the complex is formed.
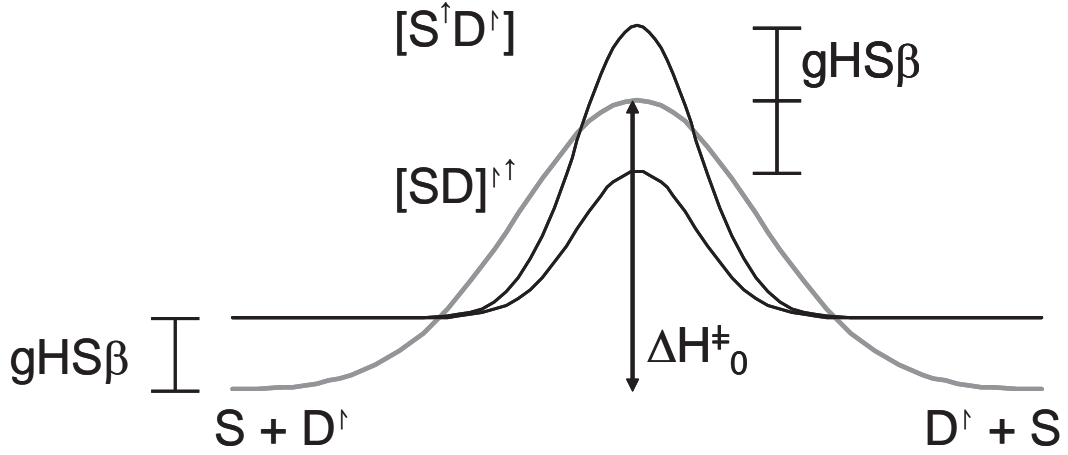
Figure 2. Reaction coordinate diagram for the energetics associated with magentic field effects.

To this point, the rate of electron transfer is set by the rate of the formation and disassociation of the electron nuclear spin polarized complex, $k \propto k_1 - k_{-1}$.

**Prepolarization:** The other event to considered is pre-polarization of the electron spins on the radical prior to formation of the complex. For a pre-polarization rate, $k_p$, the rate is

$$k = k_p \left( k_1 - k_{-1} \right) \tag{8}$$

If the magnetic field is sufficiently strong, as to prepolarize the unpaired spin, then two effects are observed. First, the energy of the reactants is raise by $gHS\beta$ before the complex is formed. This is an impact on enthalpy in which the height of the barrier is reduced by $gHS\beta$. The second impact is on the entropy of the system. In consideration of magnetic effects, the entropy of the unpaired spins is important. Boltzmann's equation specifies the entropy $S$ in terms of the probability of states,

$P_i$ for each $i^{th}$ state.

$$\frac{S}{k_b} = -\sum_i P_i \ln P_i \tag{9}$$

In the absence of an external field, one unpaired spin which can be in either of two states (up or down) such that $S_{spin}/k_b = -\ln\frac{1}{2} = 0.7$, where $S_{spin}$ is the entropy with spin in the absence of a sufficient magnetic field. In this model, the spin of the complex $\left[SD^\dagger\right]$ is inherited from the reactants so that the spin entropy of the product $\left[SD^\dagger\right]$ is zero. Then, for insufficient applied field and one unpaired electron, $\Delta S_{spin}/k_b = 0 - \left(-\ln\frac{1}{2}\right) = \ln\frac{1}{2}$. In the presence of a sufficient field that prepolarization occurs, there is only one state and $P_i = 1$ such that $S_{p,spin} = 0$, where $S_{p,spin}$ characterizes the entropy under a sufficient magnetic field that prepolarization of reactants occurs. Again spin is inherited in the complex, so when prepolarized, $\Delta S_{p,spin}/k_b = 0$ and the entropy of the spin is eliminated.

The prepolarization event occurs without collision but with a time constant similar to ensp events. For sufficient field, the prepolarization constant is expressed as follows where $\Delta H_p$ and $\Delta S_p$ are the enthalpy and entropy of the prepolarization. $\Delta S_p = \Delta S_{p,spin} = 0$.

$$\begin{aligned} k_p(H) &= \exp\left[-\frac{\Delta H_p}{k_b T}\right] \exp\left[\frac{\Delta S_p}{k_b}\right] \tag{10} \\ &= \exp\left[-\frac{gHS\beta}{k_b T}\right] \tag{11} \end{aligned}$$

In the absence of sufficient external field, where $gHS\beta \longrightarrow 0$, the electron spin contribution $\Delta S_{spin}$ is found. Define the prepolarization constant, $k_p(H = 0)$ to account for a field insufficient to prepolarize the reactant spins and $gHS\beta \longrightarrow 0$. Allow there are $m$ unpaired spins on the radical, such that there are $\left(\frac{1}{2}\right)^m$ states,

each with probability $P_i = \left(\frac{1}{2}\right)^m$. Then, for spin inherited and reaction of a singlet

and a radical, $\Delta S_{spin}/k_b = 0 - \left(-\sum_i P_i \ln P_i\right) = \ln P_i = m \ln \frac{1}{2}$

$$k_p\left(H = 0\right) = \lim_{gHS\beta \to 0} \exp\left[-\frac{\Delta H_p}{k_b T}\right] \exp\left[\frac{\Delta S_{spin}}{k_b}\right] \tag{12}$$

$$= \exp\left[\frac{\Delta S_{spin}}{k_b}\right] = \exp\left[\ln\left(\frac{1}{2}\right)^m\right] \tag{13}$$

$$= \left(\frac{1}{2}\right)^m \tag{14}$$

Without sufficient field, entropy is higher because of possible states for unpaired

electrons by $\Delta S_{spin} = k_b m \ln \frac{1}{2}$ In the applied field, the spin entropy is removed and

the height of the barrier is reduced by $gHS\beta$.

The entropy is therefore greater without the applied magnetic field. This

reduction in entropy is reflected as a narrowed Gaussian in Figure 2. Also note that

when a sufficient field is applied, the energy of the reactants is shifted up, as shown

on the left side of Figure 2.

The rate expression is now defined.

$$k = k_p\left(k_1 - k_{-1}\right) \tag{15}$$

Define $\Delta G_1^{\ddagger}$ and $\Delta G_{-1}^{\ddagger}$ as the total free energies of activation for the ensp forward

and backward steps. Allow that the total free energy of activation is composed of

the classical value that does not include magnetic effects, $\Delta G_0^{\ddagger}$, and the magnetically

susceptible components $\Delta G_{m,1}^{\ddagger}$ and $\Delta G_{m,-1}^{\ddagger}$. That is, $\Delta G_1^{\ddagger} = \Delta G_0^{\ddagger} + \Delta G_{m,1}^{\ddagger}$ and

$\Delta G_{-1}^{\ddagger} = \Delta G_0^{\ddagger} + \Delta G_{m,-1}^{\ddagger}$. Include the frequency factor, $A$.

$$k \quad = \quad k_p \left( k_1 - k_{-1} \right) \tag{16}$$

$$= \quad Ak_p \left( \exp\left[ -\frac{\Delta G_1^\ddagger}{k_b T} \right] - \exp\left[ -\frac{\Delta G_{-1}^\ddagger}{k_b T} \right] \right) \tag{17}$$

$$= \quad Ak_p \left( \exp\left[ -\frac{\Delta G_0^\ddagger + \Delta G_{m,1}^\ddagger}{k_b T} \right] - \exp\left[ -\frac{\Delta G_0^\ddagger + \Delta G_{m,-1}^\ddagger}{k_b T} \right] \right) \tag{18}$$

$$= \quad Ak_p \left( \begin{array}{c} \exp\left[ -\frac{\Delta H_0^\ddagger + \Delta H_{m,1}^\ddagger}{k_b T} \right] \exp\left[ \frac{\Delta S_0^\ddagger + \Delta S_{m,1}^\ddagger}{k_b} \right] \\ - \exp\left[ -\frac{\Delta H_0^\ddagger + \Delta H_{m,-1}^\ddagger}{k_b T} \right] \exp\left[ \frac{\Delta S_0^\ddagger + \Delta S_{m,-1}^\ddagger}{k_b} \right] \end{array} \right) \tag{19}$$

The only magnetic entropy effect is embedded in $k_p$, such that $\Delta S_{m,1}^\ddagger = \Delta S_{m,-1}^\ddagger = 0$. The enthalpy change relative to $\Delta H_0^\ddagger$ for the ensp is $\pm gHS\beta$ such that $\Delta H_{m,1}^\ddagger = -gHS\beta$ and $\Delta H_{m,-1}^\ddagger = +gHS\beta$.

$$k \quad = \quad Ak_p \left( \begin{array}{c} \exp\left[ -\frac{\Delta H_0^\ddagger \; gHS\beta}{k_b T} \right] \exp\left[ \frac{\Delta S_0^\ddagger}{k_b} \right] \\ - \exp\left[ -\frac{\Delta H_0^\ddagger + gHS\beta}{k_b T} \right] \exp\left[ \frac{\Delta S_0^\ddagger}{k_b} \right] \end{array} \right) \tag{20}$$

$$= \quad Ak_p \exp\left[ -\frac{\Delta H_0^\ddagger}{k_b T} \right] \exp\left[ \frac{\Delta S_0^\ddagger}{k_b} \right] \left( \begin{array}{c} \exp\left[ \frac{gHS\beta}{k_b T} \right] \\ - \exp\left[ -\frac{gHS\beta}{k_b T} \right] \end{array} \right) \tag{21}$$

The Zeeman energy, $gHS\beta \ll k_b T$ for all but the largest magnetic fields. The Zeeman energy would typically be dismissed as negligible as compared to other reaction enthalpies. But in Equation 21, the differences in the rates $k_1$ and $k_{-1}$ is included, such that the rate constant $k$ will be proportional to the Zeeman energy. For $\lim_{x \to 0} \exp\left[ x \right] \longrightarrow 1 + x$. Because $gHS\beta \ll k_b T$, the above exponentials are

expanded as

$$
\begin{aligned}
k &= Ak_p \exp\left[-\frac{\Delta H_0^{\ddagger}}{k_b T}\right] \exp\left[\frac{\Delta S_0^{\ddagger}}{k_b}\right] \left(\begin{array}{c} 1 + \frac{gHS\beta}{k_b T} \\ -\left[1 - \frac{gHS\beta}{k_b T}\right] \end{array}\right) & (22) \\
&= Ak_p \frac{2gHS\beta}{k_b T} \exp\left[-\frac{\Delta H_0^{\ddagger}}{k_b T}\right] \exp\left[\frac{\Delta S_0^{\ddagger}}{k_b}\right] & (23) \\
&= Ak_p \frac{2gHS\beta}{k_b T} \exp\left[-\frac{\Delta G_0^{\ddagger}}{k_b T}\right] & (24)
\end{aligned}
$$

The rate is proportional to the Zeeman energy. Note that in the earth's magnetic field, $H \sim 1\ G$. For one unpaired electron, $gS \sim 1$ so that $gHS \sim 1\ G$. For a classical frequency factor $A = k_b T/h$

$$
\begin{aligned}
k &= k_p \frac{k_b T}{h} \frac{2gHS\beta}{k_b T} \exp\left[-\frac{\Delta G_0^{\ddagger}}{k_b T}\right] & (25) \\
&= k_p \frac{2gHS\beta}{h} \exp\left[-\frac{\Delta G_0^{\ddagger}}{k_b T}\right] & (26)
\end{aligned}
$$

The temperature dependence in the non-exponential term is lost. The time constant for magnetic effects $\tau_{magnetic}$ is now defined. Compared to diffusion in solution and the earth's magnetic field, $\tau_{magnetic}$ is small.

$$
\tau_{magnetic} = \frac{h}{gHS\beta} \tag{27}
$$

The full expression is

$$
\begin{aligned}
k &= k_p \frac{2gHS\beta}{h} \exp\left[-\frac{\Delta G_0^{\ddagger}}{k_b T}\right] & (28) \\
&= \frac{2gHS\beta}{h} \exp\left[-\frac{gHS\beta}{k_b T}\right] \exp\left[-\frac{\Delta G_0^{\ddagger}}{k_b T}\right] \quad \text{in a sufficient applied field} & (29) \\
&= \left(\frac{1}{2}\right)^m \frac{2gHS\beta}{h} \exp\left[-\frac{\Delta G_0^{\ddagger}}{k_b T}\right] \quad \text{in the absence of a sufficient applied field} & (30)
\end{aligned}
$$

It is likely that the calculated pre-equilibrium constant $K$ encompasses at least most

of the enthalpy portion of $\Delta G_0^{\ddagger}$.

This is the model for homogeneous electron transfer. It is anticipated that as throughout kinetic modeling, the heterogeneous kinetics will be expressed in a manner analogous to the homogeneous kinetics. The model for heterogeneous kinetics is not yet specified. If the heterogeneous kinetics reflect rate enhancements in accord with the Marcus approximation, then a method for modeling is implied.

Marcus theory specifies that the heterogeneous and homogeneous electron transfer rates are well interrelated by the expression

$$\frac{k^0}{A_{el}} = \sqrt{\frac{k_{11}}{A_{\text{soln}}}} \tag{31}$$

where $k^0$ and $k_{11}$ are the heterogeneous and homogeneous self exchange rates and $A_{el}$ and $A_{\text{soln}}$ are the collision frequencies at the electrode and in the solution. The homogeneous preexponential is calculated from equation 32.

$$A_{ex} = \frac{8\pi kT}{\mu} \times \sigma^2 \tag{32}$$

The heterogeneous preexponential factor is calculated from equation 33.

$$A_{el} = \frac{kT}{\sqrt{2\pi\mu}} \tag{33}$$

Where k is the Boltzmann constant, T is temperature in kelvin, $\mu$ is reduced mass, and $\sigma$ is the molecular diameter.

In this study of homogeneous and heterogeneous electron transfer events under a magnetic field, several questions arise. First, are both homogeneous and heterogeneous electron transfer rates increased by a magnetic field? Second, are the increases in homogeneous and heterogeneous electron transfer rates governed by the

Marcus approximation of Equation 31? Following is a study to explore some of these questions.

## 2.2    Experimental: Methods and Materials

To perform these measurements, a critical modification of Nafion was necessary. The modified polymer, TMODA Nafion, incorporates the hydrophobic ammonium salt trimethyloctadecylamine. This incorporation acts to increase the pore size of the polymer micellar structure, reduces ion selectivity, makes the membrane less acidic, and increases mass transport through the structure. Minteer et al. observed an 11-fold increase in redox species transport in TMODA. Unmodified Nafion has the chemical structure of Figure 3. Ion extraction (specifically cation) is minimized
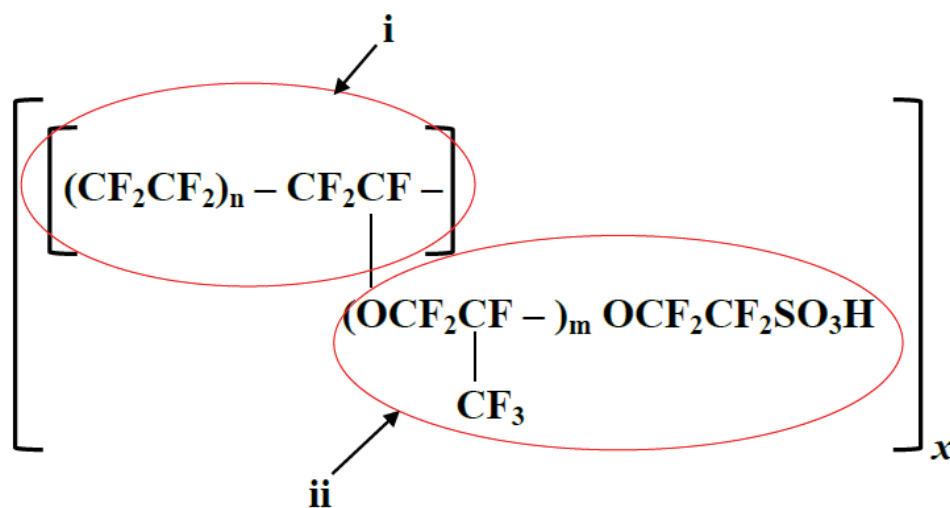


Figure 3. Nafion structure: i.   Teflon fluorocarbon backbone; ii.   sulfonic acid side chains, where m is 1, and n varies from 6 to 14.

with TMODA Nafion. $Fe(CN)_6^{3-}$, the first anion analyzed for magnetic enhancement, validates that anion exclusion is minimized with TMODA. Additionally, due to the
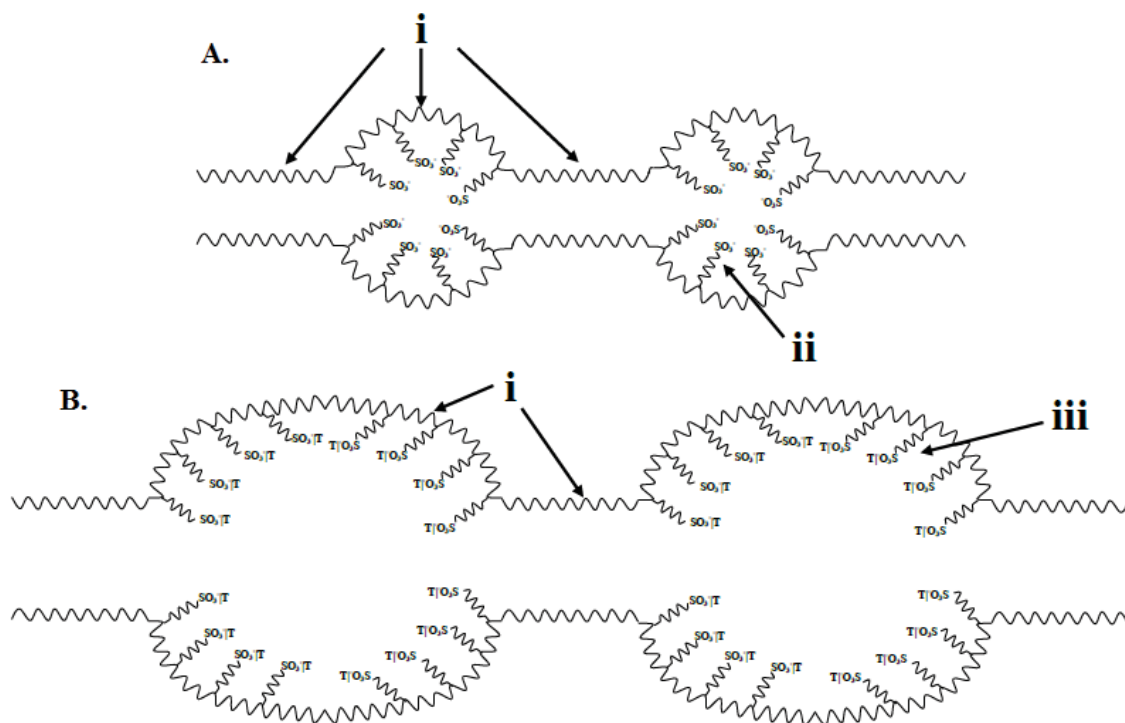
Figure 4. Representation of the micellar structure of Nafion based polymer films: A. Unmodified Nafion; i. Teflon fluorocarbon backbone; ii. sulfonic acid chains; B. TMODA Nafion; i. Teflon fluorocarbon backbone; iii. hydrophobic TMODA sulfonic acid sidechains

increased flux in TMODA Nafion, solution equilibration occurs on the minutes scale

($\approx$5 minutes) versus hours ($\approx$2) in unmodified Nafion [11, 13]. Extraction in Nafion

requires long equilibration as the micellar pore size in Nafion is $\approx$ the radius of redox

species (pore size Figure 4, where Figure 4-A. is unmodified Nafion, and Figure 4-B

is TMODA Nafion). Minteer et.al. observed an 11-fold increase in mass transport

through modified Nafion polymers compared to unmodified Nafion [22].

In theory, the increased micellar pore size and increased transport through

TMODA modified Nafion creates an environment in which the concentration of

probe in the film is comparable to probe in solution. A schematic of heterogeneous

reduction is seen in Figure 5. This means that the probe to probe distance within the
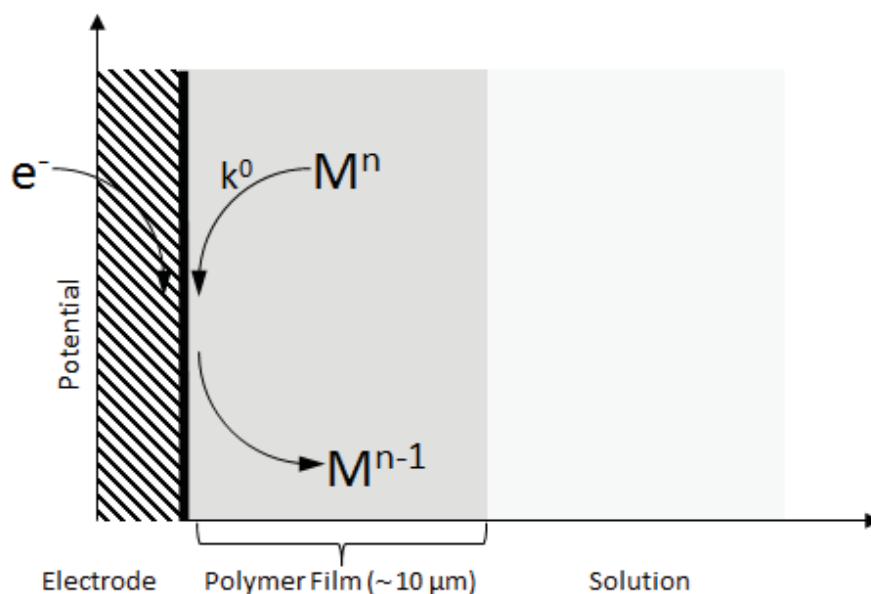


Figure 5. Scheme of heterogeneous electron transfer reaction at polymer modified electrode, M represents solution based redox active species, $k^0$ is the heterogeneous rate constant (cm/s), $M^{n-1}$ represents a reduced species.

film is low so that hopping is discouraged. TMODA Nafion creates an environment

that heterogeneous ET measurements can be made that the heterogeneous rate constant, $k^0$, can be extracted.

Experimentally, the measurements performed here are similar to previous studies [11–13]. In general, electrodes were modified with thin polymer films, while magnetically modified electrode films contain a volume loading of magnetic microparticles. (A more detailed description follows.) Cyclic voltammetry is the primary characterization method. Cyclic voltammetry, a potential sweep method, produces peak currents ($i_p$) for diffusionally limited systems. In the analyses here, the peak currrents and their associated peak potentials ($E_p$) are essential for the determination of heterogeneous electron transfer rates. Preliminary electrochemical impedance spectroscopy (EIS) measurements were also performed. These measurements are meant to complement the voltammetric data and analysis. EIS data for the $Fe(CN)_6^{3-}$ redox couple is presented near the end of the Chapter.

Most often, cyclic voltammetry is used for measurements of self exchange. In the self exchange analysis, a plot of current ($i_p$) versus the square root of scan rate ($v^{1/2}$) allows for the determination of the diffusion constant. For reversible systems, where peak splitting is $\leq 59\text{mV/n}$, these plots are usually linear. The systems analyzed here are quasi-reversible ($61 \text{ mV/n} \leq \Delta E_p \leq 212 \text{ mV/n}$) and linear plots are not necessarily expected. However, plots of this type are used here. These plot illustrate the effects magnetic fields have on the system and are a good first approximation of the system.

### 2.2.1 iR Compensation

iR-compensation has two functions, to decrease error associated with iR drop and to increase cell response [27]. Modern potentiostats often account for iR-compensation in the measurement by utilizing feedback iR-compensation during data acquisition. This process also minimizes charging currents (capacitance). The instrument takes an initial measurement of solution resistance before running a scan (i.e., voltammogram) through an applied potential measurement, determining resistance from the resulting current-transient. Data was collected here on two different potentiostats, a CH Instruments 760B bipotentiostat with an 8-channel multiplexer, and a CH Instruments 1030 8-channel potentiostat. The 760B, a bipotentiostat that can run eight electrodes sequentially, performs automatic iR-compensation. The 1030 multichannel potentiostat, which can perform simultaneous measurements, does not perform iR compensation. Data collected on the 1030 were therefore adjusted manually during the analysis to account for uncompensated resistance.

To account for resistance, the resistance of the solution is measured. All measurements were performed in 0.1 M $Na_2SO_4$. This electrolyte solution has a resistance of 65 $\Omega$. As electrode geometry affects resistance, a symmetrical arrangement of electrodes was used throughout to minimize variance between measurements; the arrangement is seen in Figure 6. The potential drop associated with resistance is

$$V_{drop} = i_p R \tag{34}$$

Figure 6. Symmetrical arrangement of RDE electrodes used in heterogeneous analysis. Counter electrode (CE) and reference electrode (RE) placed in center of eight working electrodes.

Peak splitting is then accounted for by

$$\Delta E_p(corrd) = \Delta E_p(measd) - 2\left|i_p\right| R \qquad (35)$$

where $i_p$ is the maximum peak current. It is noted where peak splitting and charging currents were corrected.

### 2.2.2 Experimental Preparation

TMODA Nafion was prepared in house from a literature procedure [22, 23]. To a suspension of 5 wt. % Nafion in ethanol (Aldrich) is added trimethyloctadecylammonium bromide (Aldrich) at three times the concentration of sulfonic acid sites. The solution is rotated overnight in a 15 mL Eppendorf vial with glass beads to increase solution agitation. The polymer is then washed in $18\Omega$ Millpore water to remove excess bromine salt before being resuspended in absolute ethanol (Aesper).

Aqueous solutions of conventional redox probes at 1 mM were prepared with 0.1 M $Na_2SO_4$ supporting electrolyte. Solutions were prepared freshly in 18 $\Omega$ Millpore water to ensure accurate concentrations. Commercially available redox probes include tris(bypiridyl)ruthenium(II) chloride ($Ru(bpy)_3Cl_2$, Sigma), potassium ferricyanide ($K_3Fe(CN)_6$, Aldrich), 2,6-dimethylbenzoquinone (2,6-DMBQ, Aldrich), while tris(bypiridyl)cobalt(II) chloride ($Co(bpy)_3Cl_2$), and tris(bypiridyl)cobalt(III) chloride($Co(bpy)_3Cl_3$) were prepared in-house as before [12]. The magnetic properties of the Bangs particles were analyzed by Lee [13] while magnetic properties of the probes were analyzed by Gellett [12]. The solution resistance of $Na_2SO_4$ was measured by potential step and EIS measurements. iR-compensation is accounted for either instrumentally or in the analysis process.

Electrodes are modified with TMODA Nafion via an adjusted Nafion casting protocol. Due to the nature of cast TMODA-Nafion , estimating particle loadings in the film is difficult. In comparison to Nafion, TMODA-Nafion forms a waxy-globular film with inconsistencies in thickness and distribution (Figure 7). However, loadings of magnetic particles are estimated at 15% vol/vol of the TMODA film. Additionally, to account for volume differences between modified and unmodified films, casting volumes are adjusted (5 $\mu$L for unmodified TMODA films, 5.4 $\mu$L for modified TMODA).

Pine Instruments glassy carbon rotating disk electrodes (RDE) with geometric surface areas of 0.458 cm$^2$ are used here. A three electrode setup is used, including the RDE as working electrode (WE) , a platinum mesh counter electrode (CE), and a saturated calomel electrode reference (RE). All control electrodes are modified
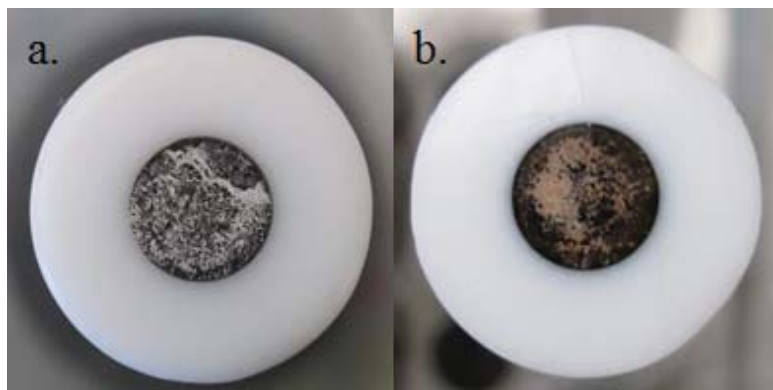
Figure 7. Image of modified glass carbon, rotating disk electrodes (Pine Inc.) with $A_{geo}$ = 0.458 cm$^2$; a. TMODA Nafion polymer modified electrodes surface; b. TMODA Nafion + 15 % coated magnetite particles (Bangs, dia. $\sim$2.5 $\mu$m).

with TMODA Nafion and modified electrodes all contain 15% vol/vol Bangs magnetite. Cast films are air dried for at least 15 minutes (no additional drying under desiccant is performed). Modified electrodes are air-dried within a NdFeB permanent ring magnet (OD = 7.5cm, ID = 5 cm, h = 1 cm ). Electrodes are allowed to equilibrate in solution for at least 10 minutes before electrochemical measurements are performed.

## 2.3 Results and Analysis

In the first part of this section, methods of determining the heterogeneous and homogeneous rate constants are presented. This is followed by the presentation of values.

### 2.3.1 Analysis Methodology

Many steps are involved in the analysis to determine the heterogeneous electron

transfer constant, $k^0$. These steps are more thoroughly described below, but in gerenal they follow the outline of:

1. Determination of peak currents ($i_p$ (A)) and peak splittings ($\Delta E_p$ (V)) from cyclic voltammagrams.

2. Determination of the diffusion constants (D ($cm^2/s$)) from plots of peak current ($i_p$) versus ($v^{1/2}$).

3. Nicholson and Shain analysis (including work by Leddy and Paul) to determine the dimensionless parameter $\Psi$.

4. From $\Psi$ can be determined $k^0$ (cm/s)

5. Lastly, the values of $k^0$ and D (as well as the transfer coefficient $\alpha$) are simulated with DigiSim (BASi) to fit the data.

Post experimental analysis for determining the heterogeneous electron transfer rate constant $k^0$ utilizes a diagnostic developed by Nicholson and Shain [24, 25]. This analysis is dependent upon criteria similar to the homogeneous analysis, such as determinations of the diffusion constants of the redox species.

Cyclic voltammetry measurements in diffusion limited systems produce peak currents. The peak current equation 36 correlates current to scan rate.

$$i_p = (2.69x10^5)n^{3/2}AD^{1/2}C_O^*v^{1/2} \tag{36}$$

Where n is the number of electrons transferred, A is electrode area ($cm^2$), D is the diffusion constant ($cm^2/sec$), C* is the concentration of electroactive species (M), $v$ is the scan rate (V/sec). Peak currents for forward ($i_p^f$) and backward ($i_p^b$) sweeps were used to determine the diffusion constants for the oxidized and reduced forms

of the redox probes from plots of $i_p$ versus $\sqrt{v}$. This is a good first approximation for the heterogeneous system. At $i_p^f$ and $i_p^b$, the associated potentials $E_p^f$ and $E_p^b$ are used to determine peak splitting, $\Delta E_p$.

Diffusion is composed of two processes, physical diffusion ($D_p$) and diffusion through electron hopping ($D_{et}$). This is modeled with Dahms Ruff (equation 37) conduction.

$$D_{obs} = D_p + D_{et} \qquad (37)$$

In Nafion, physical diffusion is slow and concentration of the redox species is high. Electron hopping, or conduction, predominates and $D_p << D_{et}$. As such,

$$D_{obs} = D_{et} \qquad (38)$$

This quality allows for the determination of the self exchange rate constant, $k_{11}$ (the process is described below) However, for heterogeneous measurements, the concentration of redox probe needs to be low enough that hopping does not predominate where $D_{et} \leq D_p$ and physical diffusion exists.

For the Nicholson and Shain diagnostic, a dimensionless kinetic parameter $\Psi$, is determined from using scan rate ($v$), diffusion coefficient ($D_O$), the heterogenous rate constant ($k^0$), and the transfer coefficient ($\alpha$). Where

$$\Psi = \frac{(D_A/D_B)^{\alpha/2} k^0}{[(nF/RT)\pi v D_A]^{1/2}} \qquad (39)$$

Alternatively, if $\Psi$ is unknown, a working curve can be used to determine $\Psi$ by plotting $\Delta E_p$ vs. $\Psi^{-1}$, which returns a linear curve, where

$$\Delta E_p(nF/RT) = M_1(1/\Psi) + B_1 \qquad (40)$$

Table 1. Values for M1 and B1 for a range of alpha values.

| $\alpha$ | $M_1$ | $B_1$ | Std. error in $M_1$ | Std. error in $B_1$ | Corr. Coeff |
|---|---|---|---|---|---|
| 0.3 | 0.87266 | 2.2736 | 0.00250 | 0.0036 | 0.9993 |
| 0.4 | 0.84473 | 2.3366 | 0.00577 | 0.0102 | 0.9962 |
| 0.5 | 0.8428 | 2.3243 | 0.00699 | 0.0118 | 0.9960 |
| 0.6 | 0.78946 | 2.3791 | 0.00750 | 0.0140 | 0.9959 |
| 0.7 | 0.75913 | 2.3727 | 0.00555 | 0.0104 | 0.9975 |

A table of values from Paul and Leddy [26] covers a range of alpha values, $0.3 < \alpha < 0.7$. The working curve holds for $0.2 \leq D_A/D_B \leq 5$.

The method was initially intended to determine $\Psi$ from a working curve of $\Delta E_p$ vs. $\Psi^{-1}$, used then to determine $k^0$ where all other parameters are known. However, this reverse analysis allows for an approximation of $\Psi$ by approximating $\alpha$, which can then be used to find $k^0$, as long as the determined values of diffusion forward ($D_f$) and backward ($D_b$) satisfy $0.2 \leq D_f/D_b \leq 5$. $\Psi$ is dependent upon scan rate, for this analysis, values of $\Psi$ will be calculated from $\Delta E_p$ values taken at 100 mV/sec, a mid-range value. $\Psi$ is calculated from experimental and generated data as

$$\Psi = ABS \left| \frac{M1}{\Delta E_p - B1} \right| \tag{41}$$

$k^0$ is the calculated from as

$$k^0 = \frac{\Psi[(nF/RT)\pi v D_A]^{1/2}}{(D_A/D_B)^{\alpha/2}} \tag{42}$$

The approximation of $\alpha$ and the calculation of $k^0$ values are validated in DigiSim (BASi). Simulations in DigiSim generate model voltammograms based on parameters both measured experimentally and estimated from the analysis. For primary and secondary ET reactions, DigiSim allows for determinations of $\alpha$ by finding the 'best

fit' to simulated data from experimental data. Here, forward waves are fit, more information on fitting and data is found in Appendix A.

Following are the analyses for the four transition metal complexes, $Ru(bpy)_3^{2+}$, $Co(bpy)_3^{2+}$, $Co(bpy)_3^{3+}$, and $Fe(CN)_6^{3-}$. Determination of the diffusion constants of control and magnetically modified systems, for both the forward and reverse species, is performed. Values for the associated peak splittings are also given here.

## 2.3.1.1 Relating $k^0$ and the transfer coefficienct, $\alpha$

The standard heterogeneous rate constant, $k^0$, is measure of the kinetic facility of a redox couple. The magnitude of this constant, like others, indicates the time scale of the equilibrium; large $k^0$ values (1 to 10 cm/s) indicate fast equilibrium while small $k^0$ values ($10^{-9}$ cm/s) indicate slow equilibrium. Lower values of $k^0$ are associated with species that experience associated chemical steps along with the electron transfer. $k^0$ is defined at $E = E^{0'}$.

The transfer coefficient is a measure of the kinetic facility of a redox couple, where $0 < \alpha < 1$. It is a measure of symmetry about the energy barrier on a reaction coordinate [1]. In Figure 8 of reaction coordinate diagrams show the symmetry of this barrier and the corresponding values of $\alpha$. The dash line indicates the coordinate as a potential is applied to the electrode.

The heterogeneous rate constant is related to current-potential characteristics
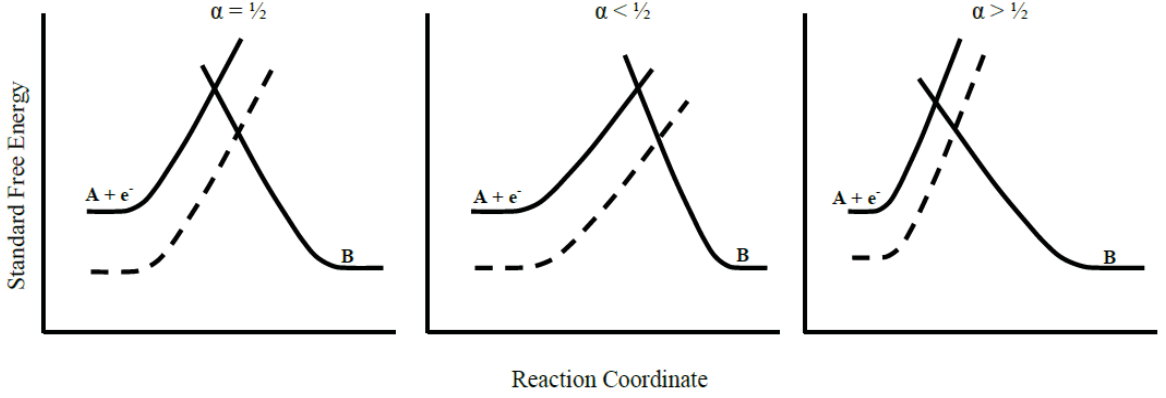
Figure 8. Reaction coordinate diagrams over a variety of transfer coefficient, $\alpha$, ranges. The transfer coefficient is representative of the symmetry of the intrinsic energy barrier [1].

through Butler-Volmer formulations of electrode kinetics, here by

$$i = FAk^0[C_O(0,1)e^{-\alpha f(E\text{-}E^{0\prime})} - C_R(0,1)e^{1\text{-}\alpha f(E\text{-}E^{0\prime})}] \tag{43}$$

where F is the Faraday constant (9.648x10$^4$ C). $C_O$ and $C_R$ denote the concentration of the reduced and oxidized form of the redox species, denoting them here as such is relative depending upon the form of the redox couple being analyzed. For quasireversible systems, chemical and molecular processes affect the ET process, such that $\Delta E_p$ falls between 61 mV/n $\leq \Delta E_p \leq$ 212 mV/n.

In the case of a quasireversible system,

$$A + ne \underset{k_b}{\overset{k_f}{\rightleftharpoons}} B \tag{44}$$

The forward rate constant, $k_f$, and the reverse rate constant, $k_b$ are defined as

$$k_f = k^0 \exp\left(-\alpha \left(\frac{nF}{RT}\right)(E - E^{0\prime})\right) \tag{45}$$

and

$$k_b = k^0 \exp\left((1 - \alpha)\left(\frac{nF}{RT}\right)(E - E^{0\prime})\right) \tag{46}$$

where n is the number of electrons, R is the gas constant, and T is absolute temperature. In the systems analyzed here, the transfer coefficient is assumed to fall between $0.3 < \alpha < 0.7$.

### 2.3.2  Results

Data for the redox species, including peak currents, peak splittings, and values of rate constants are presented here.

### 2.3.2.1  Tris(bipyridine)ruthenium(II) chloride

For measurements on $Ru(bpy)_3^{2+}$, solutions of 1 mM redox probe in 0.1 M $Na_2SO_4$ (aq) were prepared freshly before measurements were recorded to ensure accurate concentrations. Measurements were taken sequentially from all electrodes at scan rates of 5, 25, 50, and 100 mV/sec, where all measurements were take in quadruplet (n = 4). No specific attention was given for rest between measurements as the scans were sequential (i.e., electrode 1 scanned first, followed by electrode 2, etc.), and adequate re-equilibriation is assumed. $Ru(bpy)_3^{2+}$ undergoes the following redox reaction

$$Ru(bpy)_3^{2+} + e \;\; \rightleftharpoons Ru(bpy)_3^{2+} \tag{47}$$
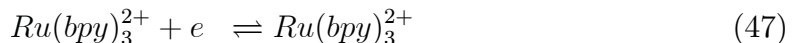
Figure 9 shows typical flux enhancement between modified and unmodified electrodes at $v = 100$ mV/sec. Figure 10 shows the effect on diffusion constants for the oxidized $(D_R)$ and reduced $(D_O)$ form of the species as determined from plots of $i_p$ (A) versus
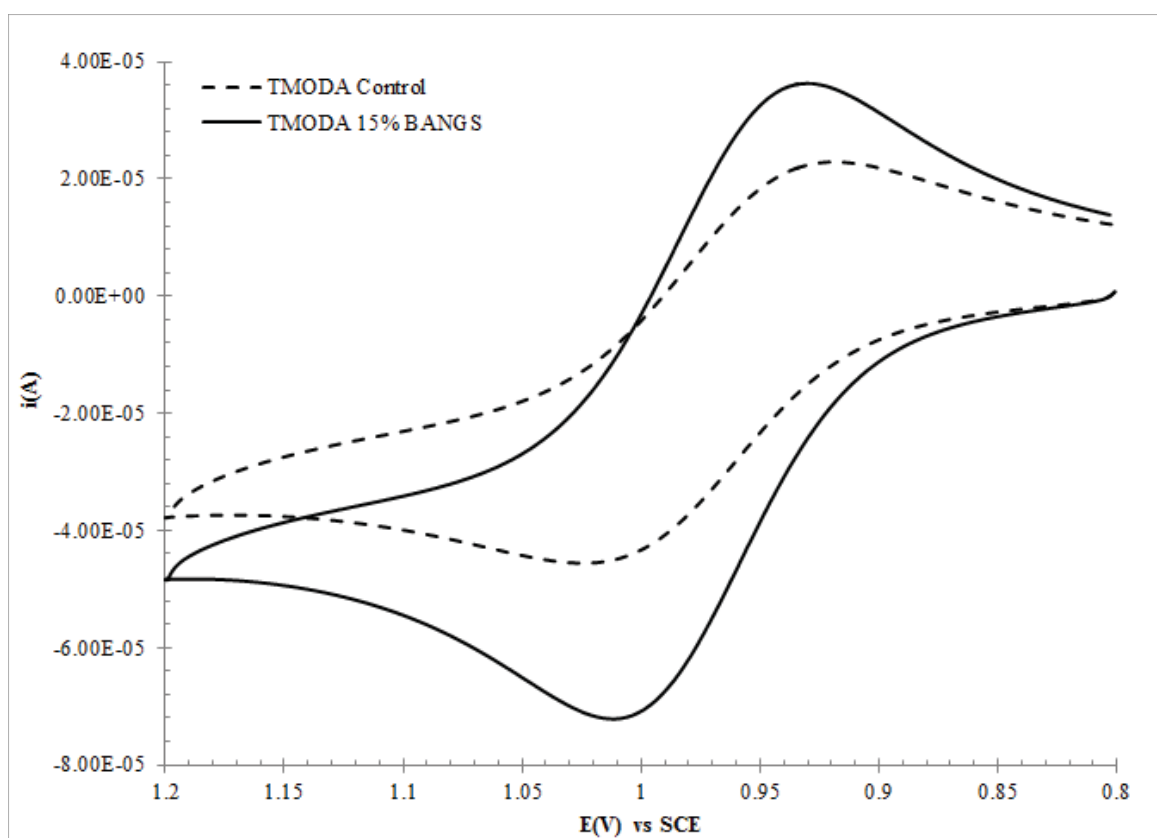
Figure 9. CV for Ru(bpy)$_3^{2+}$ at TMODA modified glassy carbon electrodes. 1 mM redox couple in 0.1 M Na$_2$SO$_4$ (aq.), $v = 100$ mV/sec; potential versus saturated calomel electrode (SCE).

square root of scan rate ($v$), for $D_R$ Linear treatment of TMODA control electrodes
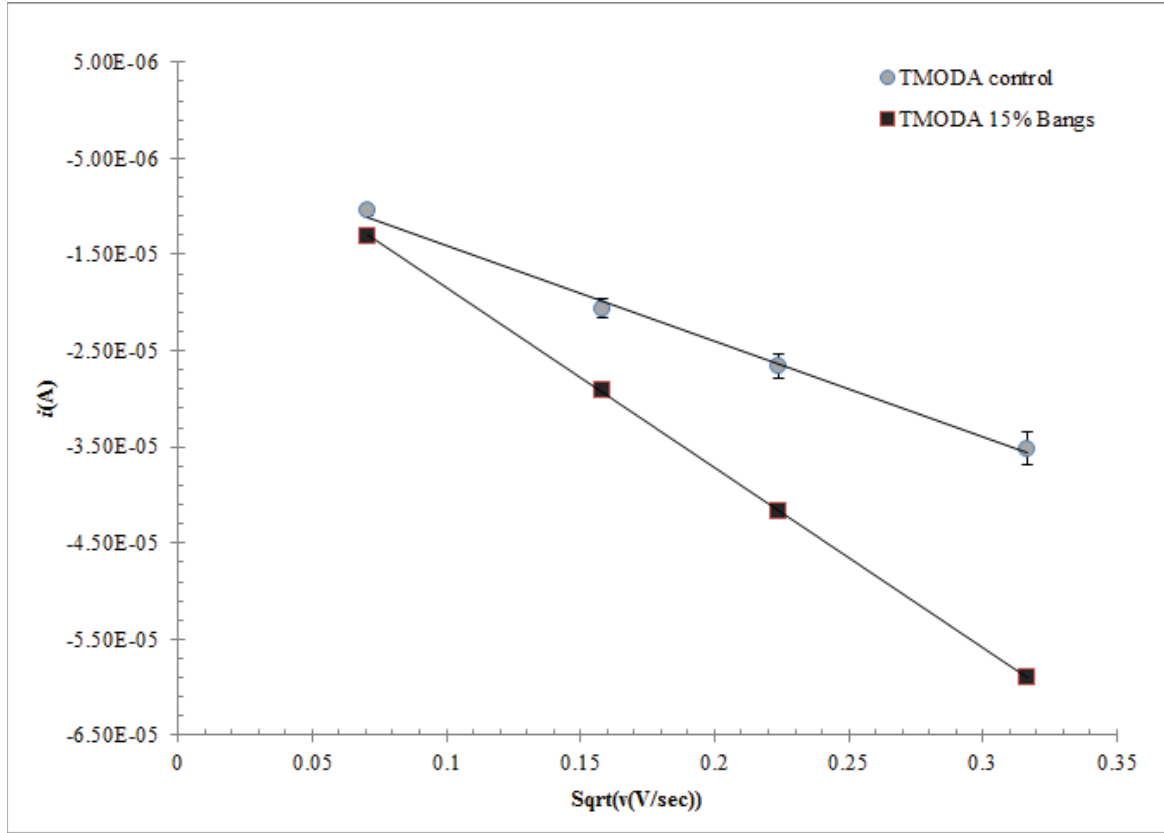


Figure 10. Plot of $i_p^f$ (A) versus $\sqrt{v}$ for the forward wave ($D_R$) for Ru(bpy)$_3^{2+}$.

yields y $= -1.002 \times 10^{-4}$x $- 3.962 \times 10^{-6}$ with an R$^2 = 0.996$; from the slope this returns

a $D_R = 6.61 \times 10^{-7}$ cm$^2$/sec. Likewise, linear treatment of the magnetically modified

electrodes yields a fit of y $= -1.872 \times 10^{-4}$x $+ 2.578 \times 10^{-7}$, with a correlation of R$^2 = 1$.

This returns a $D_R = 2.3 \times 10^{-6}$ cm$^2$/sec. While for $D_O$, linear treatment of TMODA

control electrodes yields y $= 8.882 \times 10^{-5}$x $+ 4.214 \times 10^{-6}$ with an R$^2 = 0.991$; from

the slope this returns a $D_O = 5.2 \times 10^{-7}$ cm$^2$/sec. Likewise, linear treatment of the

magnetically modified electrodes yields a fit of y $= 1.748 \times 10^{-4}$x $+ 7.953 \times 10^{-7}$, with
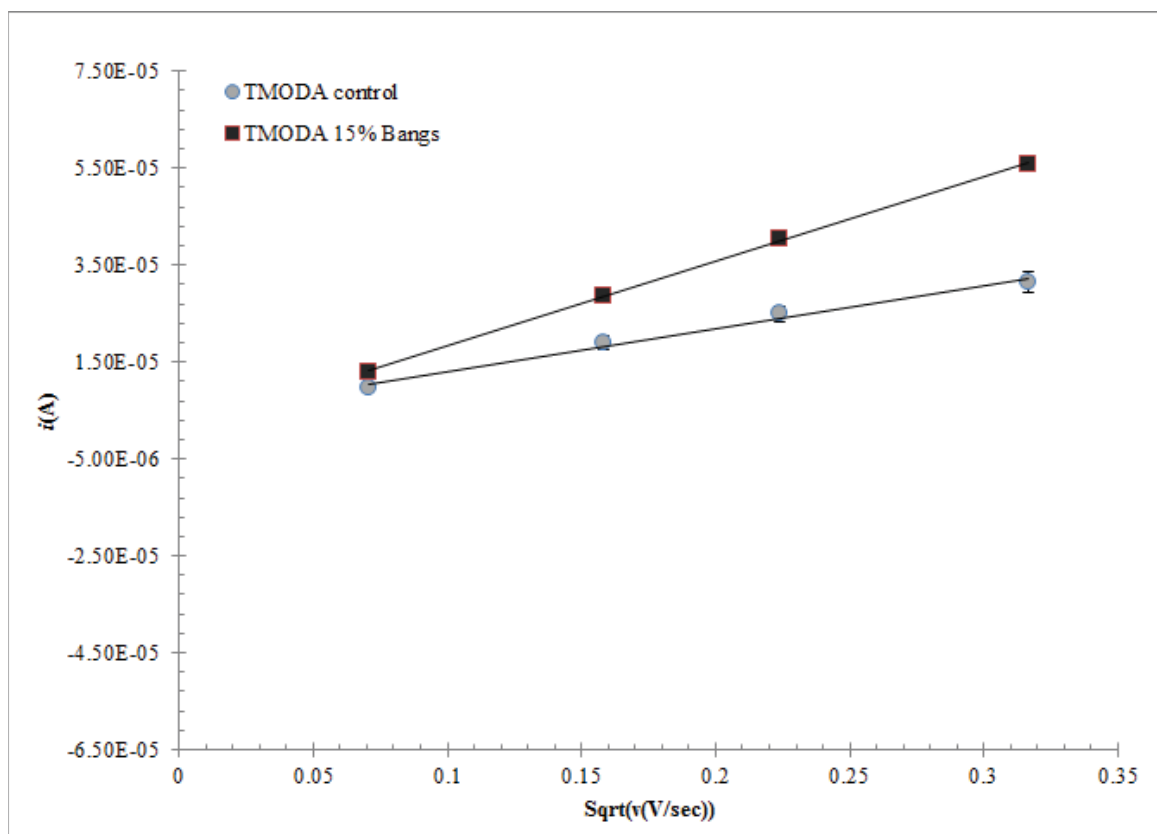
Figure 11. Plot of $i_p^b$ (A) versus $\sqrt{v}$ for the reverse wave (D$_O$) for Ru(bpy)$_3^{2+}$.

Table 2. Values of peak currents and peak splittings for Ru(II)(bpy).

| $v$ (mV/sec) | $i_p^f$ ($\mu$A) | | $i_p^b$ ($\mu$A) | | $\Delta E_p$ (mV) | |
|---|---|---|---|---|---|---|
| | TMODA | BANGS | TMODA | BANGS | TMODA | BANGS |
| 5 | -10.4($\pm$ 0.6) | -13.1($\pm$ 0.7) | 9.7($\pm$ 0.4) | 12.8($\pm$ 0.3) | 86($\pm$ 4) | 74($\pm$ 3) |
| 25 | -21($\pm$ 1) | -29($\pm$ 2) | 19($\pm$ 1) | 29($\pm$ 1) | 88($\pm$ 9) | 67($\pm$ 2) |
| 50 | -27($\pm$ 2) | -42($\pm$ 2) | 25($\pm$ 2) | 40($\pm$ 2) | 93($\pm$ 13) | 69($\pm$ 2) |
| 100 | -35($\pm$ 2) | -59($\pm$ 3) | 32($\pm$ 3) | 56($\pm$ 3) | 99($\pm$ 16) | 72.9($\pm$ 0.5) |

a correlation of $R^2 = 0.999$. This returns a $D_O = 2.01\text{x}10^{-6}$ cm$^2$/sec. If $D_O$ and $D_R$ are identical, or if one value is unknown, they are assumed to be the same. This treatment reveals a slight difference in the diffusion constants between reduced on oxidized species ($\sim$10%), and therefore both values are considered in the treatment. However, the working curve holds for $0.2 \leq D_A/D_B \leq 5$; this is in agreement here (and for the following species). Values for Ru(bpy)$_3^{2+}$ at TMODA electrodes are tabulated. These values are correct for resistance and capacitance. The differences in $i_p^f$ and $\Delta E_p$ are different at the 99.5 and 95 % confidence levels, respectively at $v$ = 100 mV/sec.

2.3.2.2 Tris(bipyridine)cobalt(II) chloride

For measurements on Co(bpy)$_3^{2+}$, solutions of 1 mM redox probe in 0.1 M Na$_2$SO$_4$ (aq) were prepared freshly before measurements were recorded to ensure accurate concentrations. Measurements were taken sequentially from all electrodes at scan rates of 25, 50, and 100 mV/sec, where all measurements were take in quadruplet (n = 4). Adequate re-equilibration between measurements was assumed. Co(bpy)$_3^{2+}$

undergoes the following redox reaction.

$$Co(bpy)_3^{3+} + e^- \rightleftharpoons Co(bpy)_3^{2+} \tag{48}$$
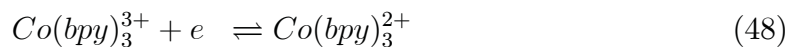
Figure 12 shows typical flux enhancement between modified and unmodified electrodes at $v = 100$ mV/sec. Figure 13 shows the effect on diffusion constants
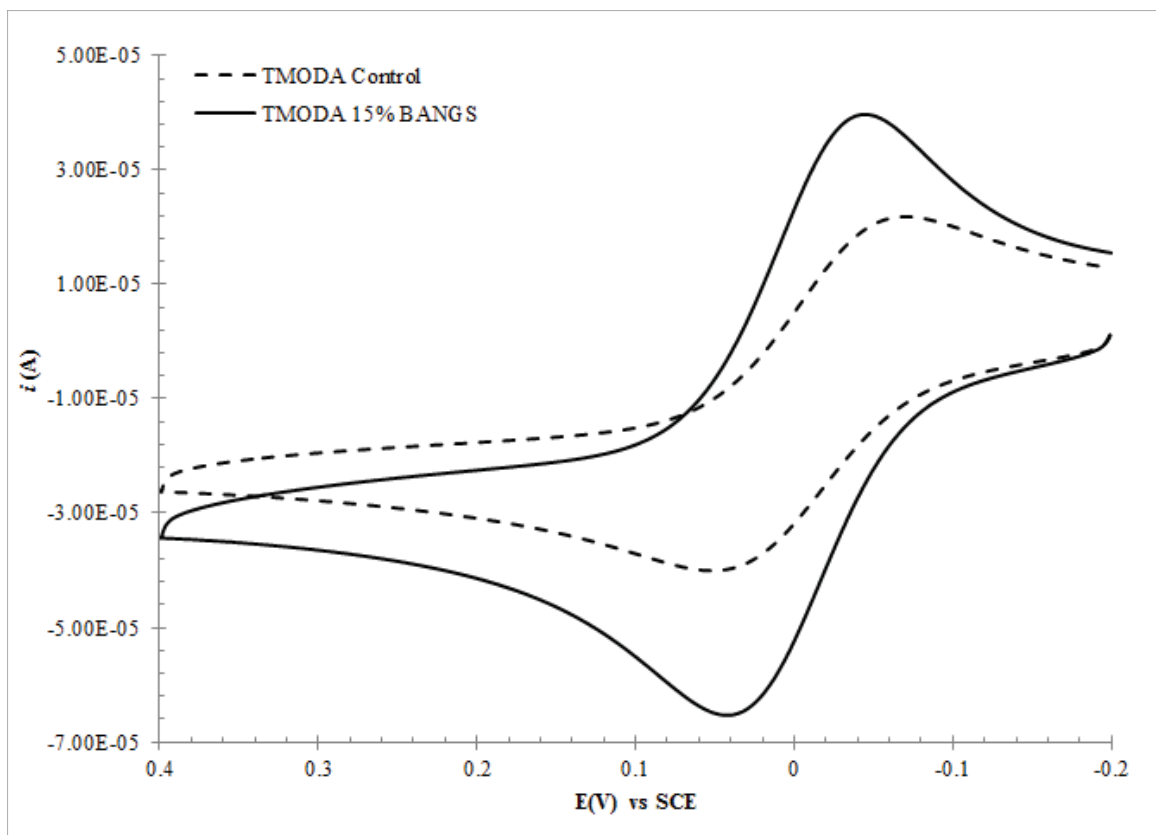


Figure 12. CV for $Co(bpy)_3^{2+}$ at TMODA modified glassy carbon electrodes. 1 mM redox couple in 0.1 M $Na_2SO_4$ (aq.), $v = 100$ mV/sec; potential versus saturated calomel electrode (SCE).

for the oxidized ($D_R$) and reduced ($D_O$) form of the species as determined from plots of $i_p$ (A) versus square root of scan rate ($v$), Linear treatment of TMODA control electrodes yields y = -7.643x10$^{-5}$x - 2.333x10$^{-6}$ with an $R^2 = 0.99$; from
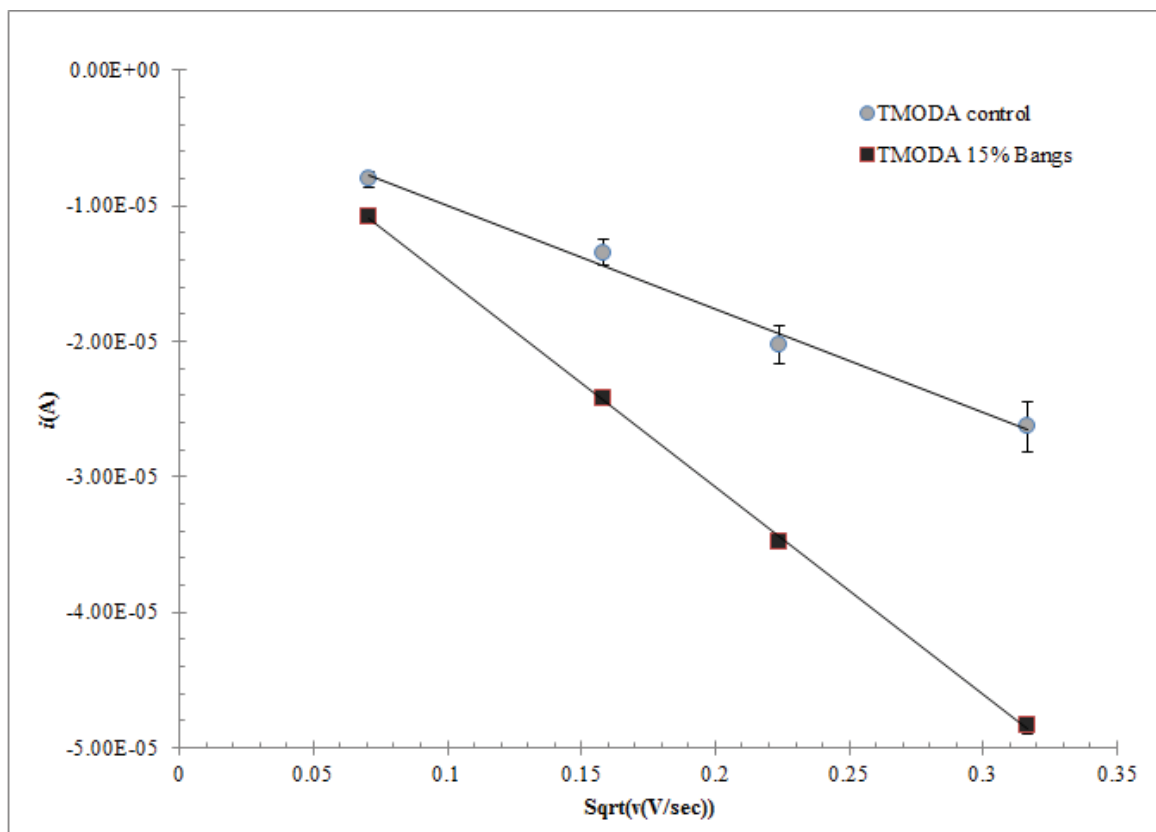
Figure 13. Plot of $i_p^f$ (A) versus $\sqrt{v}$ for the forward wave ($D_R$) for Co(bpy)$_3^{2+}$.

the slope this returns a $D_R = 3.85 \times 10^{-7}$ cm$^2$/sec. Likewise, linear treatment of the

magnetically modified electrodes yields a fit of y = $-1.533 \times 10^{-4}$x - $5.720 \times 10^{-8}$, with a

correlation of $R^2 = 0.9996$. This returns a $D_R = 1.55 \times 10^{-6}$ cm$^2$/sec. While for $D_O$

in Figure 14. Linear treatment of TMODA control electrodes yields y = $9.813 \times 10^{-5}$x
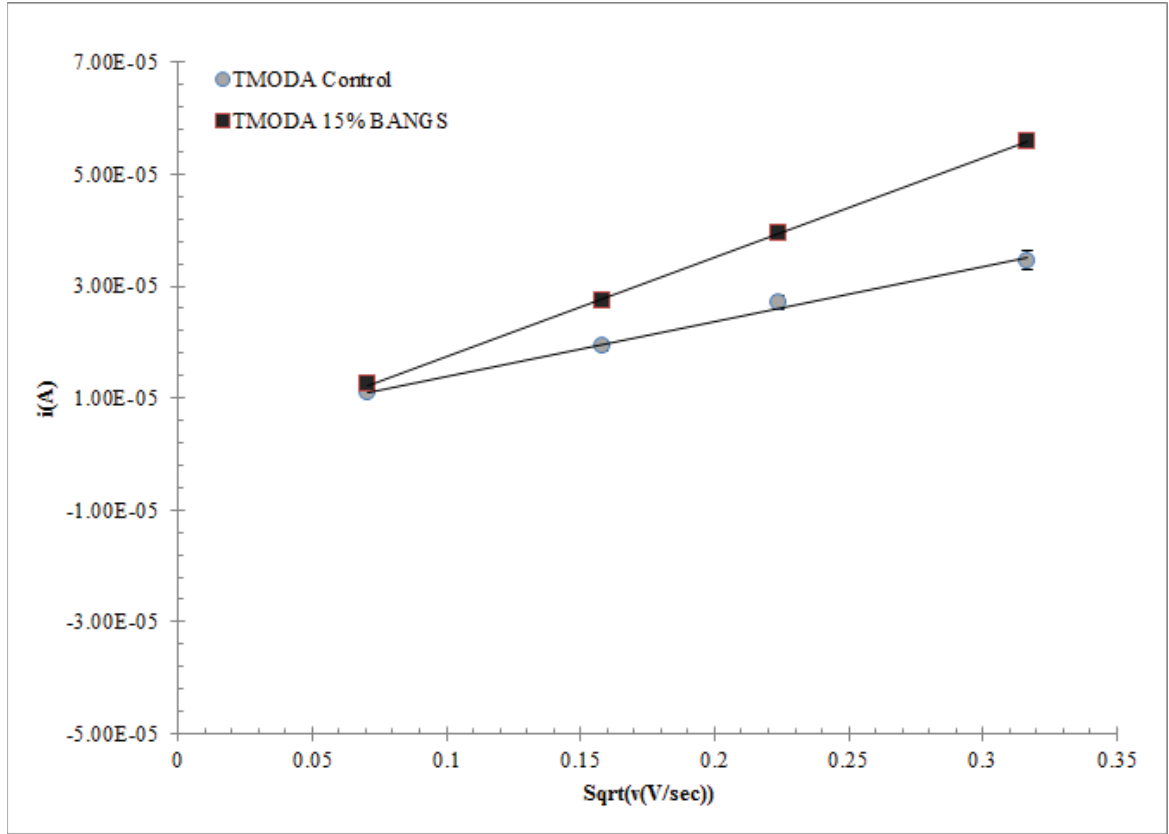


Figure 14. Plot of $i_p^b$ (A) versus $\sqrt{v}$ for the reverse wave ($D_O$) for Co(bpy)$_3^{2+}$.

+ $4.122 \times 10^{-6}$ with an $R^2 = 0.995$; from the slope this returns a $D_O = 6.34 \times 10^{-7}$

cm$^2$/sec. Likewise, linear treatment of the magnetically modified electrodes yields a

fit of y = $1.765 \times 10^{-4}$x - $1.662 \times 10^{-7}$, with a correlation of $R^2 = 0.999$. This returns a

$D_O = 2.06 \times 10^{-6}$ cm$^2$/sec. If $D_O$ and $D_R$ are identical, or if one value is unknown,

Table 3. Values of peak currents and peak splittings for Co(II)(bpy).

| $v$ (mV/sec) | $i_p^f$ ($\mu$A) | | $i_p^b$ ($\mu$A) | | $\Delta E_p$ (mV) | |
|---|---|---|---|---|---|---|
| | TMODA | BANGS | TMODA | BANGS | TMODA | BANGS |
| 25 | -23($\pm$ 2) | -36($\pm$ 2) | 9.3($\pm$ 0.9) | 16($\pm$ 2) | 78($\pm$ 5) | 71($\pm$ 3) |
| 50 | -26($\pm$ 2) | -48($\pm$ 2) | 17.2($\pm$ 0.9) | 26($\pm$ 2) | 108($\pm$ 9) | 71($\pm$ 5) |
| 100 | -40($\pm$ 2) | -65($\pm$ 3) | 24($\pm$ 1) | 41($\pm$ 3) | 117($\pm$ 12) | 78($\pm$ 5) |

they are assumed to be the same. This treatment reveals a slight difference in the diffusion constants between reduced and oxidized species ($\sim$10%), and therefore both values are considered in the treatment. However, the working curve holds for $0.2 \leq D_A/D_B \leq 5$; this is in agreement here (and for the following species). Values for Co(bpy)$_3^{2+}$ at TMODA electrodes are tabulated. These values are correct for resistance and capacitance. The differences in $i_p^f$ and $\Delta E_p$ are different at the 99.9 and 95 % confidence levels, respectively at $v = 100$ mV/sec.

2.3.2.3 Tris(bipyridine)cobalt(III) chloride

For measurements on Co(bpy)$_3^{3+}$, solutions of 1mM redox probe in 0.1 M Na$_2$SO$_4$ (aq) were prepared freshly before measurements were recorded to ensure accurate concentrations. Measurements were taken sequentially from all electrodes at scan rates of 5, 25, 50, and 100 mV/sec, where all measurements were take in quadruplet (n = 4). Adequate re-equilibriation between measurements was assumed. Co(bpy)$_3^{3+}$ undergoes the following redox reaction, written here as the reduction,

$$Co(bpy)_3^{3+} + e^- \; \rightleftharpoons Co(bpy)_3^{2+} \tag{49}$$
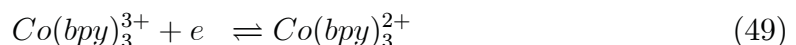
Figure 15 shows typical flux enhancement between modified and unmodified

electrodes at $v = 100$ mV/sec. Figure 16 shows the effect on diffusion constants
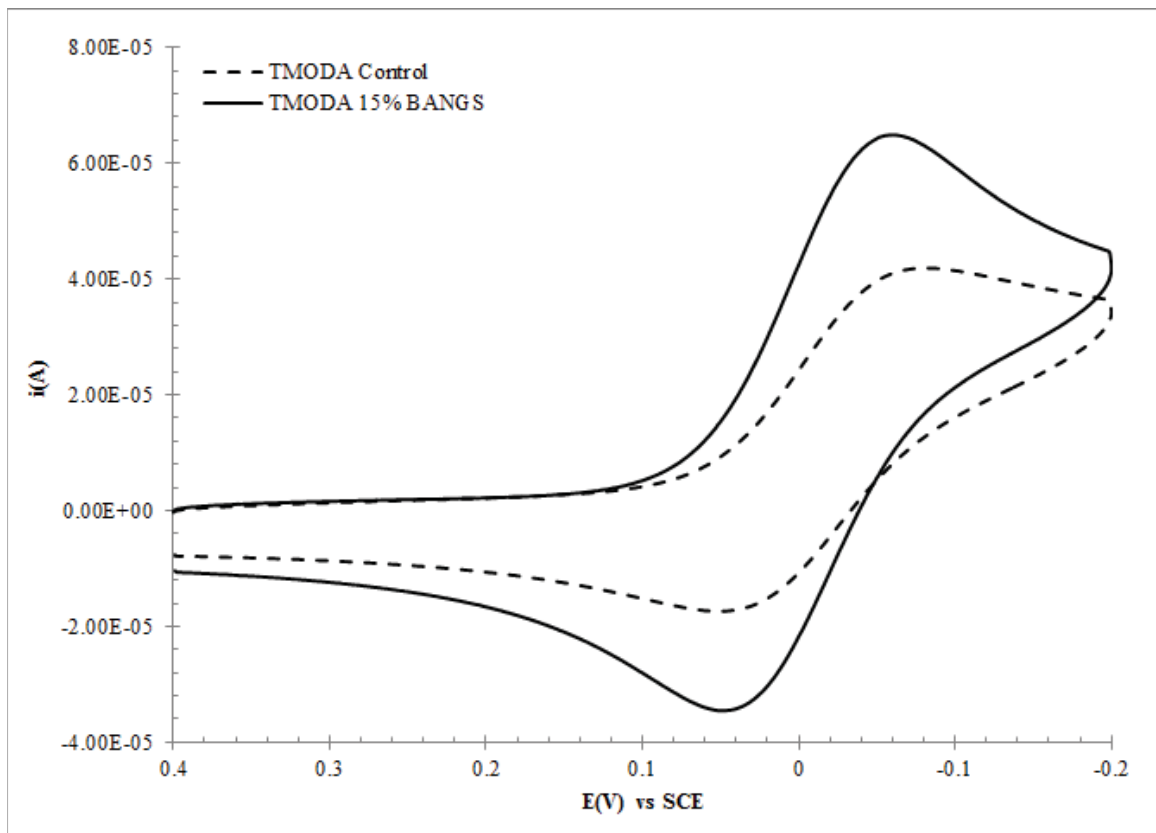


Figure 15. CV for Co(bpy)$_3^{3+}$ at TMODA modified glassy carbon electrodes. 1 mM redox couple in 0.1 M Na$_2$SO$_4$ (aq.), $v = 100$ mV/sec; potential versus saturated calomel electrode (SCE).

for the oxidized (D$_R$) and reduced (D$_O$) form of the species are determined from

plots of $i_p$ (A) versus square root of scan rate ($v$), and for D$_R$ in Figure 17. Linear

treatment of TMODA control electrodes yields y $= 9.536$x10$^{-5}$x $+ 6.963$x10$^{-6}$ with

an R$^2 = 0.98$; from the slope this returns a D$_O = 5.99$x10$^{-7}$ cm$^2$/sec. Likewise, linear

treatment of the magnetically modified electrodes yields a fit of y $= 1.831$x10$^{-4}$x $+$

$2.940$x10$^{-6}$, with a correlation of R$^2 = 0.999$. This returns a D$_O = 2.21$x10$^{-6}$.
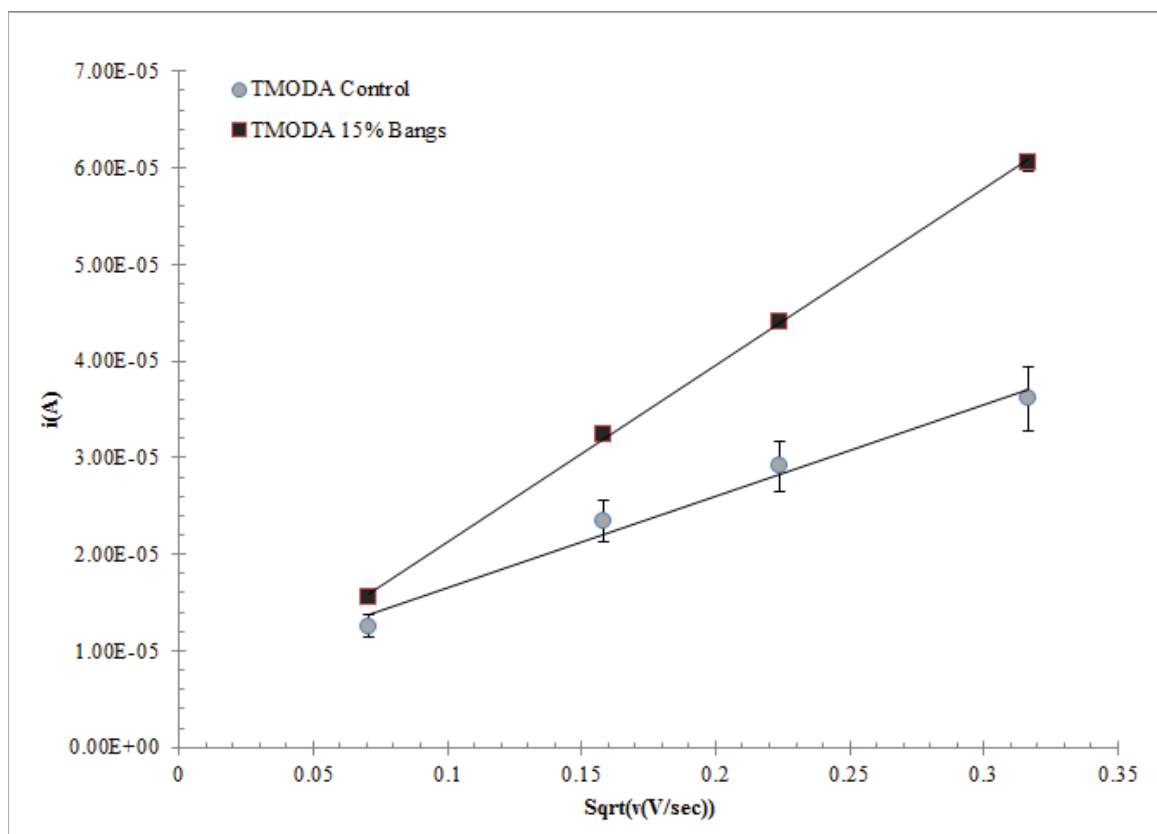
Figure 16. Plot of $i_p^f$ (A) versus $\sqrt{v}$ for the forward wave (D$_O$) for Co(bpy)$_3^{3+}$.
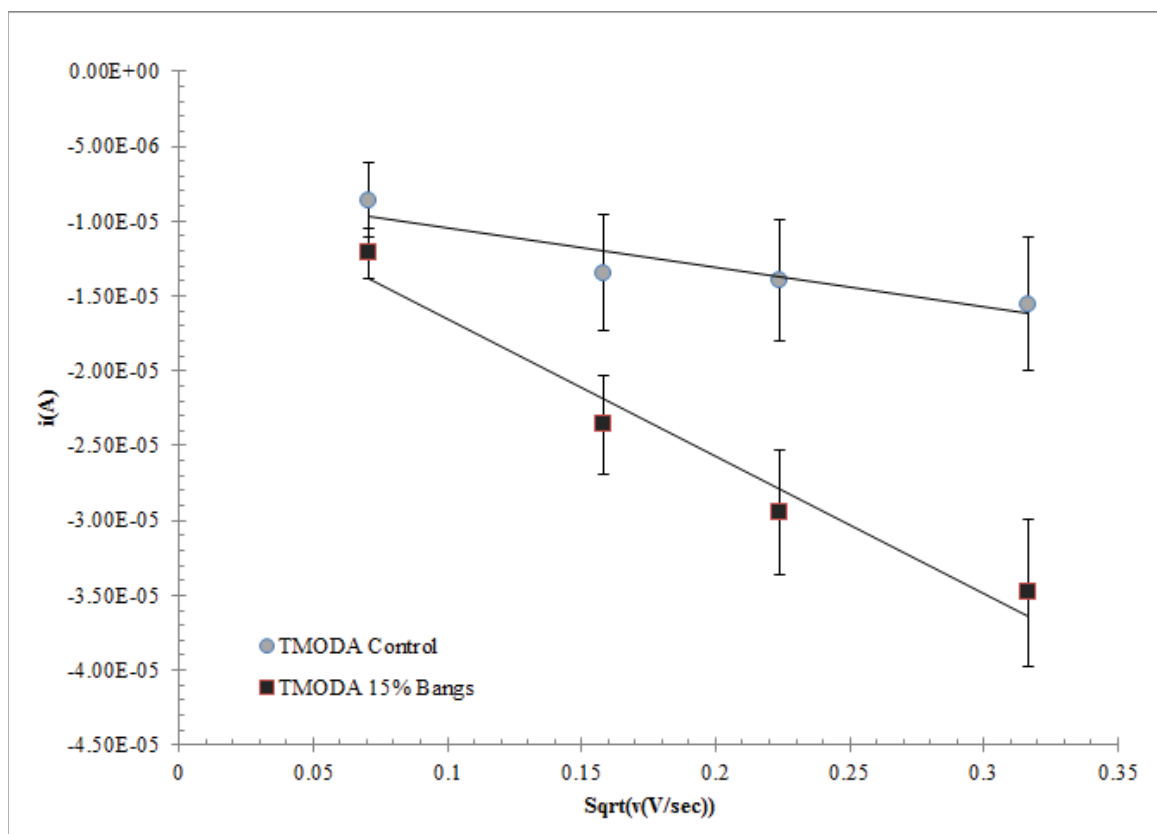
Figure 17. Plot of $i_p^b$ (A) versus $\sqrt{v}$ for the reverse wave ($D_R$) for $Co(bpy)_3^{3+}$.

Table 4. Values of peak currents and peak splittings for Co(III)(bpy).

| $v$ (mV/sec) | $i_p^f$ ($\mu$A) | | $i_p^b$ ($\mu$A) | | $\Delta E_p$ (mV) | |
|---|---|---|---|---|---|---|
| | TMODA | BANGS | TMODA | BANGS | TMODA | BANGS |
| 5 | 12.5($\pm$ 0.6) | 16($\pm$ 1) | -8.6($\pm$ 0.6) | -12.2($\pm$ 0.9) | 90($\pm$ 4) | 76($\pm$ 3) |
| 25 | 23.4($\pm$ 0.9) | 32($\pm$ 3) | -13($\pm$ 1) | -24($\pm$ 2) | 103($\pm$ 9) | 86($\pm$ 7) |
| 50 | 29($\pm$ 1) | 44($\pm$ 1) | -14($\pm$ 3) | -30($\pm$ 2) | 121($\pm$ 13) | 96($\pm$ 8) |
| 100 | 39($\pm$ 3) | 61($\pm$ 5) | -15($\pm$ 1) | -35($\pm$ 3) | 139($\pm$ 16) | 108($\pm$ 12) |

Linear treatment of TMODA control electrodes yields y = -2.668x10$^5$x - 7.774x10$^{-6}$ with an $R^2$ = 0.86; from the slope this returns a $D_R$ = 4.69x10$^{-8}$ cm$^2$/sec. Likewise, linear treatment of the magnetically modified electrodes yields a fit of y = -9.189x10$^{-5}$x - 7.365x10$^{-6}$, with a correlation of $R^2$ = 0.96. This returns a $D_R$ = 5.56x10$^{-7}$ cm$^2$/sec. This treatment reveals a slight difference in the diffusion constants between reduced and oxidized species ($\sim$10%), and therefore both values are considered in the treatment. However, the working curve holds for 0.2 $\leq$ $D_A/D_B \leq$ 5; this is in agreement here (and for the following species). Values for Co(bpy)$_3^{3+}$ at TMODA electrodes are tabulated. The differences in $i_p^f$ and $\Delta E_p$ are different at the 99.8 and 80 % confidence levels, respectively at $v$ = 100 mV/sec.

2.3.2.4 Potassium ferricyanide, $K_3Fe(CN)_6$

For measurements on $Fe(CN)_6^{3-}$, solutions of 1mM redox probe in 0.1 M $Na_2SO_4$ (aq) were prepared freshly before measurements were recorded to ensure accurate concentrations. Measurements were taken sequentially from all electrodes at scan rates of 5, 25, 50, and 100 mV/sec, where all measurements were taken in quadruplet (n = 4). Adequate re-equilibriation between measurements was assumed. $Fe(CN)_6^{3-}$

undergoes the following redox reaction, written here as the reduction,

$$Fe(CN)_6^{3-} + e^- \rightleftharpoons Fe(CN)_6^{4-} \tag{50}$$
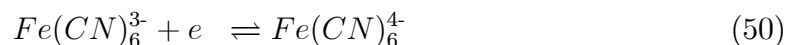
Figure 18 shows typical flux enhancement between modified and unmodified electrodes at $v = 100$ mV/sec. Figure 19 shows the effect on Diffusion constants
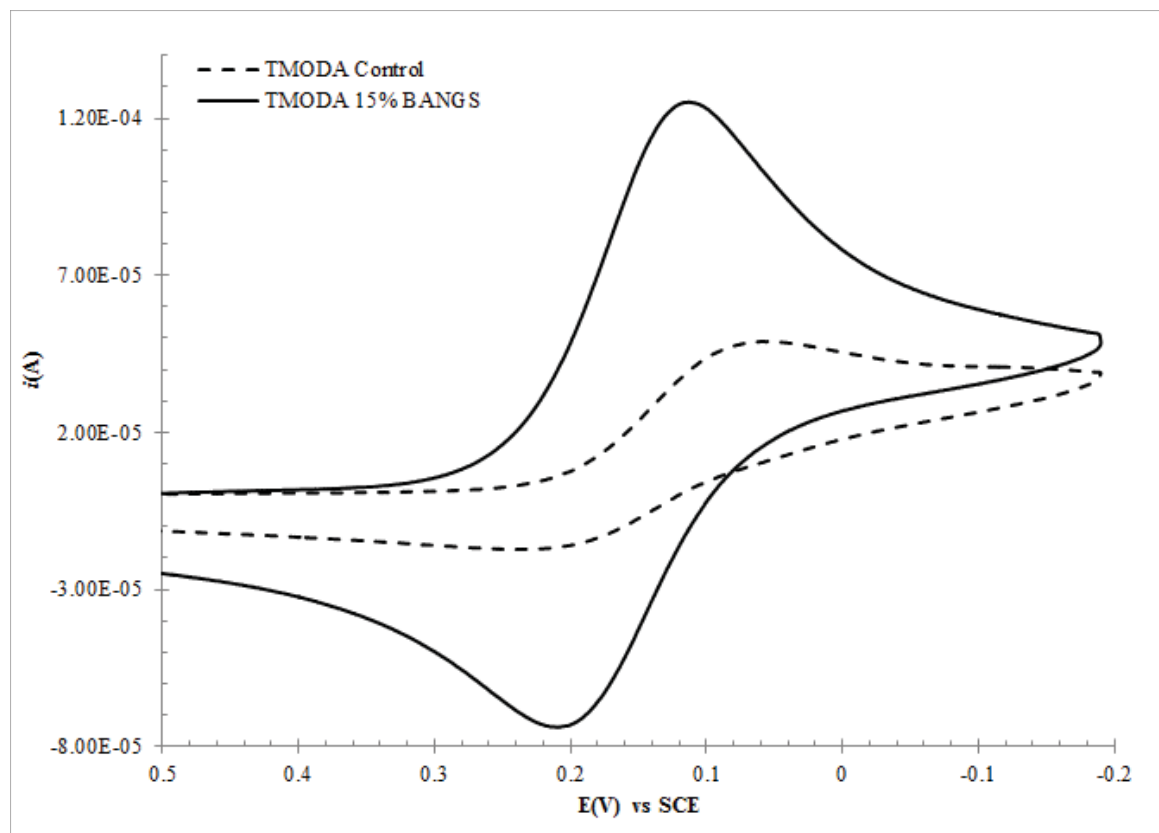


Figure 18. CV for $Fe(CN)_6^3$ at TMODA modified glassy carbon electrodes. 1 mM redox couple in 0.1 M $Na_2SO_4$ (aq.), $v = 100$ mV/sec; potential versus saturated calomel electrode (SCE).

for the oxidized ($D_R$) and reduced ($D_O$) form of the species are determined from plots of $i_p$ (A) versus square root ($v$), and for $D_R$ in Figure 20. Linear treatment of TMODA control electrodes yields y $= 1.173$x$10^{-4}$x $+ 1.171$x$10^{-5}$ with an $R^2 = 0.99$;

Figure 19. Plot of $i_p^f$ (A) versus $\sqrt{v}$ for the forward wave ($D_O$) for Fe(CN)$_6^{3-}$.

from the slope this returns a $D_O = 9.06 \times 10^{-7}$ cm$^2$/sec. Likewise, linear treatment of the magnetically modified electrodes yields a fit of y $= 3.830 \times 10^{-4}$x - $1.262 \times 10^{-6}$, with a correlation of $R^2 = 0.99$. This returns a $D_O = 9.66 \times 10^{-6}$.



Figure 20. Plot of $i_p^b$ (A) versus $\sqrt{v}$ for the reverse wave ($D_R$) for Fe(CN)$_6^{3-}$.

Linear treatment of TMODA control electrodes yields y $= -3.270 \times 10^{-5}$x - $7.441 \times 10^{-6}$ with an $R^2 = 0.99$; from the slope this returns a $D_R = 7.04 \times 10^{-8}$ cm$^2$/sec. Likewise, linear treatment of the magnetically modified electrodes yields a fit of y $= -2.210 \times 10^{-4}$x - $5.212 \times 10^{-6}$, with a correlation of $R^2 = 0.99$. This returns a $D_R = 3.22 \times 10^{-6}$ cm$^2$/sec. Again, this treatment reveals a slight difference in the diffusion

Table 5. Values of peak currents and peak splittings for ferricyanide.

| | $i_p^f$ ($\mu$A) | | $i_p^b$ ($\mu$A) | | $\Delta E_p$ (mV) | |
|---|---|---|---|---|---|---|
| $v$ (mV/sec) | TMODA | BANGS | TMODA | BANGS | TMODA | BANGS |
| 5 | 28($\pm$ 3) | 51($\pm$ 1) | -12($\pm$ 3) | -36($\pm$ 2) | 149($\pm$ 25) | 74($\pm$ 3) |
| 25 | 39($\pm$ 5) | 84($\pm$ 2) | -15($\pm$ 4) | -56($\pm$ 4) | 172($\pm$ 28) | 84($\pm$ 6) |
| 50 | 49($\pm$ 8) | 125($\pm$ 4) | -17($\pm$ 5) | -74($\pm$ 6) | 183($\pm$ 12) | 100($\pm$ 5) |
| 100 | 64($\pm$ 11) | 167($\pm$ 7) | -22($\pm$ 5) | -104($\pm$ 10) | 194($\pm$ 17) | 112($\pm$ 6) |

Table 6. Calculated values of the heterogeneous rate constant for cationic redox probes.

| | $Ru(bpy)_3^{2+}, k^0$ | | $Co(bpy)_3^{2+}, k^0$ | | $Co(bpy)_3^{3+}, k^0$ | | $Fe(CN)_6^{3-}, k^0$ | |
|---|---|---|---|---|---|---|---|---|
| $v$ (mV/sec) | TMODA | BANGS | TMODA | BANGS | TMODA | BANGS | TMODA | BANGS |
| 5 | $2.3\times10^{-4}$ | $4.3\times10^{-4}$ | —— | —— | $1.2\times10^{-4}$ | $3.1\times10^{-4}$ | $3.1\times10^{-4}$ | $1.4\times10^{-4}$ |
| 25 | $5.1\times10^{-4}$ | $9.6\times10^{-4}$ | $4.0\times10^{-4}$ | $8.7\times10^{-4}$ | $2.7\times10^{-4}$ | $6.9\times10^{-4}$ | $4.9\times10^{-4}$ | $2.2\times10^{-4}$ |
| 50 | $7.2\times10^{-4}$ | $1.4\times10^{-3}$ | $5.8\times10^{-4}$ | $1.2\times10^{-3}$ | $3.9\times10^{-4}$ | $9.9\times10^{-4}$ | $6.9\times10^{-4}$ | $3.1\times10^{-3}$ |
| 100 | $1.0\times10^{-3}$ | $1.9\times10^{-3}$ | $8.2\times10^{-4}$ | $1.8\times10^{-3}$ | $5.5\times10^{-4}$ | $1.4\times10^{-3}$ | $9.8\times10^{-4}$ | $4.5\times10^{-3}$ |

constants between reduced on oxidized species ($\sim$10%), and therefore both values are considered in the treatment. However, the working curve holds for $0.2 \leq D_A/D_B \leq 5$; this is in agreement here (and for the following species). Values for $Fe(CN)_6^{3-}$ at TMODA electrodes are tabulated. The differences in $i_p^f$ and $\Delta E_p$ are different at the 98 and 90 % confidence levels, respectively at $v = 100$ mV/sec.

Values for $k^0$ were determined as described in at the beginning of this section. We observe an increase in the value for $k^0$ (cm s$^{-1}$) across all transition metal redox probes examined. This increase is seen for both cationic and anionic redox probes.

Values of the homogeneous electron transfer rate constant are compared to the heterogeneous rate constant as proposed by Marcus in his theory of macroscopic charge transfer [1]. These values are for electron transfer reactions without an external magnetic field. In Equation 31, it is estimated that the square root of the

Table 7. Calculated values of the heterogeneous rate constant for potassium ferricyanide.

| | $Fe(CN)_6^{3-}, k^0$ | |
|---|---|---|
| $v$ (mV/sec) | TMODA | BANGS |
| 20 | $3.1\text{x}10^{-4}$ | $1.4\text{x}10^{-4}$ |
| 50 | $4.9\text{x}10^{-4}$ | $2.2\text{x}10^{-4}$ |
| 100 | $6.9\text{x}10^{-4}$ | $3.1\text{x}10^{-3}$ |
| 200 | $9.8\text{x}10^{-4}$ | $4.5\text{x}10^{-3}$ |

homogeneous rate over the self exchange pre-exponential factor is approximately that of the heterogeneous rate over the electrode reaction pre-exponential factor. Values for the homogeneous preexponential constant in literature range between approximately $10^{11}$ and $10^{12}$ M$^{-1}$s$^{-1}$, while values for the heterogeneous preexponential constant are approximately $10^4$ to $10^5$ cm/s.

The values for the pre-exponentials used for the analysis were calculated from Equations 32 and 33. Values of the homogeneous rate constant are determined by assuming Dahms Ruff conduction model, where observed diffusion is both physical ($D_p$) and by hopping ($D_{et}$), this is given by equation 37. However, when $D_p << D_{et}$ or in domains of high concentration (as in Equation 38) then,

$$D_{et} = \frac{k_{11}c^{*}\delta^2}{6} \tag{51}$$

Where $k_{11}$ is the self exchange electron transfer constant, c* is concentration of the redox species (1 mM), $\delta^2$ is the moiety size squared, and 6 is the three dimensional geometric factor. Solving for $k_{11}$ gives 52.

$$k_{11} = \frac{6D}{c^{*}\delta^2} \tag{52}$$

Table 8. Values for the heterogeneous and homogeneous rate constants at control TMODA Nafion modified electrodes.

| Species | $Ru(bpy)_3^{2+}$ | $Co(bpy)_3^{2+}$ | $Co(bpy)_3^{3+}$ | $Fe(CN)_6^{3-}$ |
|---|---|---|---|---|
| $k_{11}$ $(M^{-1}s^{-1})$ | $2.0 \times 10^{11}$ | $1.2 \times 10^{11}$ | $1.8 \times 10^{11}$ | $6.3 \times 10^{11}$ |
| $k^0$ $(cm/s)$ | $3.6 \times 10^{-4}$ | $2.7 \times 10^{-4}$ | $1.9 \times 10^{-4}$ | $2.9 \times 10^{-4}$ |
| $\delta$ $(cm)$ | $1.4 \times 10^{-7}$ | $1.4 \times 10^{-7}$ | $1.4 \times 10^{-7}$ | $9.2 \times 10^{-8}$ |
| $D$ $(cm^2/s)$ | $6.6 \times 10^{-7}$ | $3.9 \times 10^{-7}$ | $5.9 \times 10^{-7}$ | $9.1 \times 10^{-7}$ |
| $k^0/\sqrt{k_{11}}$ | $\mathbf{7.9 \times 10^{-10}}$ | $\mathbf{7.8 \times 10^{-10}}$ | $\mathbf{4.4 \times 10^{-10}}$ | $\mathbf{3.7 \times 10^{-10}}$ |

Table 9. Values for the homogeneous and heterogeneous rate constants at magnetically modified TMODA Nafion electrodes.

| Species | $Ru(bpy)_3^{2+}$ | $Co(bpy)_3^{2+}$ | $Co(bpy)_3^{3+}$ | $Fe(CN)_6^{3-}$ |
|---|---|---|---|---|
| $k_{11}$ $(M^{-1}s^{-1})$ | $7.1 \times 10^{11}$ | $4.7 \times 10^{11}$ | $6.8 \times 10^{11}$ | $6.7 \times 10^{11}$ |
| $k^0$ $(cm/s)$ | $6.6 \times 10^{-4}$ | $6.2 \times 10^{-4}$ | $4.9 \times 10^{-4}$ | $9.2 \times 10^{-4}$ |
| $\delta$ $(cm)$ | $1.4 \times 10^{-7}$ | $1.4 \times 10^{-7}$ | $1.4 \times 10^{-7}$ | $9.2 \times 10^{-8}$ |
| $D$ $(cm^2/s)$ | $2.3 \times 10^{-6}$ | $1.6 \times 10^{-6}$ | $2.2 \times 10^{-6}$ | $9.66 \times 10^{-6}$ |
| $k^0/\sqrt{k_{11}}$ | $\mathbf{8.0 \times 10^{-10}}$ | $\mathbf{9.0 \times 10^{-10}}$ | $\mathbf{6.0 \times 10^{-10}}$ | $\mathbf{3.5 \times 10^{-10}}$ |

Values for $k^0$ were extracted from plots of $k^0$ versus $v$ at $v = 0$ mV/sec, the y-axis intercept. Values for $k_{11}$ and $k^0$ in control TMODA films are given in Table 8. Values for $k_{11}$ and $k^0$ in magnetically modified films are given in Table 9. Ratios approximating Marcus theory, including $k^0/\sqrt{k_{11}}$, are given in the tables, we assume no affects on the collision frequencies, $A_{el}$ or $A_{ex}$. The assumption is that magnetic effects are affecting the heterogenous rate. If the ratios of these values are similar in both the unmodified and modified system, then the current enhancements observed are not only attributed to increases in homogeneous self exchange, but rather contributions from both increased heterogeneous ET and homogeneous ET. This is what is observed. In the tables, $\mu$ is the reduced mass of the chemical species, given

by Equation 53.

$$\mu = \frac{m_1 m_2}{m_1 + m_2} \tag{53}$$

For homogeneous (self exchange) electron transfer process, $m_1 = m_2$.

2.3.2.5 Electrochemical Impedance Spectroscopy (EIS) Measurements

Electrochemical impedance spectroscopy is a technique that measures impedance over a range of frequencies [1]. The impedance results from resistance to an alternating current perturbation of the electrochemical system. These perturbations are of much smaller magnitude than those in voltammetric analyses, and as such, can result in highly sensitive measurements with little system impact. For example, batteries and electrochemical capacitors (like those in Chapter 5) can be analyzed with EIS as an unintrusive method; evaluating the electrochemical capacity of the system without having to charge or discharge the system.

The applied frequency oscillates around a set potential, typically near the standard reduction potential of the chemical species being examined. EIS measurements result in complex plane plots, returning impedance in both real and complex variables. Complex plane plots, also call Nyquist plots, provide a semi-quantitative assesment of the impedance properties of a system. For a more quantitative analysis, the data is fit to circuit elements (e.g., resistors and capacitors).

Here, impedance data was collected for the $Fe(CN)_6^{3-}$ redox couple at glassy carbon electrode modified with TMODA films. These are the same films describe previously. Figure 21 is a complex plot for TMODA modified and 15 % (v/v) BANGS particles in TMODA. Again, films replicates were tested where n = 3. The
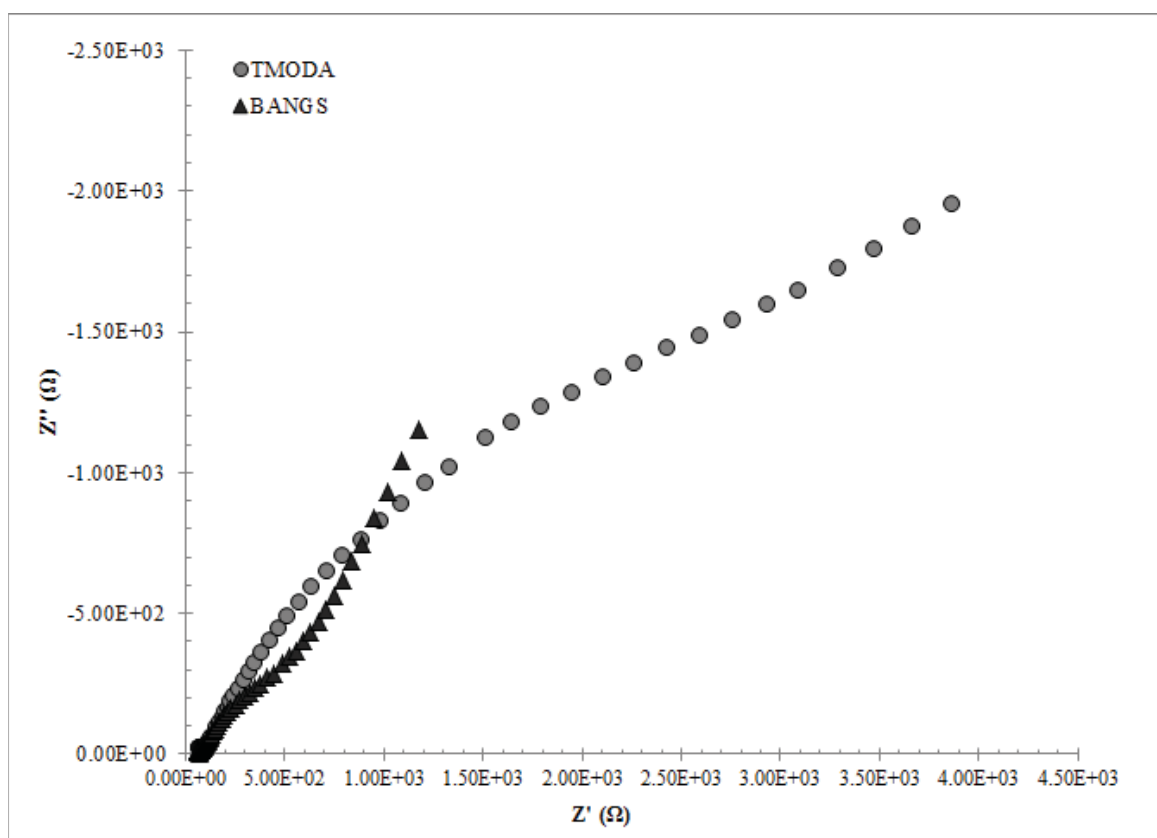
Figure 21. Complex plane plot of $Fe(CN)_6^{3-}$ at TMODA modified glassy carbon electrodes. TMODA control electrodes and 15 % BANGS (v/v) TMODA magnetically modified electrodes an average response of n = 3 films.

Table 10. Results of EIS data fitting to Randles equivalence circuit at TMODA modified glassy carbon electrodes.

| Modification | $R_S$ ($\Omega$) | $C_{dl}$ (F) | $R_F$ ($\Omega$) | $C_F$ (F) |
|---|---|---|---|---|
| TMODA | 96.9 ($\pm$ 12) | 1.7 x $10^{-5}$ ($\pm$ 2 x $10^{-6}$) | $1._9$ x $10^3$ ($\pm$ 12) | 4.3 x $10^{-4}$ ($\pm$ 2 x $10^{-5}$) |
| BANGS | 75.2 ($\pm$ 11) | $4._4$ x $10^{-5}$ ($\pm$ 1 x $10^{-5}$) | 5.5 x $10^2$ ($\pm$ 17) | 8.35 x $10^{-3}$ ($\pm$ 7 x $10^{-6}$) |

data from the plot is fit to the Randles equilvance circuit, a common electrochemical

representation of a system that undergoes faradaic electron transfer.The Randles
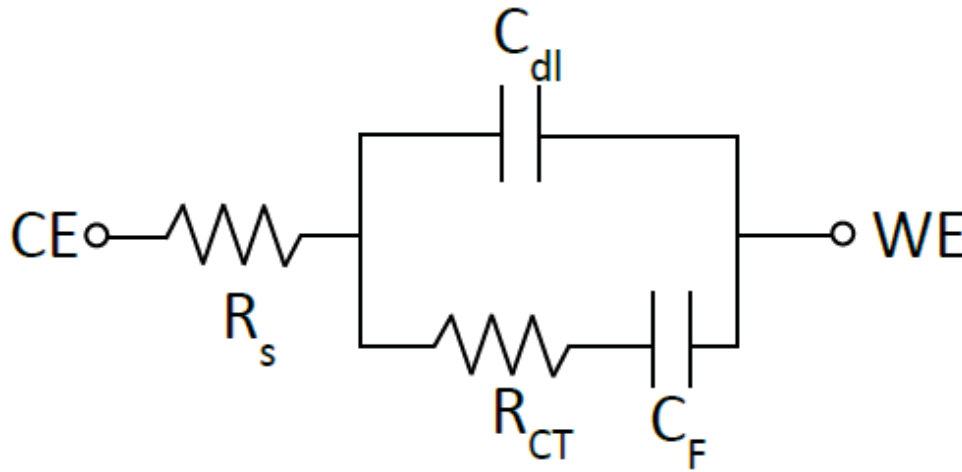


Figure 22. Randles equivalence circuit. Counter electrode (CE), solution resistance ($R_S$), double layer capacitance ($C_{dl}$, non-faradaic), charge transfer resistance ($R_{CT}$), faradaic capacitance ($C_F$), working electrode (WE).

equivalence circuit countains elements of solution resistance ($R_S$), electrochemical

double layer capacitance ($C_{dl}$), as well as faradiac elements including charge transfer

resistance ($R_{CT}$) and faradaic capacitance ($C_F$). The results of this fitting are given

in Table 10. The fitting returns a decrease in the resistance to charge transfer at

magnetically modified electrodes. This is in agreement with the voltammetric data

of increased current response at modified electrodes as $i \propto R^{-1}$. Additionally, and

most significant to the work in Chapter 5, we observe an increase in the faradaic capacitance of of 18 fold. Faradaic capacitance is believed to be responsible for the high normalized capacitances in electrochemical supercapacitors, The principle of faradaic capacitance and the impacts of magnetic modification of electrochemical capacitors will be expanded upon in Chapter 5.

### 2.3.2.6 Measurements on Organic Redox Couples

In addition to transition metal redox probes, two organic species, 2,6-dimethyl 1,4-benzoquinone (DMBQ) and hydroquinone, were analyzed at TMODA modified electrodes. These species undergo more complicated ET reaction than the inorganic species, including two-step ET reactions coupled with complicated chemical intermediates. Minteer analyzed a variety of organic redox probes [11]. In organic media, these species may or may not experience magnetic field effects. In the aqueous system used here (0.1 M $Na_2SO_4$), both chemical species experience field effects.

### 2.3.2.6.1 2,6-dimethyl 1,4-benzoquinone (DMBQ)

In aqueous media, DMBQ undergoes an apparent one ET reaction. Increased peak currents are observed at magnetically modified electrodes, however, decreases in peak splitting are not observed. For measurements on DMBQ, solutions of 1mM redox probe in 0.1 M $Na_2SO_4$ (aq) were prepared freshly before measurements were recorded to ensure accurate concentrations. Measurements were taken sequentially from all electrodes at scan rates of 5, 25, 50, and 100 mV/sec, where all measurements

were take in quadruplet (n = 4). No specific attention was given for rest between measurements as the scans are sequential (i.e., electrode 1 scanned first, followed by electrode 2, etc.), and adequate re-equilibriation was assumed.

DMBQ undergoes the following redox reaction 23, Figure 24 shows typical flux
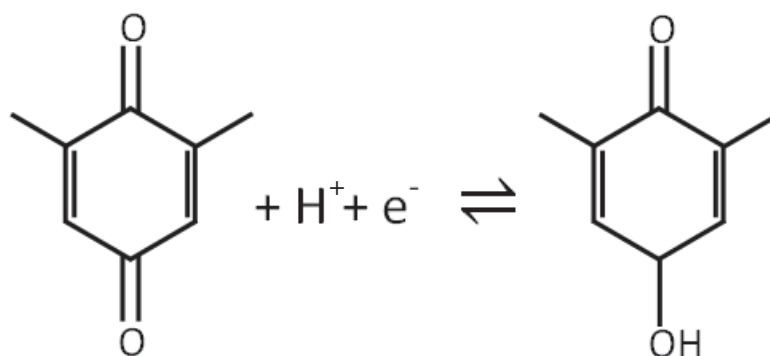


Figure 23. Reaction scheme for 2,6-dimethyl 1,4-benzoquinone.

enhancement between modified and unmodified electrodes at $v = 100$ mV/sec. Figures 25 and 26 show the effect on diffusion constants for the oxidized ($D_R$) and reduced ($D_O$) form of the species as determined from plots of $i_p$ (A) versus square root of scan rate ($v$). Linear treatment of TMODA control electrodes yields y = $4.827 \times 10^{-4}$x $+ 1.678 \times 10^{-5}$ with an $R^2 = 0.99$; from the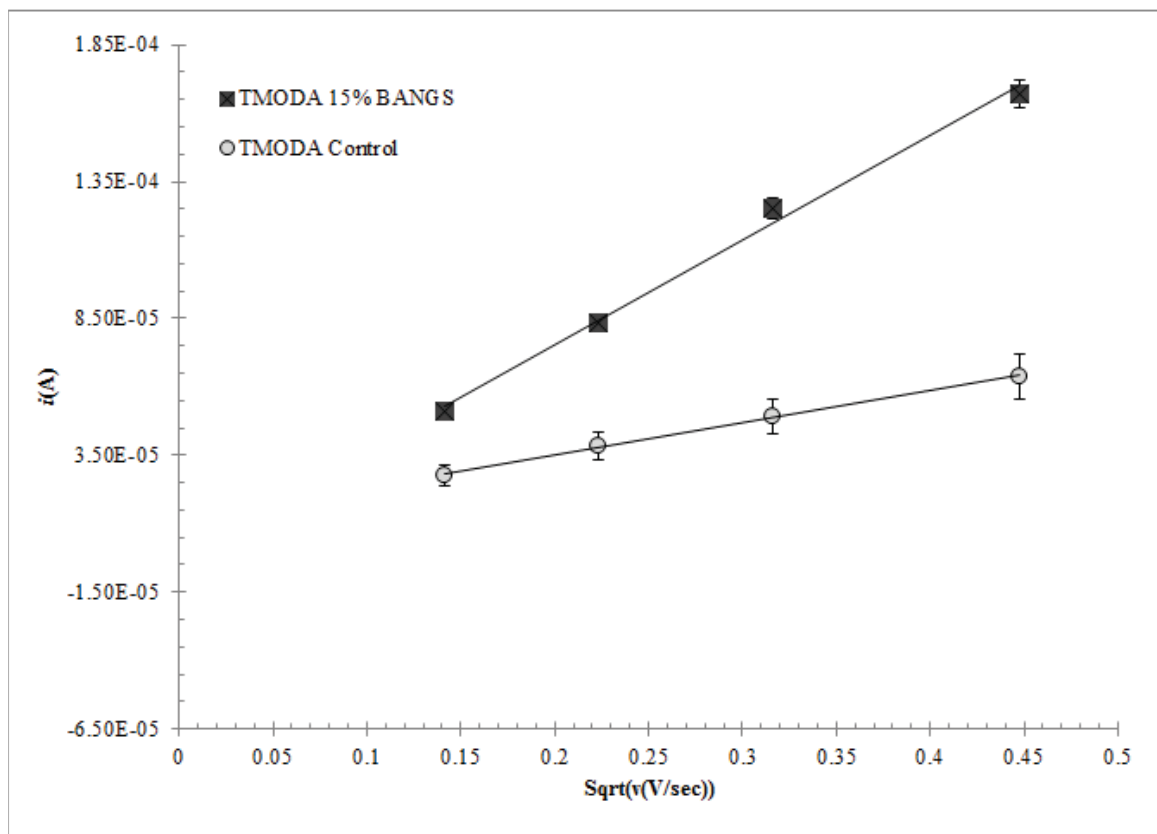 slope this returns a $D_O =$ $1.54 \times 10^{-5}$ cm$^2$/sec. Likewise, linear treatment of the magnetically modified electrodes yields a fit of y $= 8.036 \times 10^{-4}$x $+ 2.781 \times 10^{-6}$, with a correlation of $R^2 = 0.99$. This returns a $D_O = 4.25 \times 10^{-5}$.
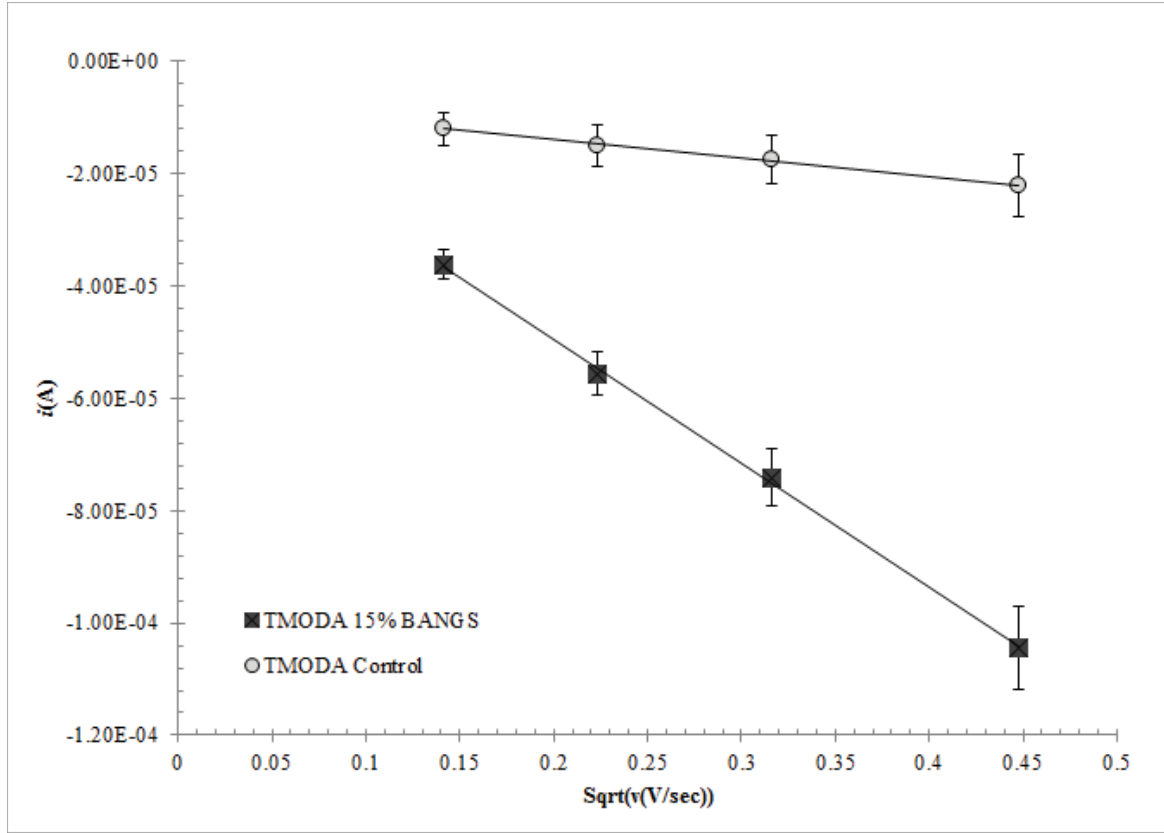
Linear treatment of TMODA control electrodes yields y $= -4.206 \times 10^{-4}$x $-$ $1.165 \times 10^{-5}$ with an $R^2 = 0.99$; from the slope this returns a $D_R = 1.17 \times 10^{-5}$ cm$^2$/sec. Likewise, linear treatment of the magnetically modified electrodes yields a fit of y
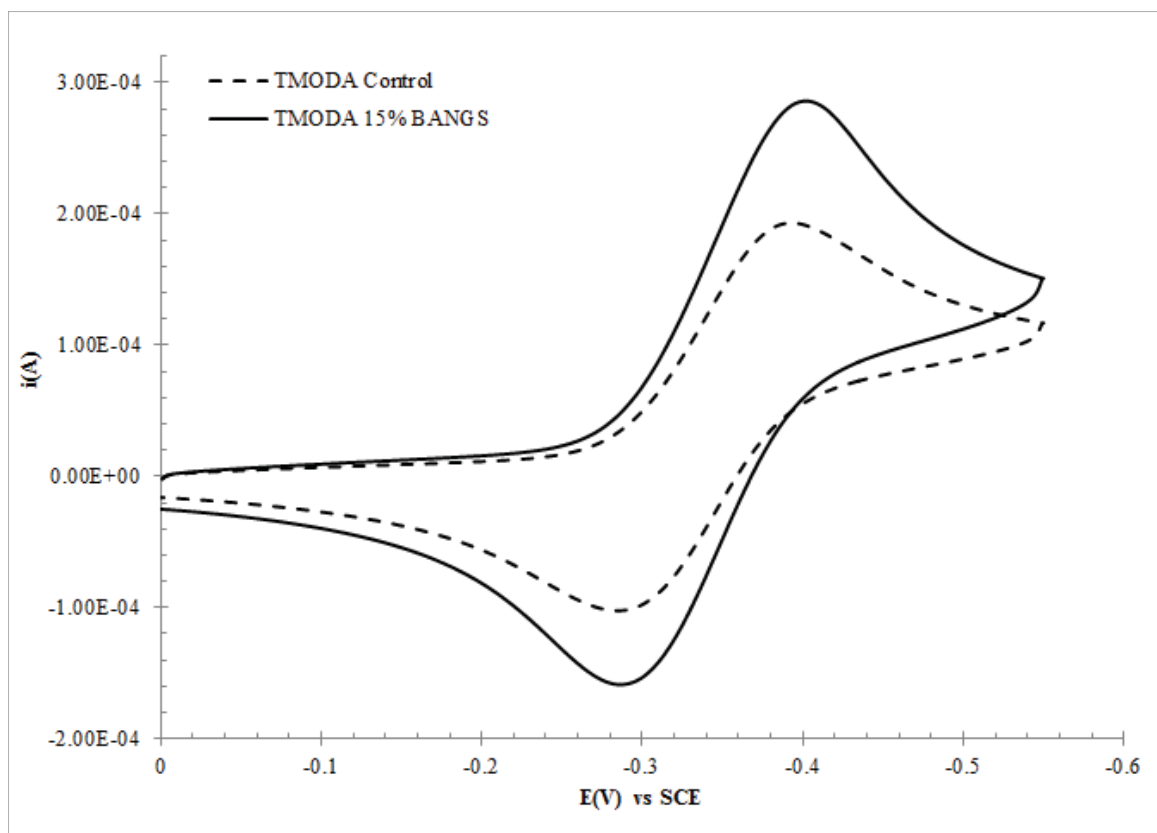
Figure 24. CV for DMBQ at TMODA modified glassy carbon electrodes, 1 mM redox couple in 0.1M $Na_2SO_4$ (aq.), $v = 100$ mV/sec; potential versus saturated calomel electrode (SCE).
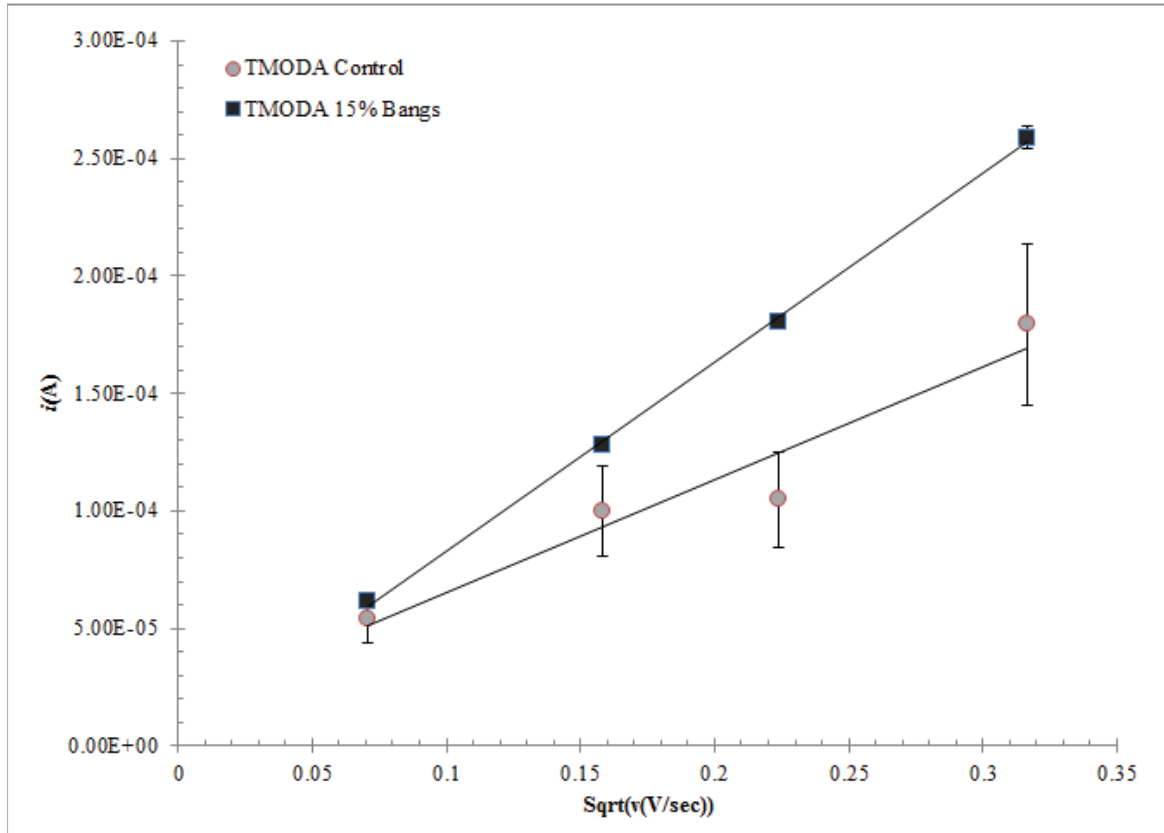
Figure 25. Plot of $i_p^f$ (A) versus $\sqrt{v}$ for the forward wave ($D_O$) for DMBQ.
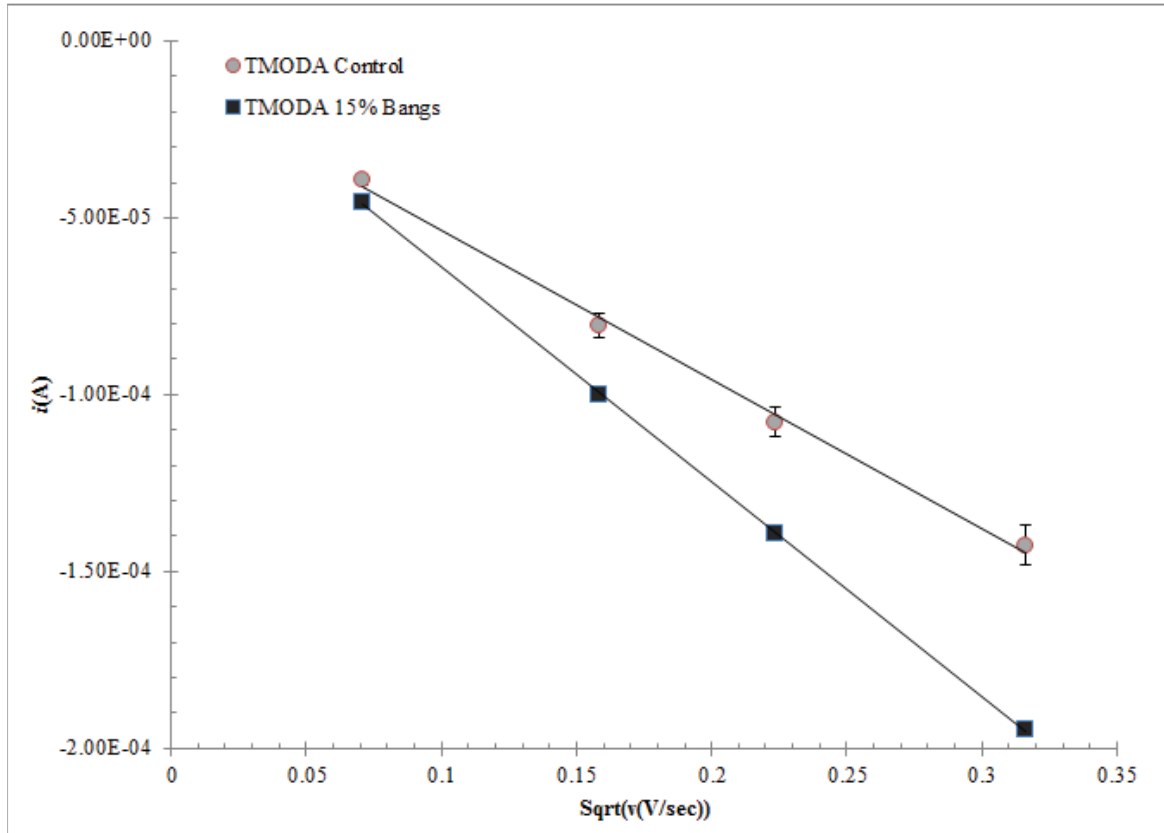
Figure 26. Plot of $i_p^b$ (A) versus $\sqrt{v}$ for the forward wave (D$_O$) for DMBQ.

$= -6.071 \times 10^{-4}x - 3.410 \times 10^{-6}$, with a correlation of $R^2 = 0.99$. This returns a $D_R = 2.43 \times 10^{-5}$ cm$^2$/sec. No peak splitting, $\Delta E_p$, was observed for DMBQ.

2.3.2.6.2 Hydroquinone (HQ)

The last redox species analyzed, hydroquinone, undergoes a complicated two ET reaction process, with a radical intermediate. Given the complexities of the system, the analysis for k$^0$ performed earlier are not performed here. However, magnetic field effects were present. It was shown that these magnetic effects are $v$ dependent, becoming more apparent at higher scan rates. Figure 27 gives the two step reduction reaction from benzoquinone to hydroquinone (however, here the initial species is hydroquinone undergoing oxidation).
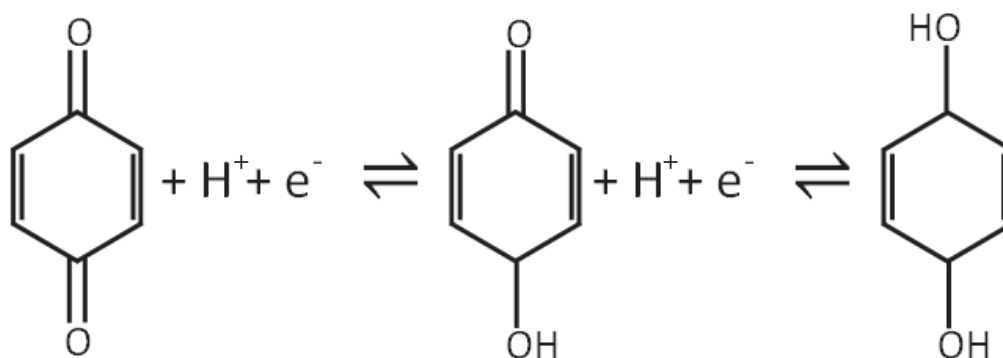


Figure 27. Second order reaction scheme for hydroquinone.

At $v = 25$ mV/sec, two distinct ET steps were observed for both magnetically modified and TMODA control electrodes.

At $v = 50$ mV/sec, two distinct processes were still observed.

As the scan rate was increased to $v = 100$ mV/sec, the forward wave for the
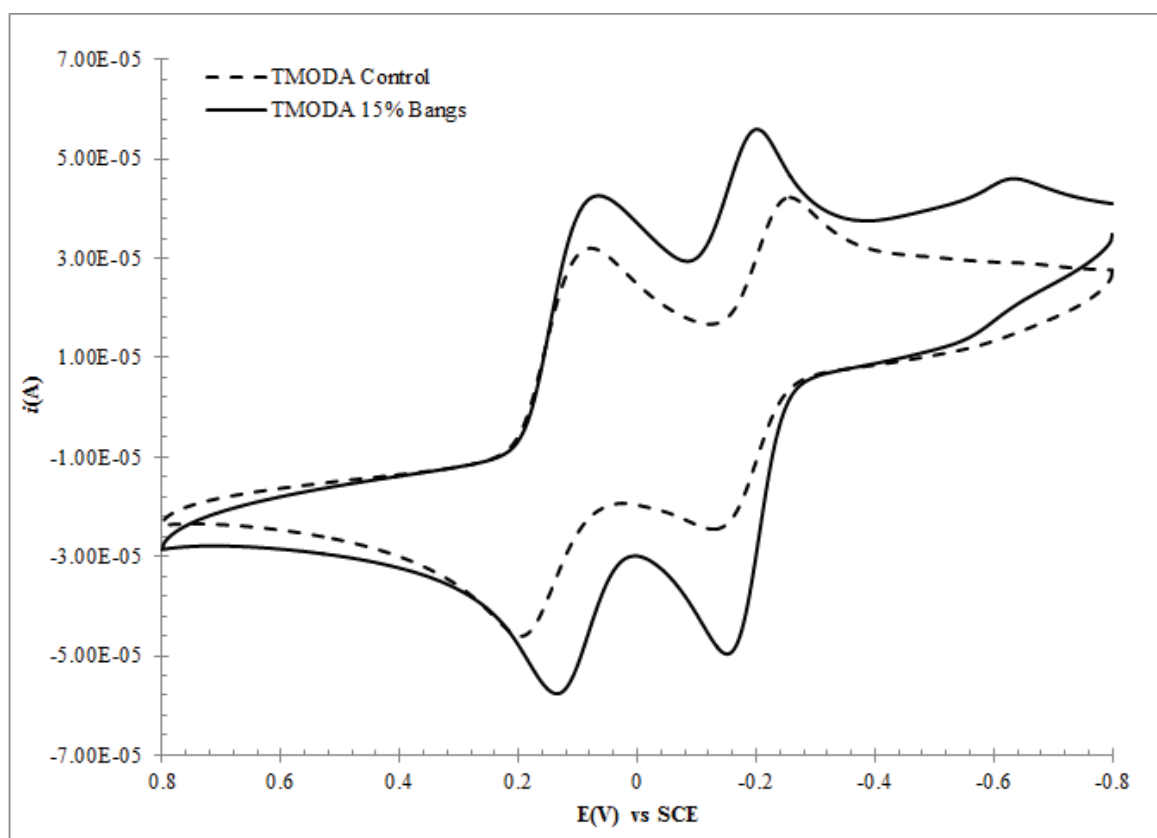
Figure 28. CV for HQ at TMODA modified glassy carbon electrodes. 1 mM redox couple in 0.1 M Na$_2$SO$_4$ (aq.), $v = 25$ mV/sec; potential versus saturated calomel electrode (SCE).
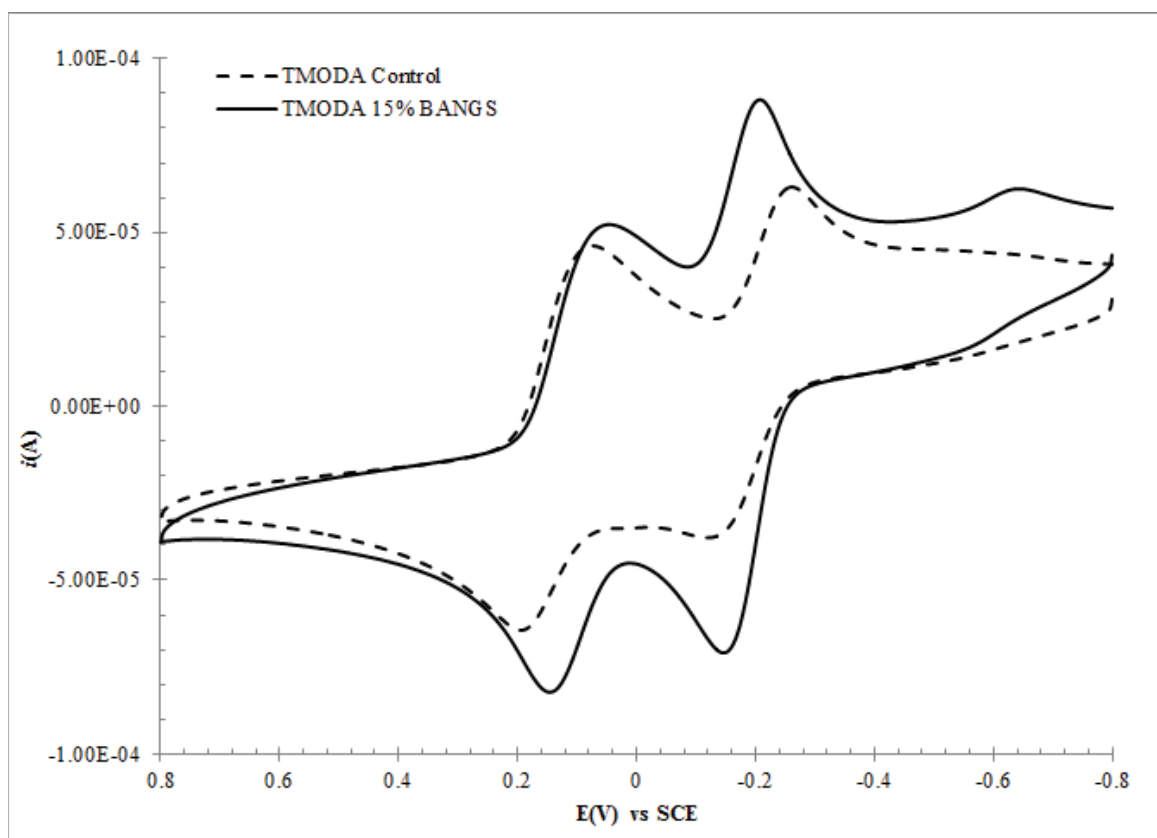
Figure 29. CV for HQ at TMODA modified glassy carbon electrodes. 1 mM redox couple in 0.1 M Na$_2$SO$_4$ (aq.), $v = 50$ mV/sec; potential versus saturated calomel electrode (SCE).

oxidation reaction begins to lose distinction for the TMODA control electrodes.
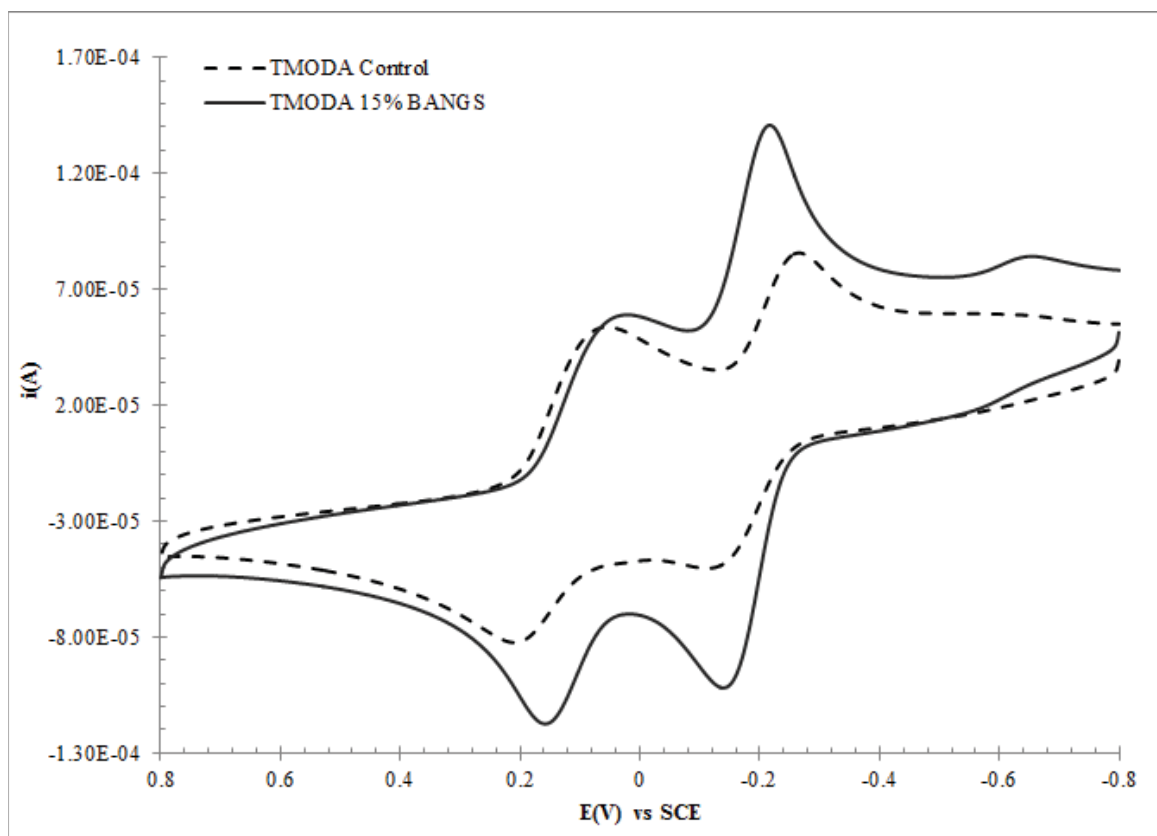


Figure 30. CV for HQ at TMODA modified glassy carbon electrodes. 1 mM redox couple in 0.1 M $Na_2SO_4$ (aq.), $v = 100$ mV/sec; potential versus saturated calomel electrode (SCE).

At scan rates above $v = 200$ mV/sec, the forward waves merge into a single signal for the TMODA control electrodes. While for magnetically modified electrodes, two distinct, ET processes were still evident.

At $v = 300$ mV/sec, current enhancement was still observed at magnetically modified electrodes, as are two distinct ET processes. At unmodified electrodes, the forward, oxidative processes are nearly indistinguishable. For modified electrodes,
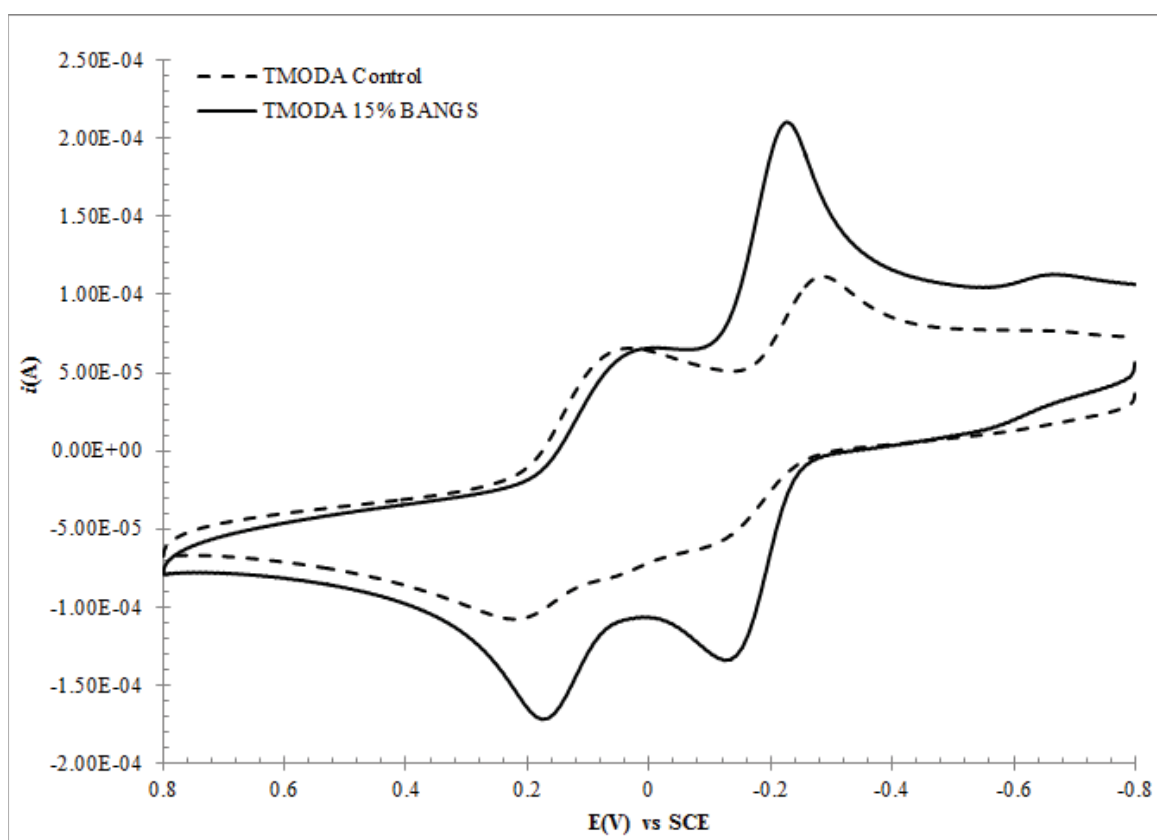
Figure 31. CV for HQ at TMODA modified glassy carbon electrodes. 1 mM redox couple in 0.1 M Na$_2$SO$_4$ (aq.), $v = 200$ mV/sec; potential versus saturated calomel electrode (SCE).

the return waves become less distinct at these higher scan rates. As scan rate
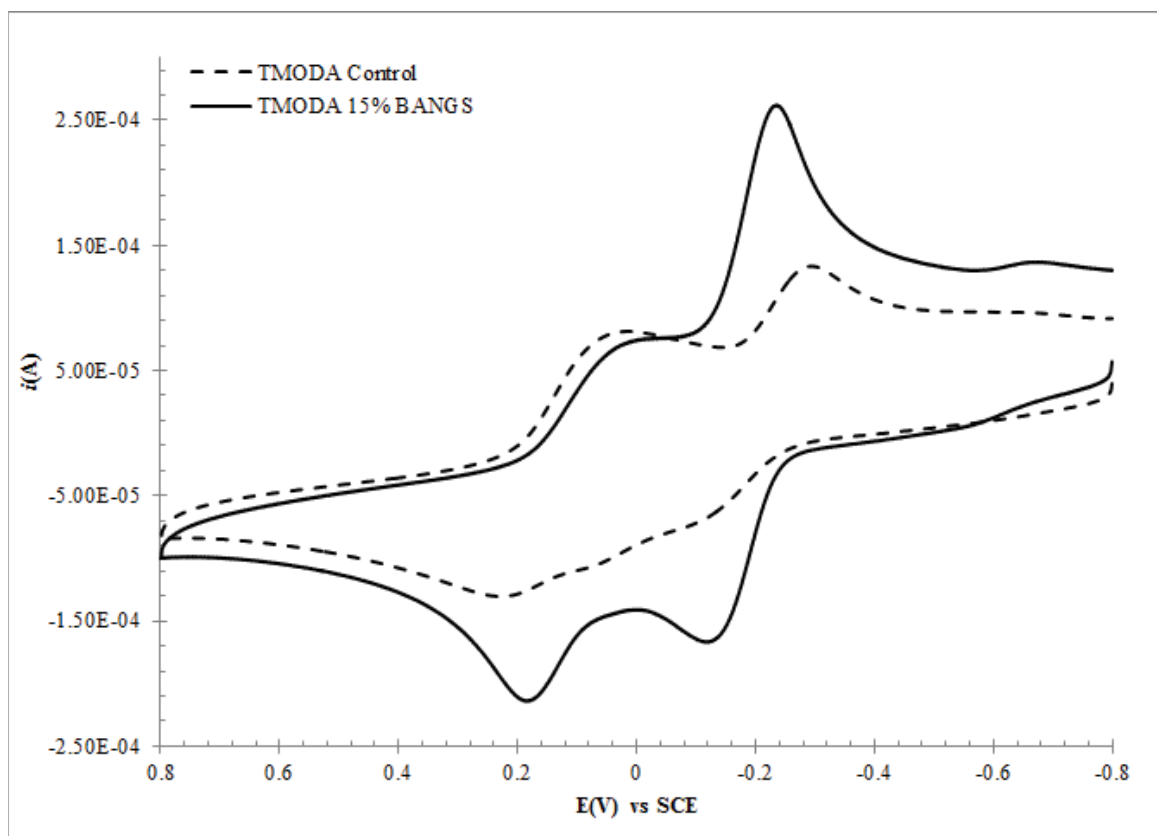


Figure 32. CV for HQ at TMODA modified glassy carbon electrodes. 1 mM redox couple in 0.1 M Na$_2$SO$_4$ (aq.), $v = 300$ mV/sec; potential versus saturated calomel electrode (SCE).

increases, the effects of magnetic fields become more pronounced on this organic redox probe. The implications for these effects may not be straight forward, however, initial speculation of the effects involves stabilization of reaction intermediates, including radical species.

### 2.3.3 Conclusions

Magnetic fields have been shown to enhance current response to a variety of redox species at TMODA Nafion modified electrodes, including common cationic transition metal redox probes, the first anion studied, $K_3Fe(CN)_6$, and two organic species. These effects are likely to arise through similar mechanisms as previously observed increases in self-exchange, that is, through kinetic enhancements. Indeed, analysis of the heterogeneous rate constant, $k^0$, using the analysis developed by Nicholson and Shain, shows increased values of $k^0$ for all transition metal redox couples analyzed. These analyses were based upon measured peak currents and peak splittings, as well as calculated diffusion constants, among other metrics.

Across the range of redox couples tested, we observe increases in $k_{11}$ and $k^0$ values, implying that magnetic field effects in occur on both heterogeneous and homogeneous electron tranfer reactions in TMODA Nafion. These values are seen in Tables 8 and 9; $k_{11}$ values were extracted from the forward diffusion constants of the redox probes in control and magnetically modified systems. Using 'back of envelope' approximations to Marcus theory, we observe no change in the ratio of $k^0/\sqrt{k_{11}}$ for control and magnetically modified electrodes, therefore the Marsuc approximation is appropriate. Lastly, we assumed for this agreement that $A_{el}/\sqrt{A_{ex}}$ does not change in the presence of a magnetic field, only the differnce in size and charge between the bipyridine and thiocyanate ligands.

In the following chapters we will look at two applications of magnetic field effects in electrochemical power and energy systems. These two systems, Grätzel cells,

a type of photoelectrochemical cell, and $MnO_2$ electrodes, utilized as capacitor electrodes, undergo both homogeneous and heterogeneous ET process. Magnetic field effects are observed to enhance these systems. The effects may be incorporated through enhancements in homogeneous rates, as observed previously [13], however, the results presented in the chapter have implications for enhancements in power systems though improved heterogeneous kinetics in the presence of magnetic fields.

CHAPTER 3

MAGNETIC MODIFICATION OF DYE SENSITIZED SOLAR CELLS: GRÄTZEL

CELLS

## 3.1   Introduction

Photoelectrochemical cells (PEC) are solar cells that operate in a manner analogous to conventional p-n-junction solar cells. PEC devices convert incident light to electrical energy (i.e., electrons) that can be used directly or stored. Energy produced by photoelectrochemical cells can be stored electrochemically (batteries) or chemically in chemical bonds. This storage mechanism is analogous to photosynthesis, and as such is sometimes referred to as artificial photosynthesis. Examples of artificial photosynthesis are reduction of water to hydrogen gas in the hydrogen evolution reaction (HER), and oxidation of water in the oxygen evolution reaction (OER) [28–30]. Artificial photosynthesis is an active area of research [6]. Heung Chan Lee recently demonstrated that magnetic fields affect the HER [13]. Lee observed that magnetic fields decrease the amount of overpotential required to drive the reaction and increase the efficiency of the reaction for a variety of p-Si and GaAs materials and morphologies.

Electrical energy production from low cost photoelectrochemical cells was optimized by Grätzel and coworkers in 1991 [17]. Grätzel's revolution was to combine nanoparticulate $TiO_2$, a wide bandgap semiconductor, a Ru-based sensitizing dye, and a regenerative redox species. In this, they created a third-generation, excitonic,

photoelectrochemical device with photoconversion efficiencies near traditional p-Si at a fraction of the cost [10, 31]. These devices are referred to as dye sensitized solar cells (DSSC) or Grätzel cells. Previous attempts at dye sensitization were unsuccessful for a variety of reasons, including photocorrosion of the electrolyte under irradiation, low surface area of semiconductor (i.e., a low roughness factor), and poor semiconductor-dye interaction [18].

The materials in DSSCs are all well tuned. The electrochemistry of the regenerative redox mediator, iodide|triiodide, is extensively studied and established [18]. Likewise, the properties of $TiO_2$ (e.g., favorable redox mediator energetics, low cost, availability, low toxicity), make it an ideal candidate for the DSSC system. Additionally, success have been found in molecular sensitizers based on transition metal complexes, organic chromophores, and quantum dots. These systems have shown remarkable efficiencies that rival traditional solar cells. Photoconversion efficiencies as high as 12.3 % have been achieved [9], yet, in the interim since Grätzel's original reporting, the efficiency has only increased from an initial efficiency of 7.9 %. Even though considerable attention has been given to improving all facets of the DSSC system, including the semiconductor [32–35], the molecular sensitizer [36–39], alternative sensitization techniques [40, 41], and to producing solid state cells that avoid unwanted organic solvents [42–47].

Despite well established materials, improvements in photoconversion efficiency are slow becuase the complex DSSC system suffers from limitations in both materials and fundamental kinetics (e.g., electron transfers and solid state diffusion). However, the Grätzel cell model offers researchers a variety of opportunities to

optimize photoconversion efficiencies. For instance, the most recent advancement in conversion efficiency was the utilization of a more efficient sensitizing dye [9]. A zinc porphyrin dye species was shown to act as both a better light absorber and electron transfer reagent than traditional ruthenium bypridal species (e.g., cis-bis(isothiocyanato)bis(2,2'-bipyridyl-4,4'-dicarboxylato)-ruthenium(II), N3).

As progress is made in the materials domains of dyes with high UV tolerance, ionic liquids to replace the organic electrolytes, and replacement materials for the counter electrode, considerations for catalysis are also necessary. Magnetic field effects, such as that reported by Lee, shows that magnetic fields enhance electron transfer (ET) reactions in various power systems that include fuel cells and alkaline batteries. The magnetic fields act as a physical catalyst for paramagnetic species. These effects have been demonstrated on homogeneous and heterogeneous ET reactions (Chapter 2), for academically interesting redox probes (e.g., $Ru(bpy)_3^{2+}$), as well as for adsorbate reactions (e.g., for CO oxidation on platinum) [11, 12]. Given the electroactive nature of the sensitizing dye and solution based redox species, the multi-electron transfer system of the Grätzel represents an ideal system for studying magnetic field effects on electron transfer reactions.

Electronically, DSSCs are constrained by the standard reduction potential of the redox mediator in solution and the Fermi level of the semiconductor. The Fermi level is the average energy of the charge carriers in the semiconductor. Nanocrystalline $TiO_2$ to date, represents the best semiconductor for DSSCs, with an $E_f$ = -0.5 V vs. saturated calomel electrode (SCE). It is commonly coupled with the iodine/triiodide system in an organic solvent (e.g., acetonitrile, propylene carbonate), with an $E^0$ =

0.4 V vs. SCE [18]. This creates the maximum open-circuit potential ($V_{OC}$) of 0.9 V. The $V_{OC}$, a thermodynamic or equilibrium process, is most likely unaffected by field effects. Given previous observation of magnetic field effects, increased current response will manifest in increased photocurrent, which translates into increased power output and increased conversion efficiencies.

Here, the effects of magnetic fields on the electrochemistry of DSSCs is examined. Magnetic modification of the system occurs in the semiconductor layer. In this Chapter, considerations for fabricating electrodes that contain magnetic particles include particle field strength, morphology, coatings, and specifically the physical constraints magnetic particles place on DSSC fabrication. Magnetic particles have been incorporated in both n- and p-type semiconductors and on both glass and plastic substrates. In the following chapter, analysis and results will be presented. Here, average photocurrent enhancements of 40 % are observed for magnetically modified electrodes versus control non-magnetic electrodes; these observations are statistically vetted.

## 3.2 Methods and Materials

In this Chapter, materials, electrode fabrication, experimental setup, and measurements are detailed.

### 3.2.1 Materials

All materials were used as received unless otherwise noted. Conductive substrates of PET and glass, coated with a transparent conductive oxide (TCO) of fluoride

doped indium tin(IV) oxide (ITO), are purchased commercially. Polyethylene terephthalate (PET) substrates with resistivities of 25 $\Omega$/cm (Sigma Aldrich) were cut into 1 in$^2$ slides for use. Borosilicate glass slides, 1 in$^2$, with 2.5 $\Omega$/cm resistivities were purchased from the Hartford Glass Company (Hartford, IN).

Two different commercial sources of TiO$_2$ were used for n-type DSSCs, nanoparticulate TiO$_2$ (Aldrich), with average particle diameter of 25 nm and anatase phase, and Aeroxide P25 (Acros), with particle diameter of 21 nm, which consists of mixed anatase and rutile phases. The use of each material is noted. Nickel (II) oxide (Aldrich) and Coumarin 343 (Aldrich) were used in p-type DSSC evaluations.

Electrodes are magnetically modified with either SmCo$_5$ (Alfa Aesar), NdFeB (spherical annealed, Magnequench), or glass coated magnetite (Fe$_3$O$_4$). An in-house coating procedure for magnetite is detailed in [12]. SmCo$_5$ and NdFeB are used uncoated as no recombination mechanisms are suspected for these materials, and these materials are stable under operating conditions. Further materials preparations (e.g., ball milling and sieving) are noted. Uncoated magnetite was used in an SEM-EDS film analysis only.

Principal components of the TiO$_2$ casting sols are Triton X100 (reduced, Sigma), acetyl acetone (Sigma), absolute ethanol (Decon Labs), and deionized water (DI). Iodine (Sigma), tetrafluoroborate iodide (Sigma), and acetonitrile (Fischer, dry - stored over molecular sieves) are used in the redox mediator solution. Ruthenizer 535 (N3) (Solaronix) and Coumarin 343 (Sigma) are prepared in ethanol solutions.

### 3.2.2 Electrode Preparation

Electrode preparation of glass substrate based electrodes, n-type and p-type, as well as PET substrate electrodes are given here.

### 3.2.2.1 A note on magnetic materials and considerations given in modified electrode fabrication

The physical properties of each magnetic material requires special attention so that the magnetic properties and morphologies of the magnetic microparticles are retained, and so that microparticles do not degrade and contaminate the DSSC electrode. These special precautions are taken at all stages of electrode fabrication. Magnetic material properties will be more thoroughly discussed in the Results Section in Chapter 4.

**Magnetite**: Glass coated magnetite is the most chemically and physically robust of the materials used here. Glass coated iron oxide was used in electrodes prepared by both pressing and annealing techniques. Uncoated magnetite electrodes were prepared for comparative analysis. Magnetite modified electrodes are annealed under air. Iron oxide is been speculated to be a contaminant in DSSC electrodes that facilitates recombination from the semiconductor [48]. Recombination decreases system efficiency. Any imperfections in the glass coatings may allow for recombination, making magnetite a less than ideal magnetic material in DSSC electrodes.

**NdFeB**: NdFeB is the least robust of the materials used. $Nd_2Fe_{17}B$ is referred to as NdFeB. Ring and disk magnets composed of pressed NdFeB are some of

the strongest permanent magnets available. However, in the powder form NdFeB materials are susceptible to leaching (e.g., in the case of acetyl acetate used in the casting sol) and have a low Curie temperature ($T_C$ = 300 $^\circ$C). When a magnetic material is heated above the Curie temperature, loss of magnetic saturation occurs. (Attempts to re-magnetize magentically modified electrodes were unsuccessful.) Leaching and oxidation also degrade the magnetic properties and semiconductor interface. NdFeB modified casting solutions were adapted to contain no acetyl acetate to prevent leaching. Bulk NdFeB was used as received, precisison sieves (AdvanTech Mfg.) were used for particle size selection, sieved particles were characterized with SEM, results given below.

**SmCo**: SmCo, available in a variety of stoichiometries (e.g., $Sm_2Co_{17}$, $Sm_2Co_7$, and $SmCo_5$). $SmCo_5$ was used here. $SmCo_5$ has a high Curie temperature ($T_C \simeq$ 800 $^\circ$C) , however the material suffers from a low oxidation temperature in air ($\sim$120 $^\circ$C) from Co oxidation [49]. Oxidized SmCo is not magnetic. Additionally, DSSC electrodes modified with $SmCo_5$ annealed under air are contaminated and unusable. Special precautions were given for the annealing of SmCo modified electrodes. 5 g bulk $SmCo_5$ was ball milled in hexanes for 3 hours to reduce particle size. Milling takes place in a Retsch S1000 planetary mill using a ceramic mill set. Milled particles were sieved and sized using SEM as with NdFeB, these results are seen below.

## 3.2.2.2 Glass substrate based electrodes

n-type and p-type electrodes were prepared on glass substrates. Semiconductor layers prepared on glass substrates were cured by either pressing or annealing. The

semiconducting materials are particulate (nanoscale) metal oxides. These materials have very high roughness factors ($\sim$ 1000). Films are cast by doctor blading from a ink like slurry or sol. Doctor blading is a common technique employed to create uniform, thin films. The common Scotch tape (3M) template method is used here [17]. In this technique the Scotch tape is used to define the film thickess ($\sim$15 $\mu$m), template the electrode area (1 cm$^2$), and provide a guide for the doctor blade. Within the template, a meaure of sol is added. A doctor blade, either a microscope slide or razor blade, is then used to uinformly distribute the sol across the template. After an initial drying period ($\sim$ 30 seconds), the tape is removed. Doctor blading is a common industrial method of producing thin films; in printing the technique referred to as rotogravure.

Following the doctor blading, a curing step is mandatory to stabilize the semiconductor, both to drive off organic additives used in the casting slurry, and to encourage electronic interaction between the TCO substrate and neighboring semiconductor particulates (particle necking). Electrodes are allowed to dry for 15 minutes at room temperature before annealing. On glass substrates, annealing produces the most consistent mechanically stable layer.

### 3.2.2.2.3 n-type TiO$_2$ based electrodes

Casting sols contain 1 g TiO$_2$, 5 drops Triton X100, and 0.05 mL acetyl acetone (acac) in a mixture of 0.5 mL DI H$_2$O and ethanol (in equal proportions) mixed in 20 mL glass scintillation vials. The viscosity of the casting sol effects layer thickness, and final layer stability. Use the quanitities of solvent, Triton X100 and acac as a

guide for sol preparation, however, it should be noted that fresh sols should always be prepared before use.

Annealing is optimized at 450 °C; electrodes are placed in a room temperature oven that is ramped to 450 °C. The electrodes are held at temperature for 1 hour and are then removed and allowed to cool to room temperature before sensitization.

Pressed electrodes are prepared in an analogous manner. Curing occurs by pressing on a Carver oil press (Model C) to 1.2 tons at 125 °C for 2 minutes. (Approximately 20 % of electrodes crack during the procedure.)

Modified control electrodes, modified with glass beads, contain 10 % (w/w $TiO_2$), 5 $\mu$m glass beads (PolySciences). Glass beads are commonly used to represent a nonmagnetic and nonconductive analogue [11]. When glass beads are used, it is so noted. Electrodes modified with glass coated magnetite contain a weight based loading percentage of magnetic material and glass beads so that all electrodes contain 10 % nonsemiconducting material by mass. For example, 5 % modified electrodes contain 5 % glass coated magnetite and 5 % glass beads by w/w $TiO_2$. Magnetization of modified electrodes is so noted.

Electrodes modified with $SmCo_5$ on glass were also fabricated and evaluated. The low oxidation temperature of $SmCo_5$ requires special consideration for annealing. Two methods of annealing were attempted. Electrodes were cast and annealed at low T in a vacuum oven at 260 °C for 2 hours. Electrodes were also annealed in a tube furnace in a glass tube specially adapted for slide annealing by UI glass blower Peter Hatch. The tube is seen in Figure 33. Six electrodes can be loaded into the tube. Annealing with the tube furnace was attempted under both vacuum conditions

and under positive $N_2$ (g) pressure. Vacuum conditions led to $SmCo_5$ oxidation, the possible the result of an air leak. Electrodes annealed under $N_2$ are reported.
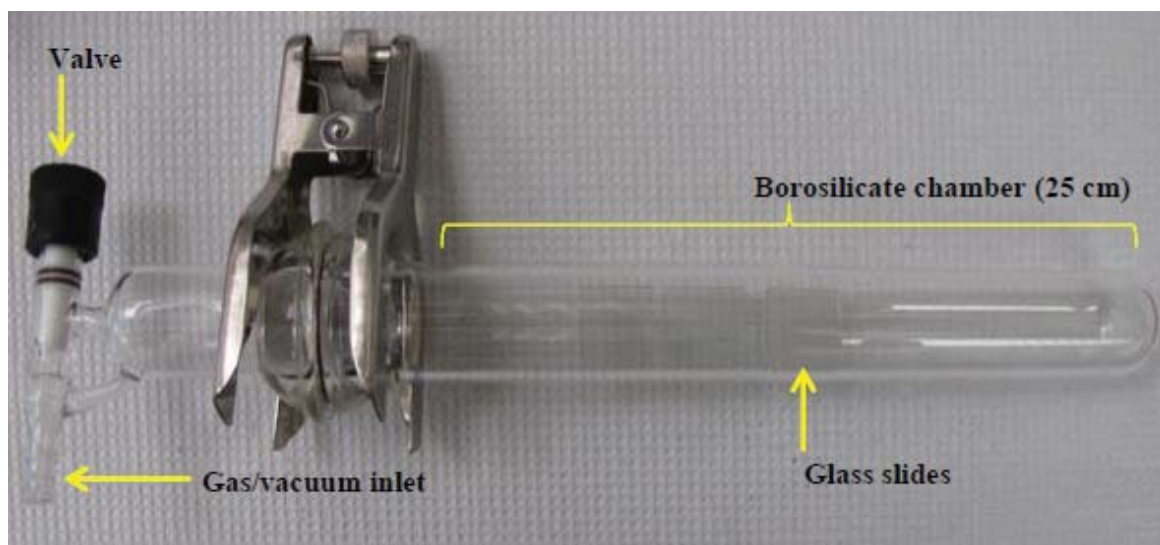


Figure 33. Modified borosilicate tube furnace reaction chamber for annealing $SmCo_5$ modified electrodes. $d = 3.5$ cm, $l = 25$ cm, accomodates six - 1 in$^2$ glass slides within the heating zone of a traditional tube furnace. The area highlighted as borosilicate chamber is placed within the furnance.

### 3.2.2.2.4 p-type NiO based electrodes

NiO electrodes are also doctor bladed from a sol. Suspensions are mixed in 20 mL glass scintillation vials; the sols contain 0.5 g NiO powder, 5 drops Triton X100, 0.05 mL acac, 0.5 mL DI and 0.5 mL ethanol. To maintain consistency, a fresh slurry is prepared before each use, as the evaporation of solvent and the resultant change in viscosity was observed to affect electrode casting and film thickness. As with n-type electrodes, electrodes are modified to contain a total of 10 % additives, either 10 % glass beads or 10 % glass coated magnetite.

Cast electrodes are allowed to dry for 15 minutes before annealing. Magnetically modified electrodes were dried within a NdFeB permanent ring magnet. NiO annealing is carried out at 550 $^\circ$C for 10 minutes. Electrodes are place in a preheated oven, and removed after the allotted time - this protocol was optimized by [50].

### 3.2.2.3 PET substrate based electrodes

PET based substrates were utilized for a variety of reasons. End product use applicability, cost, and similarities between the physical constraints of the substrate and magnetic particles. The upper limit for annealing PET based electrodes is restricted to the melting point of PET ($\sim$250 $^\circ$C). At 250 $^\circ$C, TiO$_2$ films achieve sufficient stability for electrochemical analysis. When modified with SmCo$_5$, annealing occurred under vacuum ($\sim$900 mTorr), which prevents Co oxidation. Advantageously, 250 $^\circ$C is below the Curie temperature of all magnetic materials. Annealing was carried out for a total of two hours, with an approximately ramp rate of 10 $^\circ$C/min from room temperature to 250 $^\circ$C. Electrodes were held at temperature for the remaining two hours, and were then allowed to cool to room temperature under vacuum.

Electrodes prepared on PET substrates were prepared as two layers. These two layer electrodes contain a single layer of unmodified TiO$_2$ (annealed) on the ITO substrate. A second layer is bladed atop the first layer - being careful not to disturb the primary layer. The second layer contains 10 % magnetic particles (w/w TiO$_2$). Control electrodes were prepared similarly, two layer configuration without particles in the second layer. Figure 54 shows a representation of the two layer prep. (A

comparative analysis between one and two layer controls was conducted and no statistical difference between them, these results are given in Chapter 4.)

### 3.2.2.4 Dye sensitization

Cured semiconductor layers are sensitized in dye solutions. n-type electrodes are soaked in an ethanol solution of N3 (Ruthenizer 535, Solaronix) dye overnight (time > 18 hours). N3 dye (Figure 34, a.), cis-bis(isothiocyanato)bis(2,2'-bipyridyl-4,4'-dicarboxylato)-ruthenium(II), is a dark purple powder with $F_w$ = 741.7 g/mol, and is absorbance for $\lambda \leq 750$ nm. Solutions of 1 and 4 mM (saturated) are utilized; the concentrations use are noted. p-type electrodes are soaked in a 1 mM ethanol solution of Coumarin 343, a common laser dye. Coumarin 343 (Figure 34, b.) has a $F_w$ = 285.29 g/mol and a $\lambda_{max}$ = 443 nm. Resultant electrodes resemble Figure 35.
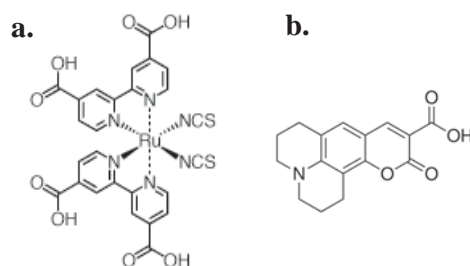


Figure 34. Sensitizing dyes: a) Ruthenizer 535 (N3) for n-type TiO$_2$ sensitization, a dark red complex; b) Coumarin 343 lazer dye for p-type NiO sensitization, a yellow species.

### 3.2.3 Experimental Setup

A two electrode configuration was used for all electrochemical analyses. A
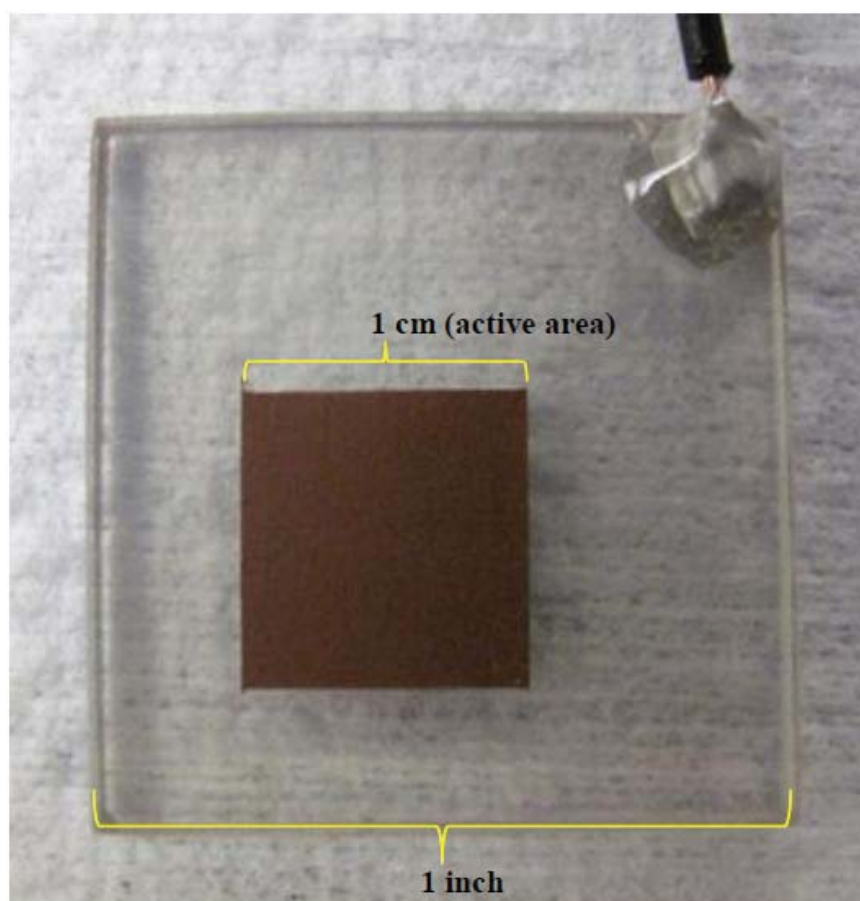
Figure 35. Image of N3 sensitized TiO$_2$ DSSC electrode. Electrical contact made with Cu wire attached with two-part silver epoxy (Chemtronics), silver epoxy and Cu lead covered with two part, non-conductive epoxy (Devcon) for electrical and chemical inertness.

quartz cuvette with an optically flat window was used for photoelectrochemical measurements (Figure 36). A platinum mesh in a Teflon$^{\circledR}$ housing serves as the counter/reference electrode. A Teflon spacer was used to minimize the interelectrode distance (0.3 mm). Approximately 1 mL of redox solution is added to the cuvette before analysis. The redox solution in all experiments is 0.5 M tetrabutylammonium iodide (TBAI) and 0.04 M $I_2$ in acetonitrile unless otherwise noted.

Electrochemical measurements were performed with a CH Instruments 760B potentiostat. The light source, an Oriel Solar Simulator with a 150 W Xe halogen lamp, was used in conjuction with an air mass (AM) 1.5 filter. Cyclic voltammetry or linear sweep voltammetry were used for characterization. Light power measurements were taken with a ThorLabs D3MM Thermal Head Sensor. Output from the solar simulator is 20 mW/cm$^2$, the value used for efficiency calculations. (The standardized value for solar evaluations in 100 mW/cm$^2$ by the IEEE).

Particle were characterized by scanning electron microscopy (SEM, Hitachi S-3400N). Surface characterizations were by SEM complimented with elemental mapping on a Bruker energy dispersive spectroscopy (EDS) system - targeting iron and titanium.

### 3.2.4 Magnetic Particle and Surface Characterizations

Particles and surface characterizations of the semiconductor films were undertaken to verify film homogeneity. Magnetically modified semiconductor electrodes are magnetized with an external NdFeB permanent magnet (OD = 7.5cm, ID = 5 cm, h = 1 cm ) prior to annealing. Unless otherwise noted, magnetization is
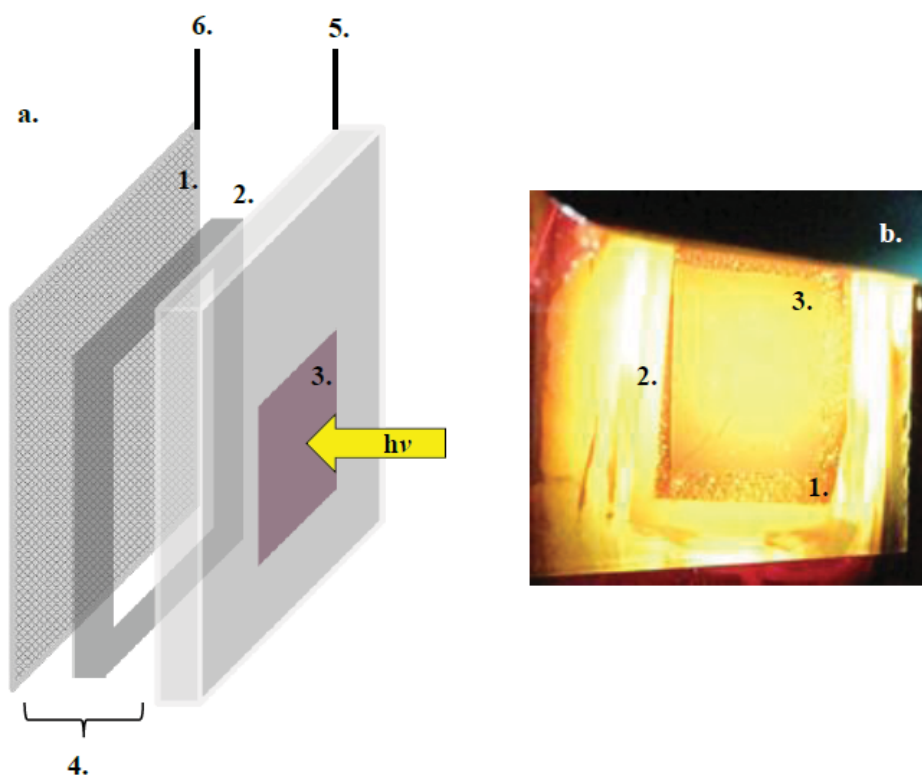
Figure 36. a. Scheme of electrode setup; b. image of DSSC in quartz cuvette with mediator solution, under illumination; 1. platinum RE/CE, 2. Teflon spacer; 3. active semiconductor area; 4. 300 $\mu$m interelectrode distance; 5. WE to potentiostat; 6. RE-CE to potentiostat.

applied while the casting slurries dry. To ensure that magnetic materials did not agglomerate during this procedure, samples for SEM were prepared analogously to the working electrodes, substituting an aluminum SEM sample stub for the TCO coated substrates. SEM of an annealed $TiO_2$ film, modified with uncoated magnetite (Chemalloy) that was milled in the same process as described for $SmCo_5$, can be seen in Figure 37 a with the complementary energy dispersive spectrograph characterization shown in Figure 37 b.
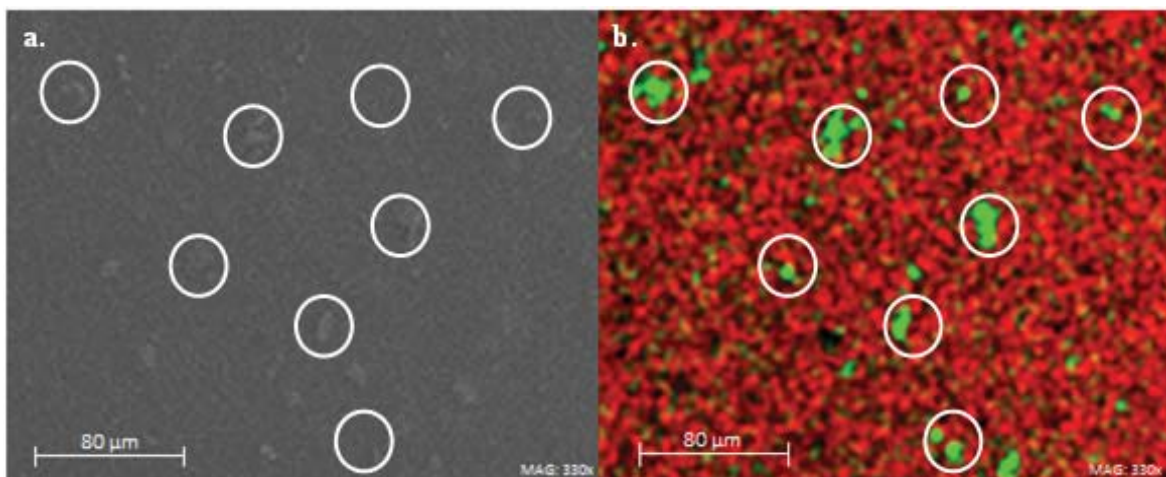


Figure 37. SEM and EDS of annealed $TiO_2$ film. a. SEM of annealed $TiO_2$ film, magnification 330x, secondary electron imaging (SE); b. energy dispersive spectroscopy (EDS) of the same surface area as in a. with Ti falsely colored red, Fe falsely colored green. The circles correlate $Fe_3O_4$ particles in the film as those identified with EDS in b. to the surface morphology in a.

Magnetic particle sizes were also measured to ensure size homogeneity and that particle diameter < film thickness, particle sizes were measured with ImageJ software package. Bulk $SmCo_5$ particles (Figure 38, a.), with an average diameter of 14.9 $\pm$18.4 $\mu$m (n = 36), were ball milled in hexanes for ~3 hours. After milling sieved

particles (Figure 38, b.) have an average size of $3 \pm 1.26$ $\mu$m (n = 50). Bulk NdFeB

particles (Figure 39, a) have an average size of $13.2 \pm 11.6$ $\mu$m (n = 100), sieved

NdFeB particles have an average size of $9.3 \pm 3.9$ $\mu$m (n = 50).
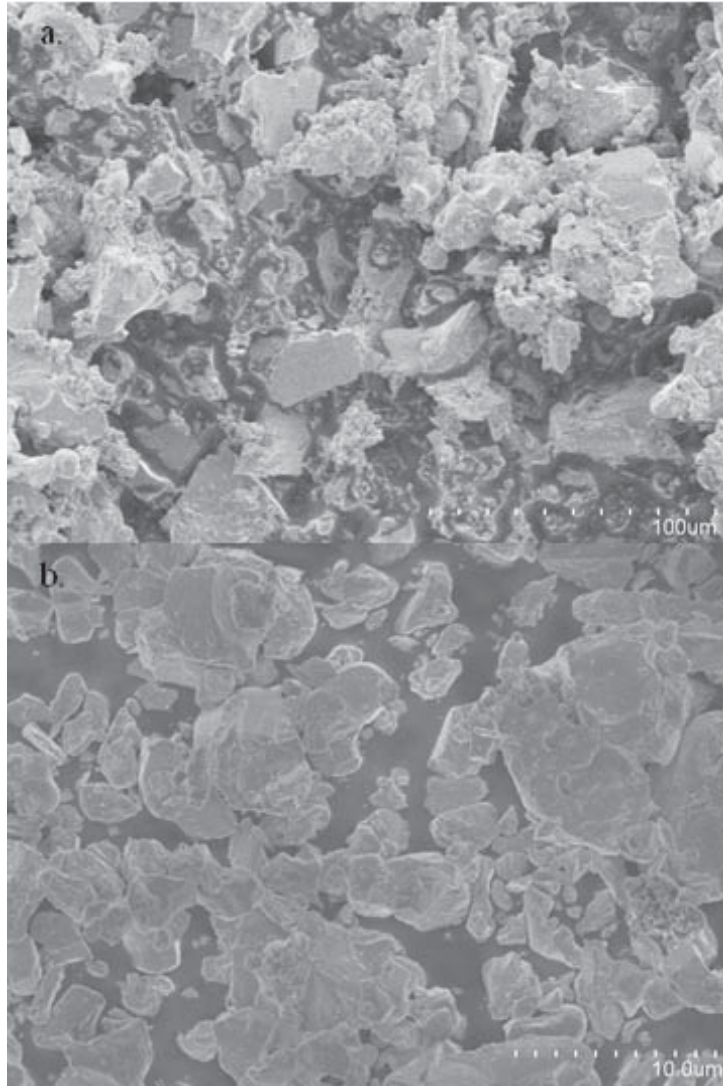


Figure 38. SEM image of $SmCo_5$ microparticles. a. Bulk $SmCo_5$, d = $14.9 \pm 18.4$ $\mu$m; b. milled $SmCo_5$ and sieved particles, d = $3 \pm 1.26$ $\mu$m.

In addition to surface morphology and size characterization, magnetic

microparticles are characterized by the materials magnetic energy product.
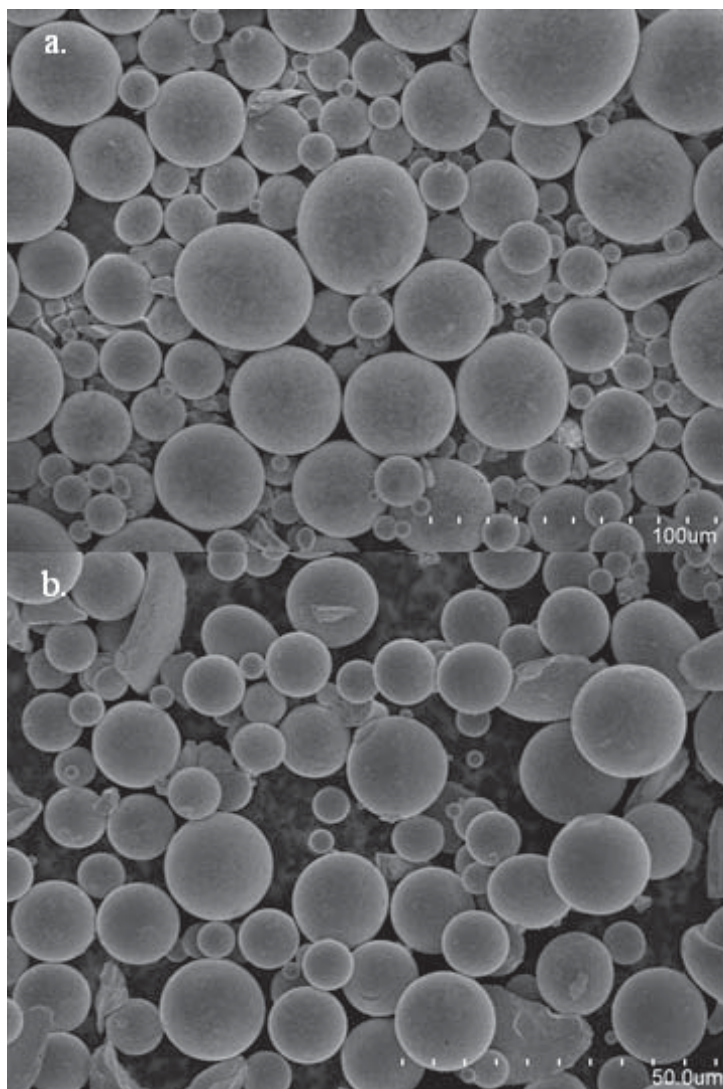
Figure 39. SEM image of NdFeB microparticles. a. Bulk NdFeB particles, d = 13.2 ± 11.6 $\mu$m; sieved NdFeB particles, d = 9.3 ± 3.9 $\mu$m.

The magnetic energy product, measured in MegaGauss-Oerstads (MGOe), is representative of the degree of magnetization (M). The energy product is measured as a magnetic volume susceptibility, $\chi_\nu$, which correlates magnetization response of a material to an external, applied field [12]. Volume susceptibility is converted to mass susceptibility, $\chi_g$ (cm$^3$ g$^{-1}$), by

$$\chi_g = \chi_v \left( \frac{h_{sample} \cdot \pi \cdot r^2_{sample}}{m_{sample}} \right) \tag{54}$$

where h is sample height (cm), r is sample radius (cm), and mass in grams. Mass susceptibility can then be converted to magnetic permeability, $\mu_g$, a more common value by,

$$\mu_g = 2.83 \cdot \sqrt{\chi_g \cdot T(K)} \tag{55}$$

where $\mu_g$ has units of Bohr Magnetons (BM). The permeability of the substance can be related to magnetic flux density (i.e., lines of force in the sample) B to the magnetic field H by

$$B = \mu H \tag{56}$$

This can then be related back to susceptibility by,

$$\chi = \frac{M}{H} \tag{57}$$

For paramagnetic species (i.e., species with unpaired electrons), positive $\chi$ values are observed. Negative $\chi$ values are observed for diamagnetic species (i.e., no unpaired electrons). The samples of $SmCo_5$ used here have mass susceptibility values of 1.11 x 10$^{-1}$ ±0.01 CGS and the NdFeB used here has values of 1.72 x 10$^{-2}$ ± 0.005 CGS.These measurements were taken with the help of graduate student

Nate Coleman in Professor Ed Gillan's group at The University of Iowa.

### 3.2.5   Electrochemical Measurements

Electrodes were analyzed here in a fundamental, electrochemical manner.

#### 3.2.5.1  Analysis of dye leeching and rationale for short-term measurements

Only electrochemical measurements for initial scans are recorded and analyzed. This procedure is consistent with standard voltammetric protocol [1]. Preliminary evaluations of reptitive sweep measurements found a decrease in electrode performance with increasing sweep number. It was concluded that performance loss was due to dye desorption into the redox solution, owing to the relatively large redox solution volume ($\sim$1 mL) in the quartz cuvette and the corresponding lopsided equilibrium of surface adsorbed dye species and redox solution. A dye desorption effect was observed over a series of electrode trials (Figure 40), and was qualitatively assessed by UV-vis of spent redox solution with an Ocean Optics USB4000.



Figure 40. Image of sensitized $TiO_2$ before (left) and after (right) photoelectrochemical evaluation. Leeching or desensitization of molecular sensitizer leads to loss in device performance.

Figure 41 shows a comparison between unused redox solution (0.5 M I$^-$/0.04 M I$_2$ in acetonitrile), spent redox solution, and a dilute (0.1 mM) solution of N3 dye in ethanol (secondary axis).
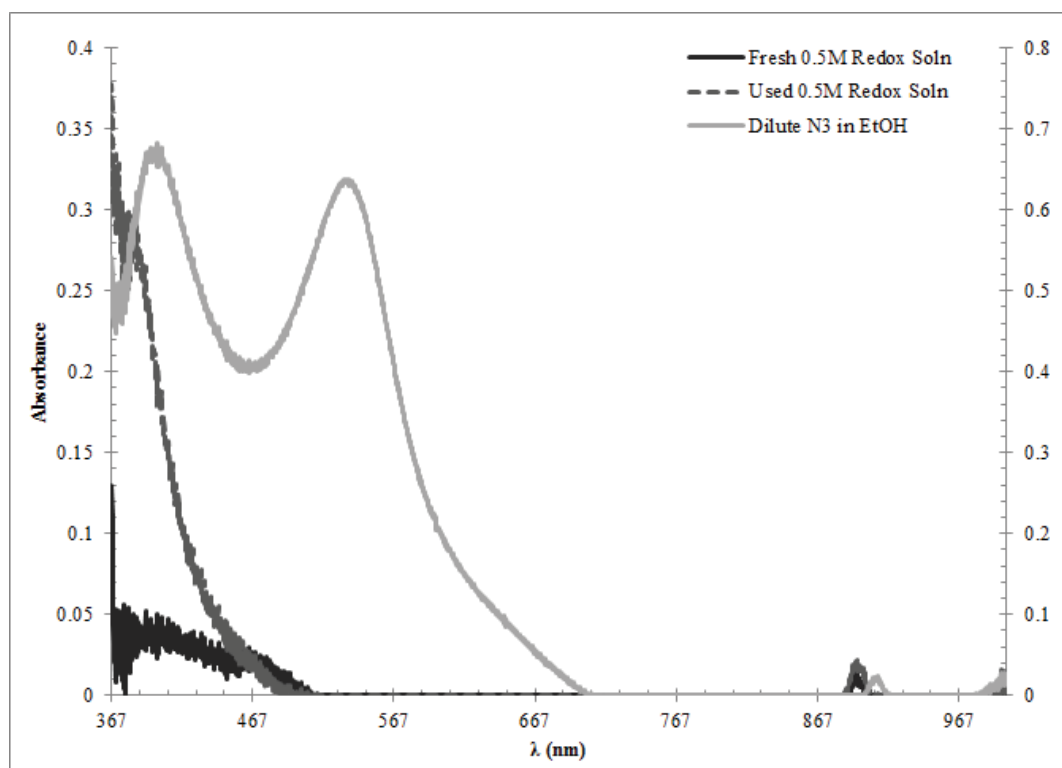


Figure 41. UV-vis analysis of spent redox solution. A dilute ($\sim$0.1 mM) N3 solution in light grey, used redox solution in medium grey, and fresh redox solution in dark grey.

A variety of samples were measured, both magnetic and control systems, and the trending persisted. It has been shown that potentials greater than -1.0 V vs. SCE facilitate dye desorption [18]. Our photoelectrochemical evaluations are within the working potential range of the system. However, any potential biasing most likely facilitates dye desorption given the amount of energy for 1 volt potential biasing in comparison to the energy associated with chemisorption (5 kJ/mol) and

physisorption (1 to 10 kJ/mol) bonding. Given the initial phase of this research, our methodologies and means, the first scans or short term measurement, were deemed representative of the photoelectrochemical potential of these electrodes.

3.2.5.2 Voltammetry

Voltammetry was used to characterize the photoelectrochemical performance of DSSC electrodes. Figure 42 is a representation of a sensitized n-type semiconductor in the dark and under illumination. The useful data range is between 0.0 and $\sim$-0.9 V vs. Pt. The actual cutoff is electrode dependent, occurring at the open circuit potential ($V_{oc}$) of each individual cell. In the data analysis section, the voltammogram are analyzed between only 0 V and the $V_{oc}$. The current at 0 V is referred to as the short circuit current or short-circuit current density ($J_{sc}$). Additionally, the voltammogram are inverted over the current axis (y-axis), a practice consistent with semiconductor analysis.

The operation of a n-type Grätzel cell produces anodic, or oxidative, photocurrent responses. (A brief explanation of a working DSSC is described here, a more complete description is found in Chapter 4.) This oxidation is associated with the injection of electrons from sensitizer (S) in the photon induced, excited state (S*) to the conduction band (CB) of the semiconductor. Injected electrons then diffuse through the semiconductor to the TCO. Electrons then progress through an external load to the counter electrode, at which they reduce the organic mediator species. The accepted representation for an operating DSSC is seen in Figure 43. The operating principal for p-type semiconductors is analogous, however, a cathodic
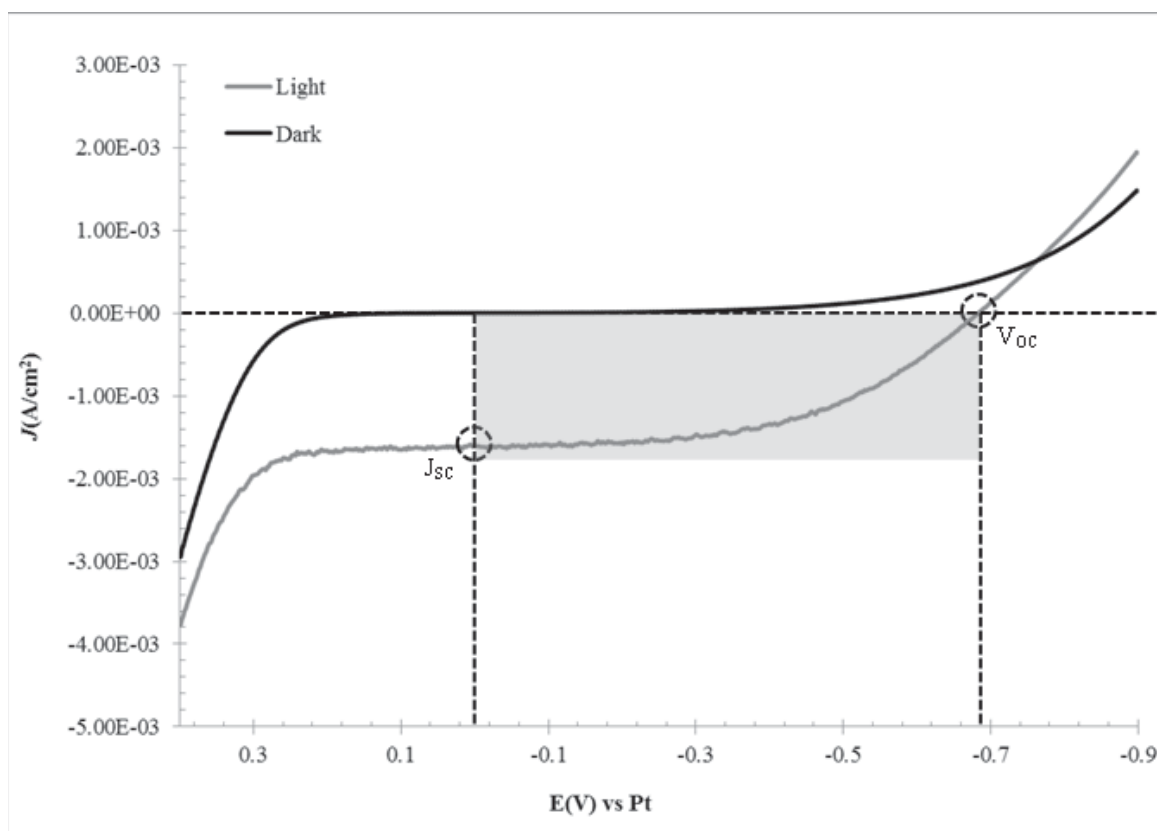
Figure 42. The voltammetric response of a DSSC electrode under dark and light condition. $i$V curves are generated from the voltammetric sweeps. From the scan, the area highlighted in gray is inverted over the y (or E) axis and is used to analyze an electrode to find the short circuit current density ($J_{SC}$) and the open circuit potential ($V_{OC}$).

or reductive response is recorded - associated with the reduction of the molecular sensitizer.
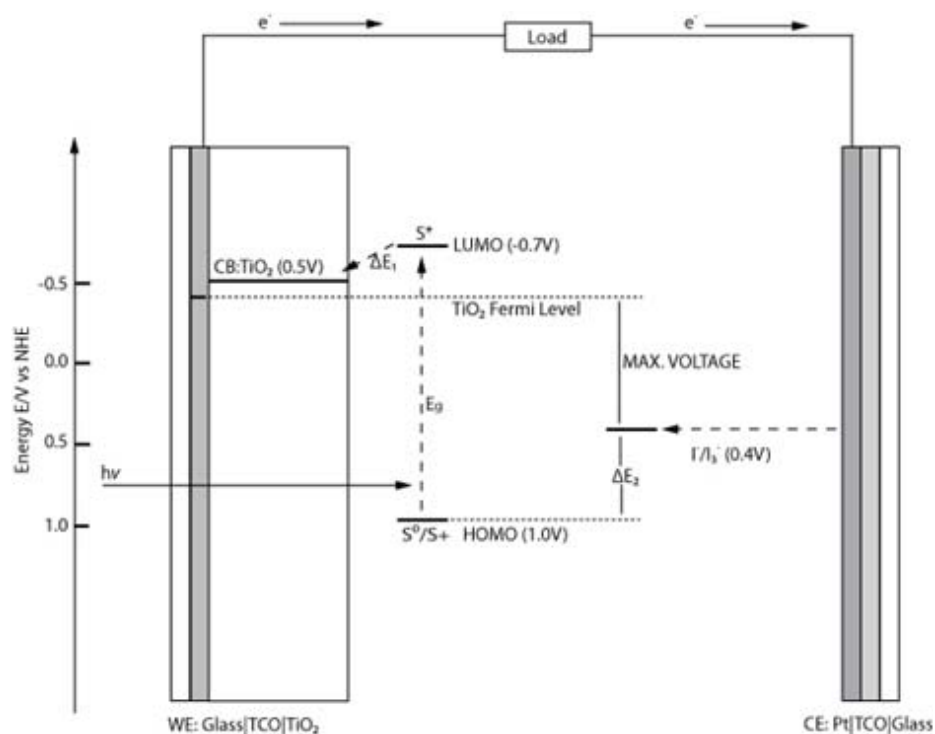


Figure 43. The accepted DSSC operating scheme; Molecular sensitizer (S), excited sensitizer (S*), oxidized sensitizer (S$^+$) conduction band (CB), working electrode (WE), highest occupied molecular orbital (HOMO), lowest unoccupied molecular orbital (LUMO), counter electrode (CE).

Electronically, DSSCs are constrained by the standard reduction potential of the redox mediator in solution and the Fermi level of the semiconductor. For the traditional Grätzel cell utilizing $TiO_2$ and the iodine/iodide redox mediator, the maximum $V_{oc}$ is restricted to approximately 0.9 V, where the $E_f$ for $TiO_2$ is -0.5 V vs. saturated calomel electrode (SCE) and the $E^0$ for $I^-/I_3^-$ is 0.4 V vs. SCE.

3.2.5.3 Electrode Analysis Criteria

Precise measurements of open circuit potentials, short circuit current densities,
and input power ($W_{in}$) are important for calculating fill factor (FF) and photovoltaic
conversion efficiency ($\eta$) [8]. Values of open circuit potential and short circuit current
densities are extracted from voltammograms, also referred to as $i$V curves. From
the data obtained in the voltammetric sweep, more conventional $i$V curves are used
to analyze the DSSC electrodes, these curves resemble the curve in Figure 44. Fill
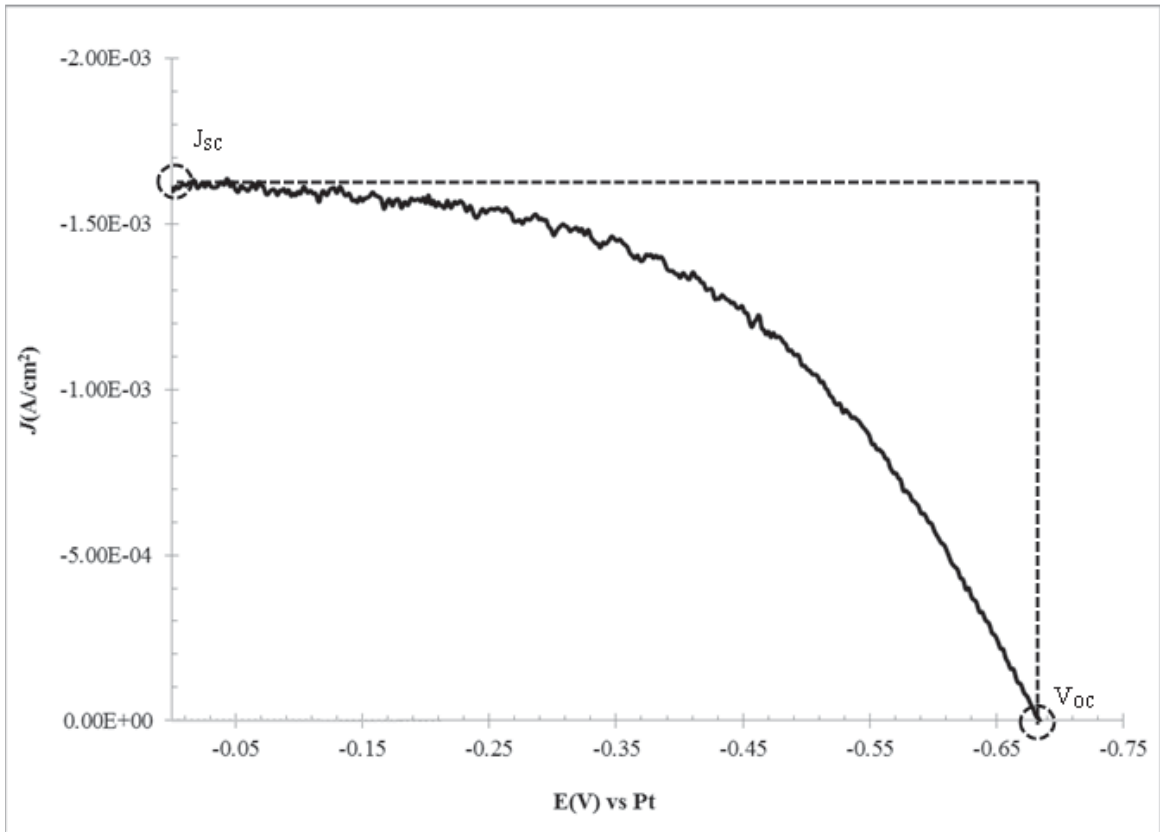


Figure 44. An $i$V curve generated from the illumination voltammetric data in Figure 42. The convention of the $i$V curves also for quick, qualitative assement of an electrodes performance as well as $V_{OC}$ and $J_{sc}$.

factor, maximum power, and electrode efficiency were used as criteria for evaluating the enhancement of modified cells versus unmodified cells. Fill factor is defined as

$$FF = \frac{J_{mp}V_{mp}}{V_{oc}J_{sc}} \tag{58}$$

where $J_{mp}$ is current density at maximum power and $V_{mp}$ is potential at maximum power; maximum power values are taken from power curves (P (W) vs. E (V)). The fill factor of an 'ideal electrode' is represented by the dashed lines in Figure 44. $i$V curves are used to generate power curves. Power curves are instantaneous product curves generated from voltammograms, where P(watts) = J(amps)·E(volts) (Ohm's law). A power curve generated from the $i$V curve in Figure 44 is seen in Figure 45. The $i$V curves and power curves presented here are the average responses for each system.Photovoltaic efficiency is defined as

$$\eta = \frac{(V_{mp}J_{mp})}{W_{in}} \times 100 \tag{59}$$

where $W_{in} = 20$ mW/cm$^2$, the input light power.

3.2.5.4 Statistical Evaluation

The photoelectrochemical responses of all DSSC electrodes tested herein are statistically evaluated. Criteria for evaluation (e.g., FF, $\eta$, W$_{max}$) were measured in multiples (n $\geq$ 3) , over a variety of trials or series. The nature of magnetic field effects and composite-electrode fabrication necessitate statistical evaluation. Averages, standard deviations, and relative standard deviations of photoelectrochemical responses are considered. Additionally, confidence levels are attributed to the evaluation criteria; Students-t values are calculated from 60 and
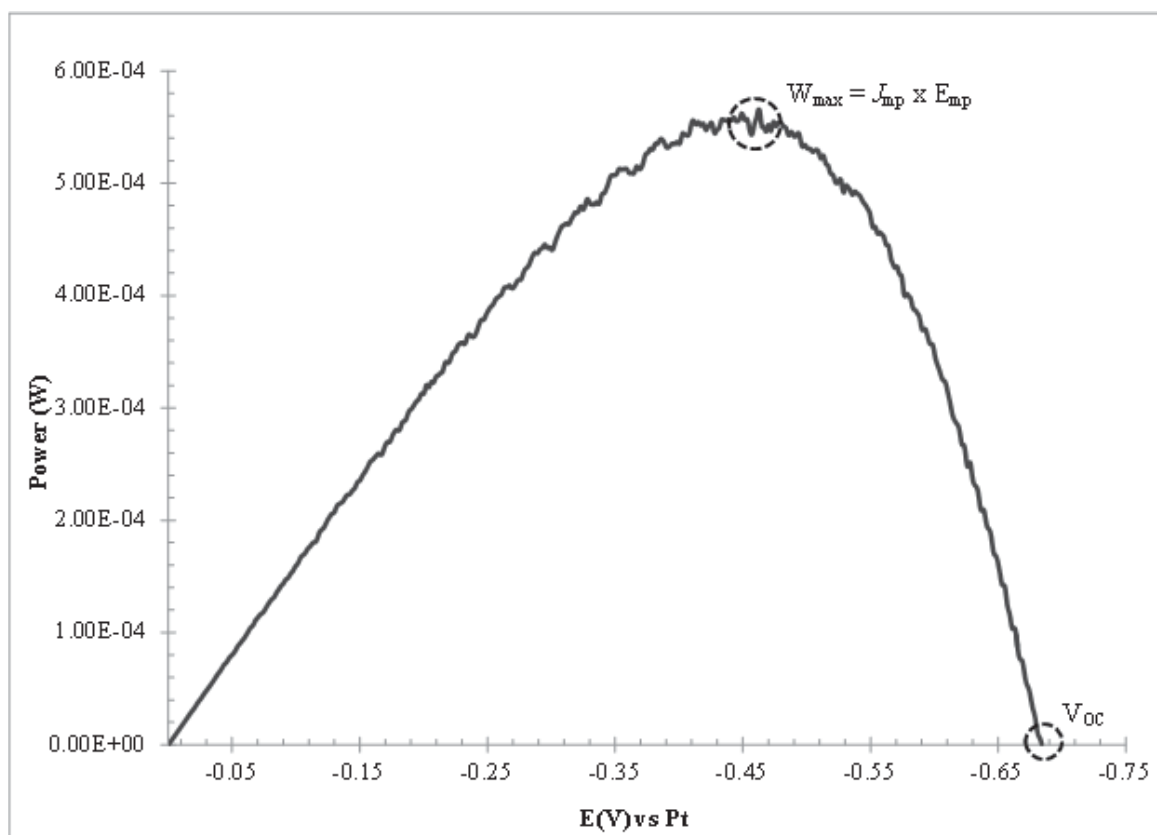
Figure 45. A power curve generated from the $i$V curve in Figure 44. The power curve is used to determine maximum power ($W_{max}$) from which photoconversion efficiency can be determined.

compared to generated values in Excel.

$$t_{calc} = \frac{|\overline{x}_1 - \overline{x}_2|}{s_{pooled}} \sqrt{\frac{n_1 n_2}{n_1 + n_2}} \tag{60}$$

and

$$s_{pooled} = \sqrt{\frac{s_1^2(n_1 - 1) + s_2^2(n_2 - 1)}{n_1 + n_2 - 2}} \tag{61}$$

where $\overline{x}$ is the mean value of a population, n is the number of observations in the

population, and s is the standard deviation within the population.

## 3.3 Conclusions

A variety of methods for fabricating magnetically modified dye sensitized solar

cells were presented here. The complexity of incorporating magnetic microparticles

into dye sensitized solar cells, or any electrochemical cell, should not underestimated.

When fabricating magnetically modified cells, important considerations for

the magnetic particles include chemical stability, Curie temperature, oxidation

temperature, and particles size and coating. Additionally, how the magnetic particles

affect the system (given the contaminating nature of some materials) should be

considered. In the case of magnetite, a glass coating is necessary to ensure that

unwanted recombination effects associated with iron oxide dissolution are minimized.

In the following Chapter we will see the effects that magnetic particles have on

the photo conversion efficiency of dye sensitized cells. The results of the analyses

presented here are detailed in Chapter 4. Lastly, the next chapter will consider

more closely the effects of magnetic fields and future considerations for magnetic

microparticles in dye sensitized solar cells.

CHAPTER 4

ANALYSIS OF MAGNETICALLY MODIFIED DYE SENSITIZED SOLAR CELLS

## 4.1   Introduction

In the previous Chapter, we discussed the methodologies involved in magnetically modifying dye sensitized solar cells. Here, we will see that magnetic fields enhance photocurrent response, conversion efficiency, and power output and the results are statistically verified. Given the variety of systems tested, the analysis includes specifics for the variety of materials and systems tested; these are variations to the aforementioned general preparation techniques in Chapter 3. The majority of the analyses considers experimental data of $i$V curves, and power curves, detailed data analyses, statistical assesment and tables of values. The Chapter is concluded with a brief analysis of the enhancement and relates enhancements in heterogeneous ET reactions shown in Chapter 2 as well as increased homogeneous ET reactions as previously studied at The University of Iowa.

## 4.2   Discussion of Chapter 3 Results

In Chapter 3, formulation of magnetically modified DSSC electrodes was explained. In Chapter 4, results for magnetically modified n-type $TiO_2$ and p-type NiO, on glass and PET substrates is presented.

4.2.1  n-type DSSC Electrodes

n-type semiconducts utilize electrons (i.e., negatively charged particles "n") as their majority carrier. n-type semiconductos are formed by doping intrinsic semiconductor materials with trace amounts of a more electron rich material.

4.2.1.1  Pressed Electrodes

The first DSSC electrode preparation method attempted was a heat and press method [17]. This method was selected in order to avoid the the effects high temperatures have on magnetic microparticles, including demagnetization and particle oxidation. Additionally, roll-to-roll pressing methods attractively have the capability of manufacturing scale up. Pressed electrodes prepared on glass, however, were prone to cracking ($\sim$20 % loss), while electrodes pressed on PET suffered from unstable $TiO_2$ layers. Mechanically unstable titania layers were brittle and flaky and could not be sensitized.

Electrodes were pressed to 1.2 tons with a Carver oil press (Model C) for approximately two minutes inside a Teflon$^{\textcircled{R}}$ (DuPont) sandwich where the Teflon prevents adhesion. A low plate temperature (125 $^o$C) was selected because 125 $^o$C $<<$ T$_C$ (Fe$_3$O$_4$) for electrode pressing on glass substrates. Control electrodes contained no additives while modified electrodes contained 5 % glass coated magnetite (w/w $TiO_2$). The $iV$ curve in Figure 46 shows the photoresponse of typical control and magnetically modified electrodes pressed on glass substrates. Modified electrodes have an average increase in short circuit current density ($J_{sc}$) of

72.9 % versus unmodified electrodes, no significant increase in open circuit potential ($V_{oc}$) is observed.
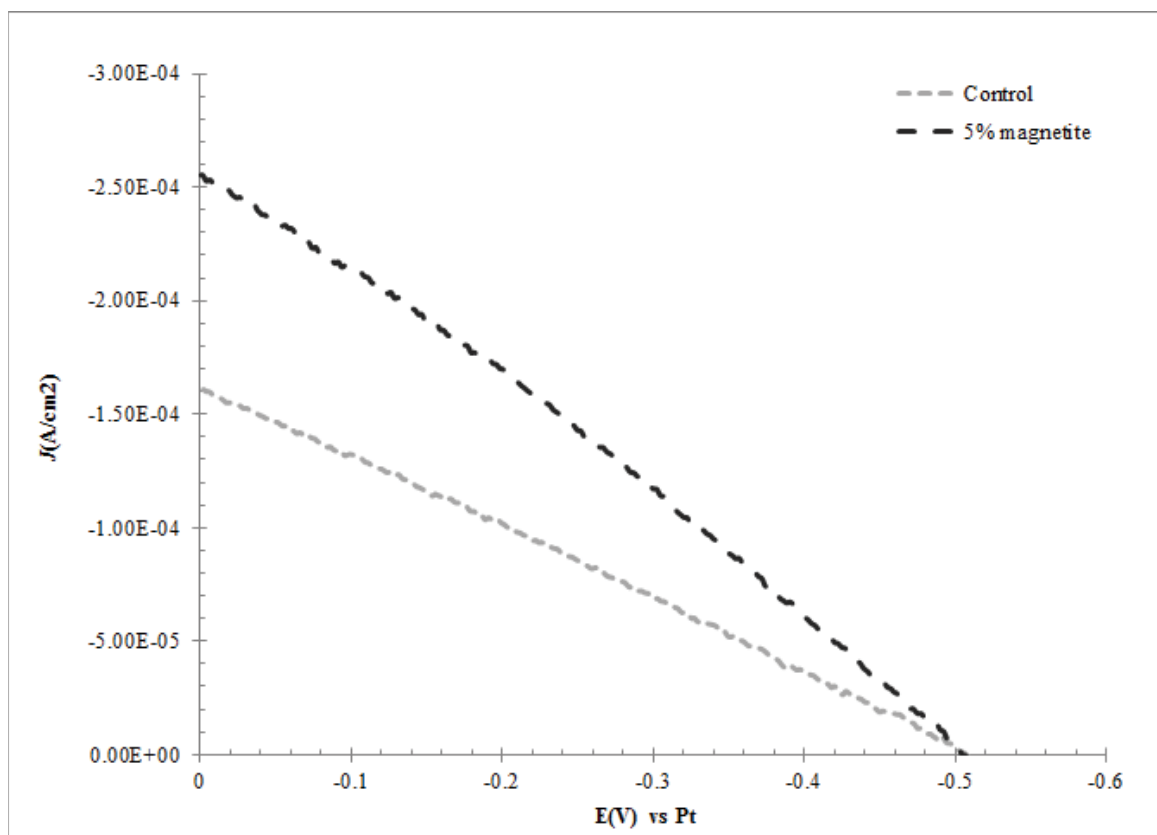


Figure 46. $iV$ curve for DSSC electrodes. 5 % glass coated magnetite ($Fe_3O_4$) (dark grey), no additive unmodified control electrodes (light grey); $W_{in} = 20$ mW/cm$^2$.

The power curve in Figure 47 shows an enhancement of 86.7 % in maximum power and efficiency for modified electrodes over control electrodes. Electrodes were tested in replicates, with n = 4 for control electrodes and n = 5 for modified electrodes. Table 11 contains the evaluation criteria for pressed electrodes. Students-t values, calculated from Equation 60, indicate that the $J_{sc}$ between data sets is significantly different at the 50 % confidence level. The difference between data sets exceeds the
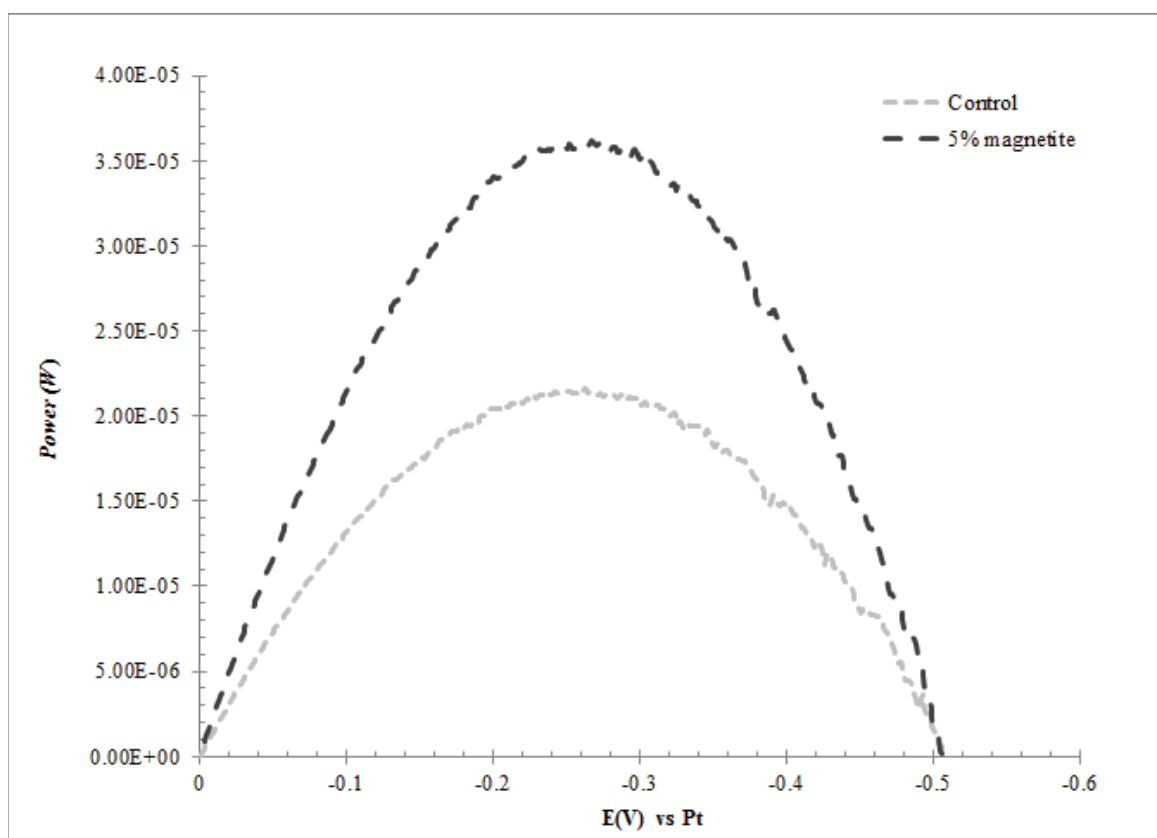
Figure 47. Power curve for pressed electrodes shown in Figure 46. 5 % magnetite modified electrodes (dark grey), unmodified control electrode (light grey).

Table 11. Values for pressed electrodes of controls and modified with glass coated magnetite microparticles.

| Control | | | | |
|---|---|---|---|---|
| Cell | $V_{OC}$ | $J_{SC}$ | $P_{max}$ | FF |
| 1 | -0.335 | $-1.2x10^{-4}$ | $1.3x10^{-5}$ | 0.32 |
| 2 | -0.521 | $-1.6x10^{-4}$ | $2.2x10^{-5}$ | 0.26 |
| 3 | -0.558 | $-1.2x10^{-4}$ | $1.9x10^{-5}$ | 0.29 |
| 4 | -0.378 | $-2.3x10^{-4}$ | $2.4x10^{-5}$ | 0.29 |
| Avg | -0.45 | $1.5x10^{-4}$ | $1.9x10^{-5}$ | 0.29 |
| Stdev | 0.01 | $4x10^{-5}$ | $4x10^{-6}$ | 0.02 |
| Rel. Stdev | 24 | 29 | 24 | 9 |
| 5% $Fe_3O_4$ | | | | |
| 1 | -0.517 | $-2.5x19^{-4}$ | $3.62x10^{-5}$ | 0.27 |
| 2 | -0.428 | $-2.0x19^{-4}$ | $2.53x10^{-5}$ | 0.29 |
| 3 | -0.423 | $-4.9x19^{-4}$ | $5.59x10^{-5}$ | 0.27 |
| 4 | -0.472 | $-1.9x19^{-4}$ | $2.68x10^{-5}$ | 0.30 |
| 5 | -0.653 | $-1.9x19^{-4}$ | $3.65x10^{-5}$ | 0.29 |
| Avg | -0.49 | $-3x10^{-4}$ | $4x10^{-5}$ | 0.29 |
| Stdev | 0.09 | $2x10^{-4}$ | $1x10^{-5}$ | 0.01 |
| Rel. Stdev | 19 | 48 | 34 | 5 |
| $S_{pooled}$ | 0.1 | $1x10^{-4}$ | $9.7x10^{-6}$ | $1.9x10^{-2}$ |
| $T_{calc}$ | 0.751 | 1.647 | 2.571 | 0.302 |
| % Rel. Inc | 11.3 | 72.9 | 86.7 | -1.4 |

90 % confidence level for power and efficiency.

Low values for fill factor (FF) and efficiency are observed. This may be due to poorly interacting $TiO_2$ nanoparticles pressed at 125 °C. Poor interparticle interaction reduces conduction of electrons in the $TiO_2$ layer. When annealed to 450°C, particles within the titania film achieve electronic interaction through a mechanism called particle necking. When conduction is low and resistance is high, the measured current density output will also be low as $i \propto R^{-1}$. Low current output manifests as low conversion efficiency and low FF values.

Hagfeldt et al., [51] whom evaulated pressed DSSC electrodes, observed no significant difference in film surface area of pressed films as compared to the initial

powder as measured by BET. Their work concluded that film pressing minimizes film thickness, pressing further reduced $TiO_2$ particle size, resulting in an increased surface area. However, as will be shown, the pressed electrodes prepared here do not preform as well as annealed $TiO_2$ films.

An important consideration for the operation of DSSCs is actual surface area versus the geometric surface area. The thin semiconductor layer ($\sim$10 $\mu$m), composed of nanoparticle semiconductors has a surface area 1000 times greater than the apparent surface area [10]. That is, if a 10 $\mu$m thick film of 1 $cm^2$ geometric area is produced, the true surface area of the semiconductor is close to 1 $m^2$. This allows for significant adsorption of dye and makes Grätzel cells a promising solar technology.

The incorporation of glass coated particles returns an increased current output that further manifests as increased power and efficiency. In other systems such as batteries and fuel cells, magnetic effects are hypothesized to arise through homogeneous electron conduction and hopping between electroactive moieties and in heterogeneous ET events. Ardo and Meyer conducted transient anisotropic measurements on the DSSC system and concluded that self exchange reactions do indeed occur on the surface of DSSC electrodes [52]. This observation is consistent with observations of self exchange in loaded Nafion films at modified electrodes, and may contribute to the increase in photocurrent response. Heterogeneous charge transfer may be another mechanism for enhancement, as will be considered.

4.2.1.2 Annealed Films

A variety of electrodes were prepared by annealing, on both glass and PET substrates. Control electrodes were analyzed that include both unmodified films and films that contain glass bead modified analogues. These analogues represent the nonsemiconductor nature of the magnetic microparticles and have been used previously in evaluation of magnetically modified systems. Most common, the glass beads serve to eliminate structure as the means ET enhancement. The use of glass beads is noted. The magnetically modified electrodes either incorporated glass coated magnetite, uncoated SmCo, or uncoated NdFeB. Magentic loading optimizations were conducted for magnetite modified electrodes on glass. Analyses conducted include the effects of the applied external magnetic field during electrode fabrication, photocurrent response as a function of particle field strength for PET modified electrodes, and a comparison between coated and uncoated magnetite. Results presented here begin with glass coated magnetite modified electrodes.

4.2.1.2.5 Optimized Loadings with Glass coated Magnetite

Magnetite is a not an ideal material for DSSC modification. As mentioned previously, iron oxide is a suspected contaminant for recombination in DSSC electrodes [48]. Incorporation of uncoated magnetite provides a pathway for recombination and, correspondingly, decreased cell efficiency. Glass coated magnetite particles, however, produce DSSC electrodes with increased $J_{sc}$, fill factor, and power as compared to control electrodes. For magnetic loading optimizations were

attempted, all electrodes contain 10 % nonsemiconductor additive; for example, control electrodes contain 10 % glass beads while 5 % modified electrodes contain 5 % magnetite and 5 % glass beads (w/w TiO$_2$). Glass beads were incorporated here to reproduce loss in semiconductor film surface area to incident radiation ($\Phi$) and loss of electron conduction from nonconducting particles. Electrodes were prepared as previously described and were sensitized in a 1 mM N3 solution.

Figure 48 shows an $iV$ curve for glass coated magnetite modified electrodes. Enhancements in $J_{sc}, FF, P_{\max}$, and $V_{oc}$ are observed, n = 12 for each loading except for 10 % magnetite where n = 11 because 1 electrode was rejected by Q-test. Enhancements are greatest for 5 % modified electrodes. Values of FF, efficiency ($\eta$), and power for the annealed films are increased over pressed electrodes. However, these values are still lower than literature [10, 17] The results of each loading are shown in Table 12.

Particle loadings have obvious effects in reducing the observed $i_{ph}$, however, the concentration of sensitizer used to dye semiconductor films has been shown to impact overall electrode efficiency. To increase efficiency, increased dye concentrations are considered. Likewise, steps can be taken to optimize electrode efficiency the include blocking layers on the semiconductor surface to minimize recombination (e.g., poly(methylsiloxane)) and solution additives to decrease electrolyte decomposition [18]. These precautions are not used in the analyses presented here because the relative enhancements of magnetically modified electrodes to unmodified electrodes are the principal focus.
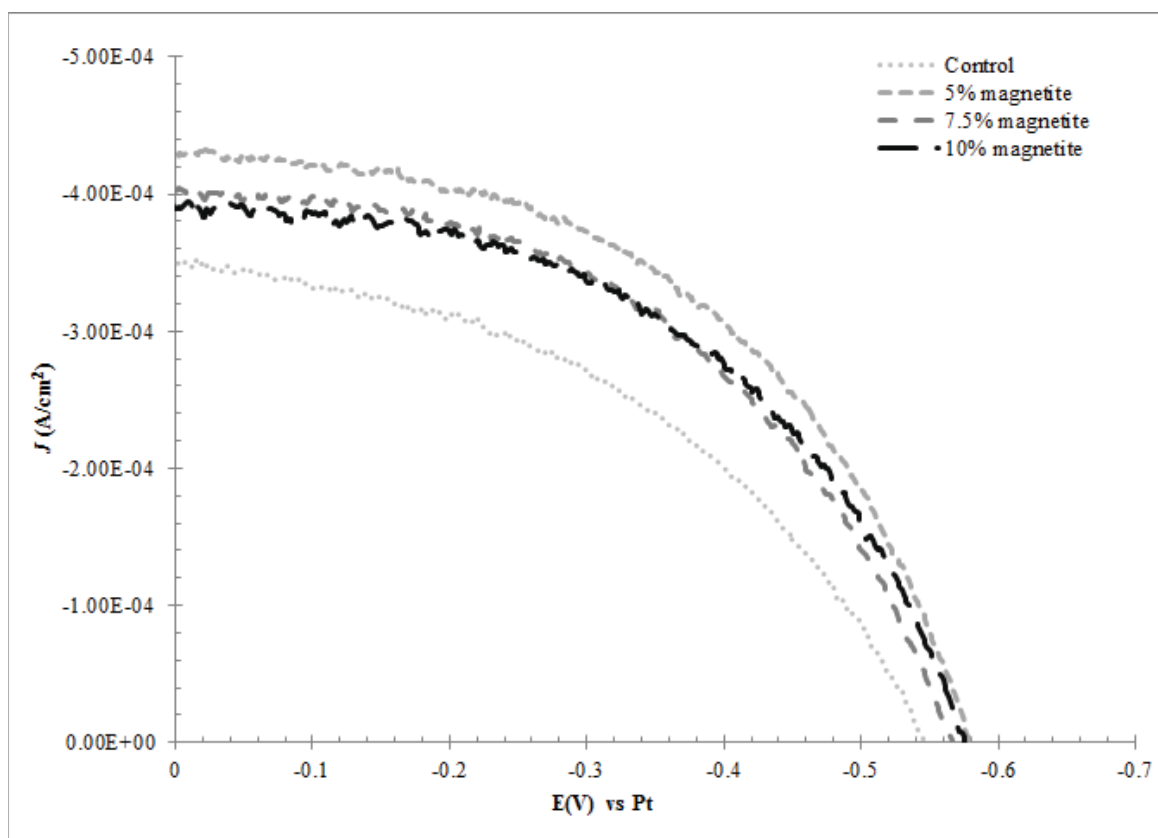
Figure 48. Optimized glass coated magnetite $iV$ curve. A total of 10 % (w/w TiO$_2$) nonsemiconducting material (glass beads + magnetite) for each loading. W$_{in}$ = 20 mW/cm$^2$. Average photocurrent response for n = 12 electrodes at each loading.
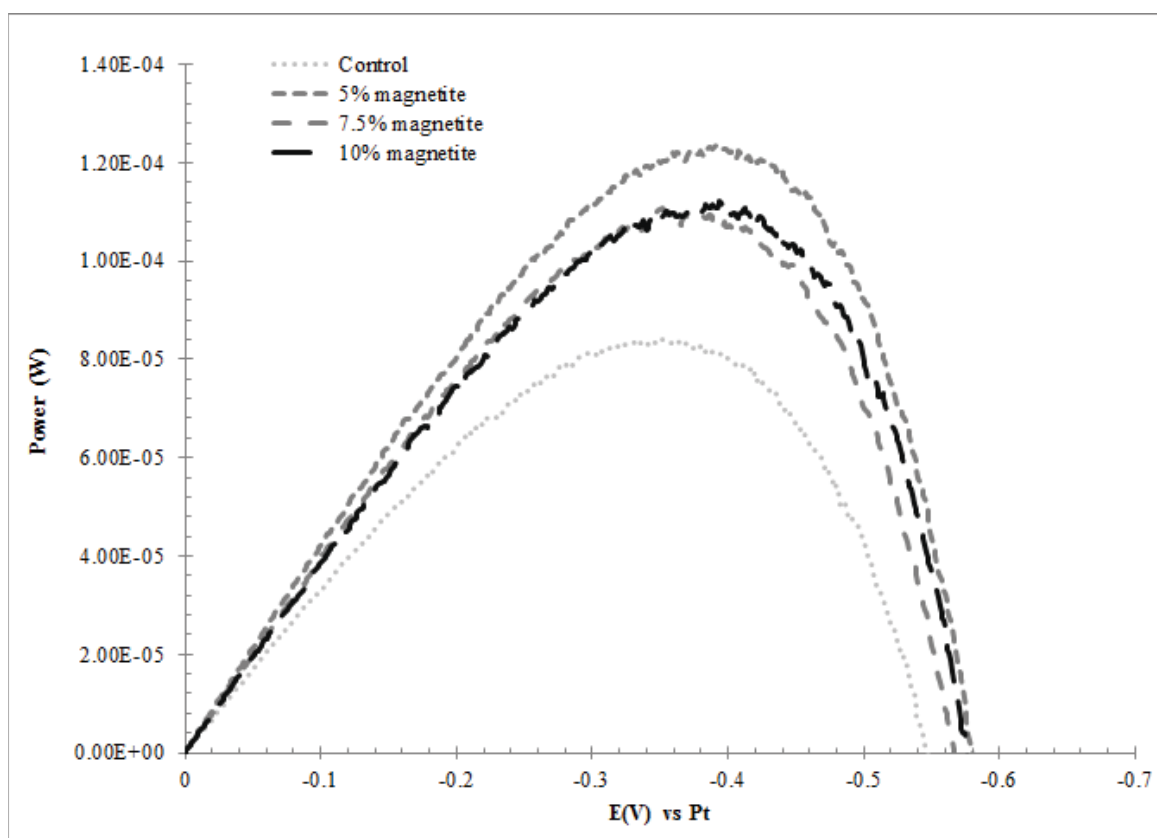
Figure 49. Power curve for optimized magnetite loadings. 10 % nonsemiconductor loadings (w/w $TiO_2$) for each modification. Power curve corresponds to data shown in Figure 48.

Table 12. Values for annealed electrodes modified with glass coated magnetite microparticles at various loading percentages, n = 12 for each loading. Electrodes are sensitized in 1 mM N3 ethanol solution.

$J_{sc}(A/cm^2)$

| Loading | Average | Enhancement | $S_{pooled}$ | $T_{calc}$ | Confidence Level |
|---|---|---|---|---|---|
| 0% | $-3._4x10^{-4}(\pm1._7x10^{-4})$ | | | | |
| 5% | $-4._4x10^{-4}(\pm1._8x10^{-4})$ | 30% | $1.8x10^{-4}$ | 1.377 | 80% |
| 7.5% | $-3._8x10^{-4}(\pm2x10^{-4})$ | 14% | $2.1x10^{-4}$ | 0.566 | —— |
| 10% | $-3._6x10^{-4}(\pm2x10^{-4})$ | 6% | $2.0x10^{-4}$ | 0.277 | —— |

$V_{OC}$ (V)

| Loading | Average | Enhancement | $S_{pooled}$ | $T_{calc}$ | Confidence Level |
|---|---|---|---|---|---|
| 0% | -0.534 ($\pm$0.07) | | | | |
| 5% | -0.574 ($\pm$0.06) | 7% | $6.7x10^{-2}$ | 1.454 | 82% |
| 7.5% | -0.557 ($\pm$0.06) | 4% | $6.9x10^{-5}$ | 0.845 | 58% |
| 10% | -0.557 ($\pm$0.09) | 4% | $6.5x10^{-5}$ | 0.823 | 57% |

$P_{max}$ (W/cm$^2$)

| Loading | Average | Enhancement | $S_{pooled}$ | $T_{calc}$ | Confidence Level |
|---|---|---|---|---|---|
| 0% | $8x10^{-5}(\pm5x10^{-5})$ | | | | |
| 5% | $1.4x10^{-4}(\pm7x10^{-5})$ | 57% | $6.6x10^{-5}$ | 1.873 | 91% |
| 7.5% | $1.1x10^{-4}(\pm8x10^{-5})$ | 27% | $5.9x10^{-2}$ | 1.601 | 86% |
| 10% | $1.1x10^{-4}(\pm7x10^{-5})$ | 25% | $5.8x10^{-2}$ | 1.965 | 92% |

Fill Factor

| Loading | Average | Enhancement | $S_{pooled}$ | $T_{calc}$ | Confidence Level |
|---|---|---|---|---|---|
| 0% | 0.46($\pm$0.07) | | | | |
| 5% | 0.52($\pm$0.05) | 12 | $6.2x10^{-2}$ | 2.212 | 95% |
| 7.5% | 0.49($\pm$0.04) | 8 | $5.9x10^{-2}$ | 1.601 | 80% |
| 10% | 0.51($\pm$0.04) | 10 | $5.8x10^{-2}$ | 1.695 | 90% |

Table 13. Values for modified and control electrodes sensitized in 4 mM N3 ethanol solution. An approximately three fold increase in photocurrent response is observed versus 1 mM N3 ethanol solutions.

| $J_{sc}(A/cm^2)$ | | | | | |
|---|---|---|---|---|---|
| Loading | Average | Enhancement | $S_{pooled}$ | $T_{cacl}$ | Confidence Level |
| 0% | $-1.2x10^{-3}(\pm 5x10^{-4})$ | | | | |
| 10% | $-1.5x10^{-3}(\pm 6x10^{-4})$ | 26.5 | $5.9x10^{-4}$ | 0.951 | 64% |
| $V_{OC}$ | | | | | |
| 0% | $-0.65(\pm 0.07)$ | | | | |
| 10% | $-0.68(\pm 0.07)$ | 4.5 | $5.9x10^{-2}$ | 0.932 | 63% |
| $P_{max}$ (W/cm$^2$) | | | | | |
| 0% | $4x10^{-4}(\pm 1x10^{-4})$ | | | | |
| 10% | $5x10^{-4}(\pm 2x10^{-4})$ | 29.1 | $2.1x10^{-4}$ | 1.084 | 70% |
| Fill Factor | | | | | |
| 0% | $0.53(\pm 0.05)$ | | | | |
| 10% | $0.54(\pm 0.04)$ | 2.4 | $4.5x10^{-2}$ | 0.513 | N/A |

4.2.1.2.6 Effects on the Concentration of the Molecular Sensitizer Solution

Electrodes were prepared as in the previous analysis to test the effects of an increased concentration of sensitizer solution. Control electrodes contain 10 % glass beads, modified electrodes containing 10 % glass coated magnetite. The electrodes are sensitized in a 4 mM N3 ethanol solution, increased from 1 mM in the previous section. At 4 mM, the sensitizing solution is at the saturation level of the dye. The results are given in Table 13. Again, an increase in photo current response is observed for modified electrodes. However, more importantly, open circuit potentials for both modified and control electrodes are observed to increased by ~100 mV. Current output has also increased by nearly three fold for both modified and control electrodes. The higher 4 mM N3 sensitizer concentrations are used here in all remaining systems. The saturated solution both increases system response and maintains consistency of sensitizer concentration between trials, which minimizes an

unwanted variance.

### 4.2.1.3 SmCo Modified Electrodes, Glass Substrate

Electrodes modified with $SmCo_5$ microparticles require special consideration for fabrication. As mentioned, $SmCo_5$ oxidizes at about $\sim$120 °C in air, as a result of cobalt oxidation. This spontaneous exothermic process affects particle morphology and renders the particles nonmagnetic. If oxidation occurs within the semiconductor layer, the DSSC is nonfunctional. Two procedures were attempted to circumvent cobalt oxidation: low temperature annealing in a vacuum oven, and high temperature annealing in an adapted vacuum tube (Figure 33).

Low temperature annealing produced electrodes with low $i_{ph}$ and $V_{oc}$. The semiconductor layers are stable for sensitizing and evaluation, but, poor interparticle interactions and particle substrate interactions may be limiting response. The $iV$ curve for these electrodes is seen in Figure 50. The resulting power curve can be seen in Figure 51, a relative enhancement in $i_{ph}$ of 56 % is observed, but the difference is significant at the 50 % confidence level with 2 degrees of freedom ($t_{calc}$ = 1.75).

To improve photocurrent response, $SmCo_5$ modified electrodes were annealed to 450 °C in an adapted vacuum tube. These electrodes were annealed under a positive $N_2$ (g) pressure. When annealed under vacuum to 450 °C, the electrodes oxidized, most likely due to exposure to air from a leak in the vacuum tube. Figure 52 shows the $iV$ curves for these electrodes. Again, an average enhancement of 42% is observed for $i_{ph}$ (n = 3). The difference in enhancement is only significant at the 50% confidence level. The difficulty in fabricating these electrodes limited the number
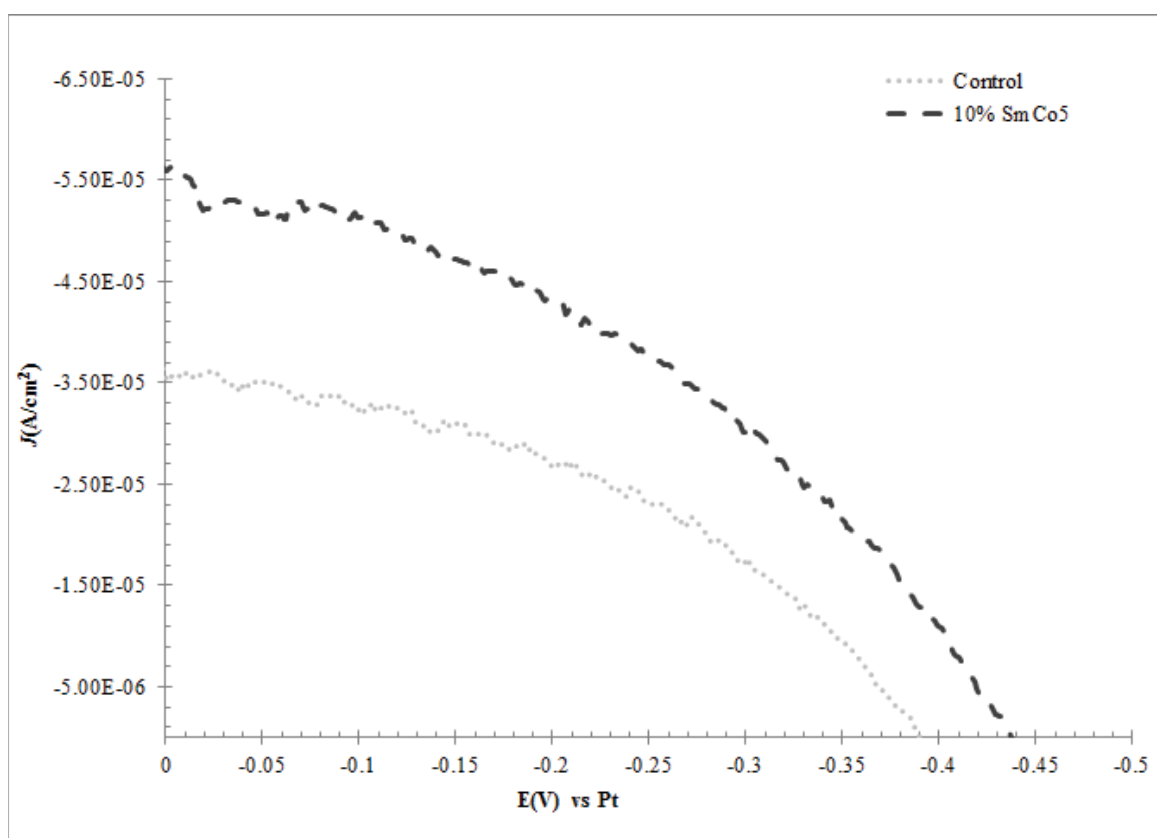
Figure 50. $iV$ curve for vacuum oven annealed SmCo$_5$ modified DSSC electrodes. Control electrodes contain 10 % glass beads, magnetically modified electrodes contain 10 % SmCo$_5$. Electrodes annealed for 2 hours at 260 $^o$C. W$_{in}$ = 20 mW/cm$^2$.
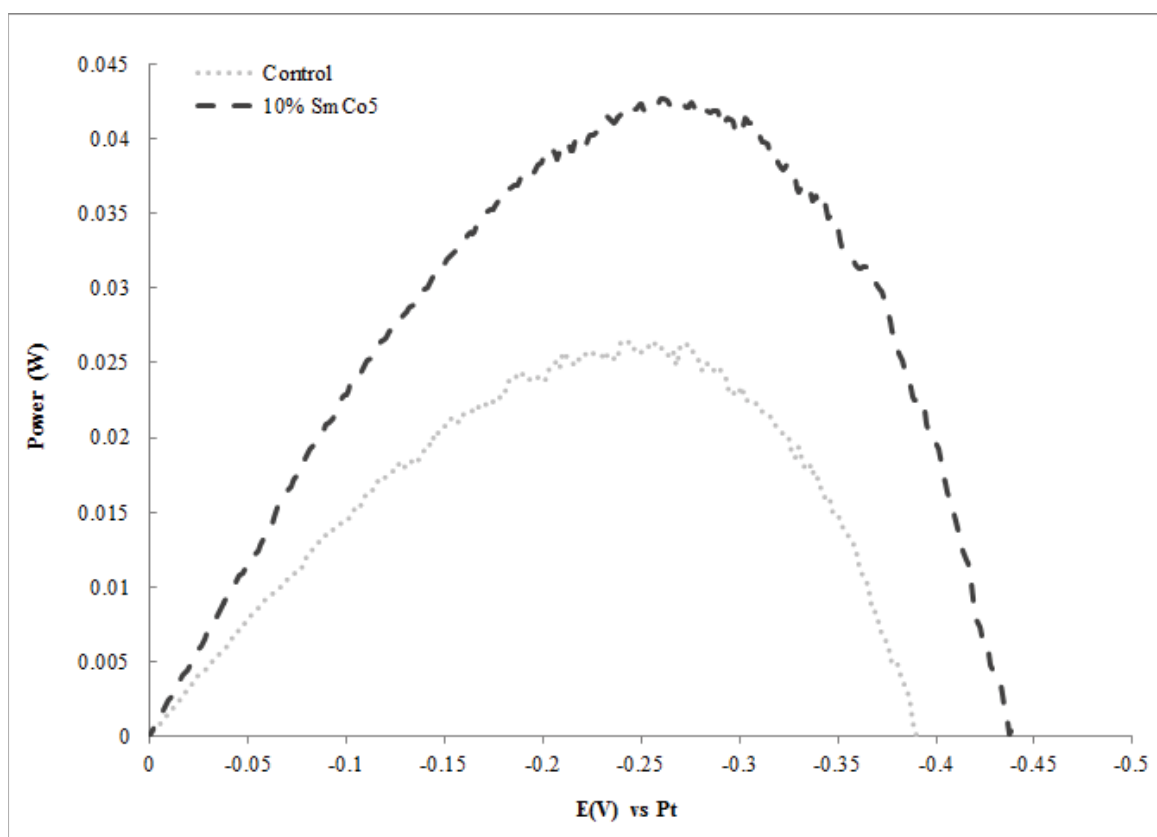
Figure 51. Power curve for SmCo$_5$ modified electrodes annealed at low temperature (260 $^o$C) for two hours under vacuum. Curves correspond to data shown in Figure 50.

of electrodes evaluated, which contributed to the low observed confidence level. In addition to average photo current enhancement for modified electrodes, modified electrodes also return lower standard deviations, 26 % for modified electrodes versus 79 % for unmodified electrodes.

This is a trend previously observed in magnetically modified systems. An average enhancement in power of 75% percent is observed (Figure 53), the efficiency for SmCo$_5$ modified electrodes were the best observed here, at $\eta \cong 4.5\%$.
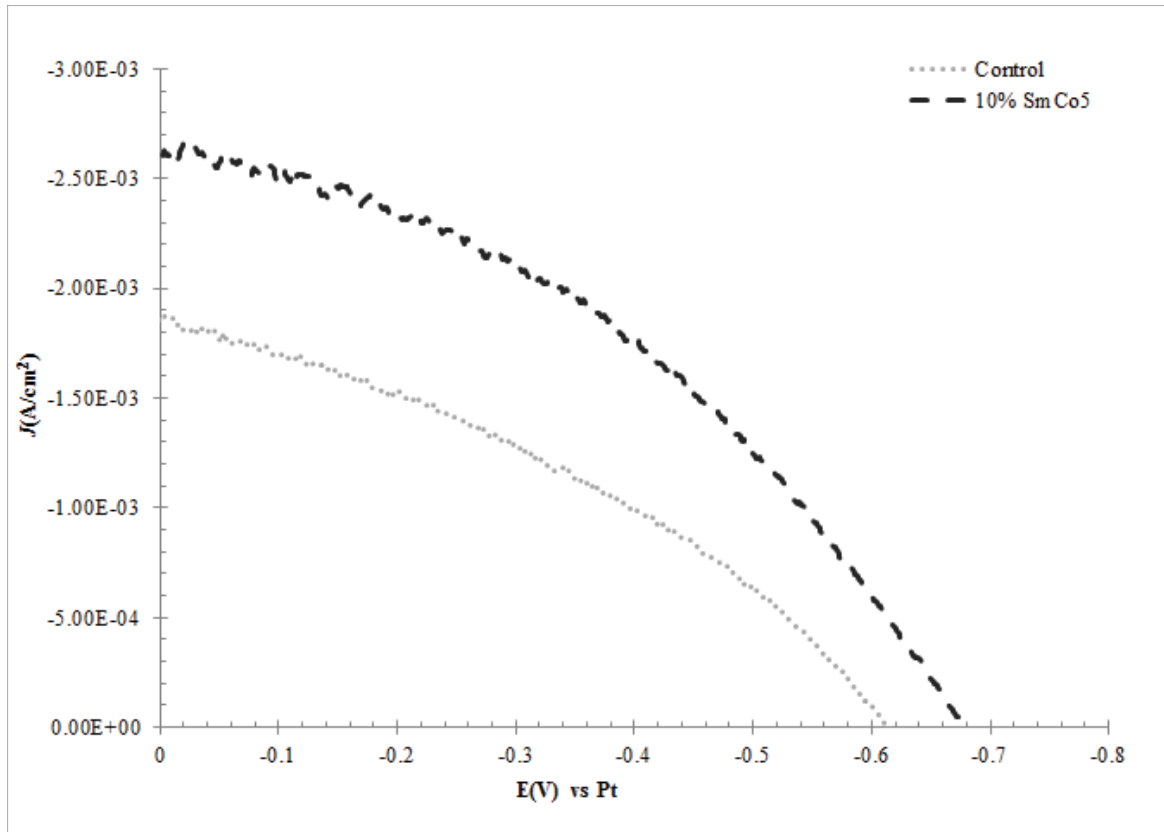


Figure 52. Representative $iV$ curve for SmCo$_5$ modified electrodes annealed under N$_2$ (g) to 450 °C for 1 hour; n = 3 for each modification; W$_{in}$ = 20 mW/cm$^2$.
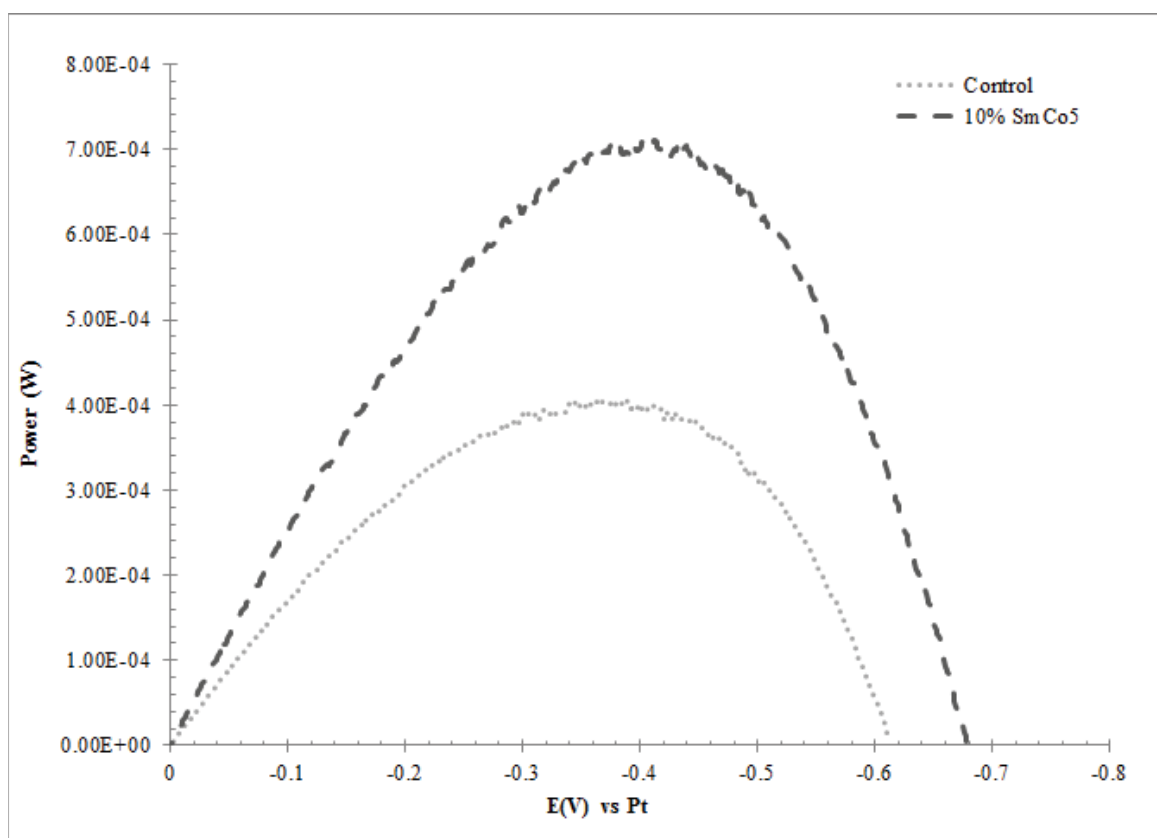
Figure 53. Power curve for high temperature (450 °C) annealed $SmCo_5$ modified electrodes, under positive $N_2$ (g) pressure. An average enhancement of 75 % percent in maximum power is observed. Curve corresponds to data in Figure 52.

4.2.1.3.7 SmCo and NdFeB Modified Electrodes on PET Substrates

Electrodes were prepared on PET substrates as an alternative to glass. The end use of PET based electrodes allows for a wide range of PV applications [51], given the materials flexibility, durability, and low cost. PET based electrodes are limited by the melting point of the substrate to $\sim$260 °C for the annealing process. However, this material limitation, in conjunction with the limitations of magnetic materials (e.g., spontaneous cobalt oxidation, Curie temperature, etc.), and the availability of a vacuum oven make PET substrates an attractive material for demonstrating the effects of magnetic modification.

Electrodes were prepared as bilayer $TiO_2$ electrodes. Incorporation of a second, modified layer on top of a primary unmodified layer resulted in the most consistent magnetic enhancement in modified electrodes. Control electrodes were also prepared as bilayers with the second layer consisting of unmodified $TiO_2$ (Figure 54). Primary
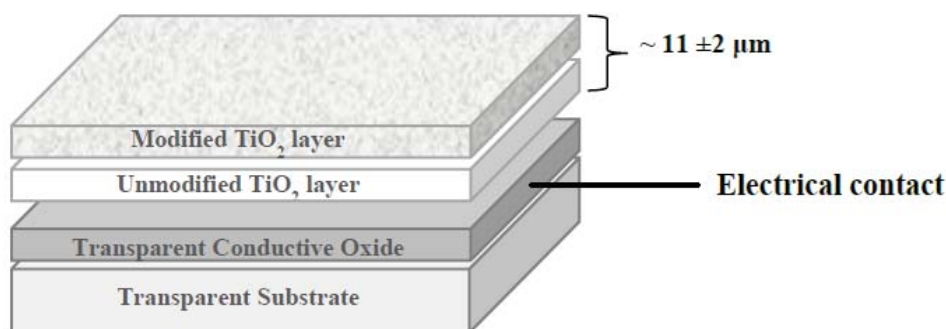


Figure 54. Bilayered $TiO_2$ DSSC electrode, primary layer unmodified $TiO_2$, second layers contain 10 % magnetic particles (w/w $TiO_2$).

layers of unmodified $TiO_2$ were cast and annealed for 2 hours. The secondary layers

Table 14. Film thickness measurements for bilayer electrodes, measurements taken with a Mitutoyo film micrometer. Magnetically modified electrodes contain magnetic microparticles in the second titania layer.

| Electrode Composition | Thickness ($\mu$m) |
|---|---|
| Unmodified control (monolayer) | 13 ($\pm$ 5) |
| Unmodified control (bilayer) | 18 ($\pm$ 3) |
| 10 % NdFeB (bilayer) | 11 ($\pm$ 3) |
| 10 % SmCo$_5$ (bilayer) | 14 ($\pm$ 3) |

(unmodified TiO$_2$, 10 % SmCo$_5$ or 10 % NdFeB), were cast with care not to disturb the primary layer. TiO$_2$ layer thicknesses were measured with a Mitutoyo film micrometer, Table 14. Each film measurement is an average of four measurements per film. The measurements were taken after electrochemical testing. A correlation between film thickness and photocurrent response was not observed.

The assembly with the second layer was annealed for an additional 2 hours under vacuum. As with the SmCo$_5$ modified electrodes prepared on glass annealed at low T, these electrodes are limited in current response and efficiency (modified electrodes approach 1 % efficiency). Lowered fill factor values were also observed. Figure 55 shows the photocurrent response of PET electrodes. No difference in $V_{oc}$ is observed, however, an increase in $i_{ph}$, power and efficiency are again observed in modified electrodes. The results are given in Table 15 (n = 13 for control and NdFeB electrodes, n = 8 for SmCo$_5$ modified electrodes).

The photocurrent response and power output of PET electrodes was correlated to the magnetic susceptibility of the NdFeB and SmCo$_5$ particles. Figure 57 shows a monotonic correlation between mass magnetic susceptibility, $X_g$ (cm$^3$/g) versus $J_{sc}$
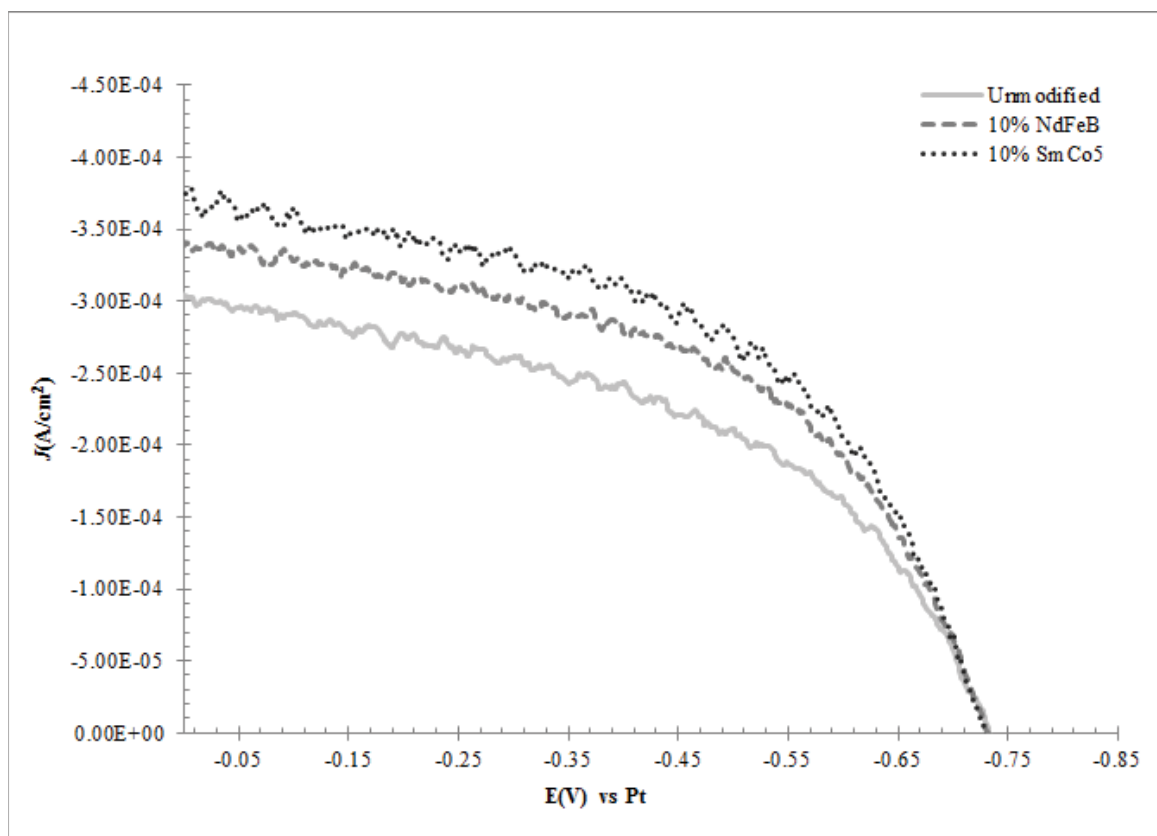
Figure 55. PET based, bilayer electrodes representative $iV$ curve. Average $i_{ph}$ response, with $W_{in} = 20$ mW/cm$^2$.
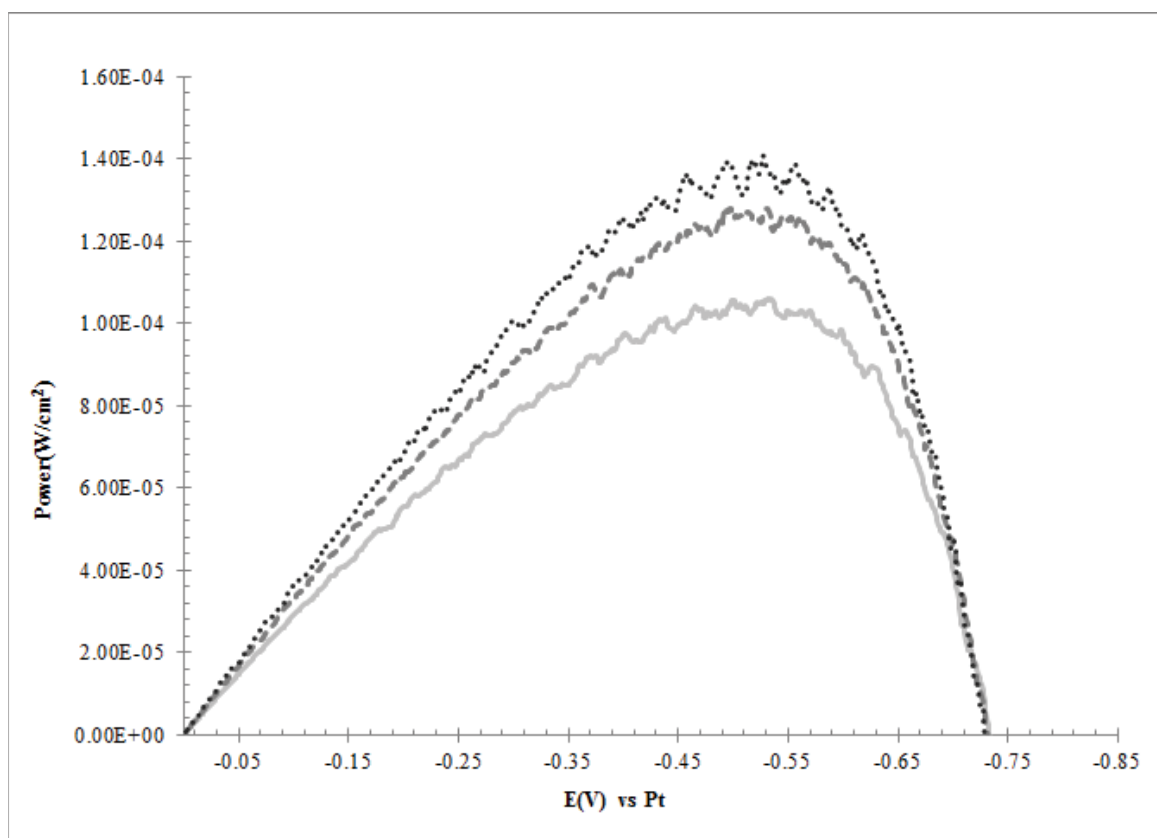
Figure 56. Power curve for PET based electrodes, average response for bilayer electrodes. Curves correspond to data in Figure 55.

Table 15. Table of values for PET substrate, bilayer DSSC electrodes (n = 13 for control and NdFeB- modified electrodes, n = 8 for $SmCo_5$ modified electrodes).

| $J_{sc}(A/cm^2)$ | | | | | |
|---|---|---|---|---|---|
| Loading | Average | Enhancement | $S_{pooled}$ | $T_{calc}$ | Confidence Level |
| Control | $-2.9x10^{-4}(\pm7x10^{-5})$ | | | | |
| NdFeB | $-3.4x10^{-4}(\pm6x10^{-5})$ | 15% | $6.9x10^{-5}$ | 1.623 | 87% |
| $SmCo_5$ | $-3.7x10^{-4}(\pm9x10^{-5})$ | 25% | $7.4x10^{-5}$ | 2.199 | 95% |
| $V_{OC}$ (V) | | | | | |
| Control | -0.73 ($\pm$0.06) | | | | |
| NdFeB | -0.73 ($\pm$0.05) | 0% | $5.6x10^{-2}$ | 0.045 | N/A |
| $SmCo_5$ | -0.73 ($\pm$0.04) | 0% | $4.8x10^{-2}$ | 0.040 | N/A |
| $P_{max}$ (W/cm$^2$) | | | | | |
| Control | $1.1x10^{-4}(\pm4x10^{-5})$ | | | | |
| NdFeB | $1.4x10^{-4}(\pm4x10^{-5})$ | 24% | $4.3x10^{-5}$ | 1.600 | 86% |
| $SmCo_5$ | $1.5x10^{-4}(\pm5x10^{-5})$ | 36% | $4.3x10^{-5}$ | 2.042 | 93% |
| Fill Factor | | | | | |
| Control | 0.50($\pm$0.07) | | | | |
| NdFeB | 0.54($\pm$0.07) | 8 | $7.1x10^{-2}$ | 1.434 | 82% |
| $SmCo_5$ | 0.54($\pm$0.06) | 9 | $5.9x10^{-2}$ | 1.711 | 88% |

and $P_{max}$. This observed is in agreement with observations by H. C. Lee [13]. Lee conducted voltammetric measurements on redox probes at magnetically modified electrodes and observed current enhancement was proportional to the magnetic strength of the magnetic microparticles.

## 4.2.2  p-type Electrodes

The minority carriers in p-type semiconductors are holes rather than electrons [8]. As a result, the measured photo-current response from a p-type based DSSC is a reductive, or cathodic, photo-current. NiO is used here as semiconductor with Courmarin 343 as the sensitizing dye. Given lower values for $V_{oc}$ and $J_{sc}$, p-type DSSCs have received only a fraction of the research interest as n-type electrodes. However, incorporating p-type electrodes as the cathode in a tandem DSSC offers
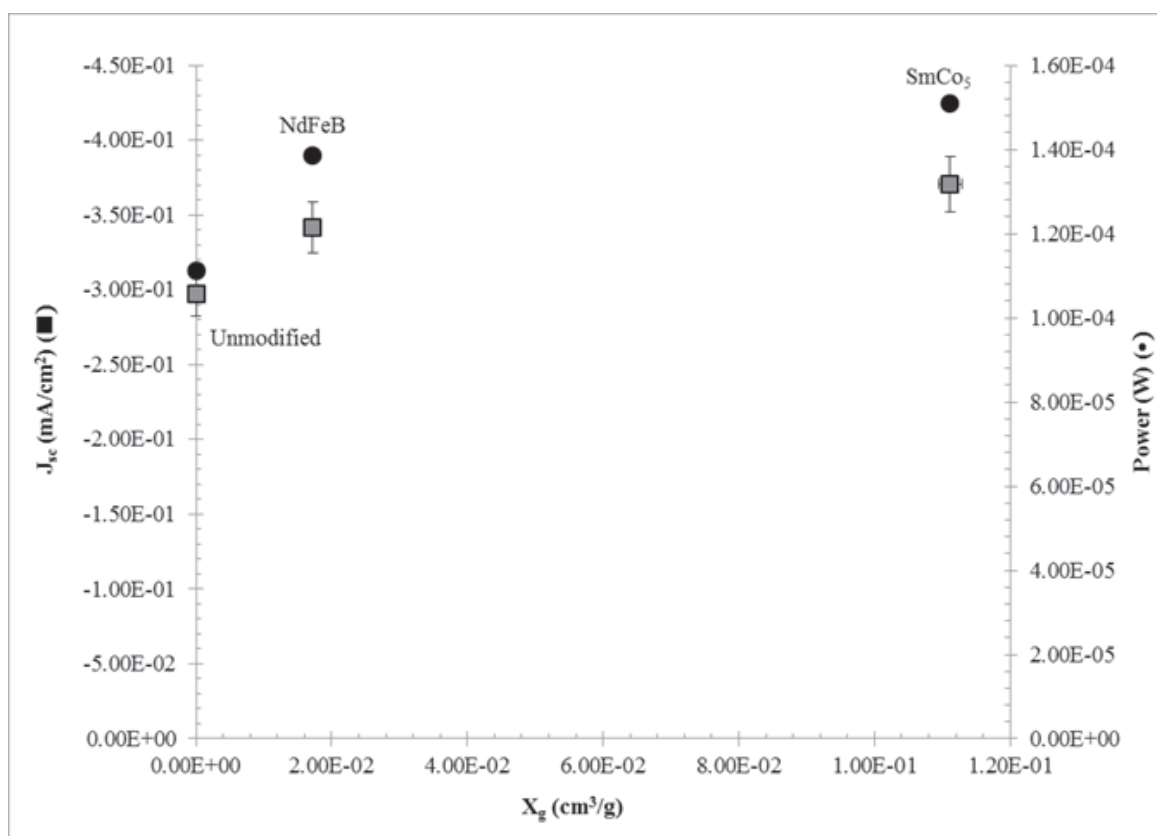
Figure 57. Correlation between observed $J_{SC}$ (mA/cm$^2$) and max power (W) versus mass magnetic susceptibility, $X_g$ (cm$^3$/g). Short circuit current density is on the left axis (■) and power is on the right axis (•).

the possibility of large cell voltages as $E_{cell} = E_{cathode} + E_{anode}$, where $E_{cathode}$ corresponds to the potential at which electrochemical reduction occurs and $E_{anode}$ is the potential at which oxidation occurs. Additonally, current densities increase as both electrodes are photo-active [50, 53, 54]. Also, tandem cells eliminate the need for counter electrode catalysts, such as platinum, and thereby lower the cost of DSSC photovoltaics.

### 4.2.2.1 Redox solution effects

NiO based electrodes are annealed to high temperature (high T) (550 °C) for 10 minutes, from a procedure optimized by Bach et. al [50]. High T is necessary to establish a mechanically stable NiO layer. Two series of p-type electrodes were modified and evaluated. Electrodes were first modified with either 10 % glass beads (control) or 10 % glass coated magnetite. A range of redox solutions were tested with the p-type system. Enhancements in power and open circuit potentials are observed. However, significant shifts in $J_{sc}$ are observed with varying the concentrations of redox active species. More specifically, with different electrolyte cations. Gregg et. al. have made similar observations on the effects of the cation in the electrolyte [18]. Figure 58 shows typical $iV$ curves for p-type electrodes, with the standard 0.5 M I⁻/ 0.04 M $I_2$ redox couple. The resultant power curve is shown in Figure 59. As with n-type electrodes an average increase in maximum power of 24 % is observed. The effects of redox solution composition are summarized in Table 16.

A changing in the electrolyte to 0.6 M LiI and 0.3 M $I_2$ produces a more evenly distributed photocurrent response. However, the increased concentration of
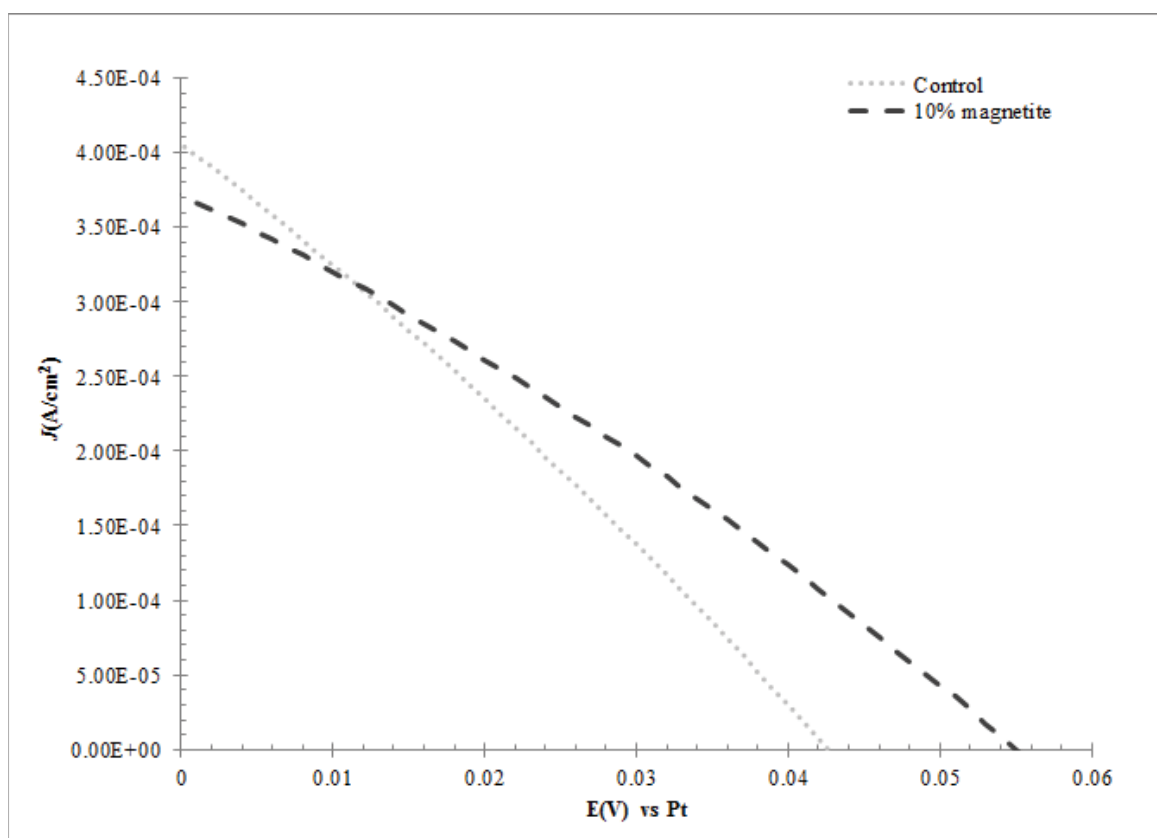
Figure 58. *iV* curve for single layer NiO electrodes sensitized with Coumarin 343 with 0.5 M TBAI/ 0.04 M I$_2$ redox solution; control electrodes contain 10 % glass beads, modified electrodes contain 10 % silane-coated Fe$_3$O$_4$, n = 4 for each modification.
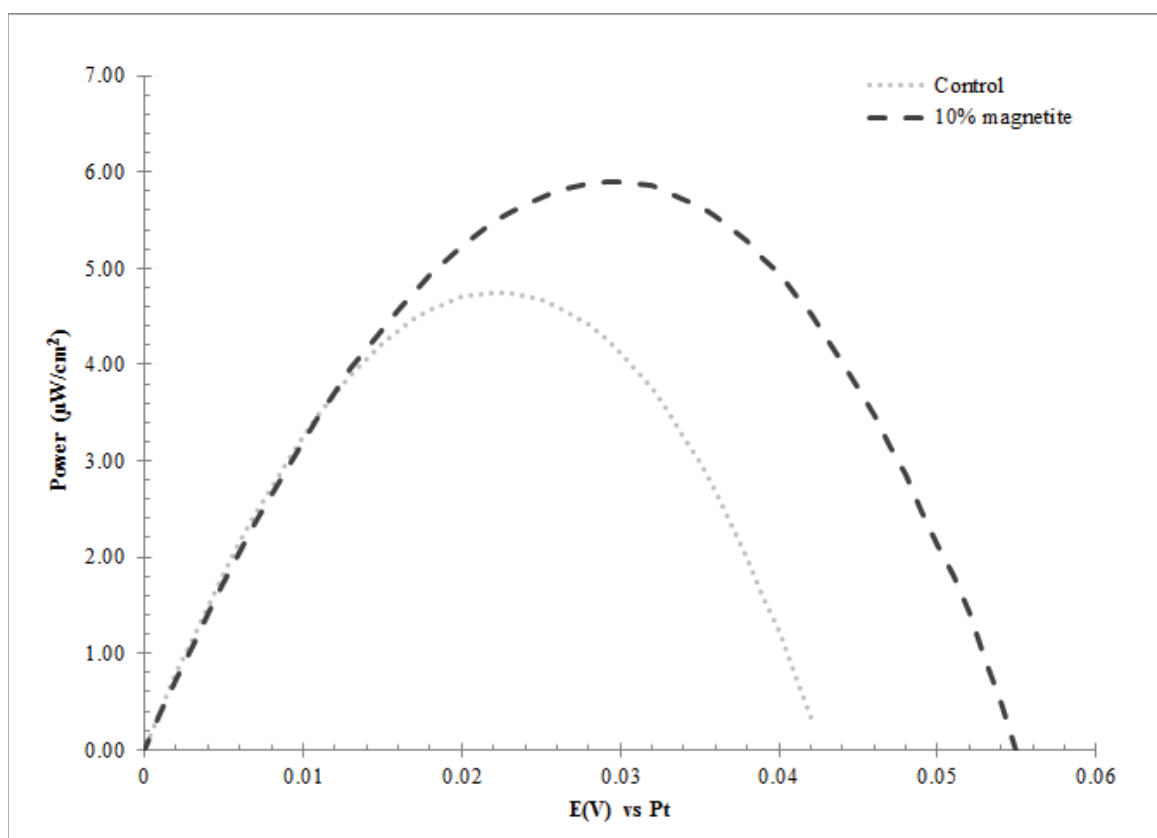
Figure 59. Power curve for p-type electrodes evaluated with 0.5 M TBAI / 0.04 M $I_2$ in acetonitrile, $W_{in} = 20$mW/cm$^2$. Curves correspond to data in Figure 58.

electrolyte reduces the amount of light incident upon the semiconductor interface,

and thereby reduces photocurrent and power output. Lastly, to remedy this effect,
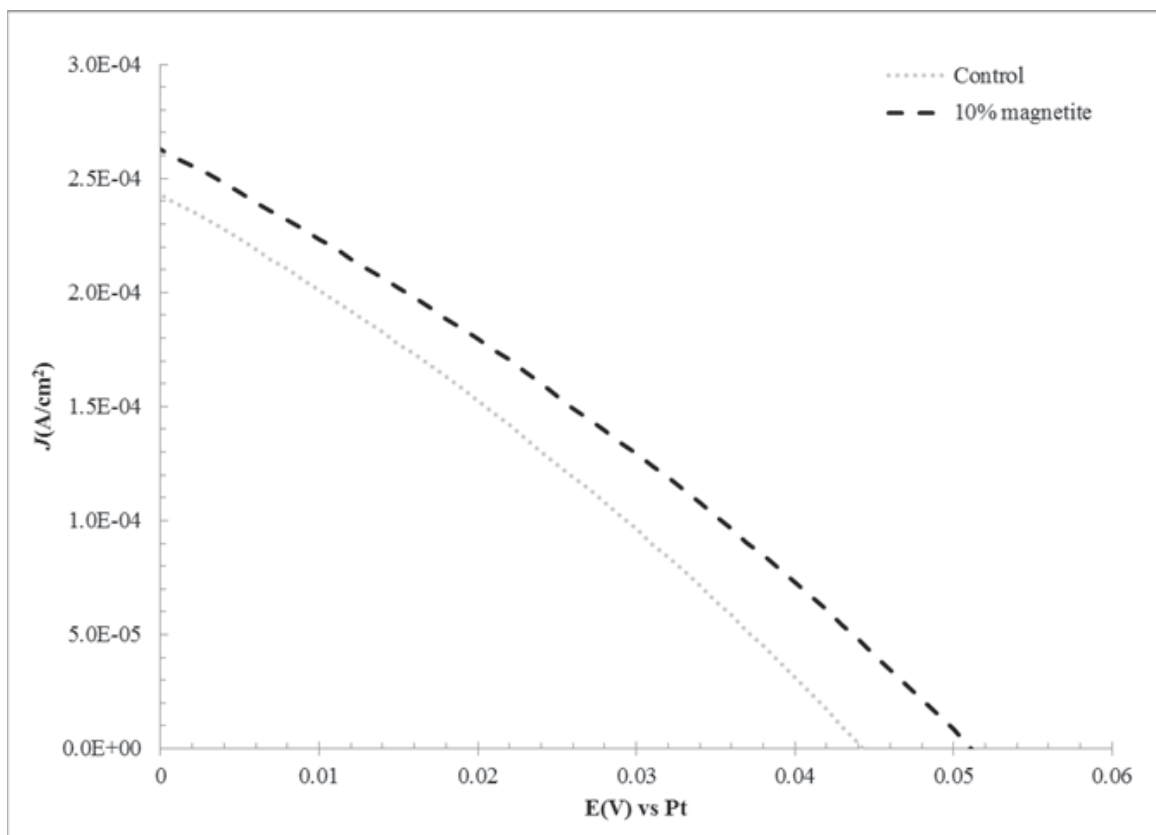


Figure 60. iV curve for p-type NiO DSSC electrode evaluated with 0.6 M LiI and 0.3 M $I_2$. Average current response of n = 3 electrodes for each.

a decreased concentration of the redox mediator was used, at 0.06 M LiI and 0.03

M $I_2$. Increased current responses was observed versus the more concentrated

solution. Magnetic enhancement was still observed, but, the electrodes at this point

had been tested in several electrolytes and this is reflected in dimished response of

photocurrent.
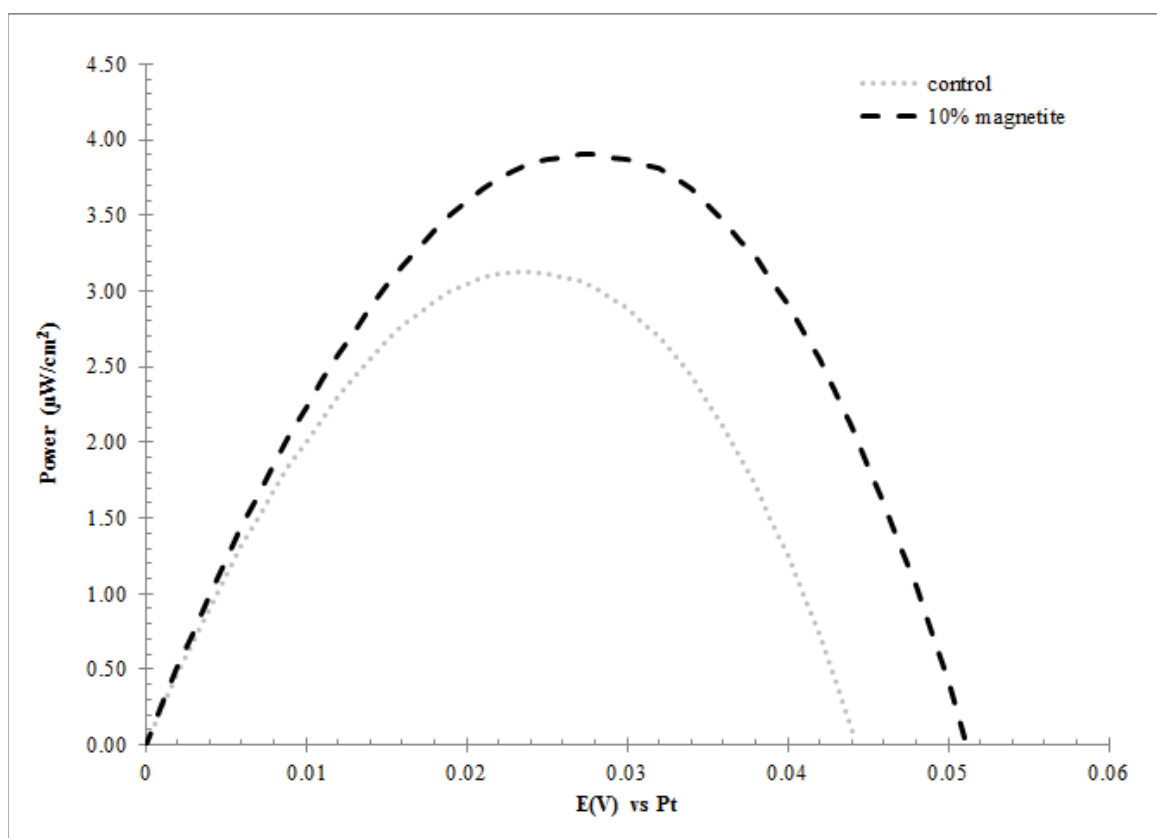
Figure 61. Power curve for p-type NiO DSSC electrode evaluated with 0.6 M LiI and 0.3 M $I_2$. Average current response of n = 3 electrodes for each. Curves correspond to data in Figure 60.
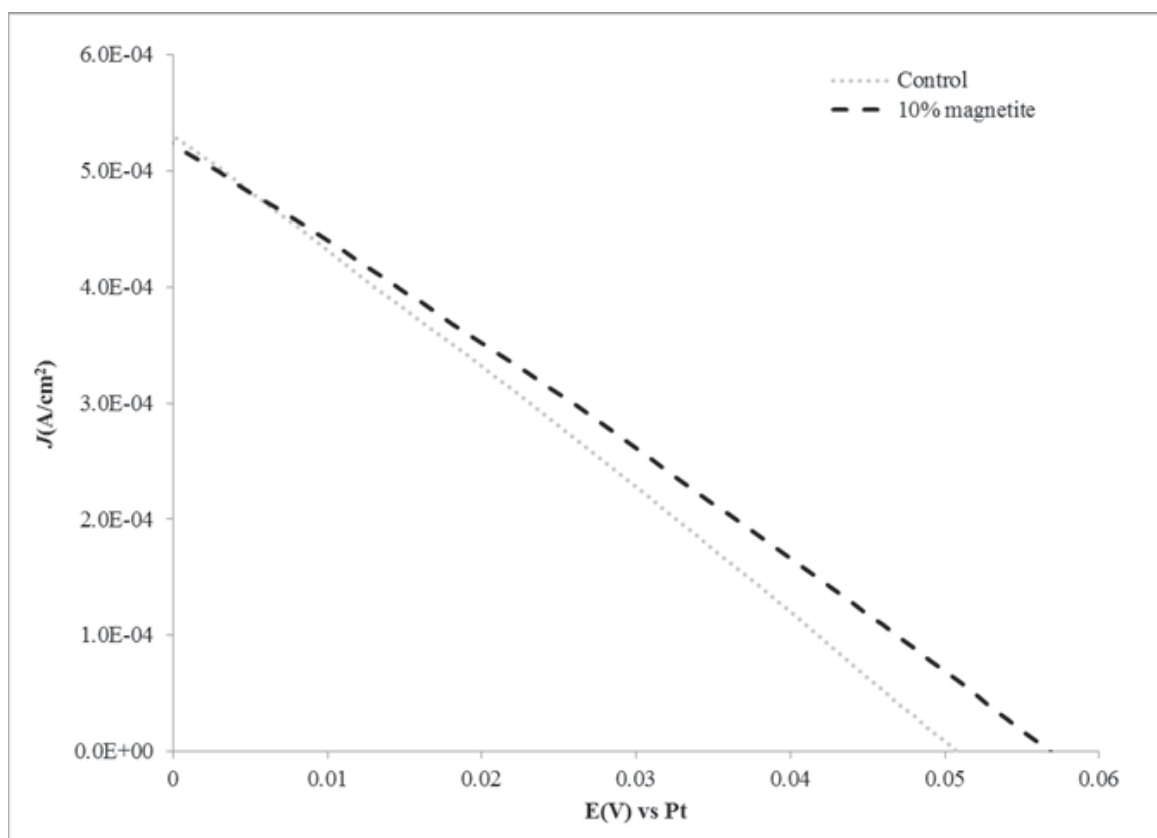
Figure 62. iV curve for p-type NiO DSSC electrode evaluated with 0.06 M LiI and 0.03 M I$_2$. Average current response of n = 3 electrodes for each.
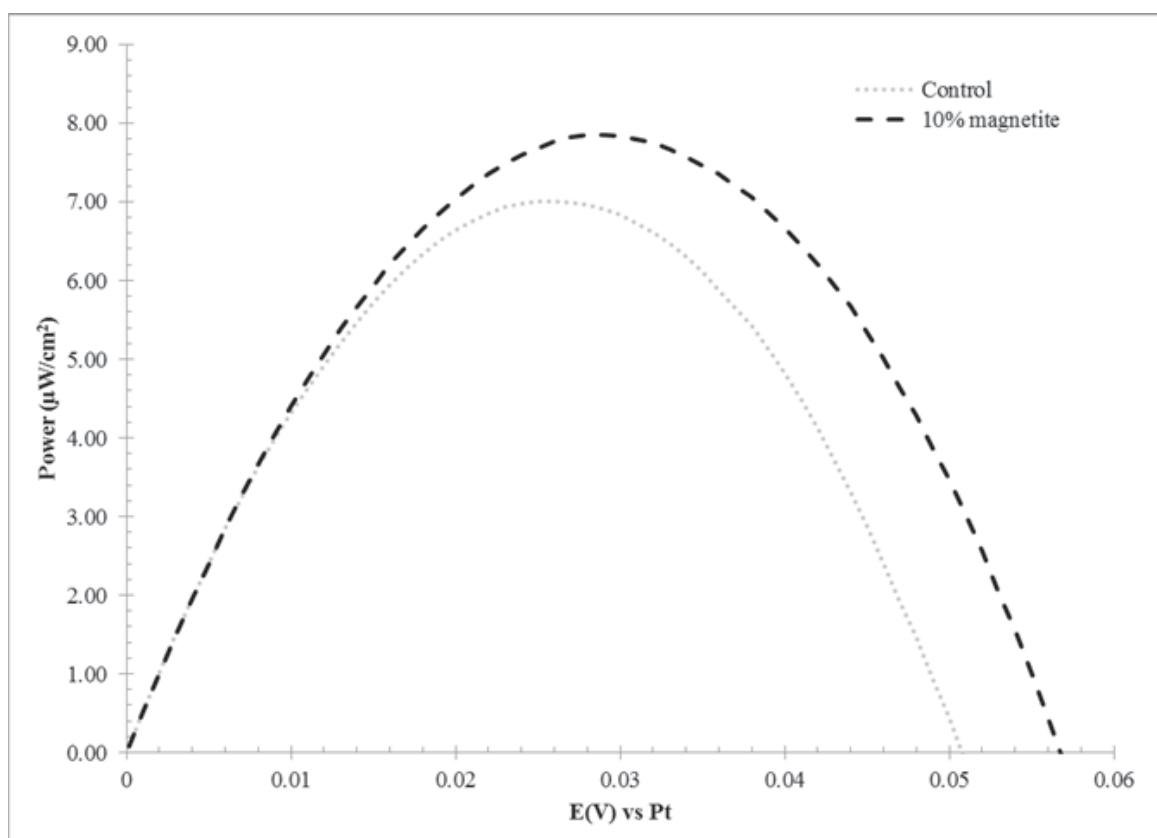
Figure 63. Power curve for p-type NiO DSSC electrode evaluated with 0.06 M LiI and 0.03 M $I_2$. Average current response of n = 3 electrodes for each. Curves correlate to data in Figure 62.

Table 16. Table of values for NiO p-type electrodes in varying redox mediator solutions, all solutions in acetonitrile. Controls contain glass beads and magnetically modified electrodes contain 10 percent by wt magnetite.

**0.5M TBAI/ 0.04 M $I_2$ in acetonitrile**

$J_{sc}(A/cm^2)$

| Loading | Average | Enhancement | $S_{pooled}$ | $T_{cacl}$ | Confidence Level |
|---|---|---|---|---|---|
| 0% | $4.1 \times 10^{-4}(\pm 3 \times 10^{-5})$ | | | | |
| 10% | $3.7 \times 10^{-4}(\pm 2 \times 10^{-5})$ | -10% | $3.2 \times 10^{-5}$ | 1.503 | 77% |

$V_{OC}$

| | | | | | |
|---|---|---|---|---|---|
| 0% | $0.042(\pm 0.008)$ | | | | |
| 10% | $0.055(\pm 0.003)$ | 6% | $6.3 \times 10^{-3}$ | 2.913 | 94% |

$P_{max}$ $(W/cm^2)$

| | | | | | |
|---|---|---|---|---|---|
| 0% | $4.8 \times 10^{-6}(\pm)$ | | | | |
| 10% | $5.9 \times 10^{-6}(\pm)$ | 23% | $1.1 \times 10^{-6}$ | 1.301 | 72% |

Fill Factor

| | | | | | |
|---|---|---|---|---|---|
| 0% | $0.3(\pm 0.2)$ | | | | |
| 10% | $0.29(\pm 0.09)$ | —— | 0.17 | $4.5 \times 10^{-3}$ | N/A |

**0.6M LiI/ 0.3 M $I_2$ in acetonitrile**

$J_{sc}(A/cm^2)$

| Loading | Average | Enhancement | $S_{pooled}$ | $T_{cacl}$ | Confidence Level |
|---|---|---|---|---|---|
| 0% | $2.4 \times 10^{-4}(\pm 1 \times 10^{-5})$ | | | | |
| 10% | $2.6 \times 10^{-4}(\pm 1 \times 10^{-5})$ | 8% | $1.4 \times 10^{-5}$ | 1.974 | 85% |

$V_{OC}$

| | | | | | |
|---|---|---|---|---|---|
| 0% | $0.044(\pm 0.001)$ | | | | |
| 10% | $0.051(\pm 0.002)$ | 16% | $1.9 \times 10^{-3}$ | 5.199 | 98% |

$P_{max}$ $(W/cm^2)$

| | | | | | |
|---|---|---|---|---|---|
| 0% | $3.1 \times 10^{-6}(\pm)$ | | | | |
| 10% | $3.9 \times 10^{-6}(\pm)$ | 26% | $6.7 \times 10^{-7}$ | 0.342 | N/A |

Fill Factor

| | | | | | |
|---|---|---|---|---|---|
| 0% | $0.29(\pm 0.07)$ | | | | |
| 10% | $0.29(\pm 0.07)$ | —— | $6.9 \times 10^{-2}$ | 1.083 | 64% |

**0.06 M LiI/ 0.03 M $I_2$ in acetonitrile**

$J_{sc}(A/cm^2)$

| Loading | Average | Enhancement | $S_{pooled}$ | $T_{cacl}$ | Confidence Level |
|---|---|---|---|---|---|
| 0% | $5.3 \times 10^{-4}(\pm 4 \times 10^{-5})$ | | | | |
| 10% | $5.2 \times 10^{-4}(\pm 2 \times 10^{-5})$ | -2% | $3.7 \times 10^{-5}$ | 0.278 | N/A |

$V_{OC}$

| | | | | | |
|---|---|---|---|---|---|
| 0% | $0.051(\pm 0.001)$ | | | | |
| 10% | $0.057(\pm 0.001)$ | 12% | $4.2 \times 10^{-3}$ | 2.021 | 86% |

$P_{max}$ $(W/cm^2)$

| | | | | | |
|---|---|---|---|---|---|
| 0% | $7.0 \times 10^{-6}(\pm)$ | | | | |
| 10% | $7.8 \times 10^{-6}(\pm)$ | 11% | $1.1 \times 10^{-6}$ | 0.522 | N/A |

Fill Factor

| | | | | | |
|---|---|---|---|---|---|
| 0% | $0.3(\pm 0.1)$ | | | | |
| 10% | $0.26(\pm 0.07)$ | —— | 0.11 | 0.162 | N/A |

4.2.2.2 NdFeB and SmCo$_5$ Modified Electrodes

Given the success of bilayer n-type electrodes, p-type electrodes were also prepared as bilayer electrodes. Controls contain two unmodified layers with no glass beads, while magnetically modified electrodes contain a primary unmodified layer and a second modified layer containing 10 % (w/w NiO) particles. Due to the already low $V_{oc}$ and $J_{sc}$ values for p-type electrodes, low T annealed electrodes with SmCo$_5$ modification were not attempted here. With the proper fabrication tools, e.g., a vacuum furnace, production of SmCo$_5$ modified p-type electrodes is probable. High T annealed electrodes modified with SmCo$_5$, however showed no enhancements. Cobalt oxidation is a likely cause, but color change of oxidation are unobservable in the black NiO layer. NdFeB modified electrodes show enhancement of 6 % in $J_{sc}$ and 11 % increase in maximum power. The oscillation of the signal is attributed to fluctuation in the light source.

4.2.3  Magnetic Enhancement in DSSC Electrodes

Many models have been proposed to examine the operation of the DSSC system. The most commonly accepted DSSC model is the kinetic or interfacial model [10]. The interfacial model postulates that the photoinjection of electrons from the excited dye (S*) to the conduction band (CB$_{TiO_2}$) is driven by the electrochemical potential gradient, $\nabla\mu$ [18]. This gradient is established by the photoinduced increase in the concentration of electrons in the CB$_{TiO_2}$ at the semiconductor|solution interface relative to the bulk semiconductor.
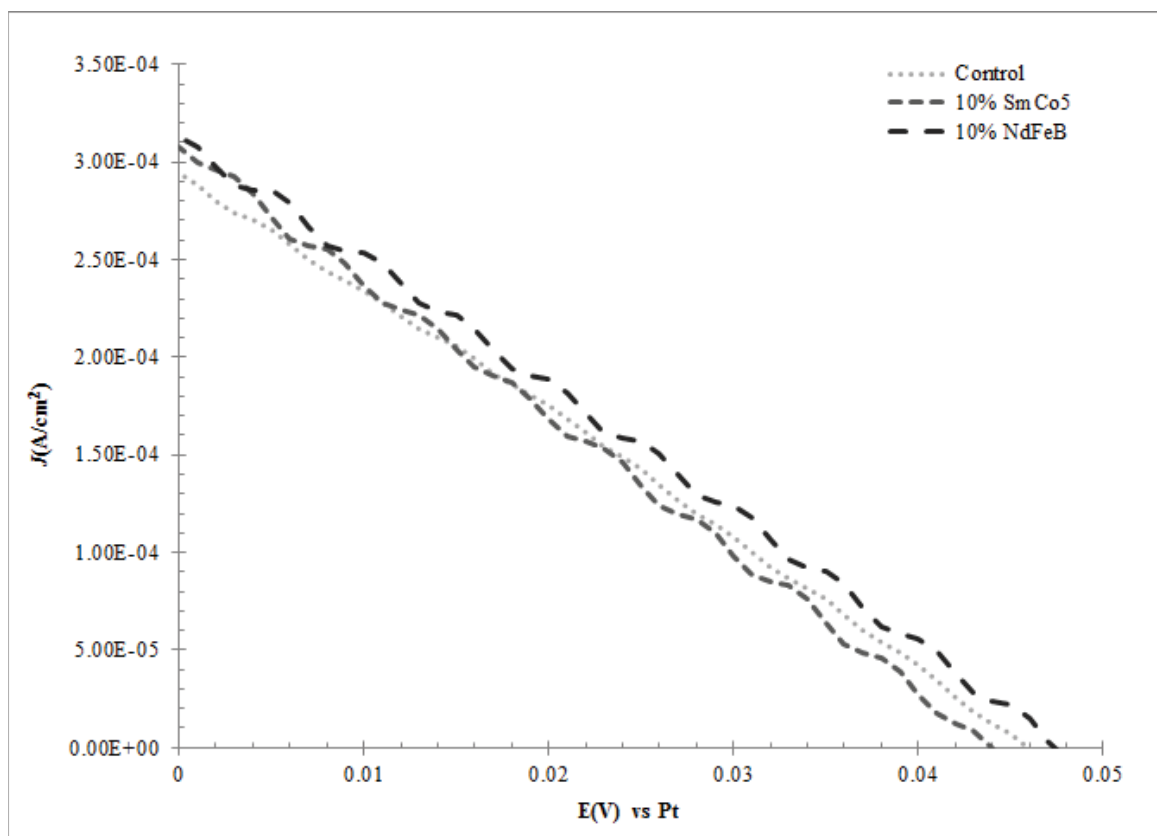
Figure 64. *iV* curve for bilayer NiO p-type electrodes sensitized with Coumarin 343, n = 2 for each modification.
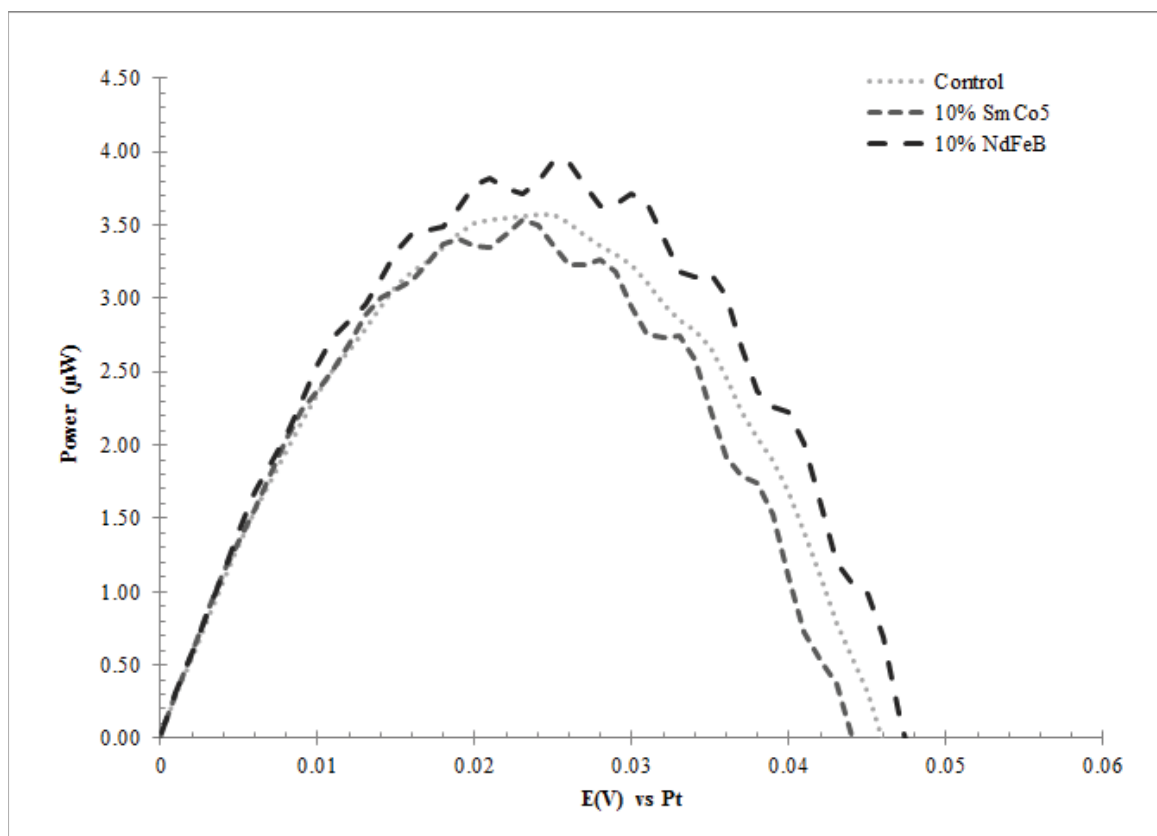
Figure 65. Power curve for NiO p-type electrodes sensitized with Coumarin 343, $W_{in}$ = 20 mW/cm$^2$. Curves correspond to data in Figure 64.

In the DSSC system, multiple steps and electron transfer reactions are required to complete the circuit and generate power (Figure 43). The rate of these steps has been measured and fast injection rates compared to recombination rates is the fundamental basis for operation of Grätzel cells. The steps can be considered as follows:

1. Incident light (photons) excites the sensitizing dye (S), traditionally a transition metal complex, to an excited state (S*).

2. The excited dye injects an electron to the conduction band (CB) of the semiconductor.

3. The conduction band electron diffuses through the CB to the transparent conductive oxide (TCO) and onto the external load. This step is realized as power.

4. To complete the circuit, electrons reduce a sacrificial donor, D to D$^-$, via the step labeled $ET_2$.

5. The sacrificial donor then reduces the dye S$^o$ back to S in step $ET_3$. This allows the cycle to repeat.

To rationalize the mechanism by which magnetic modification facilitates an increase the $i_{ph}$ response, we consider the dye sensitized system as an electrochemical cell that undergoes three, one step ET reactions. These three reactions are: $ET_1$, a heterogeneous exciton (electron/hole pair) at the dye|semiconductor interface; $ET_2$, a homogeneous cross exchange ET reaction between the dye and redox mediator; and $ET_3$, a second heterogeneous ET between the CE and the redox mediator.

It is established that magnetic microparticles increase current response in homogeneous self exchange reactions [11–14]. We saw in Chapter 2, the effects

magnetic microparticles have on heterogeneous ET reactions at modified solid state electrodes for academically interesting redox probes, both transition metal complexes and organic mediators. Also in Chapter 2, complementary electrochemical impedence spectroscopy (EIS) measurements correlated a decrease in the resistance to charge transfer ($R_{CT}$) at magnetically modified electrode. Thus, it is anticipated that magnetic field effects can impact many aspects of DSSC ET processes.

Modification occurs at the semiconductor WE. Given the distance between the CE and WE ($\sim$300 $\mu$m), $ET_3$ is most likely unaffected by the magnetic field of the particle. For spherical particles, the field decays as $r^{-3}$. At distances greater than five radii, magnetic field effects are negligible. Magnetic particles used here have radii $\sim$1.5 to 4.5 $\mu$m where at distances greater than 8 to 23 $\mu$m, the local field is assumed to be no different that the earth's magnetic field. Additionally, the reaction kinetics of the $I^-/I_3^-$ ($ET_3$) redox couple were examined at modified platinum electrodes where no current enhancements were observed. Experimentally separating $ET_1$ and $ET_2$ is difficult. Consider only magnetic effects on $ET_1$.

4.2.3.1 Evaluation of magnetic field effects on the molecular sensitizer

Why are magnetic effects observed in DSSCs?

Magnetic effects are primarily observed in systems of slow transport, such as at modified electrodes, in batteries, and PEM fuel cells [12]. This is due to the time it takes to establish a magnetic effect, that is slower than molecular in liquid phases [13]. Similarily, DSSCs are also domains of slow transport.

4.2.3.2  Enhancement as a function of spin (S)

Magnetic effects on self exchange at modified electrodes has been extensively studied by H. C. Lee [13] and others . The enhancement is described as increased hopping apparent when physical diffusion is limited. This is modeled as by Dahms Ruff conduction.

$$D_{obs} = D_p + D_{et} \tag{62}$$

The apparent or observed diffusion coefficient ($D_{obs}$) includes both physical diffusion ($D_p$) and effective diffusion from electron hopping ($D_{et}$). When physical diffusion is limited ($D_{et} >> D_p$), then hopping dominates. As such,

$$D_{obs} \rightarrow \frac{k_{ex}\delta^2 C^*}{6} \tag{63}$$

where $k_{ex}$ is the electron transfer rate constant, $\delta$ is the center to center distance between redox moieties, $C^*$ is the bulk concentration, and 6 is a three dimensional geometric factor. Increased hopping in modified systems is a manifestation of increased electron transfer rates, as $k_{exMAG} > k_{exNON\ MAG}$. For measurements performed at polymer modified electrodes by cyclic voltammetry, the increased diffusion rate yields increased peak current, $i_p$. This manifestation of the effect is analogous to the magnetic effects shown in Chapter 2.

In magnetically modified dye sensitized cells, we see photocurrent enhanced analogously. Conventions exist that to describe diode or photocurrent behavior. Traditional photocurrents can be described with the conventional diode equation,

$$i_{ph} = -qAk_{inj}C^*(e^{-qV/k_BT} - 1) \tag{64}$$

where the observed current ($i$) is proportional to charge of the electron ($q$), electrode area (A), and the rate constant ($k_{inj}$). $k_B$ is the Boltzmann constant and T is temperature in Kelvin. Likewise, injection rates can be determined using Fermi's golden rule

$$k_{inj} = \left(\frac{4\pi^2}{h}\right) |V|^2 \rho(E) \tag{65}$$

where $h$ is the Planck constant, V is the electronic coupling between the photosensitizer and the semiconductor, and $\rho(E)$ is the density of states of the conduction band [8]. Rigorous modeling of the system is not considered here.

Evidence exists that self exchange occurs in the dye sensitized system through the molecular sensitizer. Ardo and Meyer at Johns Hopkins have spectroscopically measured and modeled by Monte Carlo methods the self exchange progresses amongst anchored molecular sensitizers on $TiO_2$ substrates [52]. Their results suggest that two means of diffusion exists in the DSSC system; diffusion of the injected electron through the semiconductor conduction band and diffusion of the electrons through oxidized sensitizer moieties on the $TiO_2$ surface by self exchange. The self exchange mechanism was found to be faster than hole decay (i.e., a recombination from the semiconductor) and excited state decay.

As we saw in Chaper 2, the spin state of the chemical species is considered when evaluating magnetic effects. Again, we determine spin by

$$S = \frac{1}{2}n \tag{66}$$

where spin (S) is one half the number of unpaired electrons (i.e., no unpaired electrons is a singlet, 1 unpaired electron is a doublet, etc.). The molecular sensitizer,

N3, (*cis*-bis(isothiocyanato)bis(2,2'-bipyridal-4,4'-dicarboxylato)-ruthenium(II)) is a group 6, octahedral complex. In the excited state (S*)/oxidized state (S$^o$), the dye species is paramagnetic, a doublet. (See Figure 66.) The unoccupied 3d-orbital of the Ti(IV) is a singlet, diamagnetic. As is consistent with previous observations and modeling of homogeneous self exchange, the magnetic field facilitates the rate of electron nuclear spin polarization between the singlet of the groud state dye (S) and the doublet of the excited state dye (S*) that in turn accelerates the homogeneous electron transfer rate. In the case of heterogeneous electron transfer, the singlet of the TiO$_2$ interacts with the doublet of the excited state dye (S*), facilitating enhancement in a similar manner.
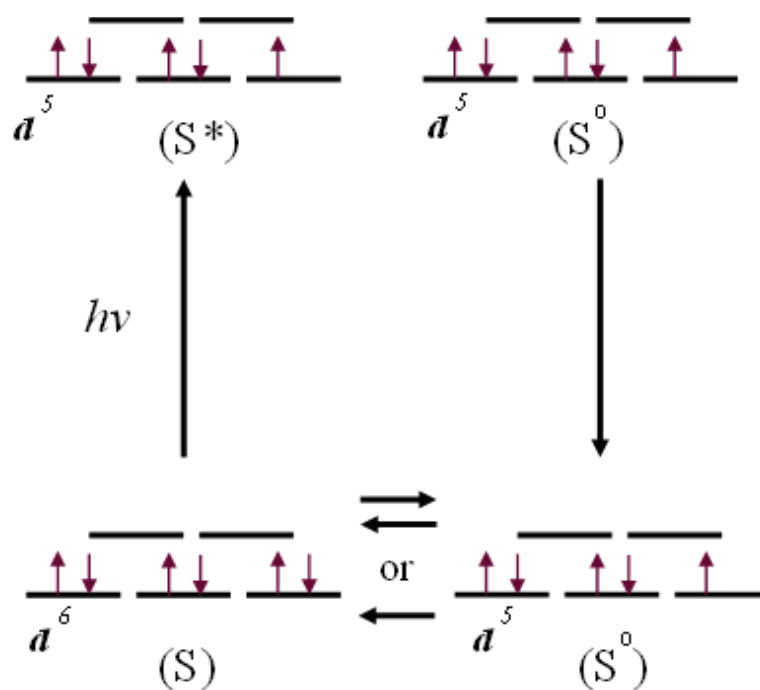


Figure 66. Spin state diagram for N3 dye in the ground state (S), excited state (S*), and oxidized state (S$^o$).

4.2.3.3 Enhancement as a function of field strength (H)

We saw in Chapter 2 that magnetic fields influence heterogeneous electron transfer rate. This effect manifests as increased current. The analysis revealed increased values of $k^0$, the heterogeneous electron transfer rate. In the multistep process of the DSSC system, excited state electron injection under illumination determines cell operation as shown by light and dark currents. Injection is fast. Time resolved spectroscopy places the rate of injection on the order of femtoseconds versus recombination which is estimated at microseconds [18]. Carboxyl groups that anchor the molecular sensitizer are suspected as the mechanism through which fast electron injection can occur. This interaction produces large potential (V) values, a result of the interaction of the $\pi^*$-orbital of the excited state of the sensitizer and the conduction band of the $TiO_2$ film that is primarily unoccupied 3d orbitals of Ti(IV).

The magnetic enhancement in the dye sensitized system is considered analogous to other chemical systems that experience magnetic field effects in that effect is proportional to the magnetic field, H. In Figure 57, we see that the $J_{sc}$ and power output of modified systems increases monotonically with the particle field strength. The effects may be analogous to processes previously explored by Lee and Minteer. The enthalpy of the reaction in the field is shifted by the Zeeman energy, $gSH\beta$, in the electron nuclear spin polarization process. (Where g is Lande g factor, S is spin, H is the external magnetic field strength, and $\beta$ is the Boltzmann constant.) In turn, the mechanism yields a rate that varies with the Zeeman energy. The rate of ET increases with H [13].

To summarize, description of magnetic field effects in the dye sensitized systems strongly reflects the work of H. C. Lee and S. Minteer at modified electrodes, the enhancements in magnetically modified power systems such as batteries by Tesene and in fuel cells by Gellett, as well as the work here in Chapter 2 [11–13, 15]. These systems share many commonalities of electron flow and the description for magnetic effects are strongly linked. First, the system exhibits slow transports. The molecular sensitizer is an absorbate ($D_{et} >> D_p$), and electron conduction in the $TiO_2$ is slow as solid state conduction in a semiconductor. Second, radical species exist through which magnetic effects can influence the energy of reactions, both the homogeneous and heterogenous ET reactions. Effects are anticipated to be proportional to $gHS\beta$. Lastly, magnetically modified DSSC electrodes experience enhancement proportional to H.

## 4.3    Conclusions

We have demonstrated that magnetic fields impact the performance of magnetically modified dye sensitized solar cells. Photocurrent enhancements of 20 to 40 % are typical for magnetically modified DSSC compared to unmodified controls. $SmCo_5$ modified electrodes, on glass substrates, achieve nearly 5 % conversion efficiency. Additionally, magnetic fields statistically enhance performance versus unmodified controls as measured by metrics of short circuit current density, fill factor, and output power. These enhancements were rationalized to occur through magnetic field effects on electron transfer rates, both homogeneous and heterogeneous.

Unexpectedly, variations in the effects of magnetic fields on $V_{oc}$ were also

observed. Calculated open circuit potential ($V_{OC}$) values are based on the difference in energy between the $E_f$ of the semiconductor and the standard reduction potential of the redox mediator both thermodynamic values. Experiemtnal values of $V_{OC}$ are usually below the calculated values.

Magnetic particles of varying materials, include glass coated magnetite, $SmCo_5$, and NdFeB were incorporated into both n-type and p-type Grätzel cells and supported on different substrates. Special attention was given to electrode fabrication that includes consideration of the magnetic, chemical, and physical properties of the magnetic additives and electrode materials. Glass coated magnetite particles were used as uncoated iron oxide has been shown as a contaminant of recombination in $TiO_2$ based DSSCs. Though not shown, data for electrodes modified with uncoated $Fe_3O_4$ confirms this. In some instances, the physical and chemical properties of the magnetic particles made electrode fabrication cumbersome. $SmCo_5$ modified electrodes, for example, showed average enhancements but complex fabrication means additional methods are need to increase electrode fabrication and the number of electrodes that can be tested. Further throughts on continuing and future experiments on magnetically modified Grätzel cells are given in Chapter 6.

CHAPTER 5

MAGNETICALLY MODIFIED $MnO_2$ ELECTRODES FOR CAPACITOR

APPLICATIONS

5.1   Introduction

$MnO_2$ is ubiquitous in batteries and electrochemical capacitors. The material is environmentally safe, abundant (elementally twelfth most), and above all, cheap. Edison and others developed $MnO_2$ battery chemistry in the early 1900s, however, commercialization of the technology occurred nearly 60 years later [19, 55, 56]. In primary cells, $MnO_2$ is employed in a highly basic medium (6 to 9 M KOH). In this system, the $MnO_2$ is the active component of the cathode, where it undergoes an irreversible electron transfer reactions as in [67]

$$2MnO_2 + H_2O + 2e^- \longrightarrow Mn_2O_3 + 2OH^-$$ (67)
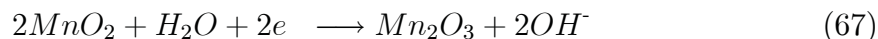
In this irreversible process, the manganese undergoes morphological changes which prevent the system from recharging. Work by Tesene [15] thoroughly reviews this process and the associated morphological changes.

Capacitors are also systems that store electrical energy. Capacitors predate the American Revolution. Referred to as Leyden Jars, these devices could accommodate upwards of 1 nanofarad of charge electrostatically on foils carefully wrapped around glass jars. Current electrochemical capacitors operate in an analogous, albeit more efficient, manner. Electrochemical capacitors utilize the electrochemical double layer

formed at an electrode surface when a potential is applied to an electrode surface. In a cyclic voltammetric measurement, this is manifest as a charging current and is sometimes referred to as the solvent envelope. A scheme of the double layer is shown in Figure [67]
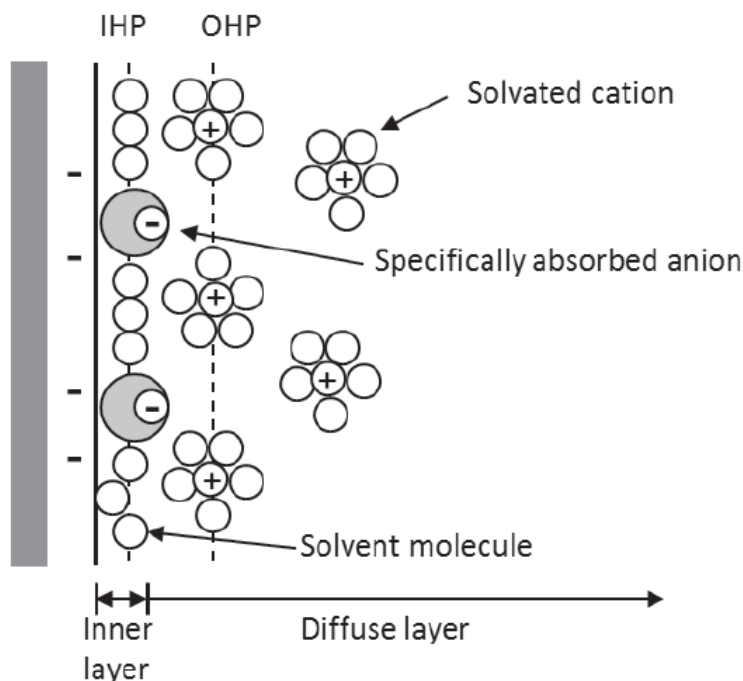


Figure 67. Model of double layer capacitance, anion adroption process [1]. Where the inner Helmholtz plane and outer Helmholtz plane are IHP and OHP respectively.

In modern electrochemical capacitors, electrodes are formed from activated carbon (AC), a high surface area material that allows for the storage of 50 to 200 Farads (F) per gram AC [21]. These materials are cheap and abundant. (The most common source of activated carbon is pyrolyzed coconut shell.) However, electrochemical capacitors have low energy density. Electrostatic charge is dissipated on the one to tens of seconds time scale. Higher energy and power densities are needed for

processes such as load leveling, in electric and hybrid vehicles and for wind and solar power storage.

Hybrid supercapacitors (or ultracapacitors) meet this criteria of high power and energy densities. A hybrid capacitor combines both the nonfaradaic electrostatic charge storage mechanism of the electrochemical capacitor with the faradaic charge storage mechanism of batteries [19]. The faradaic component of these systems is often referred to as pseudocapacitance. In hybrid capacitors, one electrode (typically the anode) acts as the traditional capacitor that stores charge in the double layer. At the cathode, a metal oxide replaces the activated carbon. This metal oxide increases charge storage through specific adsorption with solution based cation species that is coupled to a reversible faradaic charge transfer.

Recently developed, thin films of $RuO_2$ have charge storage densities of 600 to 900 F/g [20]. This occurs in acidic aqueous solution, where one proton is adsorbed at each available Ru site in an extremely efficient adsorption and charge storage process. However, the precursor for $RuO_2$, $RuCl_3$ is costly ($\sim$\$75 /gram) and prevents commercialization. $MnO_2$ is investigated as an alternative as its precursor is much less expensive ($KMnO_4$ $\sim$\$0.10 /gram). Given its high abundance and low cost, $MnO_2$ is a suitable replacement for commercial applications. Powder based electrodes achieve 100 to 200 F/ g. Thin films ($\sim$25 nm) of $MnO_2$ achieve capacitances closer to 600 F/g as the relative surface area to volume increases and electrolyte access to the $MnO_2$ increases. In addition, $MnO_2$ operates as a capacitor under mild aqueous conditions (e.g., 0.1 M $CaCl_2$, 0.1 M $Na_2SO_4$). Ongoing research aims to increase $MnO_2$ energy density with focus on increased capacitance (e.g.,

through increased surface area/volume) and increased cell operating voltage to increase power ($P = iV$).

In the $MnO_2$ system, charge storage is proposed as

$$(MnO_2)_{surface} + M^+ + e \rightleftharpoons (MnO_2\, M^+)_{surface} \qquad (68)$$
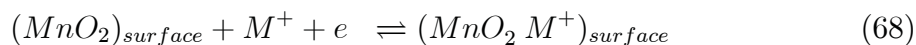
Alternative mophologically dependent mechanisms are proposed, but the faradaic process in reaction [68] is used here. As was demonstrated in Chapter 2, magnetic fields increase heterogeneous exchange rates. Electrochemical impedence spectroscopy meausrements in Chapter 2 also showed that magnetic modification can increase the faradaic capacitance of a system while decreasing resistance for faradaic charge transfer. In this Chapter, it is demonstrated that magnetic fields can increase the capacitance in the $MnO_2$ system. The increased capacitance is attributed to magnetic effects on the faradaic component of the $MnO_2$ system. The system has been prepared as powder based composite electrodes tested in half-cell configuration. Capacitance enhancement are demonstrated over a variety of loading percentages and current densities as verified statistically.

## 5.2  Methods and Materials

A variety of electrode preparation protocols were explored throughout, here is describe the optimized procedures.

### 5.2.1  Electrode Preparation

$MnO_2$ electrodes are prepared here as powder composites. A variety of pellet

architectures and mixtures were explored throughout the analysis. Regardless of the analysis, all mixtures contain three principal components: $MnO_2$, graphite ($< 20$ $\mu m$, Sigma), and binder, here polytetrafluoroethylene (PTFE, Sigma). Magnetically modified electrodes contain samarium cobalt microparticles. Control electrodes contain only the three principal components, $MnO_2$, graphite, and binder; no glass microbeads were used in this study. The ratio of the mixture components as well as the magnetic material are noted. $MnO_2$, graphite, and PTFE are all used as received. $SmCo_5$ is not milled as in Chapter 2, however, it was sieved to 25 $\mu m$.

To prepared the composite mixtures, the principal components are combined in 20 mL glass scintillation vials (approximately 10 grams of mixture total). The powders are initially mixed with a spatula in the vial. Two to four glass beads ($\sim$3 mm) are added the vials to promote further mixing. Loaded vials are then rotated for at least three days on the variable speed drill to thoroughly mix the powders. Thorough mixing of the composite powder is essential. Current methods are inadequate for producing homogeneous mixtures and alternatives are sought.

Mixed composites are cold pressed, using a pellet dye. This is consistent with previous procedures [15]. Cold pressing results in pellet electrodes. Minimum thickness for mechanical stability is 200 to 300 $\mu m$, these pellets mass at approximately 25 to 30 mg active material. Thicker pellet architectures were also tested, with total pellet masses of 0.3 grams and thickness of 2 mm. A further reduction of mass results in a pellet too fragile to test. Accurate massing of each electrode is critical for determining specific capacitance of the system.

Carbon cloth (E-TEK, Sommerset, NJ) acts as a current collector for the $MnO_2$

half-cell, this method has been used previously. The carbon cloth is nitrated before use to promote wetting in the aqueous electrolyte. For the nitrating process, the carbon cloth is cut into strips 1.5 cm x 12 cm and is soaked in concentrated nitric acid (16 M) for approximately 10 minutes. The cloth strips are then rigorously rinsed with deionized water to remove all nitric acid. A porous polycarbonate (PC) shell completes a sandwich structure in which the electrodes are tested, this is seen in Figure [68]. The internal pressure of the polycarbonate shell is not considered
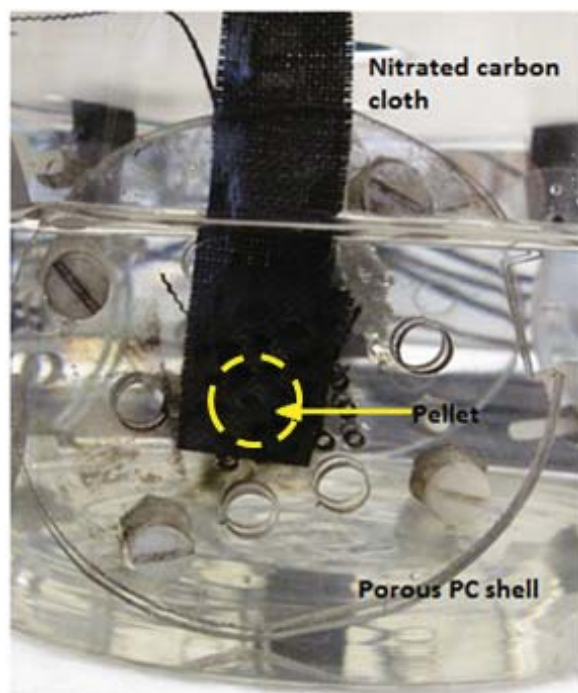


Figure 68. $MnO_2$ electrode half cell assembly; $MnO_2$ pellet contained within carbon current collector and PC shell (indicated by yellow dashed circle).

here - the assembly screws seen in figure 68 are tightened only by hand.

5.2.2  Electrochemical Setup and Evaluation

All electrochemical analyses were performed in a mild aqueous electrolyte, 0.1

M $CaCl_2$. Electrodes are tested in a conventional three electrode setup using a

CH Instruments 760B potentiostat/galvanostat, with an 8 channel multiplexer

capable of sequential analysis. The multiplexer allows for semi-automated testing.

IR-compensation is automatic. A platinum mesh is used as counter electrode with a

Ag/AgCl reference electrode. The setup is seen in Figure 69. Chronopotentiometry,
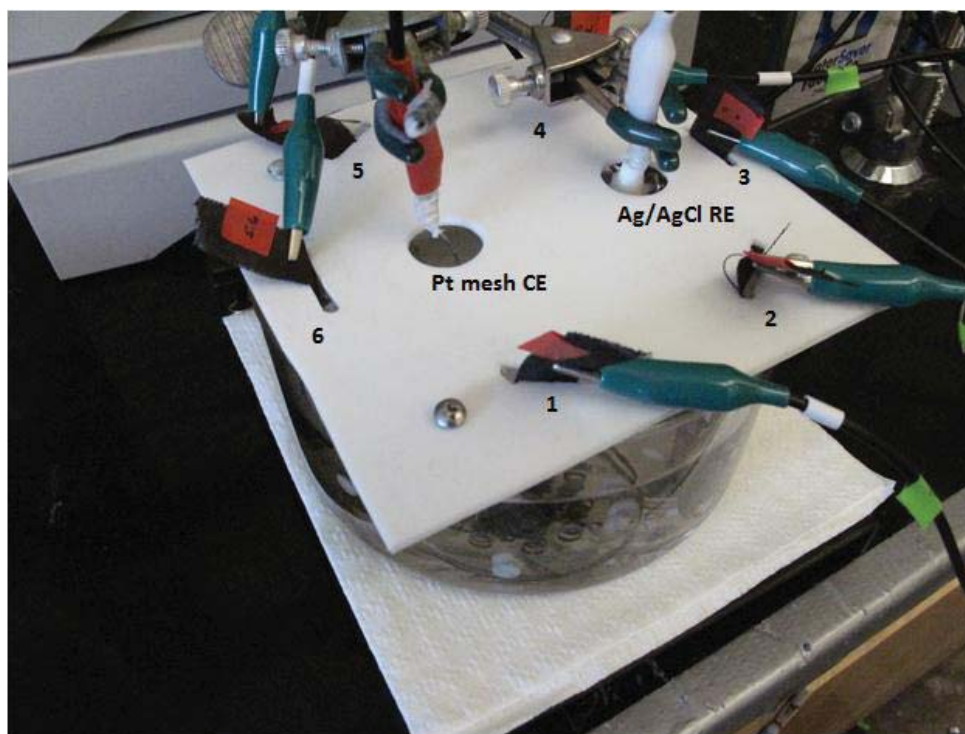


Figure 69. Electrochemical setup with six electrodes.  Ag/AgCl reference electrode
and platinum mesh counter electrode. Electrodes tested in sequence.

a constant current measurement, is used to evaluate the electrodes over a variety of

current loads in addition to cyclic voltammetry.

## 5.3    Results and Discussion

Analyses of galvanostatic measurements on $MnO_2$ electrodes, and comparisons of $MnO_2$ as capacitor electrodes versus batteries are presented here.

### 5.3.1    $\gamma$-$MnO_2$

#### 5.3.1.1  In Capacitors

The morphology and the electrochemical behavior of $MnO_2$ are interrelated [2,15]. In supercapacitors, for instance, researchers have seen increased capacitance in $\alpha$-$MnO_2$ prepared electrodes versus amorphous electrodes [57]. This increased capacitance is speculated as resulting from increased intercalation/de-intercalation of the electrolyte [57,58], given by

$$MnO_2 \; + \; M^+ \; + \; e \quad \rightleftharpoons \quad MnOOM \tag{69}$$
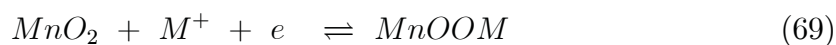
However, successful capacitance amorphous $MnO_2$ electrodes has been achieved [21,59,60]. For materials researchers, the morphology as well as the method of electrode preparation are both shown to affect device performance and are both important consideration in improving device function and life. This impact is apparent in the difference in performance in capacitance between thin-film $MnO_2$ electrodes and powder based electrodes of the same material.

For the results presented herein, $\gamma$-$MnO_2$ was selected for its availability (i.e., quantity) to complete the analysis. $\gamma$-$MnO_2$ is also referred to as electrolytic manganese dioxide (EMD), the common form of the material in alkaline batteries.

The $\gamma$-MnO$_2$ (Delta EMD, RSA) used here exists as a random intergrowth of pyrolusite ($\beta$-MnO$_2$) in a ramsdellite matrix. This was confirmed though powder
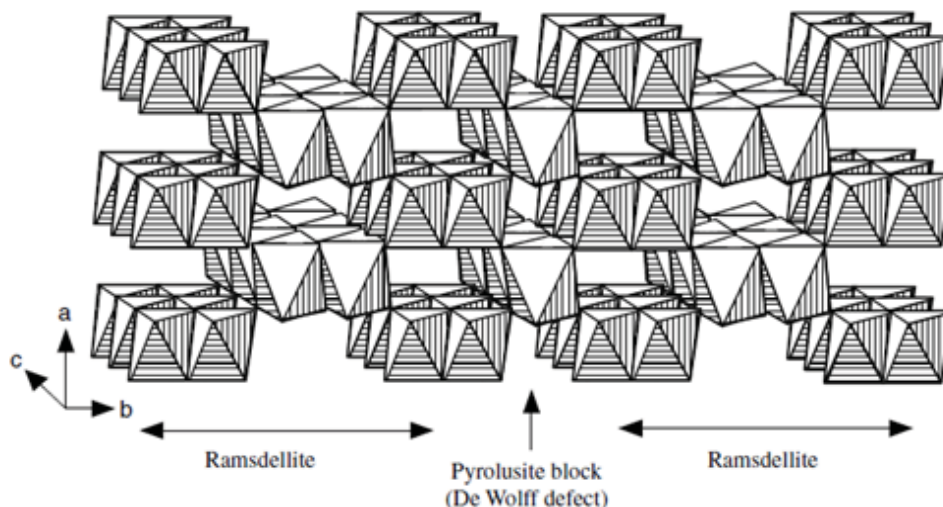


Figure 70. Representation of $\gamma$-MnO$_2$, pyrolusite (i.e., De Wolff defects) in ramsdellite matrix; a highly porous matrix with high roughness factor [2].

XRD, as seen in Figure 71. SEM of Delta EMD shows a relatively heterogenous material, with a wide size distribution. The effect of pressure (2 to 2.5 tons/in$^2$) during pellet formation on the shape and size of the MnO$_2$ is unknown.

5.3.1.2 In Batteries

In comparison to supercapacitors prepared with MnO$_2$ electrodes, morphology plays a much more substantial role in MnO$_2$ based alkaline batteries. In alkaline batteries, when MnO$_2$ undergoes a reduction, as in reaction 67, the MnO$_2$ is reduced to $\delta-$MnOOH. This $\delta-$MnOOH is an intergrowth as well, of groutite and maganite. A second morphological change during the reduction transforms $\delta-$MnOOH to Mn(OH)$_2$ that yields $\delta-$MnO$_2$, which ultimately ends up as Mn$_3$O$_4$. Mn$_3$O$_4$ cannot
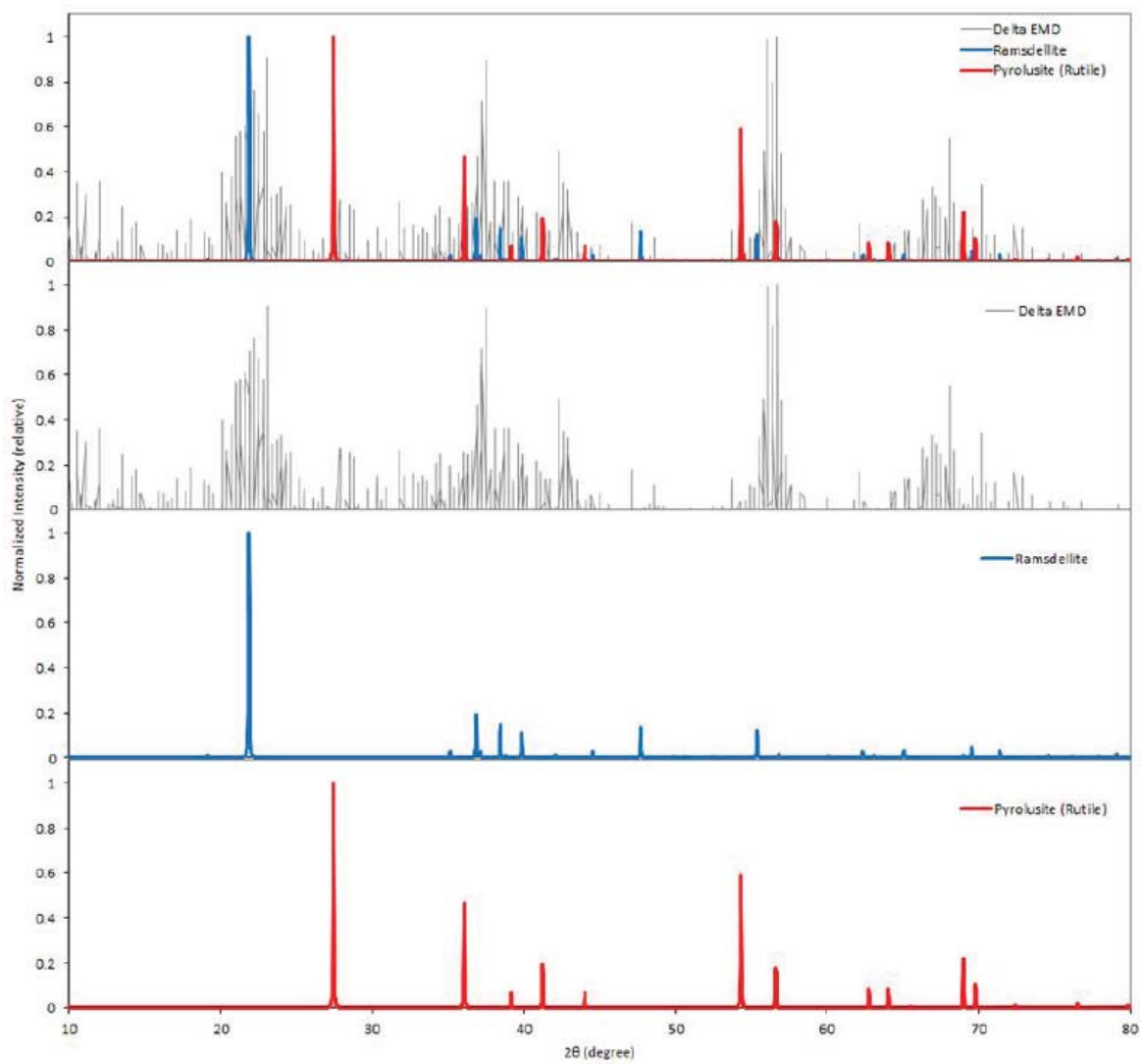
Figure 71. Powder XRD of Delta EMD ($\gamma-\mathrm{MnO_2}$) with reference spectra.
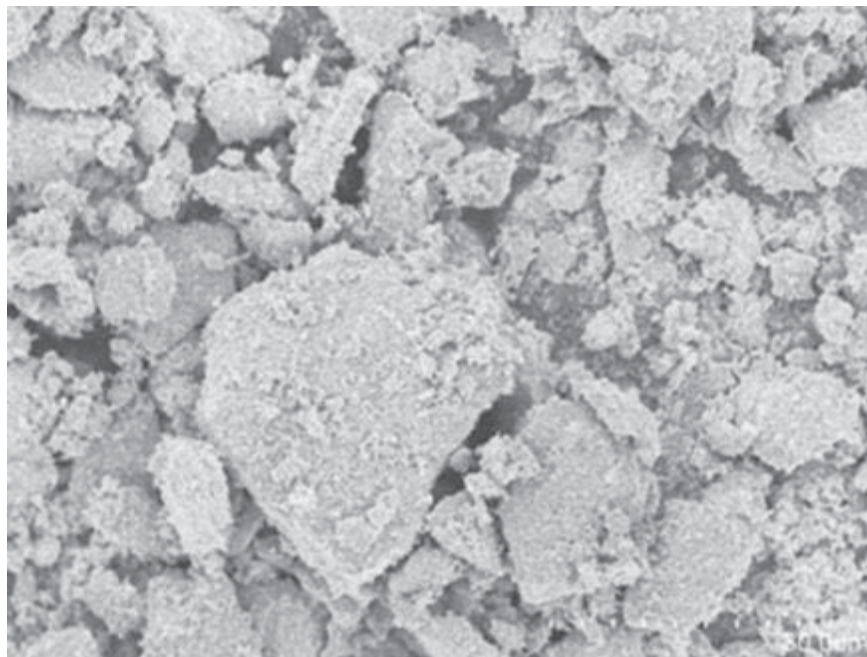
Figure 72. SEM image of untreated Delta EMD ($\gamma$-MnO$_2$). Scale bar is 30 microns.

be oxidized (recharged); recycling of the system produces oxides (e.g., Mn(OH)$_2$) which reduce electrochemical performance [15]. In supercapacitors, the application of the MnO$_2$ as an electrode is fundamentally different. The material does not undergo these morphological changes, and therefore cycling tens to hundreds of thousands of times is possible.

## 5.3.2 Chronopotentiometry

Chronopotentiometry, a galvanostatic measurement, is the principal evaluation methods used here. In chronopotentiometry, a constant current is applied to the

electrode and the potential (V) varies as a function of time,

$$E = iR_s + \frac{i}{C} \int_o^t dt \tag{70}$$

A variety of current loads were tested: 1, 2.5, 4 and 5 mA. These current were selected based upon the restrictions imposed by the pellet-shaped electrodes dimensions, and are limited on the upper end by film thickness. At 200 to 300 $\mu$m for instance, considerable internal (or Ohmic) resistance is present. At high current loads ($> 10$ mA), the magnitude of the Ohmic drop is substantial. In literature, thin films of 25 nm $<$ MnO$_2$ $<$ 100 $\mu$m are prepared on metal (e.g., Ti) grids that produce little Ohmic drop [21, 58, 59, 61]. (Initial studies on metal grids have shown promising results.) Though data is not presented here for thin films, the effects of magnetic field should not be dependent upon pellet architecture. That is, the electrodes tested here (at 200 to 300 $\mu$m thickness) show considerable, statistical enhancement to magnetic field effects, and that enhancement should be present in thinner electrode systems and at higher current densities.

Cyclic voltammetry is also used for electrode characterization. CV's of capacitors produce solvent envelopes, as previously mentioned. Determining capacitance from a voltammetric measurement is straightforward [19]. When there is a buildup of charge, capacitance is defined as

$$C = \frac{dQ}{dV} \tag{71}$$

From Gauss's law equation 72, we are able to the calculate capacitance of our

system,

$$i = \frac{dQ}{dt} \tag{72}$$

Substitution of equation 71 into equation 72 gives

$$i = C\frac{dV}{dt} = Cv \tag{73}$$

where $v$ is scan rate. Rearrangement of equation 73 allows determination of capacitance from current and scan rate. Capacitance can be normalized by mass of active material.

$$C = \frac{i}{v} \tag{74}$$

However the nature of the $MnO_2$ capacitance system complicates extraction and differentiation of faradaic capacitance from nonfaradaic capacitance. For this reason, CV is primarily used as a qualitative assessment of electrode capacitance.

### 5.3.3  Electrochemical Evaluation

Here, the electrochemical evaluation of the capacitance of $MnO_2$ electrodes is presented.

### 5.3.3.1  Electrochemical Response as a Function of Potential Window

As was mentioned in the introduction of this Chapter, $MnO_2$ is a material common to both batteries and electrochemical capacitors. Even though these two applications are similar, there exists fundamental differences in the functioning of $MnO_2$ in these applications. Two importants differences are the electrolyte, and the potential window of the system. When $MnO_2$ is used in alkaline batteries, battery discharge

occurs over a much wider potential window than in capacitors. This window includes the two electron discharge in the alkaline system, two different regimes are observed [15]. A second difference is the electrolyte solution. In capacitors, the electrolyte is a mild aqueous solution (e.g., $CaCl_2$,KCl). To emphasize this difference, Figure 73, displays the electrochemical response of $MnO_2$ electrodes in 0.1 M $CaCl_2$, discharged to -0.6 V (vs. Ag|AgCl). In the Figure are representative charge/discharge curves of a control electrode (75% $MnO_2$), and a magnetically modified electrode (5% $SmCo_5$, 70% $MnO_2$). The x-axis in the discharge curve is charge density, where charge density, in coulombs/gram $MnO_2$ is converted from discharge time by equation 75

$$Ch\arg e\ Density\ (Cg^{-1}) = \frac{time(s) \cdot current(A)}{MnO_2(g)} \tag{75}$$

In contrast to alkaline batteries, this system is high cyclable (> 10,000 cycles). However, the working potential range for capacitors is only between approximately 0.9 and -0.1 V (vs. Ag|AgCl), the first discharge regime in Figure 73. Capacitance is extracted from the linear region between 0.9 and -0.1 V as described in the previous section.

### 5.3.3.2 Capacitance of Thin Pellets Electrodes

Over a series of trials, an electrode pellet architecture was optimized at thicknesses ranging from 200 to 300 $\mu$m. These pellets are formed in a pellet dye (internal diameter ˜8 mm), by pressing approximately 40 mg of pellet mixture to 2.5 tons/in$^2$ for 1 minute. This pressure is less than Bélanger, et. al at 900 MPa [21]. However, the pellets made here are mechanically stable. Higher pressures tend to damage
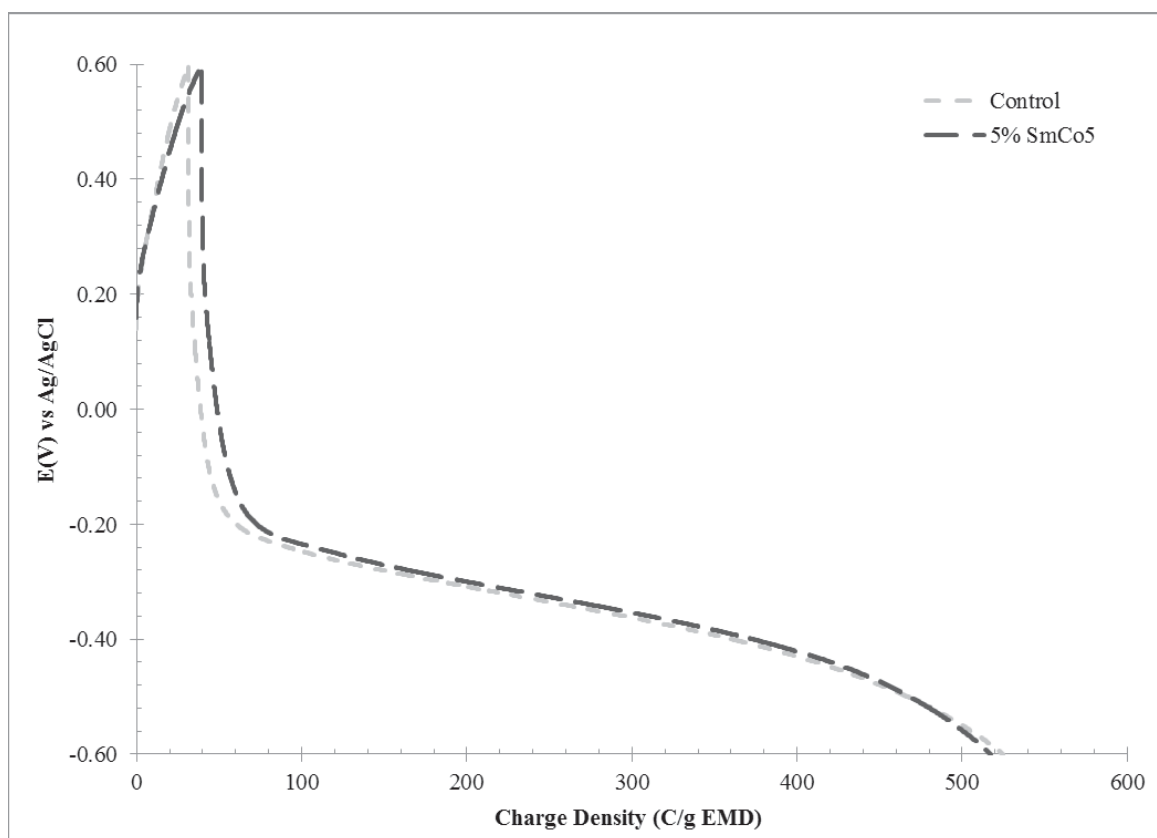
Figure 73. Representative 1.2 V charge/discharge curve for $MnO_2$ electrodes in 0.1 M $CaCl_{2(aq)}$ electrolyte.

the pellet dyes. 200 to 300 $\mu$m pellets are consistent in shape and appearance. Attempts to create thinner pellets result in unstable films and inconsistent pellet shapes. The final pellets are approximately 35 mg (the exact mass is determined after pressing). Capacitance is normalized for mass $MnO_2$ and therefore precise values are necessary. Loss of pellet mixture in the dye occurs, therefore measuring pellet mass post-pressing is necessary.

Optimized electrochemical performance and pellet stability were observed in control electrodes that contain 20 % carbon (graphite) (w/w). At 20 % graphite, control electrodes then contain 75 % $MnO_2$ (w/w), 20 % graphite (w/w), and 5 % binder (PTFE) (w/w). Alternative mixtures that contain acetylene black or other carbon black derivatives that are found in literature [62] were attempted, as these alternative components may be responsible for decreased internal resistance. However, electrodes prepared here with acetylene black and alternative binders (e.g., Kynar, PVDF) never were mechanically stable. Additionally, literature preparation methods consider extremely high pressures (900 MPa) for film formation. When these preparation methods were attempted, unstable films with inconsistent shape were formed. Mixtures for magnetically modified electrodes are described below.

### 5.3.4   Data Analysis

The half cell electrodes tested here are examined over an adjusted potential range similar to a conventional capacitance window that ranges between approximately 0.9 and -0.1 V vs. Ag|AgCl [21]. For whole cell applications, the voltage window is expanded with a the counter electrode (or anode) of activated carbon. The activated

carbon electrode operates over a range of -0.2 to -1.3 V vs Ag|AgCl. This gives a

complete cell potential in aqueous electrolyte of approximately 2.2 V. As $E_{cell} =$

$E_+ + E_-$. However, for electrochemical evaluations here, the $MnO_2$ electrodes are

cycled over the range of -0.2 V to 0.65 V vs. Ag|AgCl. This gives a linear responses

between -0.2 and 0.5 V. The linear range is seen in Figure 74 and is emphasized with

a red line. High ohmic drop between 0.65 and 0.5 V is present, while linearity at
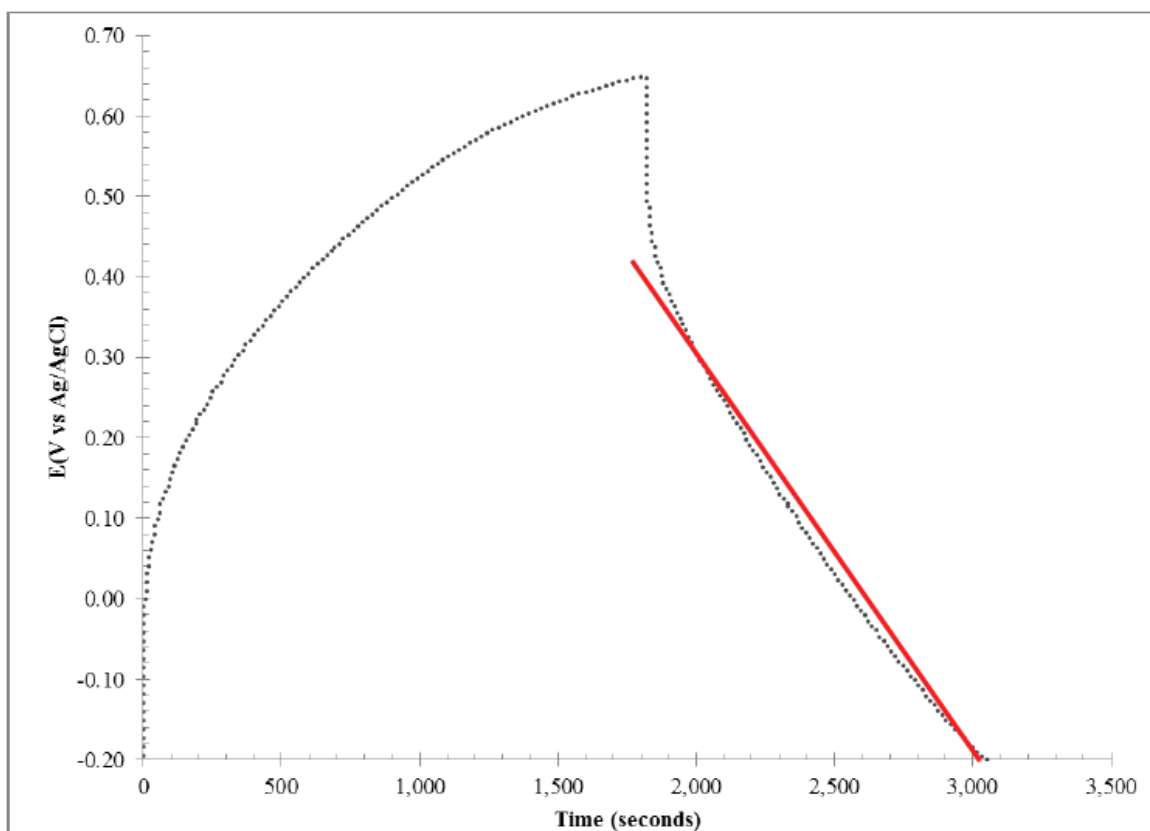


Figure 74. Representative charge/discharge curve for thin film (200 to 300 $\mu$m) $MnO_2$ electrodes. The charge/discharge region is the same as the first regime in Figure 73. The slope of the curve in red is used to extract capacitance as described above.

lower potentials may be a result of reference electrode calibration. Pellet architecture

restricts evaluation at higher potentials. Electrodes are cycled between 5 and 10

cycles before evaluation, cycling produces a consistent electrochemical response.

Figure 74 shows a representative chronoamperometric curve from which capacitant

data is extracted. The capacitance is extracted from linear region of the discharge.

A linear fit is performed on the discharge region, over an approximate 0.65 V range,

Ohmic drop prevents fitting to higher potentials. Over this 0.65 V range, correlation

coefficients average between $0.95 < R^2 < 0.98$. From the linear fit, a fitting curve of

the form $y = mx + b$ is produced. From the fitting curve, the slope m capacitance

is determined as

$$m = \frac{dV}{dt} \tag{76}$$

Therefore, dividing the defined current density by the slope gives capacitance

$$\frac{i}{m} = \frac{i}{\frac{dV}{dt}} = C \tag{77}$$

This is in agreement with Equation 73. By convention, the capcitance is then

normalized for mass of active matieral (i.e., $MnO_2$). In the case of these films, this

number ranges between 100 to 200 F/g $MnO_2$ for powder based electrodes [21]. Our

measured capacitances are approaching literature values. As mechanically stability

increases, our measured values for normalized capacitance will increase accordingly.

More importantly, however, is the increased capacitance and increased normalized

capacitance seen in magnetically modified electrodes, as will be seen in the next

section.

5.3.4.1 Optimized Magnetic Particle Loadings

Magnetically modified electrodes were examined with $SmCo_5$ microparticles. The loading of magnetic particles in pellet mixtures replaces $MnO_2$ in the mixture, that is, 5 % $SmCo_5$ (w/w) mixtures contain 70 % $MnO_2$ (w/w), 10 % $SmCo_5$ (w/w) mixtures contain 65 % $MnO_2$ (w/w), and 15 % $SmCo_5$ (w/w) mixtures contain 60 % $MnO_2$ (w/w). Accurate pellet massing is essential for normalizing capacitance by mass of active $MnO_2$ material. Magnetically modified electrodes are magnetized with a NdFeB ring magnet after the pellets are pressed; pressed electrodes are suspended within a weigh boat for 30 seconds in the center of the magnet.

5.3.5  Evaluations of Magnetically Modified $MnO_2$
       Electrodes

Two primary evaluations were conducted here. First, the effect of magnetic content on the capacitance on $MnO_2$ electrodes. And second, the effect of charge/discharge currents on magnetically modified thin pellet $MnO_2$ electrodes. These two evaluation were tested concurrently and will be presented together. For each evaluation, a series of electrodes were fabricated, both a control (0 % $SmCo_5$) and a magnetically modified batch. These electrodes were tested as replicate electrodes, the degrees of freedom are given below.

5.3.5.1 The Effects of Chronoamperometric Currents on Capacitance and
        Electrochemical Performance

External current demand was observed to directly affect the performance of the

$MnO_2$ electrodes. Electrochemical performance worsened at higher currents, with increasing ohmic drop at higher currents and lower capacitances. Kinetically this makes sense. At higher currents demands, increased electron conduction within the electrode needs to occur to satisfy the current demands of the potentiostat. However, the electrodes are apprpoximately 200 to 300 $\mu$m thick, and even though they contain 20 % conductive graphite (higher than the minimum percolation limit), substantial internal resistance is observed with currents increase above 1 mA. Figure 75 shows representative charge/discharge curves for unmodified and 5% $SmCo_5$ modified electrodes at 1 mA, 2.5 mA, and 4 mA current demand. These electrodes were evaluated between 0.6 and -0.2 V vs. Ag|AgCl. Statistical analysis of the capacitances of unmodifed and all modified (5, 10 and 15 % $SmCo_5$) electrodes are given below. Charge/discharge curves allow for qualitative assesment of electrochemical performance, however, quantitative analysis of the linear discharge region is not visually apparent and therefore these curves are not included throughout.

As can be seen in Figure 75, increasing currents results in increasing ohmic drop. An analysis on ohmic drop was conducted to determine if magnetic modification affects iR drop. Control electrodes and 5 % $SmCo_5$ modified electrodes were analyzed. Because the magnetic particles are uncoated, it may be assumed that modified pellets would have lower ohmic resistance, as the magnetic particles themselves are conductive. However, as is seen from the following data, magnetic microparticles of SmCo5 do not significantly lower ohmic resistance. To extract
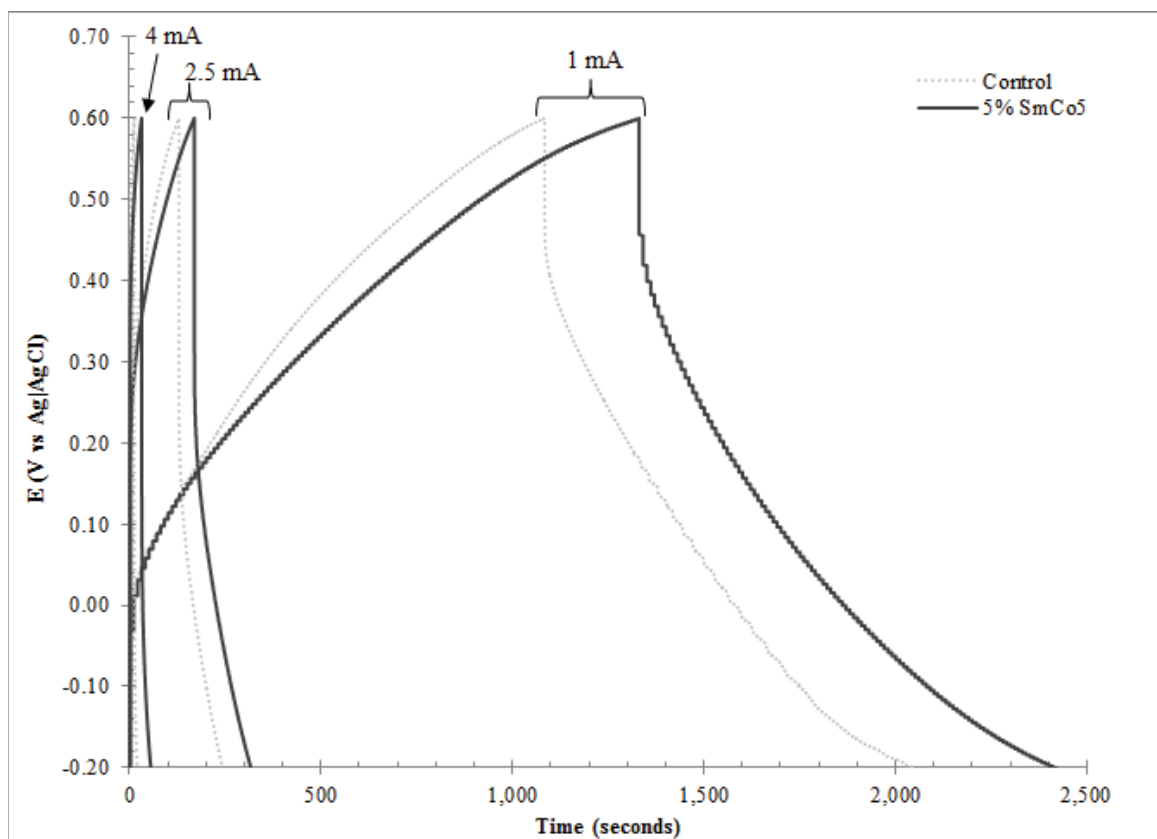
Figure 75. Represenstative charge/discharge curves for unmodified and 5 % SmCo$_5$ modified MnO$_2$ electrodes. Curves for chronoamperometric cycling at 1, 2.5, and 4 mA are shown and indicated.

Table 17. Ohmic drop data for unmodified and 5 % modified EMD electrodes.

| Current (mA) | $1/i$ (A$^{-1}$) | $1/E_{drop}$ (V$^{-1}$) (Control) | $1/E_{drop}$ (V$^{-1}$) (5 % SmCo$_5$) |
|---|---|---|---|
| 1 | 1000 | 8.69 ($\pm$ 5 %) | 8.99 ($\pm$ 9 %) |
| 2.5 | 400 | 3.22 ($\pm$ 12 %) | 3.59 ($\pm$ 8 %) |
| 4 | 250 | 1.95 ($\pm$ 11 %) | 2.22 ($\pm$ 5 %) |
| 5 | 200 | 1.53 ($\pm$ 11 %) | 81.84 ($\pm$ 8 %) |

resistance from the following data, we apply Ohm's law.

$$V = iR \tag{78}$$

Where voltage, V, is equal to the sum of current, i, times resistance, R. From equation 78 rearrangement gives resistance.

$$R = \frac{V}{i} \tag{79}$$

We can use the inverse of equation 79 to extract resistance from a double reciprocal plot of voltage drop versus current. Table 17 gives the values of $1/E_{drop}$ (V$^{-1}$) versus $1/i$ (A$^{-1}$) for control and 5 % SmCo$_5$ modified electrodes, for n = 3 electrodes. The values in Table 17 are shown in Figure. Figure 76 is a double reciprocal plot of the data. 76.

The linear fit for unmodified electrodes returns y = 9 x 10$^{-3}$x - 0.3026, R$^2$ = 0.9998, while for 5 % SmCo$_5$ electrodes, y = 9 x 10$^{-3}$x + 0.0105, R$^2$ = 0.9999. Using the form y = mx + b, the slope m = R$^{-1}$, where resistance is then the inverse of the slope. The slope for both unmodified and 5 % SmCo$_5$ modified electrodes returns a resistance of 111 $\Omega$ , with no significant difference. However, it is interesting to note that the intercepts differ by a value of V$^{-1}$ = 0.313. The implications of this are
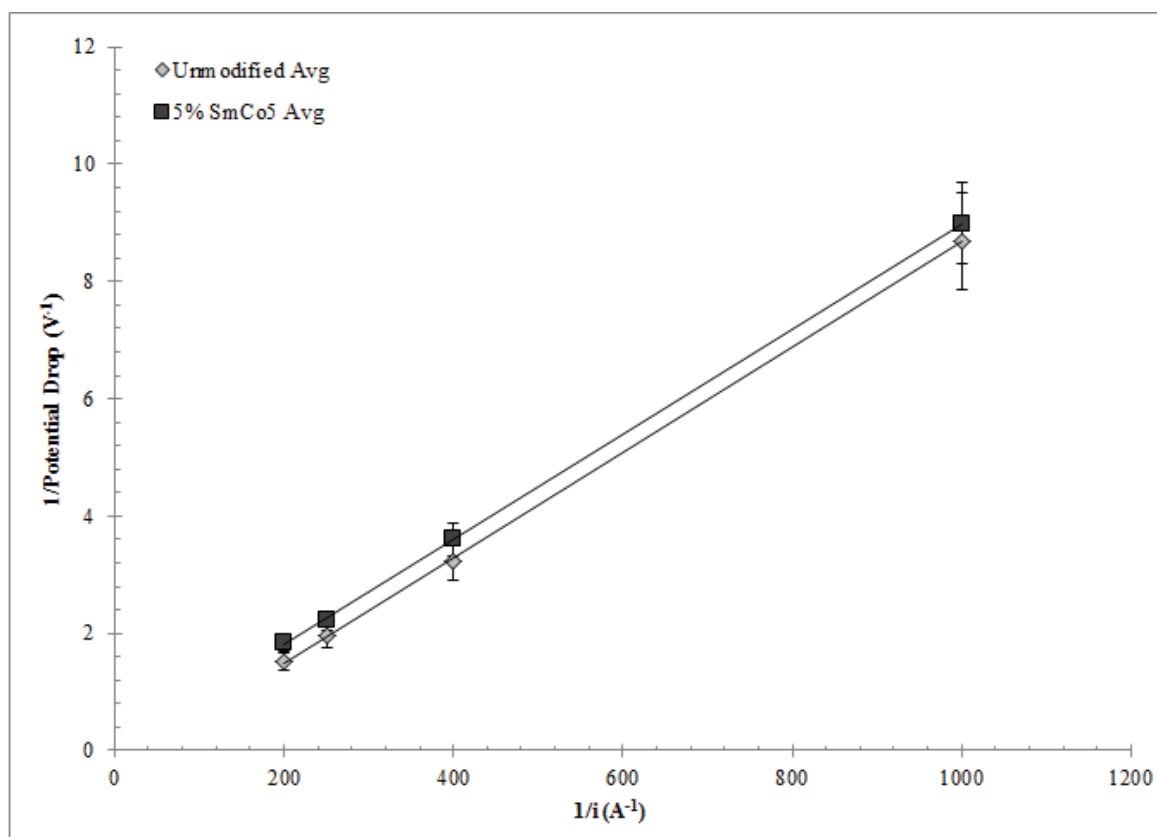
Figure 76. A double reciprocal plot of $1/E_{drop}$ ($E^{-1}$) vs. $1/i$ ($A^{-1}$) for control and 5 % SmCo$_5$ modified electrodes. Each point is an average of n = 3 for each electrode modification.

unknown. However, our observations in Chapter 2 show that magnetic fields have an impact on both the homogeneous and heterogeneous electron transfer event. The faradaic charge transfer was observed to be substantially less at modified electrodes examined by electrochemical impedance spectroscopy. This difference in ohmic drop may be a result of increased kinetic facility of the electron transfer, possibly homogeneous or heterogeneous.

Electrodes were examined at 1, 2.5, 4, and 5 mA cycling currents at $SmCo_5$ loadings of 0, 5, 10 and 15 %. An analysis of the chronopotentiometric data follows. 5 % $SmCo_5$ modified electrodes were cycled between 0.6 and -0.2 V vs Ag|AgCl. Electrodes modified with 10 % and 15 % $SmCo_5$ were cycled between 0.65 and -0.2 V vs. Ag|AgCl. Control electrodes were prepared with each batch of modified electrodes and were prepared and tested concurrently with modified electrodes. No differences in the discharge slopes were observed when the high potential was increased to 0.65 V, only increased ohmic drop. Therefore, the values of capacitance for unmodified electrodes was pooled. Figure 77 gives normalized capacitance (primary vertical axis) and capacitance (secondary vertical axis) for electrodes operating at 1 mA. For 1 mA charging/discharging current, Table 18 gives a table of values for capacitance, normalized capacitance, deviations and statistics. At 1 mA, the lowest ohmic drop values are observed as are the highest values of capacitance. Error bars are not included for absolute capacitance as they are the same relative percent error.

Increased normalized capacitance is seen at all loadings, with significant differences as high as the 99% confidence level (CL) for 15% $SmCo_5$ loadings. From

Figure 77. Chart of capacitance (F, ■) and normalized capacitance (F/g, ●) as a function of SmCo$_5$ loading percentage at 1 mA charging/discharging current.

Table 18. Discharge statistics for 1 mA chronopotentiometric analysis.

| SmCo$_5$ Loading | Cap. (F) | Cap. (F/g MnO$_2$) | Enhancement | S$_{pooled}$ | T$_{calc}$ | Difference |
|---|---|---|---|---|---|---|
| 0% (n = 10) | 1.5$_8$ (± 27 %) | 54.$_1$ (± 26 %) | | | | |
| 5% (n = 9) | 1.9 (± 16 %) | 67.$_9$ (±11 %) | 23 % | 10.238 | 2.250 | 95 % CL |
| 10% (n =6) | 2.2$_8$ (±23 %) | 80.$_6$ (± 22 %) | 58 % | 14.895 | 3.398 | 98 % CL |
| 15% (n = 7) | 1.8 (± 11 %) | 75.$_7$ (± 10 %) | 49 % | 10.087 | 5.251 | 99 % CL |

the optimization data, 10% loadings return the greatest capacitance at low currents, however, these loadings also experience the greatest relative standard deviations. At 2.5 mA, increased capacitance is still seen in modified electrodes. However, the
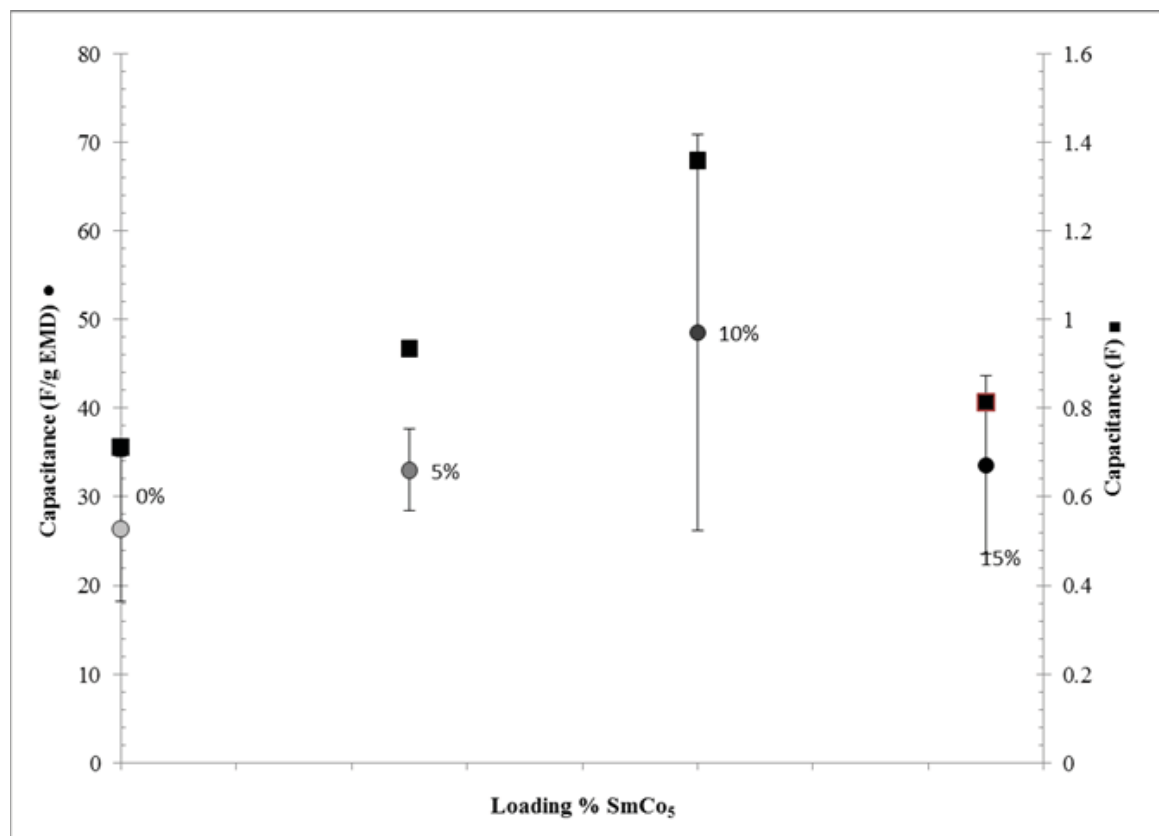


Figure 78. Chart of capacitance (F, ■) and normalized capacitance (F/g, ●) as a function of $SmCo_5$ loading percentage at 2.5 mA charging/discharging current.

relative enhancement as well as the standard deviations of capacitance increases at increasing currents, as is seen in Table 19.

Decreased capacitance and increased standard deviations in capacitance and normalized capacitance continues at higher charging and discharging current. Most likely the manifestation of thick $MnO_2$ layers - also reflected in increasing Ohmic

Table 19. Discharge statistics for 2.5 mA chronopotentiometric analysis.

| $SmCo_5$ Loading | Cap. (F) | Cap. (F/g $MnO_2$) | Enhancement | $S_{pooled}$ | $T_{calc}$ | Difference |
|---|---|---|---|---|---|---|
| 0% (n = 10) | 0.7 (± 44%) | 26.$_4$ (± 31 %) | | | | |
| 5% (n = 9) | 0.9$_4$ (± 19%) | 33 (± 14 %) | 25 % | 6.670 | 2.417 | 96 % CL |
| 10% (n =6) | 1.$_4$ (± 50%) | 48.$_6$ (± 46 %) | 84 % | 15.612 | 2.651 | 95 % CL |
| 15% (n = 7) | 0.8 (± 31%) | 33.$_6$ (± 31 %) | 27 % | 7.570 | 2.086 | 92 % CL |

Table 20. Discharge statistics for 4 mA chronopotentiometric analysis.

| $SmCo_5$ Loading | Cap. (F) | Cap. (F/g $MnO_2$) | Enhancement | $S_{pooled}$ | $T_{calc}$ | Difference |
|---|---|---|---|---|---|---|
| 0% (n = 10) | 0.2$_9$ (± 64 %) | 10 (± 67 %) | | | | |
| 5% (n = 9) | 0.4 (± 42 %) | 14 (± 41 %) | 44 % | 6.225 | 0.943 | 63 % CL |
| 10% (n =6) | 0.2 (± 78 %) | 8 (± 81 %) | -25 % | 6.490 | 0.460 | N/A |
| 15% (n = 7) | 0.3 (± 52 %) | 12 (± 31 %) | 18 % | 5.435 | 0.895 | 60 % CL |

drop at higher currents. This trending is apparent in Figure 79, and the table of values for 4 mA (Table 20) and 5 mA (Table 21) cycling currents.

Capacitance was analyzed by two methods, absolute capacitance (F/ electrode) and normalized capacitance (F/ g $MnO_2$ per electrode). General patterns appear in magnetically modified electrodes versus the unmodified system. Most striking are the 10 % $SmCo_5$ modified electrodes. At both 1 and 2.5 mA cycling currents, the 10 % $SmCo_5$ modified electrodes show that greatest increase in normalized capcitance (F/ g $MnO_2$). This enhancement is as much as 84 % at 2.5 mA. The 10 % modified electrodes also show increased absolute capacitance at 1 and 2.5 mA.

Table 21. Discharge statistics for 5 mA chronopotentiometric analysis.

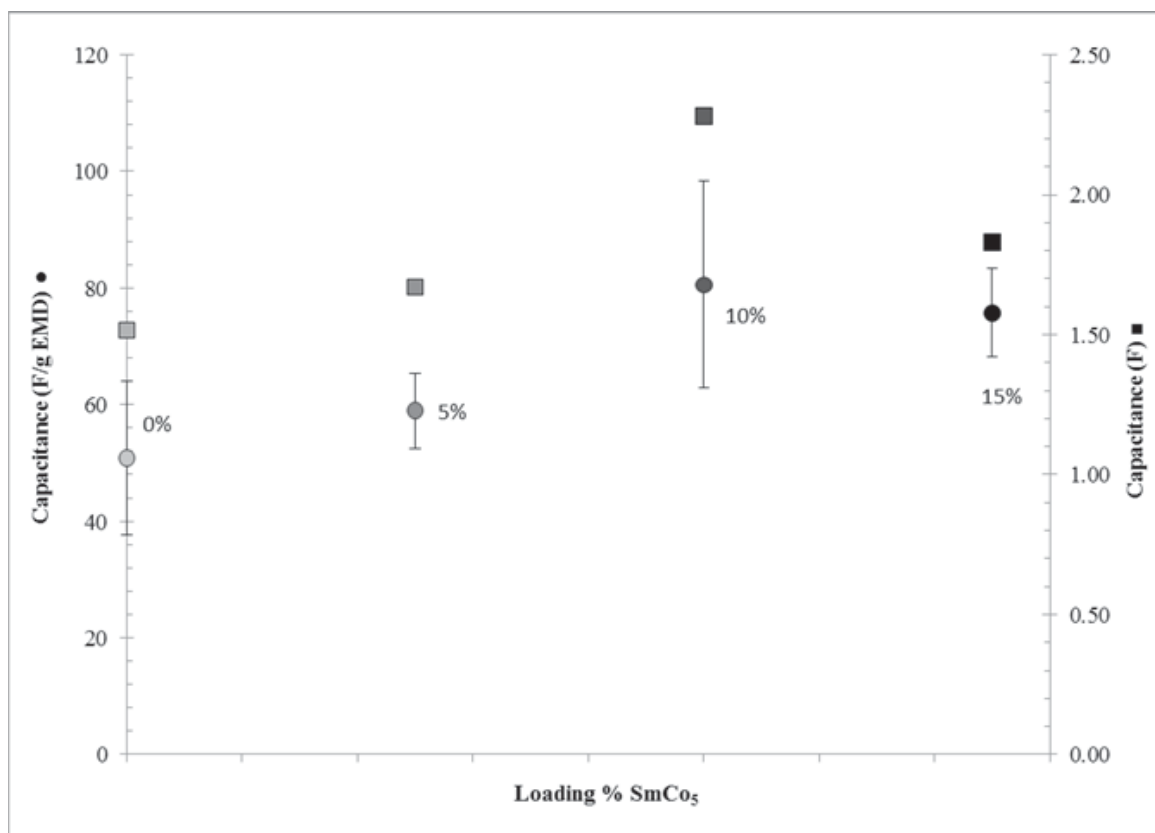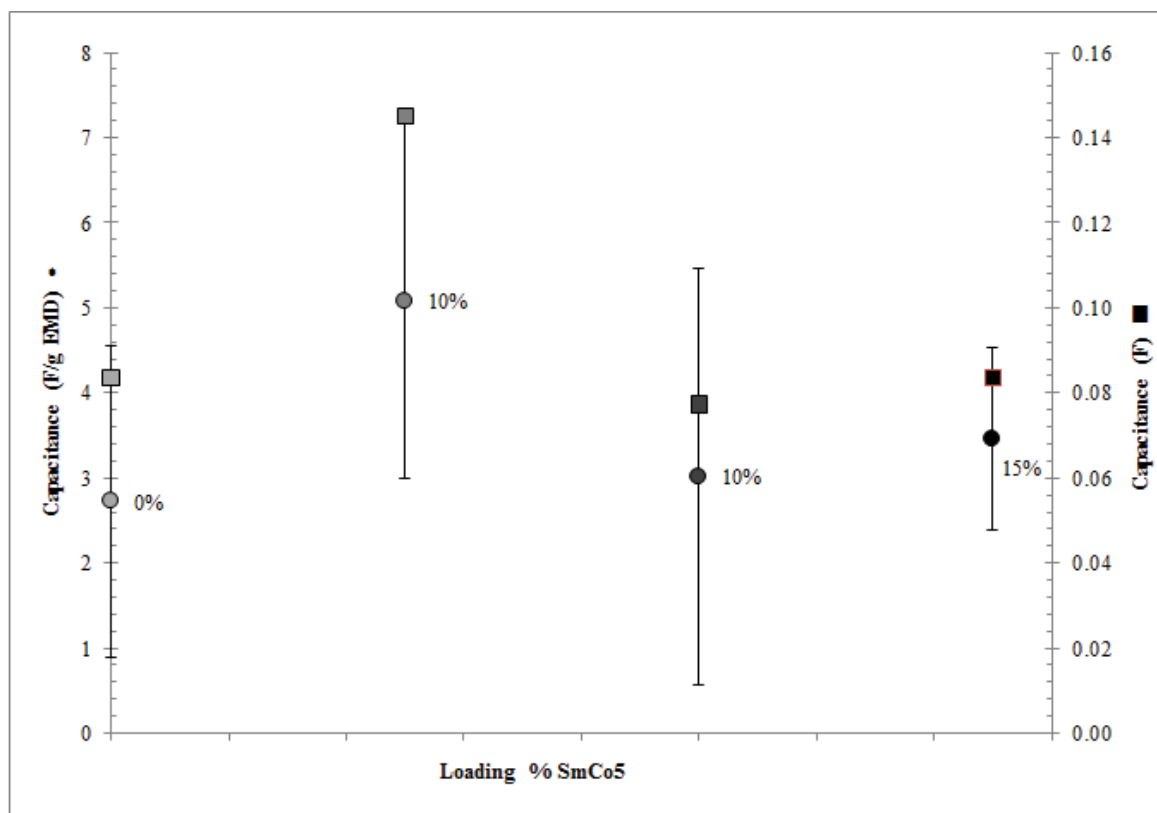| $SmCo_5$ Loading | Cap. (F) | Cap. (F/g $MnO_2$) | Enhancement | $S_{pooled}$ | $T_{calc}$ | Difference |
|---|---|---|---|---|---|---|
| 0% (n = 10) | 0.08 (± 100 %) | 2.$_8$ (± 106%) | | | | |
| 5% (n = 9) | 0.1$_5$ (± 61%) | 5.$_1$ (± 66%) | 78 % | 3.218 | 1.153 | 72 % CL |
| 10% (n =6) | 0.08 (± 123 %) | 3 (± 131%) | 6 % | 3.363 | 0.148 | N/A |
| 15% (n = 7) | 0.08 (± 84 %) | 3.$_5$ (± 85%) | 21 % | 2.513 | 0.618 | N/A |

Figure 79. Chart of capcitance (F, ■) and normalized capacitance (F/g, ●) as a function of SmCo$_5$ loading percentage at 4 mA charging/discharging current.

However, as cycling currents increases so to does the relative standard deviation of capacitance. At even higher current, the 10 % SmCo$_5$ modified electrodes no longer appear to be the ideal loading, with negative performance at 4 mA and no difference in performance at 5 mA. It is unclear whether magnetic enhancement is ineffective at higher currents system, or the electrochemical properties of the modified systems break down at higher currents.

Enhancement in normalized capacitance does persist in both the 5 % and 15 % modified electrodes throughout all cycling currents. For 5 % SmCo$_5$ modified electrodes, absolute capacitance is greater for all electrodes. Enhancements of 78 % are observed at 5 mA, but so too are increased deviation (66 %). At lower currents, 2.5 mA, the enhancement is less substantial but the significance in the measurement increases. 15 % SmCo$_5$ modified electrodes perform similarly. Enhancement in the capacitance is less at lower currents, but the confidence in the measurement and difference from the controls is greater. Given these observations, 10 % SmCo$_5$ modified electrodes may seem optimized. However, given the enhancements at 5 and 15 % loadings, the choice is less certain. Absolute capacitance may be the deciding factor, which would make 5 % SmCo$_5$ modified electrodes the optimum loading.

The linear region analyzed for capacitance falls between 0.5 and -0.2 V vs Ag|AgCl. This value is slightly shifted from literature [21], possibly from reference electrode drift. Also, this region is narrower due to high ohmic resistance. In an effort to further illustrate and present the data in Tables 18 through 21, average discharge curves over this linear capacitance region are seen in Figure 80. It is these slope from which capacitance is extracted; a shallower slope has higher capacitance.
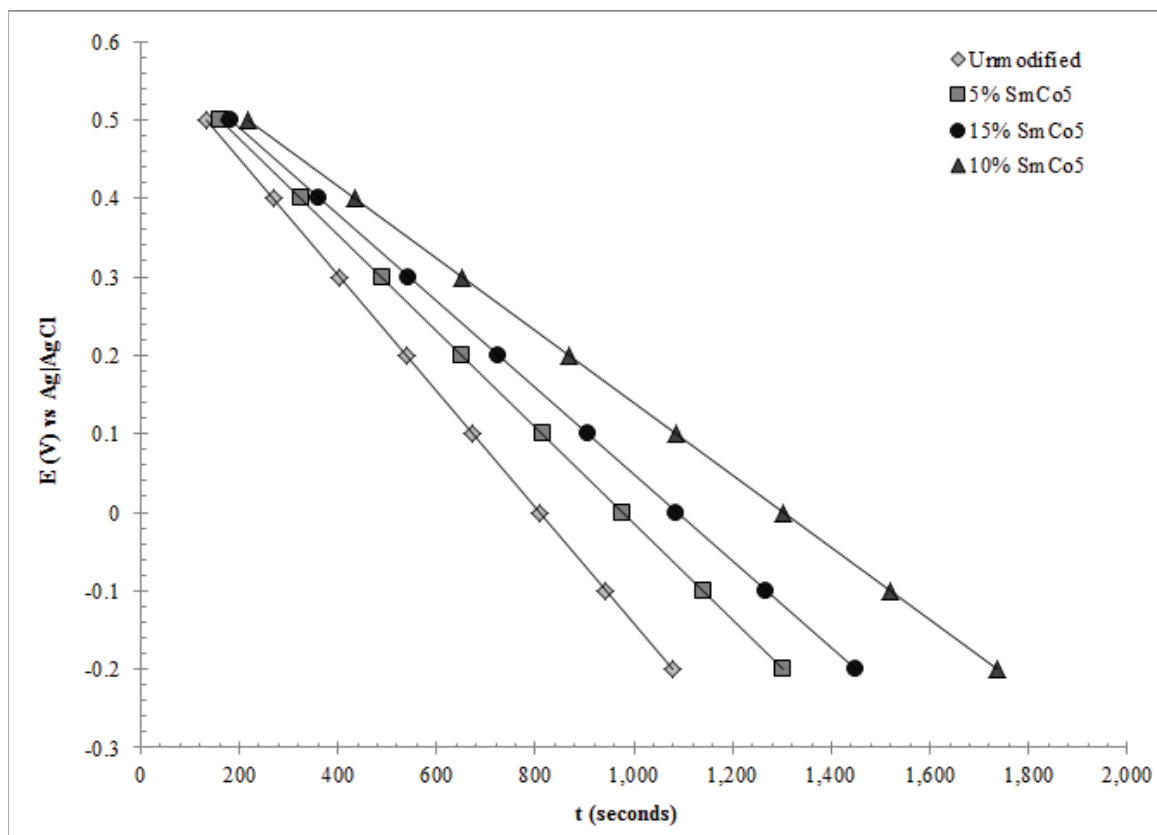
Figure 80. Comparison of discharge curves for 1 mA cycling of the linear region for control, 5, 10 and 15 % SmCo$_5$ modified MnO$_2$ electrodes. Error in discharge slope can be referred to in Tables 18 through 21.

For clarity, the error associated with these curves is not shown in Figure 80 but can be found in Tables 18 through 21.

5.3.5.2  Improving normalized capacitance with electrodes on stainless
            steel mesh substrates

To increase the normalized capacitance of the capacitor electrodes, and to decrease the ohmic resistance, thin film electrodes are desired. As per literature preparation, increased normalized capacitance is seen for modified electrodes prepared on

substrates. The substrate, typically metal mesh or foil, increases mechanical stability and decreases resistance. A preliminary electrode preparation procedure used high grade stainless steel mesh (316, 70 x 70, McMaster-Carr) as a substrate for electrodes. The electrodes are prepared by combining a pre-cut mesh (diameter = 5/16 inch) into the pellet dye along with approximately 25 mg electrode mixture. The electrodes are presses to 2.5 tons for 1 minute. This results in electrodes with final masses (less the stainless mesh) of 20 mg, $\sim$40 mg $MnO_2$/cm$^2$. This value is still three times greater than literature [63].

These thin film electrodes are cycled at least 20 times (Figure 81) before evaluation in order to stabilize the electrochemical response. Thinner films experience less Ohmic drop ($\sim$50 mV) than the 200 to 300 $\mu$m thick pellet-architecture electrodes. A capacitance of 2.09 F is observed for unmodified control electrodes. Additionally, due to the decreased amount of active material (10 mg versus 25 mg), a higher normalized capacitance is observed, 181.8 F/gram $MnO_2$.

Thin film electrodes tested here, however, are not without fault. Due to the corrosive nature of the $CaCl_{2(aq)}$ solution used, the stainless steel mesh experienced corrosion after two days of cycling. This corrosion was accelerated in the electrodes modified with $SmCo_5$. In fact, corrosion was so rapid in modified electrodes, no capacitance data was collected. Also, the corrosion was so prominent that there is no statistical data for unmodified electrodes and n = 1.

### 5.3.6   Conclusions

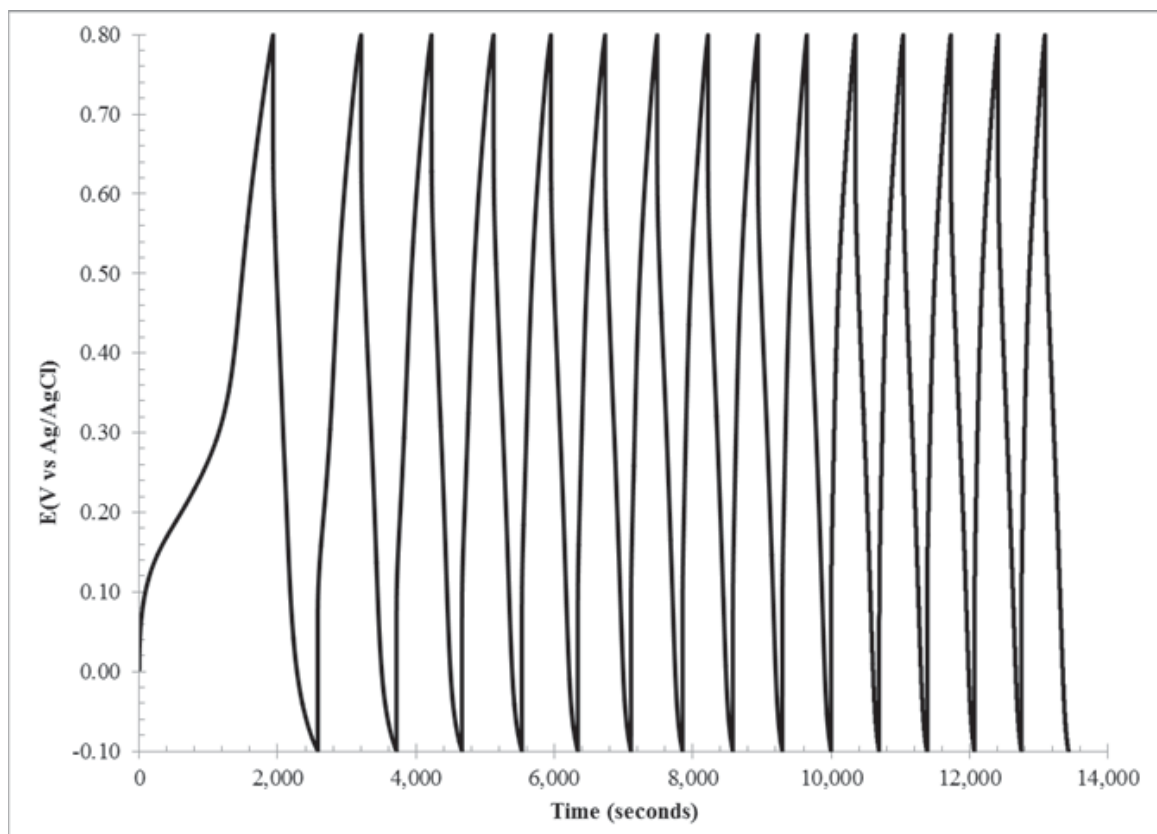Enhancements in absolute and normalized capacitance are seen in magnetically

Figure 81. Thin layer electrode cycling in 0.1M $CaCl_{2(aq)}$ solution.

modified thin pellet $MnO_2$ electrodes. These $MnO_2$ electrodes contain electrolytic manganese dioxide (EMD), a biphase $MnO_2$ material. Substantial electrochemical capacitor research focuses on the electrode materials and morphology and attempts to optimize capacitance based on these factors. Here however we are concerned with enhancing capacitance though magnetic modification.

Past magnetic modification of the similar, yet fundamentally different, alkaline battery systems has shown increases in system performance and cyclability [15]. This work applied magnetic field effects to another system, and again saw increased system performance. Increased capcitance was observed at a variety of $SmCo_5$ loadings and chronoamperometric cycling currents.These enhancements have been optimized based on particle loading, and are statistically vetted and relevant. Conduction in $MnO_2$ is theorized to occur through electron hopping [13, 15]. An increase in electron conduction may be one reason for enhancement, however, the results seen in Chapter 2 would suggest that enhancement is also occurring due to increased heterogeneous electron transfer kinetics. To belabor the point, EIS data collected at modified solid state electrodes shows both a decrease in $R_{CT}$ and an increase in $C_F$ in modified versus unmodified electrodes, both possible mechanisms for enhancement.

CHAPTER 6

CONCLUSIONS AND FUTURE DIRECTIONS

Magnetic fields, incorporated as magnetic microparticles at solid state electrodes, in Grätzel cells, and in $MnO_2$ electrodes were shown to positively enhance electrochemical performance. At modified electrodes, increased values for the heterogeneous rate constant, $k^0$ were calculated. In Grätzel cells, increased power output and photoconversion efficiencies were measured. While at $MnO_2$ electrodes utilized as electrochemical capacitors, increased capacitance was shown over a range of current densities and magnetic loadings. These are all examples of systems enhanced by magnetoelectrocatalysis. These systems also demonstrate that magnets can affect the capture, conversion, and storage mechanisms that are required to utilize efficiently renewable energy sources.

These analyses demonstrated enhancements that are statistically vetted in each systems. However, these measurements were for relatively few samples and over a short time period. The longevity of these effects and possibly prototyping will be prudent to further support arguments for magnetoelectrocatalysis.

6.1   Future Work on Grätzel Cells

The work on the magnetically modifying Grätzel cells was extensively focused on designing electrodes that incorporated magnetic microparticles. Special attention was paid to the chemical and physical properties of the magnets and how to modify the fabrication of DSSC electrodes accordingly. The properties of the system

and the magnets are not always well aligned. To form mechanically stable layers of semiconductor, for instance, semiconductor films need to be annealed to high temperatures in air. However, at these temperatures in air, spontaneous oxidation of $SmCo_5$ particles occurs. A special tube furnace tube was developed for this problem.

Future studies should attend to the materials properties when fabricating electrodes. However, additional considerations to emphasize the magnetic field effects include the following:

1. Long term analyses are important in determining the commercial utility of magnetic microparticles in Grätzel cells. Industrial standards photovoltaics are rigorous, with stable cyclibility on the order of 20 years [21]. These measurements may be unreasonable for graduate students, but cycles on the order of weeks to months are not.

2. Increasing baseline (control) performance: the analyses performed here paid no special attention to the maximizing system efficiency. Displaying magnetic enhancements versus similarly prepared unmodified controls was the goal. To more further emphasize the magnetic effect, consideration such as blocking layers (e.g., poly(methylsiloxane)) should be taken [18,64].

3. Standardized light source: a light source that meets the industry standard (100 $mW/cm^2$) is desired as incident light intensity has been shown to have implications further than producing greater output power, such as increased fill factors [10]. The source used here had 20 $mW/cm^2$ output power; the accepted standard for photovoltaic testing is 100 $mW/cm^2$ (by the IEEE Standards Association). This is an important difference as the properties of the light used to measure efficiency,

including power, wavelength, and directionality (i.e., direct vs. diffuse) can all influence photovoltaic device efficiency [17, 18].

4. Alternative molecular sensitizers, including quantum dots should be analyzed [40]. Sensitization with quantum dots was briefly explored, however, this work was not given its due diligence. Quantum dot sensitization may shed light on the mechanism for magnetic enhancement in DSSCs. That is, does magnetic enhancement in DSSCs arise from increased heterogeneous or homogeneous ET reactions?

5. Construction of tandem cell. Magnetic microparticles were incorporated in both n-type and p-type electrodes. Combining these electrodes into a single device, where both the cathode and anode are photoactive would increase photocurrent and open circuit potential, in addition to eliminating Pt at the counter electrode [50].

These considerations may further emphasize the impacts of magnetic modification.

## 6.2   Future Work on $MnO_2$ Electrodes

As with the Grätzel cells, magnetic modification of $MnO_2$ electrodes also demonstrated statistically significant enhancements in capacitance. However, these measurements were also on the relatively short time scale (tens of cycles). Again, industrial standards for capacitors are rigorous, with desired cyclibility reaching tens to hundreds of thousands of cycles. In the thin pellet architectures (200 to 300 $\mu$m), testing on these time scales is unreasonable due to internal resistance restrictions,. Thin film (10 to 50 $\mu$m) thousands of cycles can be accomplished in a matter of weeks. Therefore, the first goal of continued research is to develop mechanically

stable, thin layers of $MnO_2$. As was touched upon, the enhanced capacitance should not be architecture dependent; the enhancements observed in Chapter 4 should persist in thin films. Initial attempts at thin films on stainless steel substrates are encouraging because these films return normalized capacitance at literature standards.

Additionally, incorporating electrochemical impedance spectroscopy (EIS) analyses should be performed [19]. Though not a typical lab analysis, these measurements are industry standard. These measurements also help differentiate the nonfaradaic capacitance (i.e., double layer capacitance) from faradaic capacitance (i.e., charge transfer capacitance). Indeed, initial EIS measurements at modified solid state electrodes show increased faradaic capacitance and decreased charge transfer resistance for magnetically modified electrodes versus control electrodes.

Magnetic modification of electrochemical systems is straightforward. Put magnets on an electrodes and see currents increase. However, understanding this phenomenon is anything but. Likewise incorporating these magnets in a manner such that both magnet and electrochemical system are stable is no trivial act. The results observed here, and the results of others before encourage continued research and begin to shed light on how magnetic modification can likely increase performance in a variety of electrochemcial systems.

APPENDIX

DigiSim OUTPUTS OF HETEROGENEOUS FITTING PARAMETERS

A.I   Introduction

The electrochemical simulation software, DigiSim, was used as the principal analysis tool for peak fitting in the heterogeneous analysis for values of $k^0$ of data presented in Chapter 2. DigiSim allows for accurate fitting of wave shape and form from which values of $\alpha$, the transfer coefficient, were determined. Without these simulation, the choice of $\alpha$ is a rough approximation; when the value is unknown, $\alpha$ = 0.5 is assumed (as $0.3 \leq \alpha \leq 0.7$). However, after extensive fitting, it was shown that 0.5 is not an appropriate value for many of the species examined. Indeed, fitting in DigiSim not only allowed for a more accurate determination of the transfer coefficient, but more importantly showed the effects magnetic fields have on the intrinsic reaction barrier, and how this effect is manifested in wave shape and form. Following are the fittings in DigiSim for the transition metal complexes examined. Due to the complex nature of the organic redox species, fittings were not attempted. Overlays of DigiSim outputs, experimental data, and fitting parameters are included.

A.II  Fitting with DigiSim

DigiSim (BASi) allows for the simulation of any first or second order ET reaction. The transition metal complexes analyzed here are all first order, one ET (e)

reactions.

$$A + e \; \rightleftharpoons B \hspace{4cm} (A.1)$$

In addition to the reaction mechanism, DigiSim also requires diffusion constants, for both forward ($D_f$) and backward ($D_b$) chemical species, species solution concentration, standard reduction potential ($E^0$), solution resistance and capacitance, rate constant(s), and transfer coefficient. Diffusion constants, which are determined from experimental data from a plot of $i_p$ versus $v^{1/2}$, concentration, resistances and capacitances are all easily determined experimentally. In some instances, resistance is either removed during the experiment by automatic iR compensation or the resistance was adjusted before fitting in Excel, therefore these values are not included. The merit of DigiSim is that it allows for the determination of $k^0$ and $\alpha$ by fitting. This is a *iterative process*. For the initial simulations, $\alpha$ is estimated at 0.5; this value is adjusted according to the fit the forward wave. The values for D, concentration, $k^0$, and $\alpha$ are all provided.

A.II.i Fitting Tris(bipyridine)ruthenium(II) Chloride

Overlays of experimental data include scan rates (mV/sec) at 5, 25, 50 and 100. However, in DigiSim, data were only generated and overlays produced between 25 and 100 mV/sec. Diffusional conditions required for Nicholson and Shain models may not be satisfied at slow scan rates becuase natural convection can disrupt the diffusion concentration profile. The fitting for DigiSim curves is for the forward wave only because solution capacitance makes fitting experimental data for the reverse wave difficult.
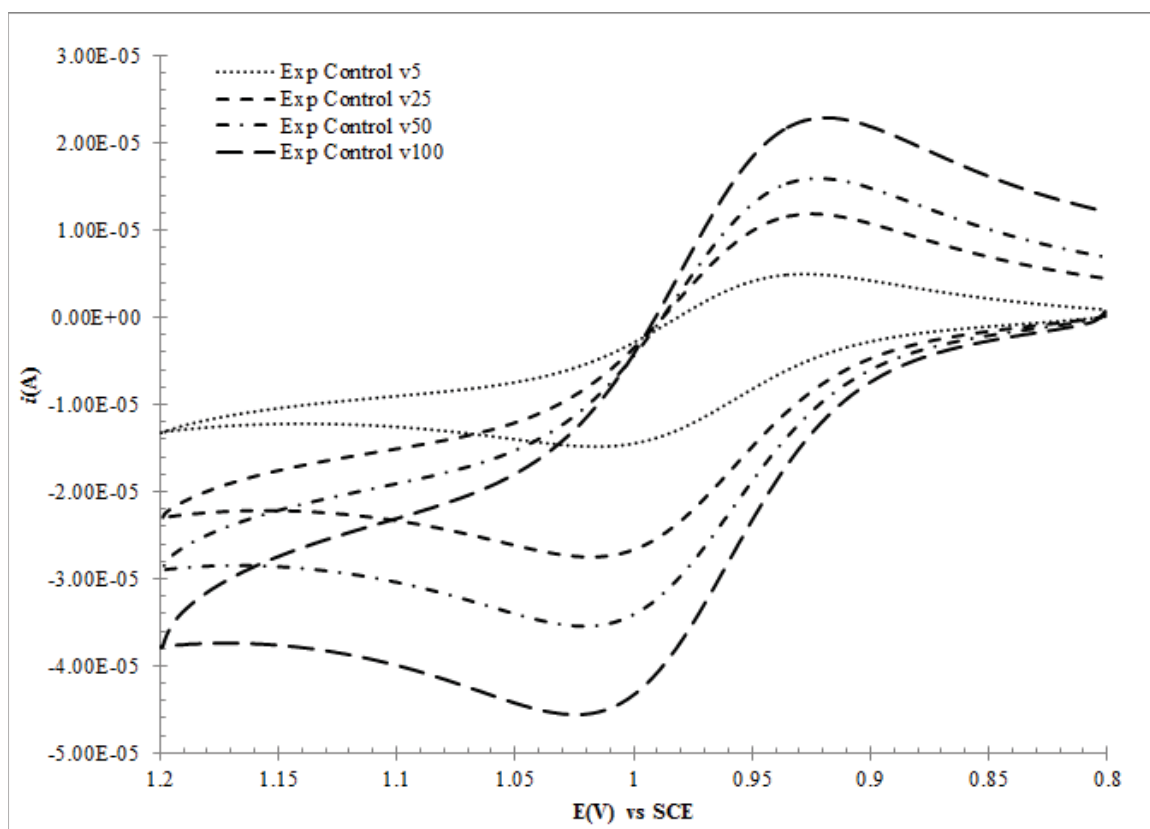
Figure A1. Experimental data for $Ru(bpy)_3^{2+}$ at TMODA Nafion modified glassy carbon rotating disk electrodes ($A_{geo} = 0.458$ cm$^2$). TMODA film thickness $\sim$10 $\mu$m. Constants given in Table 1.
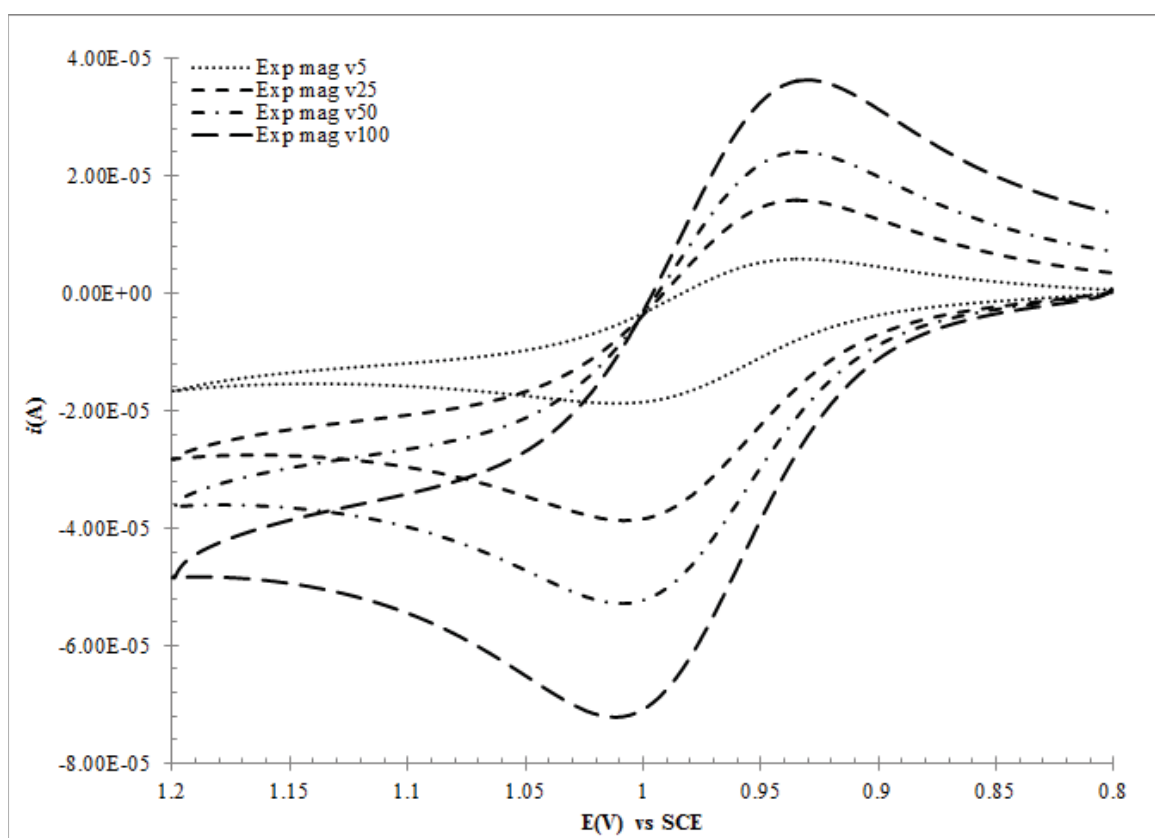
Figure A2. Experimental data for Ru(bpy)$_3^{2+}$ at magnetically modified (BANGS particles at 15 % v/v) TMODA Nafion modified glassy carbon rotating disk electrodes (A$_{geo}$ = 0.458 cm$^2$). TMODA film thickness ~10 $\mu$m. Constants given in Table 1.
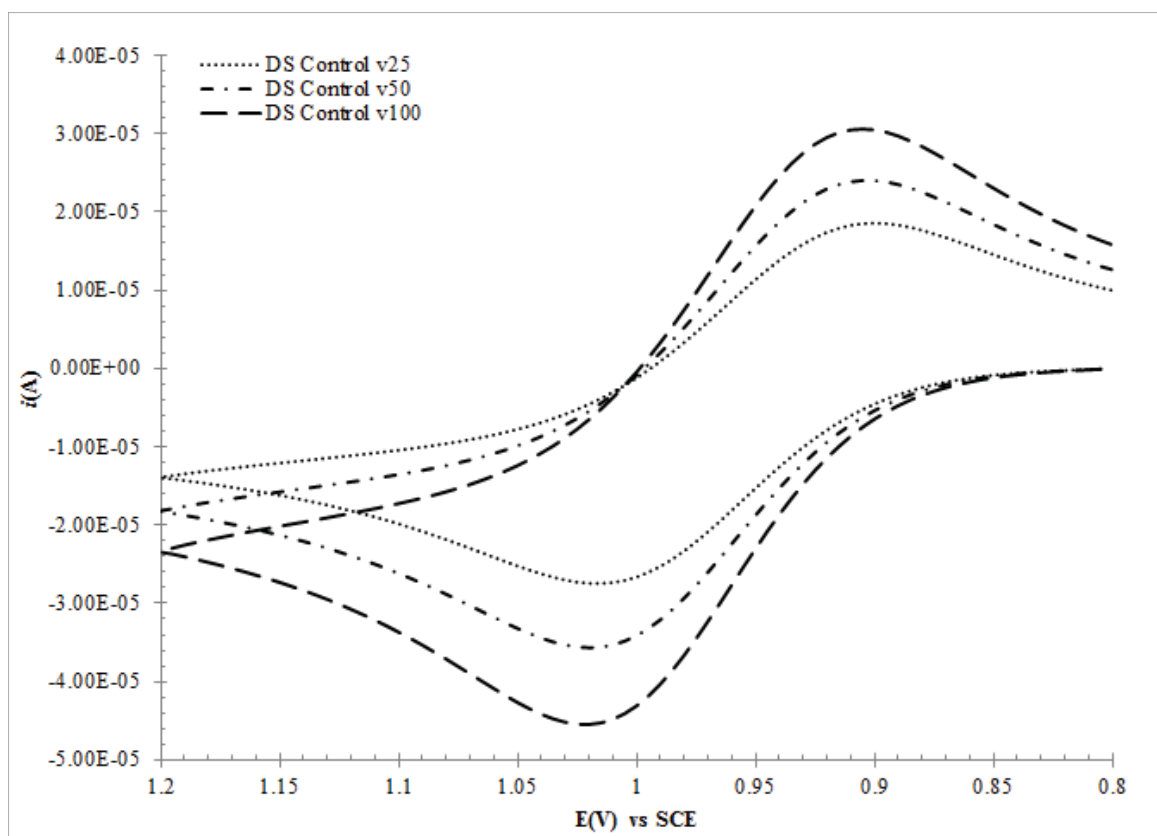
Figure A3. DigiSim (DS) fittings for Ru(bpy)$_3^{2+}$ for control electrode responses (A$_{geo}$ = 0.458 cm$^2$). Scan rates at $v$ = 25, 50 and 100 mV/sec. Constants given in Table 1.

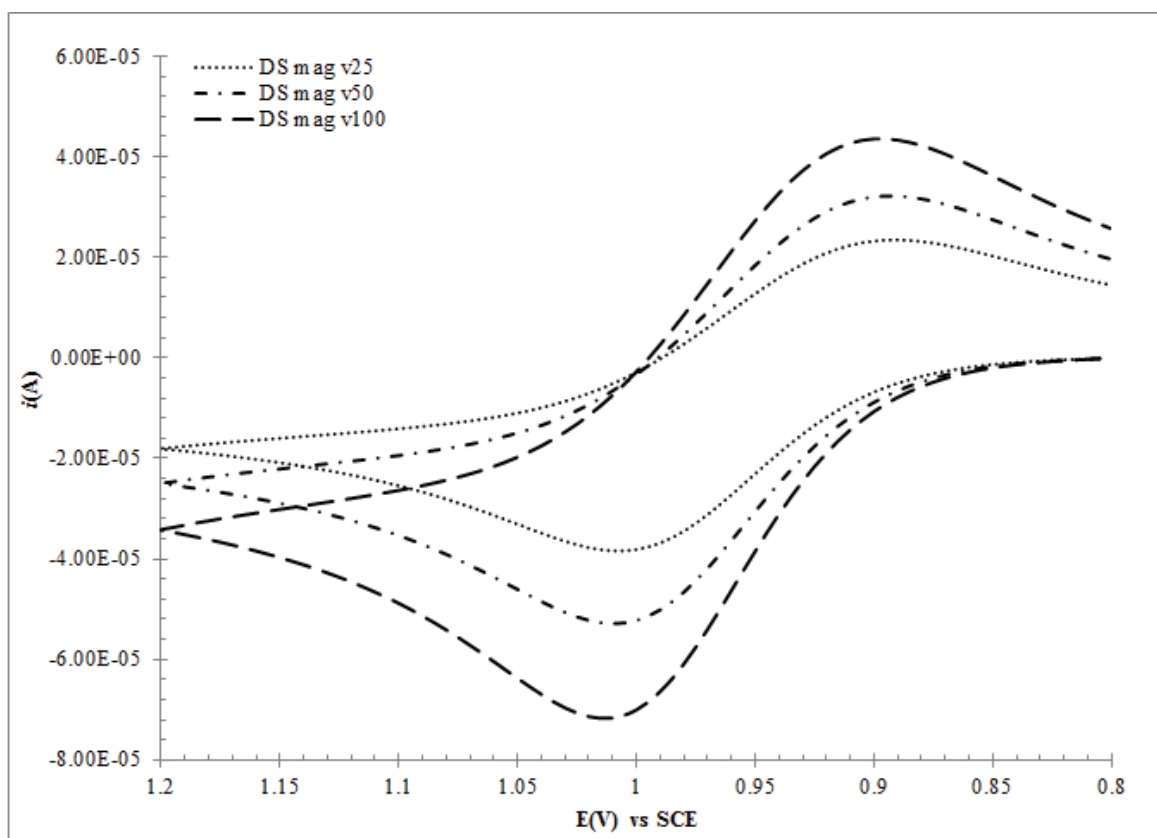Figure A4. DigiSim (DS) fittings for $Ru(bpy)_3^{2+}$ for magnetically (mag) modified electrode responses ($A_{geo} = 0.458$ cm$^2$). Scan rates at $v = 25$, 50 and 100 mV/sec. Constants given in Table 1.

Table A1. Fitting parameters for Ru(bpy) DigiSim fitting.

Ru(bpy)$_3^{2+}$ fitting parameters

|  | Control | Magnetically Modified |
|---|---|---|
| D$_f$ (cm$^2$/sec) | 6.61x10$^{-7}$ | 2.31x10$^{-6}$ |
| D$_b$ (cm$^2$/sec) | 5.20x10$^{-7}$ | 2.01x10$^{-6}$ |
| $v = 25$ mV/sec | | |
| $\alpha$ | 0.5 | 0.4 |
| E$^0$ (V) | 0.959 | 0.951 |
| [probe] (M) | 2.21x10$^{-3}$ | 1.5x10$^{-3}$ |
| k$^0$ (cm/sec) | 5.1x10$^{-4}$ | 9.5x10$^{-4}$ |
| $v = 50$ mV/sec | | |
| $\alpha$ | 0.5 | 0.4 |
| E$^0$ (V) | 0.962 | 0.953 |
| [probe] (M) | 2.03x10$^{-3}$ | 1.46x10$^{-3}$ |
| k$^0$ (cm/sec) | 7.2x10$^{-4}$ | 1.3x10$^{-3}$ |
| $v = 100.0$ mV/sec | | |
| $\alpha$ | 0.5 | 0.4 |
| E$^0$ (V) | 0.964 | 0.957 |
| [probe] (M) | 1.83x10$^{-3}$ | 1.4x10$^{-3}$ |
| k$^0$ (cm/sec) | 1.0x10$^{-3}$ | 1.9x10$^{-3}$ |

A.II.ii Tris(bipyridine)cobalt(II) Chloride

Again, overlays of experimental data include scan rates (mV/sec) at 25, 50 and 100. However, data was only generated and overlays produced between 25 and 100 mV/sec.
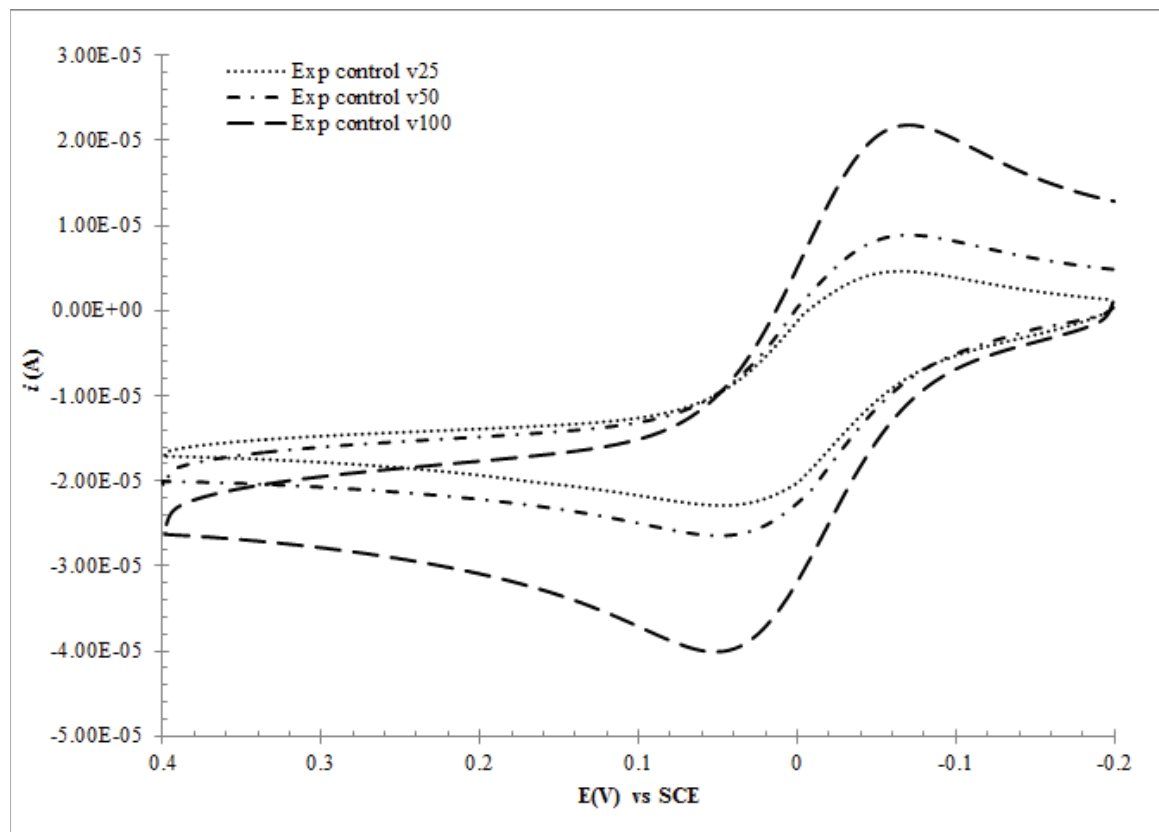


Figure A5. Experimental data for $Co(bpy)_3^{2+}$ at TMODA Nafion modified glassy carbon rotating disk electrodes ($A_{geo} = 0.458$ cm$^2$). TMODA film thickness $\sim$10 $\mu$m. Constants given in Table 2.

A.II.iii Tris(bipyridine)cobalt(III) Chloride

Lastly, overlays of experimental data include scan rates (mV/sec) at 5, 25, 50 and
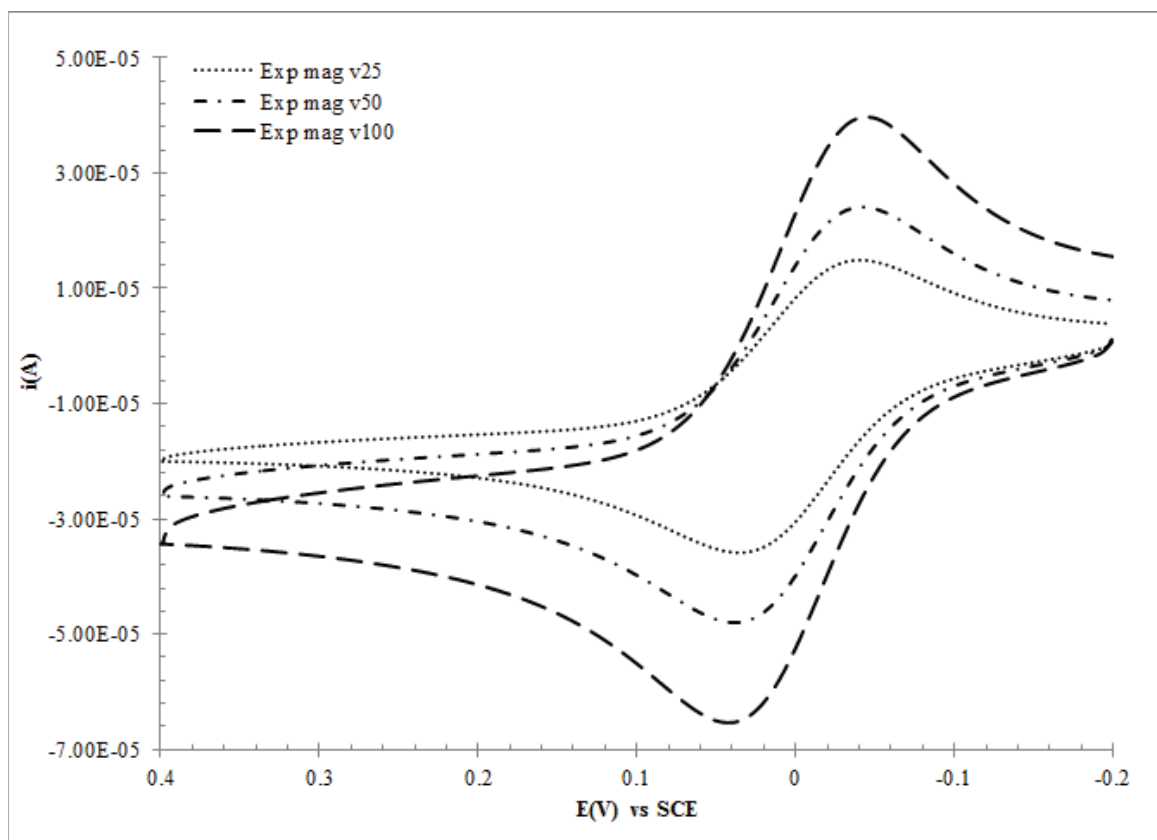
Figure A6. Experimental data for $Co(bpy)_3^{2+}$ at magnetically modfied (BANGS particles at 15 % v/v) TMODA Nafion modified glassy carbon rotating disk electrodes ($A_{geo}$ = 0.458 cm$^2$). TMODA film thickness ∼10 $\mu$m. Constants given in Table 2.
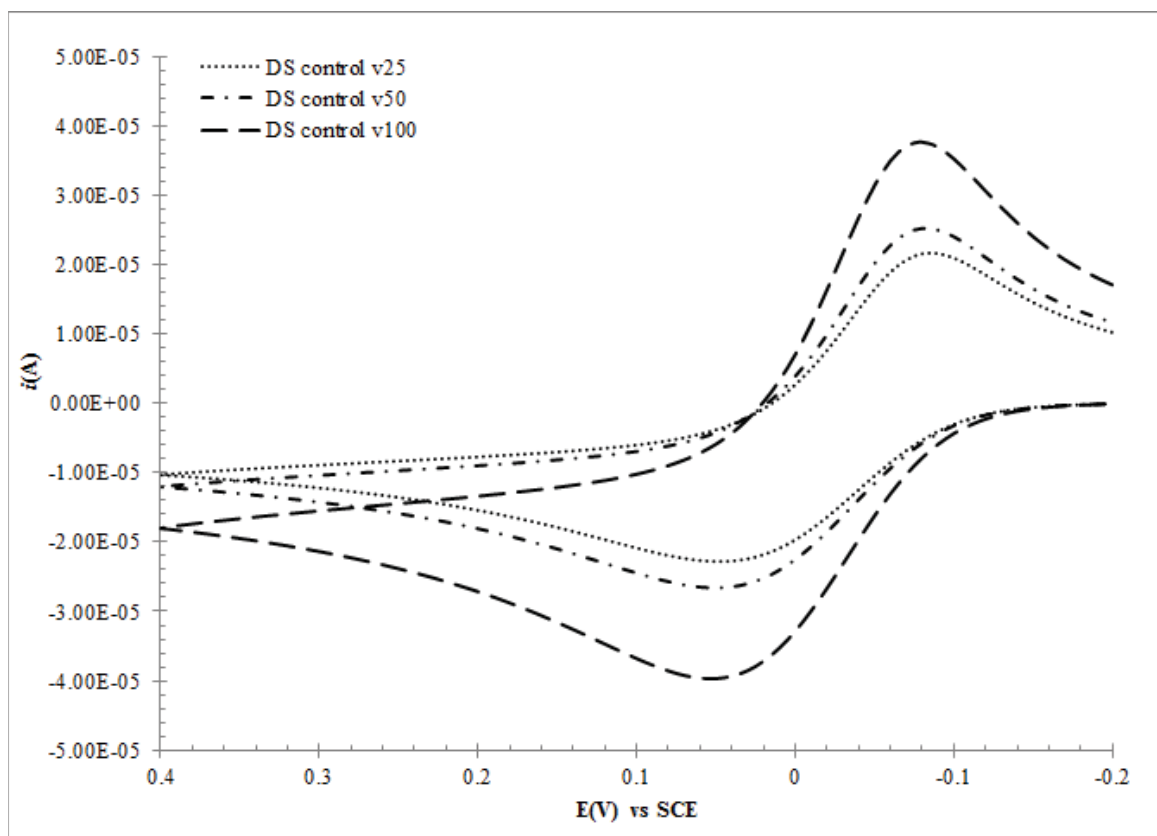
Figure A7. DigiSim (DS) fittings for $Co(bpy)_3^{2+}$ for control electrode responses ($A_{geo}$ = 0.458 cm$^2$). Scan rates at $v$ = 25, 50 and 100 mV/sec. Constants given in Table 2.

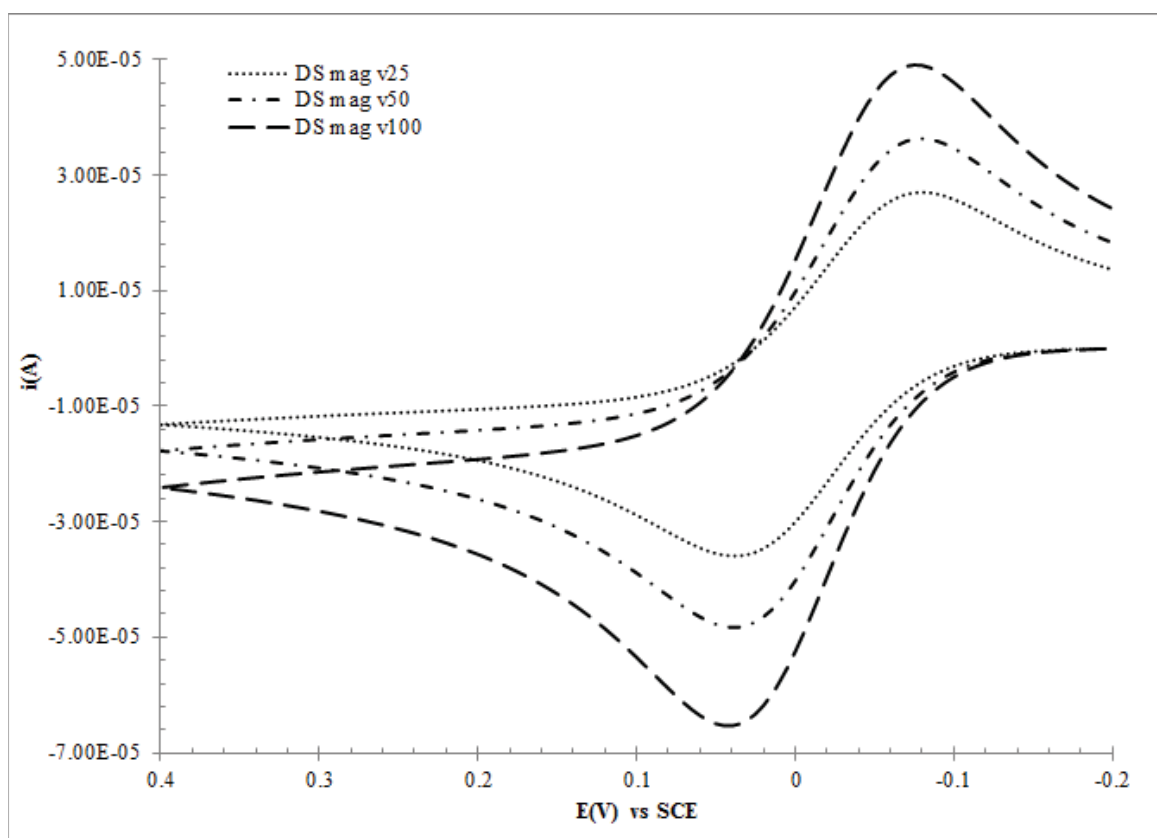Figure A8. DigiSim (DS) fittings for Co(bpy)$_3^{2+}$ for magnetically (mag) modified electrode responses (A$_{geo}$ = 0.458 cm$^2$). Scan rates at $v$ = 25, 50 and 100 mV/sec. Constants given in Table 2.

Table A2. Fitting parameters for Co(II)(bpy) DigiSim fitting.

$Co(bpy)_3^{2+}$ fitting parameters

|  | Control | Magnetically Modified |
|---|---|---|
| $D_f$ (cm$^2$/sec) | $3.85 \times 10^{-7}$ | $1.55 \times 10^{-6}$ |
| $D_b$ (cm$^2$/sec) | $6.34 \times 10^{-7}$ | $2.06 \times 10^{-6}$ |
| $v = 25$ mV/sec | | |
| $\alpha$ | 0.7 | 0.5 |
| $E^0$ (V) | -0.035 | -0.0266 |
| [probe] (M) | $1.98 \times 10^{-3}$ | $1.455 \times 10^{-3}$ |
| $k^0$ (cm/sec) | $3.84 \times 10^{-4}$ | $8.76 \times 10^{-4}$ |
| $v = 50$ mV/sec | | |
| $\alpha$ | 0.7 | 0.5 |
| $E^0$ (V) | -0.032 | -0.0265 |
| [probe] (M) | $1.63 \times 10^{-3}$ | $1.37 \times 10^{-3}$ |
| $k^0$ (cm/sec) | $5.5 \times 10^{-4}$ | $1.24 \times 10^{-3}$ |
| $v = 100.0$ mV/sec | | |
| $\alpha$ | 0.7 | 0.5 |
| $E^0$ (V) | -0.029 | -0.023 |
| [probe] (M) | $1.72 \times 10^{-3}$ | $1.31 \times 10^{-3}$ |
| $k^0$ (cm/sec) | $7.81 \times 10^{-4}$ | $1.76 \times 10^{-3}$ |

100. However, data were only simulated and overlays produced between 25 and 100

mV/sec.



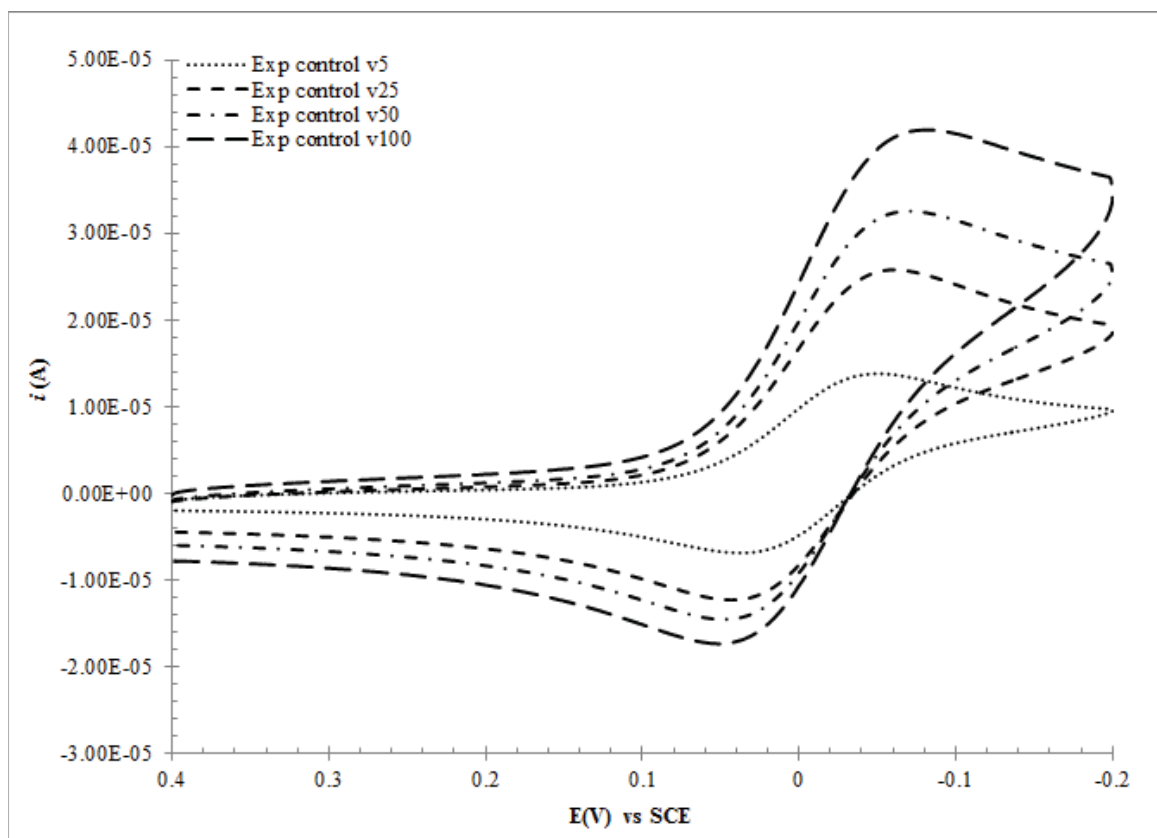Figure A9. Experimental data for $Co(bpy)_3^{3+}$ at TMODA Nafion modified glassy carbon rotating disk electrodes ($A_{geo} = 0.458$ cm$^2$). TMODA film thickness $\sim$10 $\mu$m. Constants given in Table 3.

A.II.iv Potassium ferricyanide, $K_3Fe(CN)_6$

Overlays of experimental data include scan rates (mV/sec) at 20, 50 and 100.

However, data was only generated and overlays produced between 20 and 100

mV/sec.
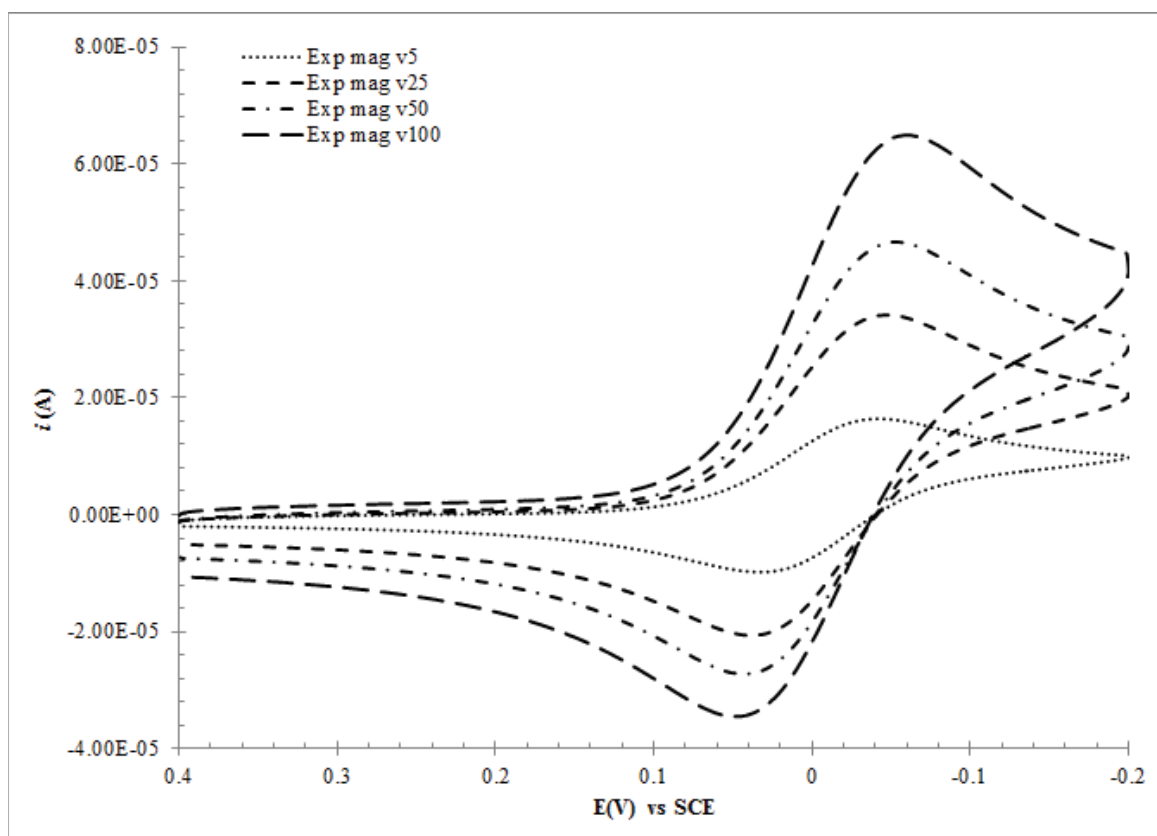
Figure A10. Experimental data for Co(bpy)$_3^{3+}$ at magnetically modfied (BANGS particles at 15 % v/v) TMODA Nafion modified glassy carbon rotating disk electrodes ($A_{geo}$ = 0.458 cm$^2$). TMODA film thickness ~10 $\mu$m. Constants given in Table 3.
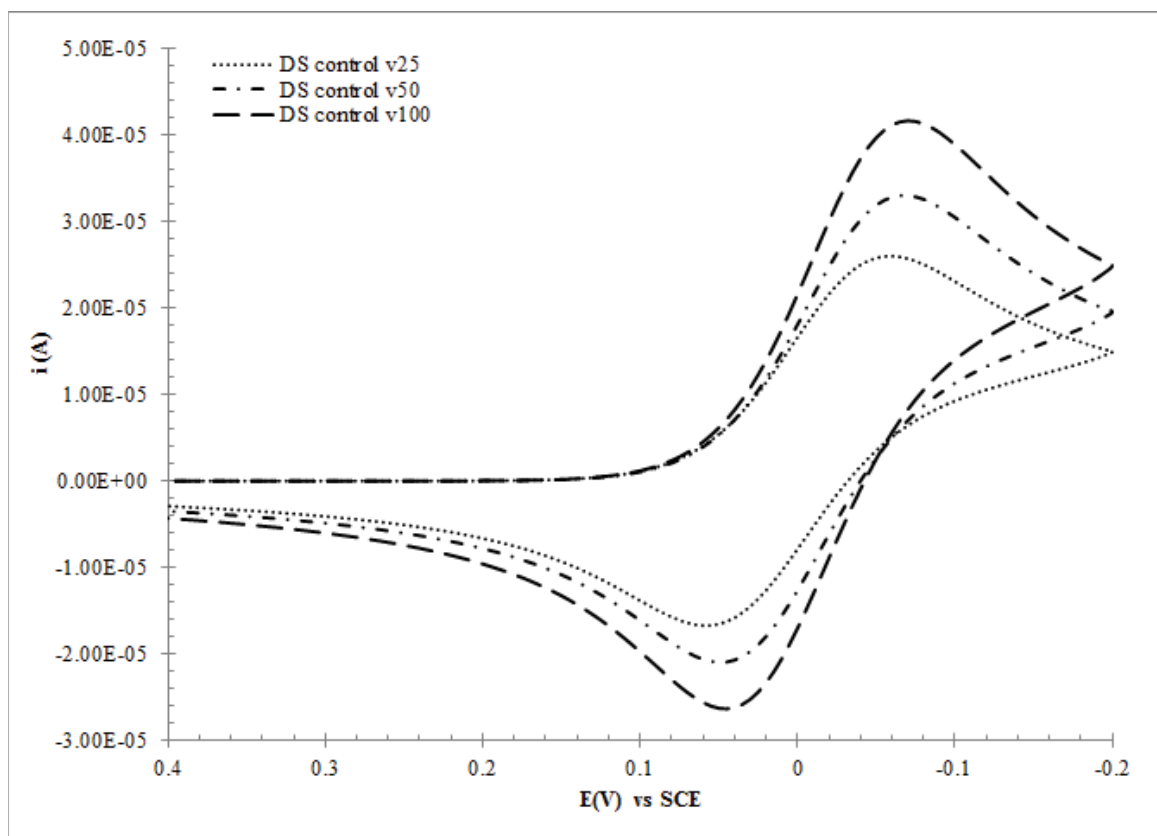
Figure A11. DigiSim (DS) fittings for Co(bpy)$_3^{3+}$ for control electrode responses (A$_{geo}$ = 0.458 cm$^2$). Scan rates at $v$ = 25, 50 and 100 mV/sec. Constants given in Table 3.
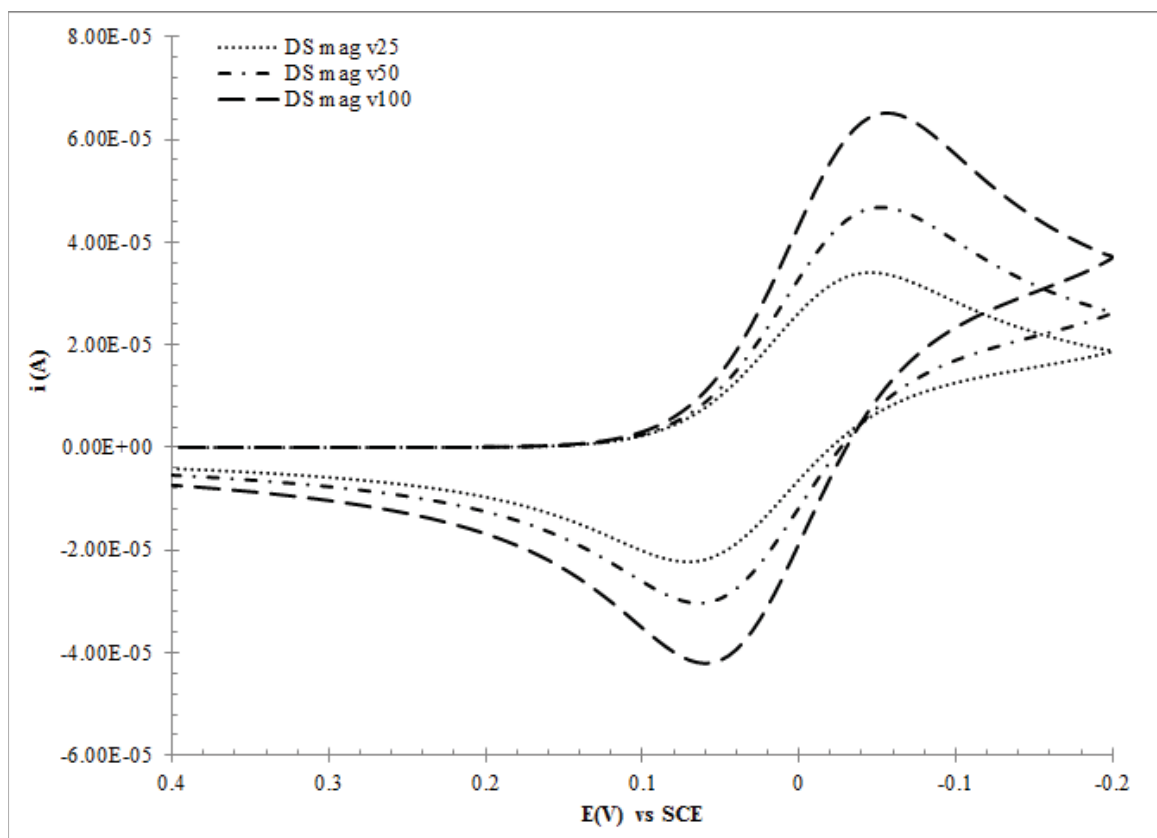
Figure A12. DigiSim (DS) fittings for $Co(bpy)_3^{3+}$ for magnetically (mag) modified electrode responses ($A_{geo} = 0.458$ cm$^2$). Scan rates at $v = 25$, 50 and 100 mV/sec. Constants given in Table 3.

Table A3. Fitting parameters for Co(III)(bpy) DigiSim fitting.

$Co(bpy)_3^{3+}$ fitting parameters

|  | Control | Magnetically Modified |
|---|---|---|
| $D_f$ (cm$^2$/sec) | $5.99x10^{-7}$ | $2.21x10^{-6}$ |
| $D_b$ (cm$^2$/sec) | $4.69x10^{-8}$ | $5.56x10^{-7}$ |
| $v = 25$ mV/sec |  |  |
| $\alpha$ | 0.5 | 0.5 |
| $E^0$ (V) | 0.035 | 0.033 |
| [probe] (M) | $1.95x10^{-3}$ | $1.33x10^{-3}$ |
| $k^0$ (cm/sec) | $2.7x10^{-4}$ | $7x10^{-4}$ |
| $v = 50$ mV/sec |  |  |
| $\alpha$ | 0.5 | 0.5 |
| $E^0$ (V) | 0.026 | 0.026 |
| [probe] (M) | $1.75x10^{-3}$ | $1.29x10^{-3}$ |
| $k^0$ (cm/sec) | $3.8x10^{-4}$ | $1x10^{-3}$ |
| $v = 100.0$ mV/sec |  |  |
| $\alpha$ | 0.5 | 0.5 |
| $E^0$ (V) | 0.023 | 0.022 |
| [probe] (M) | $1.56x10^{-3}$ | $1.27x10^{-3}$ |
| $k^0$ (cm/sec) | $5.4x10^{-4}$ | $1.42x10^{-3}$ |

Table A4. Fitting parameters for ferricyanide DigiSim fitting.

$Fe(CN)_6^{3-}$ fitting parameters

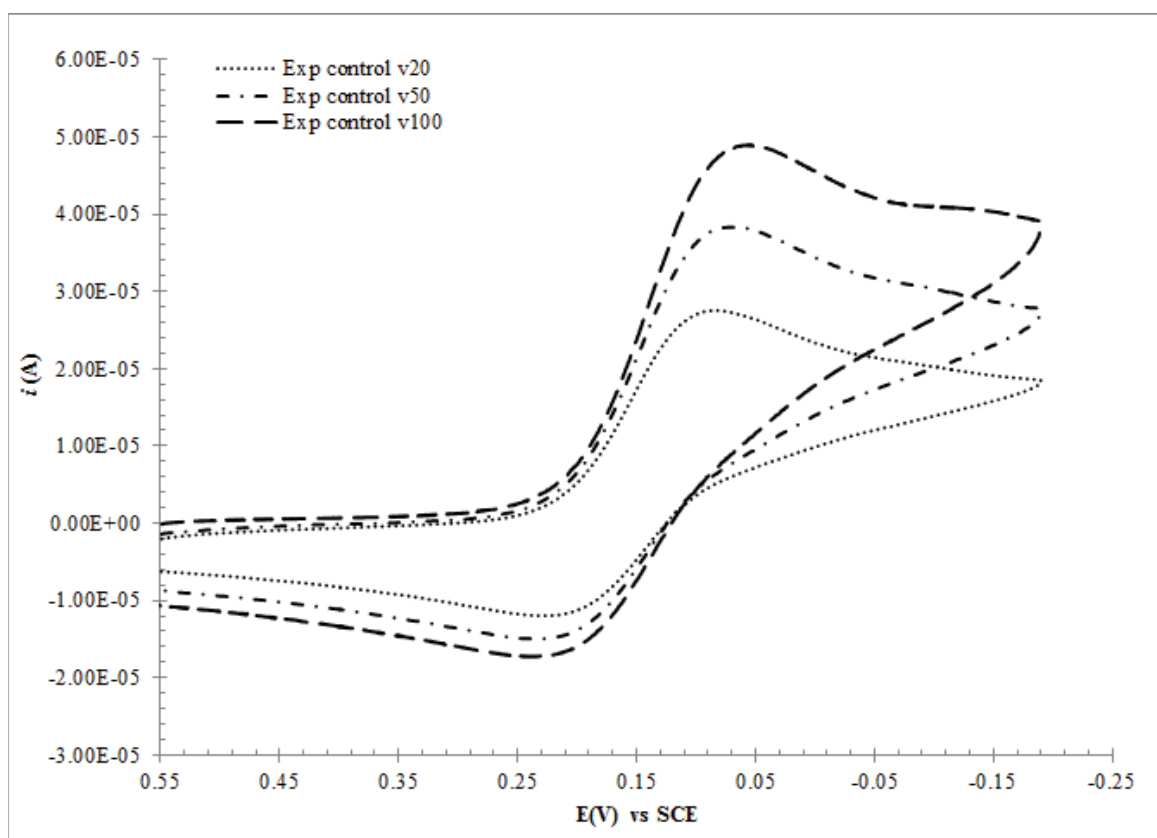|  | Control | Magnetically Modified |
|---|---|---|
| $D_f$ (cm$^2$/sec) | $9.06x10^{-7}$ | $9.66x10^{-6}$ |
| $D_b$ (cm$^2$/sec) | $7.04x10^{-8}$ | $3.22x10^{-6}$ |
| $v = 20$ mV/sec |  |  |
| $\alpha$ | 0.5 | 0.5 |
| $E^0$ (V) | 0.193 | 0.199 |
| [probe] (M) | $1.22x10^{-3}$ | $1.06x10^{-3}$ |
| $k^0$ (cm/sec) | $4.87x10^{-4}$ | $1.38x10^{-3}$ |
| $v = 50$ mV/sec |  |  |
| $\alpha$ | 0.5 | 0.5 |
| $E^0$ (V) | 0.175 | 0.192 |
| [probe] (M) | $1.64x10^{-3}$ | $1.1x10^{-3}$ |
| $k^0$ (cm/sec) | $3.1x10^{-4}$ | $2.2x10^{-3}$ |
| $v = 100.0$ mV/sec |  |  |
| $\alpha$ | 0.5 | 0.5 |
| $E^0$ (V) | 0.164 | 0.19 |
| [probe] (M) | $1.48x10^{-3}$ | $1.17x10^{-3}$ |
| $k^0$ (cm/sec) | $6.92x10^{-4}$ | $3.1x10^{-3}$ |

Figure A13. Experimental data for Fe(CN)$_6^{3-}$ at TMODA Nafion modified glassy carbon rotating disk electrodes (A$_{geo}$ = 0.458 cm$^2$). TMODA film thickness ∼10 $\mu$m. Constants given in Table 4.

Figure A14. Experimental data for Fe(CN)$_6^{3-}$ at magnetically modfied (BANGS particles at 15 % v/v) TMODA Nafion modified glassy carbon rotating disk eletrodes (A$_{geo}$ = 0.458 cm$^2$). TMODA film thickness ~10 $\mu$m. Constants given in Table 4.
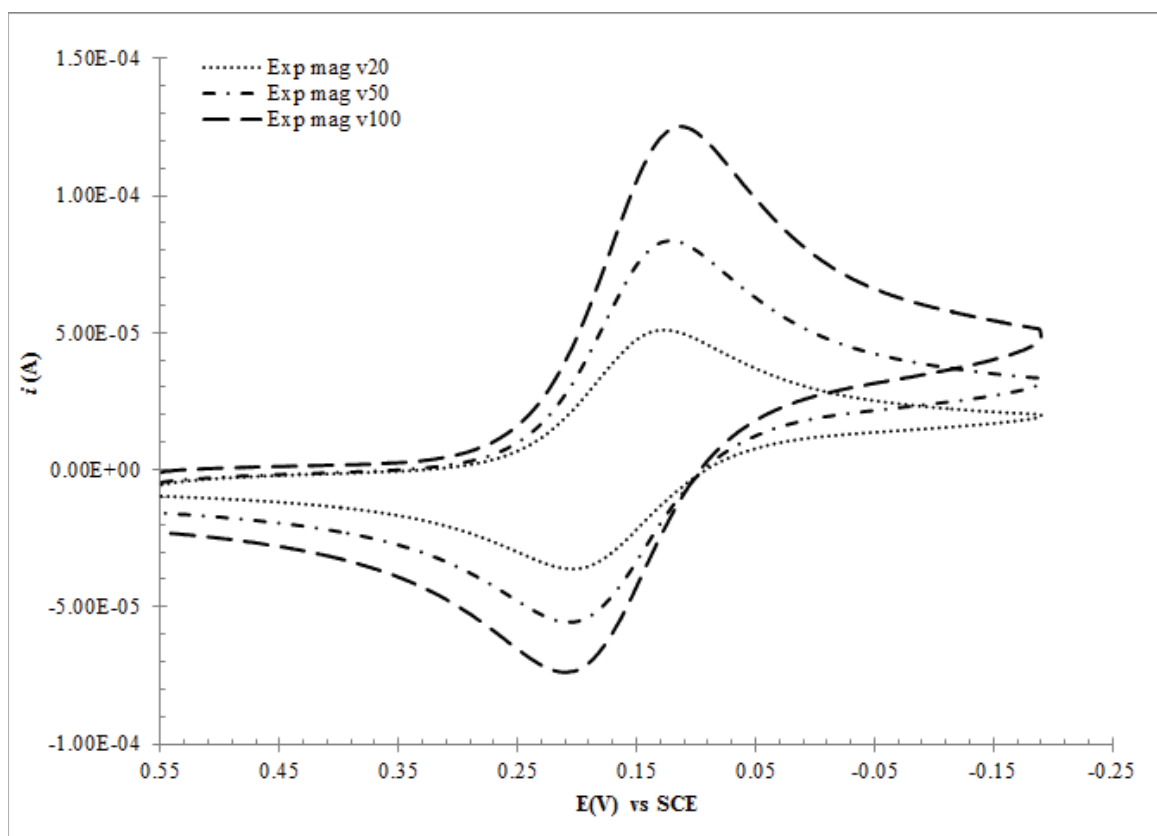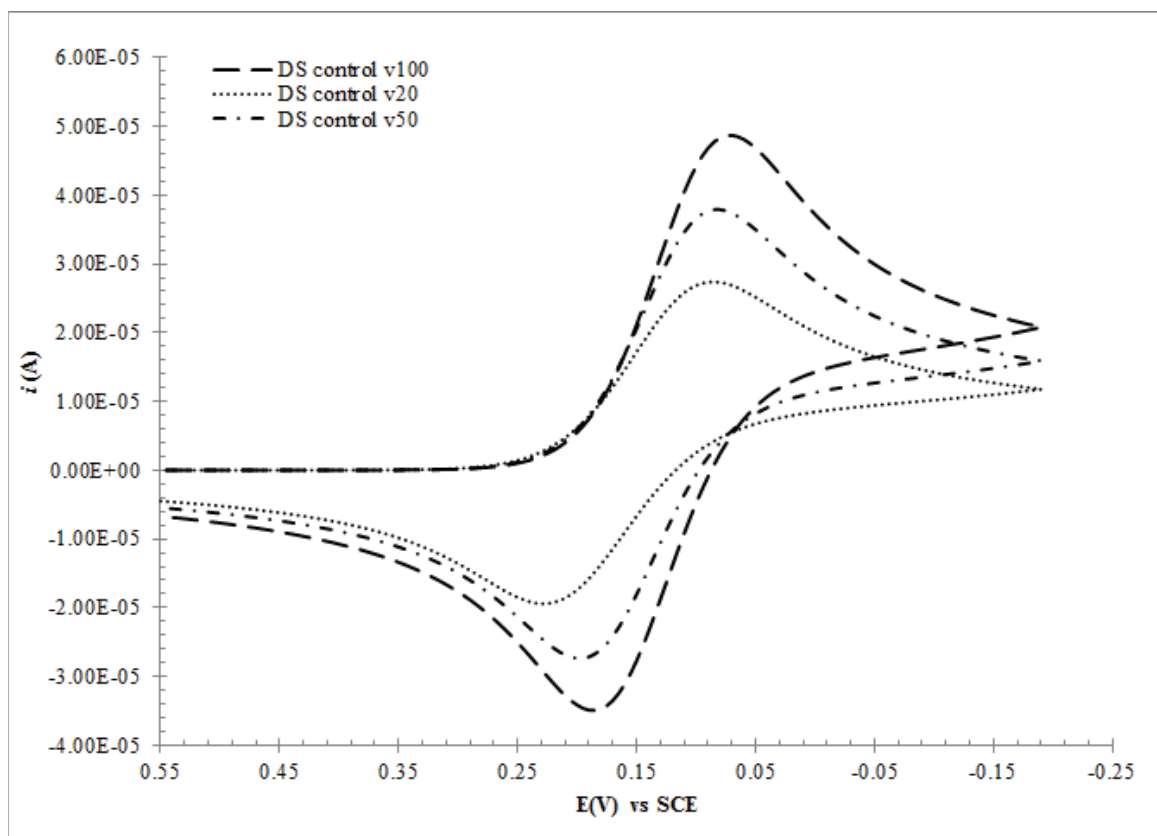
Figure A15. DigiSim (DS) fittings for $Fe(CN)_6^{3-}$ for control electrode responses ($A_{geo}$ = 0.458 cm$^2$). Scan rates at $v$ = 25, 50 and 100 mV/sec. Constants given in Table 4.

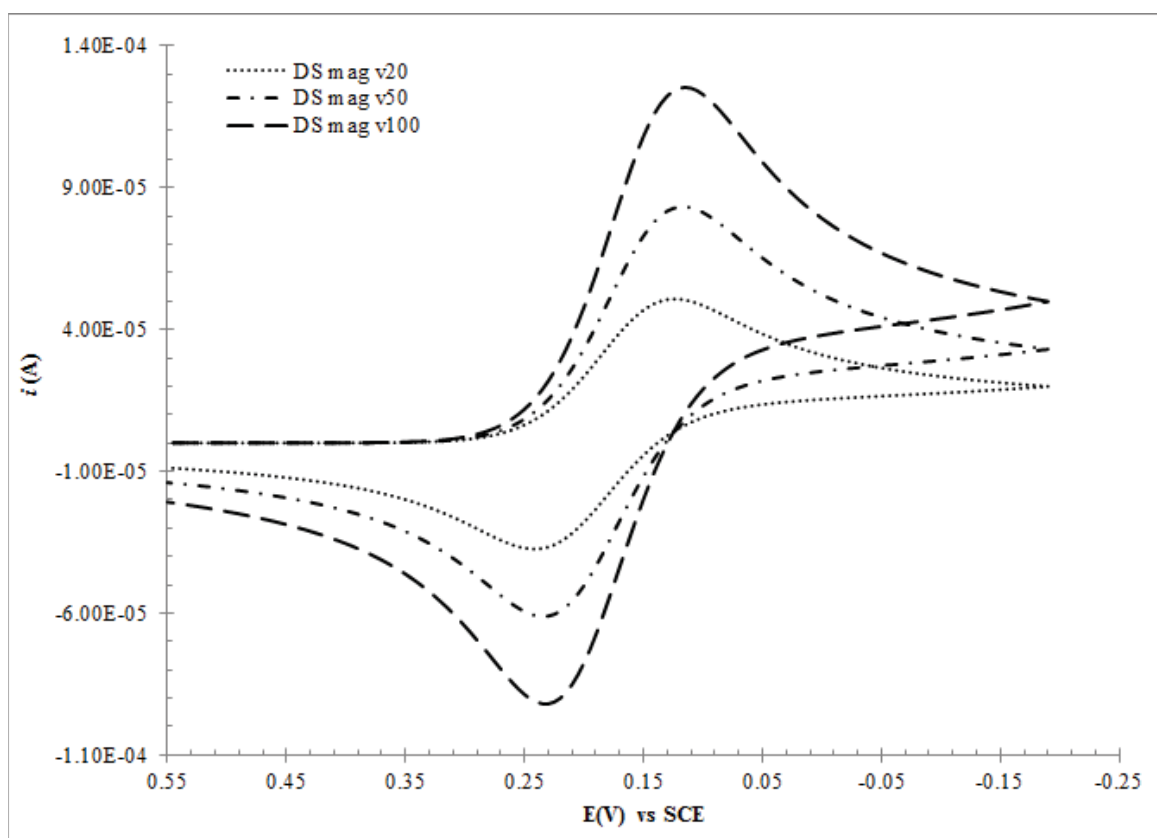Figure A16. DigiSim (DS) fittings for Fe(CN)$_6^{3-}$ for magnetically (mag) modified electrode responses ($A_{geo} = 0.458$ cm$^2$). Scan rates at $v = 25$, 50 and 100 mV/sec. Constants given in Table 4.

# REFERENCES

[1] Bard, A. J.; Faulkner, L. R. *Electrochemical Methods: Fundamentals and Applications;* John Wiley and Sons: Hoboken, 2nd Edition ed.; 2001.

[2] Julien, C.; Massot, M.; Rangan, S.; Lemal, M.; Guyomard, D. *J. Raman Spectrosc.* **2002,** *33,* 223-228.

[3] Atkins, P.; Paula, J. P. *Atkins' Physical Chemistry;* W. H. Freeman and Company: New York, 8th ed.; 2006.

[4] Lewis, N. S.; Nocera, D. G. *PNAS* **2006,** *103,* 15729-15735.

[5] Bradsher, K. "China Outpaces U.S. in Cleaner Coal-Fired Plants", 2009.

[6] Lewis, N. S. *ChemSusChem* **2009,** *2,* 383-386.

[7] Olah, G. A.; Goeppert, A.; Prakash, G. K. S. *J. Org. Chem.* **2009,** *74,* 487-498.

[8] Tna, M. X.; Laibinis, P. E.; Nquyen, S. T.; Kesselman, J. M.; Stanton, C. E.; Lewis, N. S. Priciples and Applications of Semiconductor Photoelectrochemistry. In , Vol. 41; Karlin, K. D., Ed.; John Wiley and Sons, Inc.: 1994.

[9] Yella, A.; Lee, H. W.; Tsao, H. N.; Yi, C.; Chandiran, A. K.; Nazeeruddin, M. K.; Diau, E. W. G.; Yeh, C. Y.; Zakeeruddin, S. M.; GrÃd'tzel, M. *Science* **2012,** *334,* 629-634.

[10] Hagfeldt, A.; Boschloo, G.; Sun, L.; Kloo, L.; Pettersson, H. "Dye-Sensitized Solar Cells", 2010.

[11] Minteer, S. D. *Magnetic Field Effects on Electron Transfer Reactions,* Thesis, The University of Iowa, 2000, 2000.

[12] Gellett, W. L. *Magnetic Microparticles on Electrodes: Polymer Electrolyte Membrane Fuel Cells, Carbon Monoxide Oxidation, and Transition Metal Complex Electrochemistry,* Thesis, The University of Iowa, 2004, 2004.

[13] Lee, H. C. *Magnetic Field Effects on Electron Transfer Reactions: Heterogeneous Photoelectrochemical Hydrogen Evolution and Homogeneous Self Exchange Reactions,* Thesis, The University of Iowa, 2011, 2011.

[14] Dunwoody, D. *Magnetically Modified Polymer Electrolyte Fuel Cells and Low Temperature Effects on Polymer Electrolyte Nafion,* PhD. thesis, The University of Iowa, 2003, 2003.

[15]   Tesene, J. P. *Magnetically-Treated Electrolytic Manganese Dioxide in Alkaline Electrolyte,* Thesis, The University of Iowa 2005, 2005.

[16]   Unlu, M. *Coated Magnetic Particles in Electrochemical Systems: Synthesis, Modified Electrodes, Alkaline Batteries, and Paste Electrodes,* PhD. thesis, The University of Iowa, 2008, 2008.

[17]   O'Regan, B.;  Gratzel, M. *Nature* **1991,** *353,* 737-740.

[18]   Ramamurthy, V.;  Schanze, K. S.,  Eds.; *Semiconductor Photochemistry and Photophysics;* volume 10 of *Molecular and Supramolecular Photochemistry* Marcel Dekker, Inc.: New York, 2003.

[19]   Conway, B. E. *Electrochemical Capacitors: Scientific Fundamentals and Technological Applications;* Kluwer Academic / Plenum Publishers: New York, 1999.

[20]   Zheng, J. P.;  Jow, T. R. *J. Electrochem. Soc.* **1995,** *142,* L6-L8.

[21]   Brousse, T.;  Toupin, M.;  Belanger, D. *J. Electrochem. Soc.* **2004,** *151,* A614-A622.

[22]   Klotzbach, T.;  Watt, M.;  Anasari, Y.;  Minteer, S. D. *J. Membrane Sci.* **2006,** *282,* 276-283.

[23]   Besic, S.;  Minteer, S. D. Micellar Polymer Encapsulation of Enzymes. In *Methods in Molecular Biology: Enzyme Stabilization and Immobilization,* Vol. 679; Minteer, S. D.,  Ed.; Springer: New York, 2011.

[24]   Nicholson, R. S. *Anal. Chem.* **1965,** *37,* 667-371.

[25]   Nicholson, R. S. *Anal. Chem.* **1965,** *37,* 1351-1354.

[26]   Paul, H. J.;  Leddy, J. *Anal. Chem.* **1995,** *67,* 1661-1668.

[27]   He, R.;  Faulkner, L. R. *Anal. Chem.* **1986,** *58,* 517-523.

[28]   Caramori, S.;  Cristino, V.;  Argazzi, R.;  Meda, L.;  Bignozzi, C. A. *Inorg. Chem.* **2010,** *49,* 3320-3328.

[29]   Youngblood, W. J.;  Lee, S.-H. A.;  Maeda, K.;  Mallouk, T. E. *Acct. Chem. Res.* **2009,** *42,* 1966-1973.

[30]   Chi, C.-F.;  Liau, S.-Y.;  Lee, Y.-L. *Nanotech.* **2010,** *21,* 6pp.

[31]   Hagfeldt, A.;  GrÃd'tzel, M. *Acct. Chem. Res.* **2000,** *33,* 269-277.

[32] Hossain, M. F.; Biswas, S.; Shahjahan, M.; Majumder, A.; Takahashi, T. *J. Vac. Sci. Technol. A* **2009,** *27,* 1042-1046.

[33] Brooks, K. G.; Burnside, S. D.; Shklover, V.; Comte, P.; Arendse, F.; McEvoy, A.; GrÃd'tzel, M. *Electrochem. Mat. Devices* **?,** 115-122.

[34] Santulli, A. C.; Koenigsmann, C.; Tiano, A. L.; DeRosa, D.; Wong, S. S. *Nanotech.* **2011,** *22,* 1-13.

[35] Agrios, A. G.; Cesar, I.; Comte, P.; Nazeeruddin, M. K.; GrÃd'tzel, M. *Chem. Mater.* **2006,** *18,* 5395-5397.

[36] Stergiopoulos, T.; Karakostas, S.; Falaras, P. *J. Photochem. Photobio. A: Chem.* **2004,** *163,* 331-340.

[37] Cazzanti, S.; Caramori, S.; Argazzi, R.; Elliott, C. M.; Bignozzi, C. A. *J. Am. Chem. Soc.* **2006,** *128,* 9996-9997.

[38] Yanagida, M.; Yamaguchi, T.; Kurashinge, M.; Hara, K.; Katoh, R.; Sugihara, H.; Arakawa, H. *Inorg. Chem.* **2003,** *42,* 7921-7931.

[39] Hasobe, T.; Hattori, S.; Kamat, P. V.; Urano, Y.; Umezawa, N.; Nagano, T.; Fukuzumi, S. *Chem. Phys.* **2005,** *319,* 243-252.

[40] Lee, H.; Leventis, H. C.; Moon, S. J.; Chen, P.; Ito, S.; Haque, S. A.; Torres, T.; NÃijesch, F.; Geiger, T.; Zakeeruddin, S. M.; GrÃd'tzel, M.; Nazeeruddin, M. K. *Adv. Funct. Mater.* **2009,** *19,* 2735-2742.

[41] Paci, I.; Johnson, J. C.; Chen, X.; Rana, G.; Popovic, D.; David, D. E.; Nozik, A. J.; Ratner, M. A.; Michl, J. *J. Am. Chem. Soc.* **2006,** *128,* 16546-16553.

[42] Siggh, P. K.; Bhattacharya, D.; Nagarale, R. K.; Kim, K.-W.; Rhee, H.-W. *Syn. Mat.* **2010,** *160,* 139-142.

[43] Buraudah, M. H.; Teo, L. P.; Majid, S. R.; Arof, A. K. *Optical Mat.* **2010,** *32,* 723-728.

[44] Buraidah, M. H.; Teo, L. P.; Majid, S. R.; Yahya, R.; Taha, R.; Arof, A. K. *Int. J. Photoenergy* **2010,** *2010,.*

[45] Katasaros, G.; Stergiopoulos, T.; Arabatzis, I. M.; Papadokostaki, K. G.; Falaras, P. *J. Photochem. Photobio. A: Chem.* **2002,** *149,* 191-198.

[46] Kim, J. H.; Kang, M.-S.; kim, Y. J.; Won, J.; Park, N.-G.; Kang, Y. S. *Chem. Commum.* **2004,** 1662-1663.

[47] Bai, Y.; Cao, Y.; Zhang, J.; Wang, M.; Li, R.; Wang, P.; Zakeeruddin, S. M.; GrÃd'tzel, M. *Nature* **2008,** *7,* 626-630.

[48] Ito, S.; Murakami, T. N.; Comte, P.; Liska, P.; GrÃd'tzel, C.; Nazeeruddin, M. K.; GrÃd'tzel, M. *Thin Solid Films* **2008,** *516,* 4613-4619.

[49] Pragnell, W. M.; Williams, A. J.; Evans, H. E. *Journal of Applied Physics* **2008,** *103,* 1-3.

[50] Nattestad, A.; Ferguson, M.; Kerr, R.; Cheng, Y.-B.; Back, U. *Nanotech.* **2008,** *19,* 9pp.

[51] Lindstrom, H.; Bschloo, G.; Lindquist, S.-E.; Hagfeldt, A. A New Method for Manufacturing Dye-Sensitized Solar Cells on Plastic Substrates. In *Molecules as Components of Electronic Devices*; Lieberman, M., Ed.; American Chemical Soc.: Washington, D.C., 2003.

[52] Ardo, S.; Meyer, G. J. *J. Am. Chem. Soc.* **2011,** *133,* 15384-15396.

[53] Odobel, F.; Pleux, L. L.; Pellegrin, Y.; Blart, E. *Acct. Chem. Res.* **2009,** *43,* 1063-1071.

[54] Mizoguchi, Y.; Shinobu, F. *Electrochem. Solid-State Lttrs.* **2008,** *11,* K78-K80.

[55] Ducharme, S. *ACS Nano* **2009,** *3,* 2447-2450.

[56] Miller, J. R.; Burke, A. F. *Interface* **2008,** *Spring 2008,* 53-57.

[57] Roberts, A. J.; Slade, R. C. T. *Electrochem. Acta.* **2010,** *55,* 7460-7469.

[58] Ragupathy, P.; Vasan, H. N.; Munichandraiah, N. *J. Electrochem. Soc.* **2008,** *155,* A34-A40.

[59] Lee, H. Y.; Goodenough, J. B. *J. Solid State Chem.* **1999,** *144,* 220-223.

[60] Wen, S.; Yeo, I.-H.; Park, J.; il Mho, S. *Key Eng. Mater.* **2005,** *277-279,* 703-707.

[61] Kim, H.; Popov, B. N. *J. Electrochem. Soc.* **2003,** *150,* D56-D62.

[62] Toupin, M.; Brousse, T.; Belanger, D. *Chem. Mater.* **2002,** *14,* 3946-3952.

[63] Demarconnay, L.; Raymundo-Pinero, E.; Beguin, F. *J. Power Sources* **2011,** *196,* 580-586.

[64] Palomares, E.; Clifford, J. N.; Haque, S. A.; Lutz, T.; Durrant, J. R. *J. Am. Chem. Soc.* **2003,** *125,* 475-482.